

Charles University in Prague
Faculty of Mathematics and Physics

**MICROSTRUCTURE AND PROPERTIES
OF NANOCRYSTALLINE HARD COATINGS
AND THIN FILM NANOCOMPOSITES**

DOCTORAL THESIS



Milan Dopita

Supervisor: Prof. RNDr. David Rafaja, CSc.

F3 – Physics of condensed matter and material research

Prague, 2009

Motto: „JSTE TÍM, JAKÁ JE VAŠE HLUBOKÁ ŽÁDOST, JEŽ VÁS POHÁNÍ.
JAKÁ JE VAŠE ŽÁDOST – TAKOVÁ JE I VAŠE VŮLE. JAKÁ JE VAŠE
VŮLE – TAKOVÉ JSOU VAŠE SKUTKY. JAKÉ JSOU VAŠE SKUTKY –
TAKOVÝ JE VÁŠ OSUD...”

Acknowledgements:

I would like to express my sincere gratitude to my supervisor Prof. Dr. David Rafaja for the continuous support of my Ph.D. study and research, for his patience, motivation, enthusiasm, and immense knowledge. His guidance helped me in all the time of research and completing of this thesis.

Besides my supervisor, I would like to thank my dear colleague Dipl. Ing. Christina Wüstefeld for her help, support, interest and valuable hints concerning my thesis and for friendly and pleasant working environment.

I thank my colleagues from the Institute of Materials Science, Technical University of Freiberg, namely Dr. Volker Klemm for the TEM and HRTEM investigations, Dr. Dietrich Heger for the EPMA/WDX and GDOES measurements and Dipl. Phys. Gerhard Schreiber for help with the X-ray measurements.

My sincere thanks also go to Dr. Ing. Thomas Modes and Dr. Ing. Olaf Zywitzki from Fraunhofer Institute for Electron Beam and Plasma Technology, Dresden for hardness measurements on the Nano Indenter XP device.

I also want to thank Dr. Michal Šíma from SHM Šumperk for the CAE coatings preparation, and my colleagues Prof. Dr. Radomír Kužel and Mag. Zdeněk Matěj from the Department of Condensed Matter Physics, Charles University in Prague for fruitful and helpful discussions concerning my scientific work.

Last but not the least I would like to give my special thanks to my wife Petra whose patient love enabled me to complete this work and to my son Kryštof, to whom I still believe that his face-plays and shouts are expressions of his agreement and huge admiration to his father... . To them I dedicate this thesis.

Declaration of Originality:

I hereby declare that this thesis is presentation of my original research work. Information derived from the published and unpublished work of others has been acknowledged in the text and a list of references is given in the bibliography.

Freiberg, July 2009.

Milan Dopita

Contents:

Chapter 1

Microstructure and properties of nanocrystalline M–Al–Si–N hard coatings

1. Introduction	6
2. Experimental details	8
2.1. Sample preparation	8
2.2. Chemical composition and thickness of coatings	9
2.3. X-ray diffraction	10
2.4. TEM and HRTEM investigations	14
2.5. Hardness measurements	14
3. Results and discussion	15
3.1. Phase composition	15
3.2. Residual stresses and elastic anisotropy	19
3.3. Preferred orientation of crystallites	27
3.4. Crystallite size and partial coherence of crystallites	36
3.5. Mechanical properties – hardness	40
3.6. Microstructural model	43
4. Conclusions	46
5. References	49
6. List of figures	51

Chapter 2

Dopita M., Rafaja D., Wüstefeld Ch., Růžicka M., Klemm V., Heger D., Schreiber G. and Šíma M., <i>Interplay of microstructural features in $Cr_{1-x}Al_xN$ and $Cr_{1-x-y}Al_xSi_yN$ nanocomposite coatings deposited by cathodic arc evaporation</i> , Surface and Coatings Technology, 202 , (2008), 3199-3207.	53
------------------------------------------------------------------------------------------------------------------------------------------------------------------------------------------------------------------------------------------------------------------------------------------------------------------------------------------------	----

Chapter 3

Rafaja D., Dopita M., Růžicka M., Klemm V., Heger D., Schreiber G., Šíma M., <i>Microstructure development in Cr-Al-Si-N nanocomposites deposited by cathodic arc evaporation</i> , Surface and Coatings Technology, 201 , (2006), 2835-2843.	65
------------------------------------------------------------------------------------------------------------------------------------------------------------------------------------------------------------------------------------------------------	----

Chapter 4

Dopita M., Wüstefeld Ch., Klemm V., Schreiber G., Heger D., Růžicka M., Rafaja D., <i>Residual stress and elastic anisotropy in the Ti-Al-(Si-)N and Cr-Al-(Si-)N nanocomposites deposited by cathodic arc evaporation</i> , Zeitschrift für Kristallographie, 27 , (2008), 245-252.	77
---------------------------------------------------------------------------------------------------------------------------------------------------------------------------------------------------------------------------------------------------------------------------------------------	----

Chapter 5

Rafaja D., Wüstefeld Ch., Dopita M., Ruzicka M., Klemm V., Schreiber G., Heger D. and Šíma M., <i>Internal structure of clusters of partially coherent nanocrystallites in Cr–Al–N and Cr–Al–Si–N coatings</i> , Surface and Coatings Technology, 201 , (2007), 9476-9484.	87
-----------------------------------------------------------------------------------------------------------------------------------------------------------------------------------------------------------------------------------------------------------------------------------	----

Chapter 6

Rafaja D., Poklad A., Klemm V., Schreiber G., Heger D., Šíma M., Dopita M., <i>Some consequences of the partial crystallographic coherence between nanocrystalline domains in Ti-Al-N and Ti-Al-Si-N coatings</i> , Thin Solid Films, 514 , (2006), 240-249.	99
---------------------------------------------------------------------------------------------------------------------------------------------------------------------------------------------------------------------------------------------------------------------	----

Chapter 7

Rafaja D., Wüstefeld Ch., Dopita M., Klemm V., Heger D., Schreiber G. and Šíma M.: <i>Formation of defect structures in hard nanocomposites</i> , Surface and Coatings Technology, 203 , (2008), Pages 572-578.	111
------------------------------------------------------------------------------------------------------------------------------------------------------------------------------------------------------------------------	-----

Chapter 8

Dopita M., Rafaja D., <i>X-ray residual stress measurement in titanium nitride thin films</i> , Zeitschrift für Kristallographie, 23 , (2006), 67-72.	121
--------------------------------------------------------------------------------------------------------------------------------------------------------------	-----

Chapter 9

Rafaja D., Klemm V., Dopita M., <i>Practical aspects of partial coherence of nanocrystalline domains</i> , Newsletter of the Commission on Powder Diffraction, 34 , (2007), 7-12.	129
------------------------------------------------------------------------------------------------------------------------------------------------------------------------------------------	-----

1. Introduction

Thin polycrystalline coatings play an extremely important role in a whole variety of industrial applications. Due to its unique physical, mechanical and chemical properties such as for example high hardness, abrasion resistance, temperature stability and chemical resistance, they are used as coatings improving resistance and lifetime of materials used for cutting, drilling, moulding and manufacturing of mechanical components exposed to high mechanical and thermal treating and friction. Only a few microns thick coating having ideal properties can increase the serving lifetime of steels, hardmetals or ceramics based tools several times. Extension of the tools lifetime has in consequence considerable financial and ecological savings.

The deposition of hard coatings is already used for decades as a method increasing the lifetime or improving the properties of industrial tools. Historical evolution followed coatings prepared by the physical (PVD) and chemical (CVD) deposition methods from polycrystalline layers based on the transition metal nitrides MN (where M = Ti, Cr, Zr, Hf, Ta, etc.), over multilayered systems, gradient coatings (coatings with function gradient). Nowadays, the attention and the industrial use are particularly focused to the nanocrystalline and nanocomposite coatings because of their unique properties in comparison to the classical polycrystalline materials.

Particular mechanical properties of the hard coatings are controlled by their microstructure properties, whereas the most important are: the element and phase composition, presence and magnitude of residual stresses and elastic anisotropy, preferred orientation of crystallites – texture, crystallite size, types and densities of defects. These microstructural properties can be influenced by appropriate setting of deposition parameters, which has in consequence the “tunability” of the coating physical characteristics – or, in the other words, possibility of manufacturing of coating having ideal properties for required industrial application.

During the last years, the technical importance of the nanocrystalline composites proposed in [1] increased rapidly. It was shown in [2] that on the contrary to the coarse grain coatings, the coatings based on the nanocrystalline composites have a whole variety of beneficial or better mechanical properties, for example a higher hardness and fracture toughness and better temperature stability, which are the most important parameters crucial for the coatings industrial applications. The idea to use the small crystallite size for the improvement of the hardness is based on the work of Hall [3] and Petch [4], who have shown the increase of hardness with decreasing grain size. Another essential parameter influencing strongly the super-hard nanocomposites coatings mechanical properties is the residual stress. High internal residual stresses are needed to reduce the sliding at the grain boundaries and thus to prevent a reduction of the hardness at small crystallite size [5-8].

This work is focused on the study of the real structure of nanocrystalline hard coatings and thin film nanocomposites, description and correlation of above-mentioned microstructural properties with deposition parameters and mechanical properties. To the main analytical methods used in this work for the study of coatings belong:

a) the X-ray diffraction, which was the main method. X-ray diffraction yields information on the phase composition of the coatings, on the lattice parameter, magnitude and type of the residual stresses and elastic anisotropy, preferred orientation of crystallites, size of the coherently diffracting domains, density and type of the lattice defects,

b) spectroscopic methods like the electron probe microanalysis using the wavelength dispersive and/or energy dispersive X-ray spectroscopy (WDX / EDX) and glow discharge optical emission spectroscopy (GDOES), which were used for the determination of the elemental composition of the coatings,

c) scanning electron microscopy (SEM) used for the qualitative study of the coatings morphology (adhesion of the coatings, presence of cracks and voids etc.),

d.) transmission electron microscopy (TEM) and high resolution transmission electron microscopy (HRTEM) used for the study of the crystal lattice defects and verification of the crystallite and cluster size,

e.) measurements of the mechanical properties of coatings – indentation hardness.

2. Experimental details

2.1. Sample preparation

Six series of specimens that differed in the transition metal type (Cr, Ti and Zr) and in the amount of Si and Al were deposited using the cathodic arc evaporation (CAE) process in the deposition apparatus π -80 produced by Platit AG. The π -80 device contains two vertical laterally rotating arc cathodes placed in the front of the vacuum chamber [9]. One cathode was made from the transition metal (Cr, Ti or Zr), the second one alternatively from Al or from Al containing 11 at.% of Si, in the case of deposition of M-Al-N or M-Al-Si-N coatings, respectively (M denotes the transition metal type – Cr, Ti or Zr). In order to compare the microstructural properties of the coatings with different chemical compositions, the parameters of the deposition process were kept constant for all deposited coatings. The base pressure was 5×10^{-3} Pa and the working pressure of the nitrogen atmosphere 1.3 Pa. The deposition temperature was approximately 450°C. The current on the transition metal (Cr, Ti or Zr) cathode was 80 A, the current on the Al or Al-Si cathode 120 A. The bias voltage was –75 V. Polished plates of cemented carbide having a random orientation of crystallites and dimensions of 25×15×3 mm³ were used as substrates. They were aligned horizontally with equal distances from each other on a cylindrical substrate holder, which was placed in the centre of the vacuum chamber. Schematic drawing of the samples positions in the deposition chamber and a picture of the deposition apparatus are shown in Figs. 1a, b, c. In each deposition run, seven specimens of the respective series were produced. In contrast to the commercially produced coatings, the samples were not rotated during the deposition process. Thus, the preferred orientation of crystallites as well as other microstructural parameters were not superimposed or influenced by the specimen rotation. The substrates had different distances to the respective cathode, which allowed the series of the samples to be deposited with different ratios between the transition metal contents, aluminium and silicon contents, $[M]/([M]+[Al]+[Si])$.

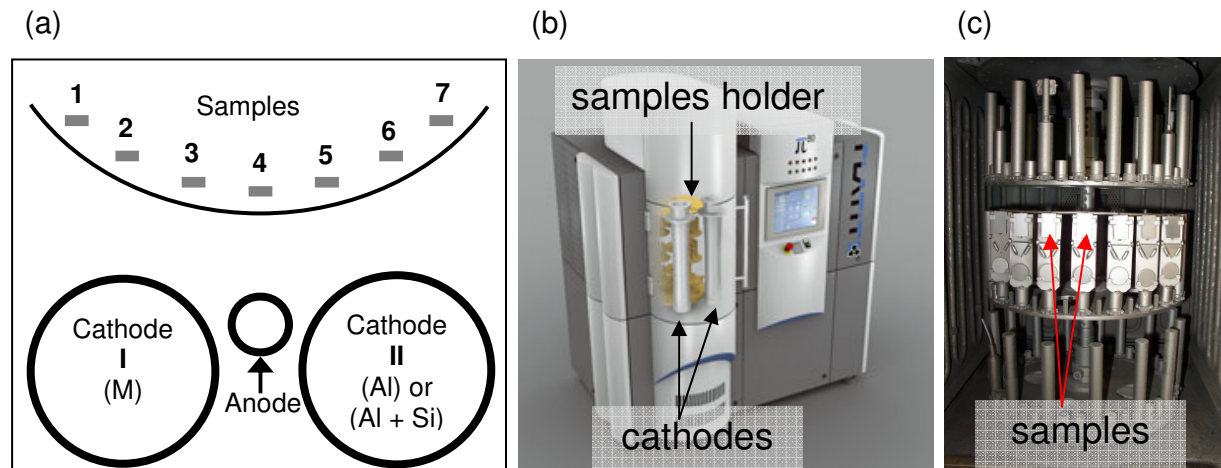


Fig. 1. Sketch of the deposition chamber from the top view (a), picture of the deposition apparatus (b) and photograph of the samples positioned in the samples holder (c).

2.2. Chemical composition and thickness of coatings

The overall chemical composition of the coatings was measured in 41 randomly distributed points in the sample using electron probe microanalysis with wavelength-dispersive X-ray spectroscopy (EPMA/WDX) on the electron probe micro-analyzer JXA 8900 RL (Jeol). The concentrations of the elements contained in the coatings (the respective transition metal, Al, Si, N) were obtained from the intensity of their spectral K lines using the ZAF correction procedure (the correction of the effects due to the atomic number Z, absorption A and fluorescence F) and external standards. Due to the overlap of the spectral lines Li(Ti) and K(N), the concentration of nitrogen in the Ti-Al-N and Ti-Al-Si-N coatings could not be measured directly. Thus, it was estimated from the analytical total and measured using the glow-discharge optical emission spectroscopy (GDOES). Within the accuracy of the experimental methods used for the chemical analysis, the nitrogen amount was 50 at.%. The maximum oxygen concentration in all coatings under study was estimated from the detection limit of EPMA/WDX to be lower than 0.1 at.% as no oxygen signal was detected. The chemical composition of all specimens is summarised in Table 1. Estimated standard deviations of the transition metal atoms amounts are shown as error bars in Figs. 22.

Table 1. The overall chemical composition of all specimens under study.

Sample no.	$\text{Cr}_{1-x}\text{Al}_x\text{N}$	$\text{Cr}_{1-x-y}\text{Al}_x\text{Si}_y\text{N}$	$\text{Ti}_{1-x}\text{Al}_x\text{N}$	$\text{Ti}_{1-x-y}\text{Al}_x\text{Si}_y\text{N}$	$\text{Zr}_{1-x}\text{Al}_x\text{N}$	$\text{Zr}_{1-x-y}\text{Al}_x\text{Si}_y\text{N}$
1	$\text{Cr}_{0.92}\text{Al}_{0.08}\text{N}$	$\text{Cr}_{0.91}\text{Al}_{0.08}\text{Si}_{0.01}\text{N}$	$\text{Ti}_{0.96}\text{Al}_{0.04}\text{N}$	$\text{Ti}_{0.96}\text{Al}_{0.04}\text{Si}_{0.00}\text{N}$	$\text{Zr}_{0.96}\text{Al}_{0.04}\text{N}$	$\text{Zr}_{0.93}\text{Al}_{0.06}\text{Si}_{0.01}\text{N}$
2	$\text{Cr}_{0.83}\text{Al}_{0.17}\text{N}$	$\text{Cr}_{0.84}\text{Al}_{0.15}\text{Si}_{0.01}\text{N}$	$\text{Ti}_{0.85}\text{Al}_{0.15}\text{N}$	$\text{Ti}_{0.85}\text{Al}_{0.14}\text{Si}_{0.01}\text{N}$	$\text{Zr}_{0.85}\text{Al}_{0.15}\text{N}$	$\text{Zr}_{0.83}\text{Al}_{0.15}\text{Si}_{0.02}\text{N}$
3	$\text{Cr}_{0.75}\text{Al}_{0.25}\text{N}$	$\text{Cr}_{0.69}\text{Al}_{0.28}\text{Si}_{0.03}\text{N}$	$\text{Ti}_{0.72}\text{Al}_{0.28}\text{N}$	$\text{Ti}_{0.71}\text{Al}_{0.26}\text{Si}_{0.03}\text{N}$	$\text{Zr}_{0.77}\text{Al}_{0.23}\text{N}$	$\text{Zr}_{0.74}\text{Al}_{0.23}\text{Si}_{0.03}\text{N}$
4	$\text{Cr}_{0.54}\text{Al}_{0.46}\text{N}$	$\text{Cr}_{0.52}\text{Al}_{0.43}\text{Si}_{0.05}\text{N}$	$\text{Ti}_{0.52}\text{Al}_{0.48}\text{N}$	$\text{Ti}_{0.52}\text{Al}_{0.43}\text{Si}_{0.05}\text{N}$	$\text{Zr}_{0.59}\text{Al}_{0.41}\text{N}$	$\text{Zr}_{0.54}\text{Al}_{0.41}\text{Si}_{0.05}\text{N}$
5	$\text{Cr}_{0.46}\text{Al}_{0.54}\text{N}$	$\text{Cr}_{0.40}\text{Al}_{0.52}\text{Si}_{0.08}\text{N}$	$\text{Ti}_{0.39}\text{Al}_{0.61}\text{N}$	$\text{Ti}_{0.38}\text{Al}_{0.53}\text{Si}_{0.08}\text{N}$	$\text{Zr}_{0.50}\text{Al}_{0.50}\text{N}$	$\text{Zr}_{0.43}\text{Al}_{0.51}\text{Si}_{0.06}\text{N}$
6	$\text{Cr}_{0.30}\text{Al}_{0.70}\text{N}$	$\text{Cr}_{0.24}\text{Al}_{0.65}\text{Si}_{0.10}\text{N}$	$\text{Ti}_{0.18}\text{Al}_{0.82}\text{N}$	$\text{Ti}_{0.19}\text{Al}_{0.72}\text{Si}_{0.09}\text{N}$	$\text{Zr}_{0.35}\text{Al}_{0.65}\text{N}$	$\text{Zr}_{0.32}\text{Al}_{0.61}\text{Si}_{0.07}\text{N}$
7	$\text{Cr}_{0.08}\text{Al}_{0.91}\text{N}$	$\text{Cr}_{0.07}\text{Al}_{0.81}\text{Si}_{0.12}\text{N}$	$\text{Ti}_{0.09}\text{Al}_{0.91}\text{N}$	$\text{Ti}_{0.06}\text{Al}_{0.82}\text{Si}_{0.12}\text{N}$	$\text{Zr}_{0.13}\text{Al}_{0.87}\text{N}$	$\text{Zr}_{0.16}\text{Al}_{0.74}\text{Si}_{0.10}\text{N}$

The thicknesses of the coatings under study were determined by the calotte grinding technique [10]. Measured values and estimated standard deviations are given in Table 2.

Table 2. Thickness of the coatings under study in μm .

Sample no.	$\text{Cr}_{1-x}\text{Al}_x\text{N}$	$\text{Cr}_{1-x-y}\text{Al}_x\text{Si}_y\text{N}$	$\text{Ti}_{1-x}\text{Al}_x\text{N}$	$\text{Ti}_{1-x-y}\text{Al}_x\text{Si}_y\text{N}$	$\text{Zr}_{1-x}\text{Al}_x\text{N}$	$\text{Zr}_{1-x-y}\text{Al}_x\text{Si}_y\text{N}$
1	3.3 ± 0.1	4.5 ± 0.2	2.7 ± 0.1	2.9 ± 0.1	5.0 ± 0.2	3.9 ± 0.1
2	5.0 ± 0.1	6.3 ± 0.2	4.7 ± 0.1	5.1 ± 0.1	2.3 ± 0.6	2.9 ± 0.2
3	5.6 ± 0.1	7.9 ± 0.3	5.8 ± 0.1	6.3 ± 0.1	8.0 ± 0.1	6.7 ± 0.3
4	7.2 ± 0.1	8.7 ± 0.3	6.1 ± 0.1	7.0 ± 0.1	11.4 ± 0.4	10.3 ± 0.3
5	6.3 ± 0.1	8.6 ± 0.3	5.5 ± 0.1	6.3 ± 0.1	9.6 ± 0.2	9.5 ± 0.2
6	5.4 ± 0.1	7.5 ± 0.3	5.2 ± 0.1	5.4 ± 0.1	7.5 ± 0.7	8.0 ± 0.2
7	4.4 ± 0.1	3.6 ± 0.2	3.7 ± 0.1	3.9 ± 0.1	3.8 ± 0.5	6.1 ± 0.2

2.3. X-ray diffraction

For the X-ray study of the thin coatings, it is beneficial to use a diffraction geometry, which allows the penetration depth of radiation into investigated material to be reduced or even adjusted and kept constant for the whole range of the diffraction angles being used for the measurement. Both of these conditions satisfy the glancing angle X-ray diffraction (GAXRD).

GAXRD geometry

In the GAXRD diffraction geometry, the primary beam impinges the sample surface with an angle γ , which is constant during the measurement, while the diffraction angle 2θ is varied as the detector moves. Therefore, for individual (hkl) reflections the normal to the corresponding scattering planes (hkl) have different inclinations with respect to the sample surface (see Fig. 2a). GAXRD (2θ scans) can be performed on two types of goniometers. The first is Seemann-Bohlin focusing geometry [11], which has however a big disadvantage in its extreme sensitivity to the exact adjustment of the goniometer, thus for precise absolute measurements it is necessary to work with suitable internal standard [12]. Utilization of the Seemann-Bohlin geometry was replaced by the parallel beam geometry nowadays, which is possible to adjust on any two-circle goniometer with the use of parallel beam of the primary radiation and suitable X-ray optics inserted into diffracted beam. If a parallel primary X-ray beam (or the beam with low divergence) is employed, there is no need to focus the diffracted beam into exact position on the focusing circle and the aberrations connected to the not exact adjustment of the diffractometer, displacement of the specimen from exact position, etc. becomes negligible. In the past the X-ray parallel beam was accessible on the synchrotron facilities only, however due to the huge progress in the development and production of parabolic multilayered X-ray mirrors, it is possible to relatively simply create the parallel X-ray beam with high intensity in each laboratory, nowadays. A sketch of the parallel beam geometry is shown in Fig. 2b.

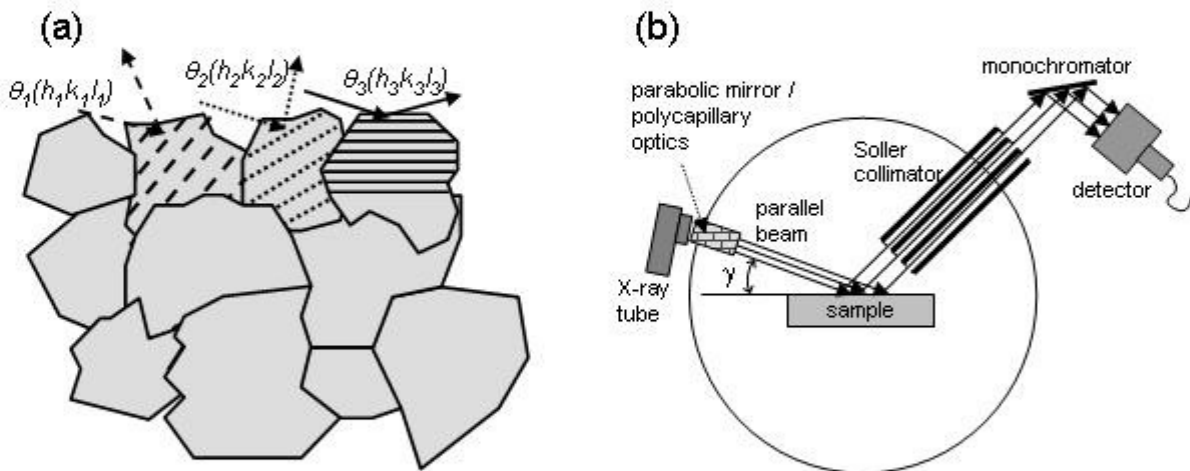


Fig. 2. Illustration of several crystallites of a polycrystalline material satisfying the diffraction condition for different families of lattice planes (different diffraction angles 2θ) – normal directions to respective diffracting lattice planes have different angle with respect to the sample surface (a). Schematic sketch of the parallel beam geometry (b).

Parallel X-ray beam can be created from divergent beam coming from the X-ray source (X-ray tube generating characteristic X-ray spectra) with the use of the multilayered parabolic mirror (Göbel mirror), whereas the divergence of the beam depends on the “quality” of the mirror and is approximately 0.05° . Illustration of the multilayered parabolic mirror is shown in Fig. 3a. Diffracted radiation is angularly selected by the system of long Soller slits, which divergence simultaneously determines the resolution of goniometer. For suppression of the fluorescence radiation and therefore the reduction of the background intensity, it is beneficial to insert a secondary monochromator behind the Soller collimator.

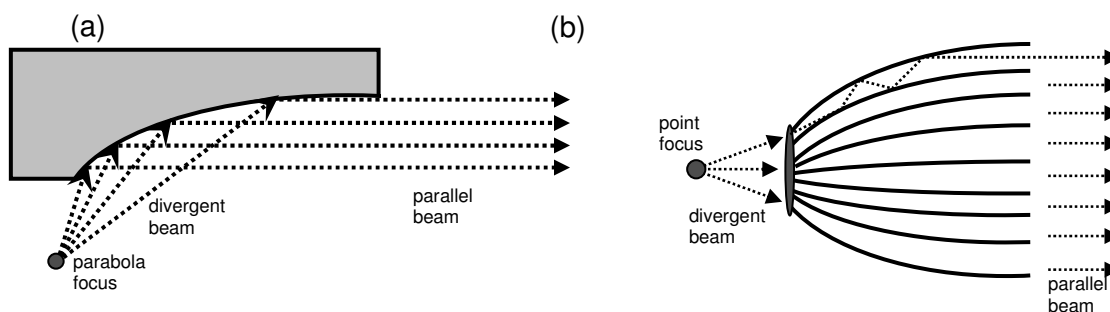


Fig. 3. Two possible methods for the production of the parallel X-ray beam from a divergent monochromatic beam emitted by a conventional laboratory X-ray tube. Scheme of the multilayered parabolic mirror (a). Sketch of the polycapillary optics (b).

Parallel beam geometry significantly suppresses problems connected to the exact adjustment of goniometer and prevents the defocusing of the X-ray beam while tilting the sample out of the symmetrical position. The critical issue while using the multilayered parabolic mirror is the adjustment of mirror with respect to the X-ray tube focus. The line focus of the X-ray tube has to coincide with parabola focus of the multilayered mirror. The only aberration, if we do not consider wrong setting of parabolic mirror with respect to the X-ray tube focus, which has fundamental influence on the primary beam intensity and therefore can easily be detected, is the incorrect setting of the zero position of the detector. This aberration is independent on the diffraction angle and for all precise absolute measurements; it is advantageous to measure the primary beam first, and to correct this eventual aberration.

The second possibility, how to create the parallel X-ray beam in conventional laboratory, is the use of a polycapillary optical module. The polycapillary optical module consists of bundle of several millions capillaries, having spherical cross-section and diameter in the order of microns. The X-ray radiation emitted by the X-ray tube with point focus propagates through the capillaries on basis of total reflection of radiation on the inner surface of the capillaries. The material of capillaries, moreover acts as a radiation filter because the radiation of longer wavelengths is absorbed. The bundle of individual capillaries is shaped to create the parallel beam at the beam exit from the originally divergent beam at the polycapillary module entry. The sketch of the polycapillary optical module is shown in Fig. 3b. The divergence of the X-ray beam at the polycapillary optical module exit is approximately 0.2° .

X-ray data measured with the asymmetric geometry (GAXRD) has the following advantages, which makes the method especially suitable for the measurements of thin films. In cubic materials, GAXRD data allows fast determination of residual stress from one diffraction pattern. Determined value of the residual stress is averaged over all measured (hkl) reflections. Moreover, because the interplanar spacings are measured on different crystallographic planes and at different inclinations of the sample from the symmetrical position, one can immediately get an information about the crystal anisotropy of investigated material, from one GAXRD scan. Another advantage of the GAXRD is the penetration depth – the depth of material where measured information comes from. For small angles of incidence of the primary beam ($\gamma < 10^\circ$) the penetration depth x_e (equation 1) [13] is nearly independent on the diffraction angle, however it is strongly dependent on the incidence angle (penetration depth increases with increasing angle of incidence of the primary beam).

$$x_e = \frac{\sin \gamma \sin(2\theta - \gamma)}{\mu(\sin \gamma + \sin(2\theta - \gamma))} \quad (1)$$

The penetration depths x_e calculated for material having linear absorption coefficient $\mu = 580 \text{ cm}^{-1}$ (which corresponds to absorption in the sample with the chemical composition of approximately $\text{Cr}_{0.46}\text{Al}_{0.54}\text{N}$) and the several different angles of incidence of the primary beam γ are shown in Fig. 4.

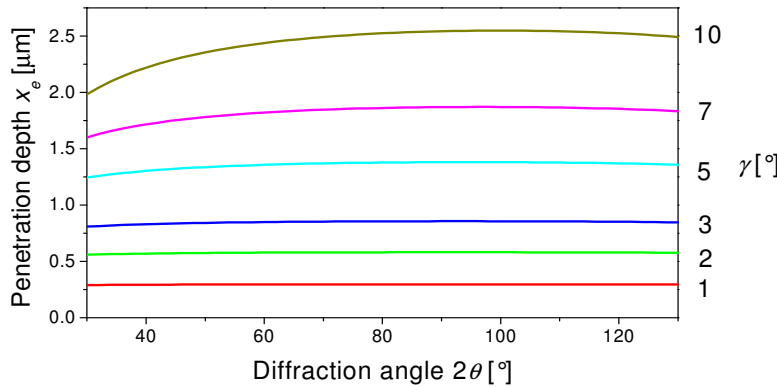


Fig. 4. Penetration depth x_e as a function of diffraction angle 2θ calculated for the GAXRD due to the equation 1 for material having linear absorption coefficient $\mu = 580 \text{ cm}^{-1}$ and angles of incidence of primary beam $\gamma = 1, 2, 3, 5, 7$ and 10° .

Varying the angle of incidence of the primary beam has in consequence different penetration depths of X-rays, and thus different information depth of diffracted data. GAXRD measurements with several different angles of incidence can provide information about the presence of residual stress gradients as well as the strain-free lattice parameter depth profile can be calculated. By setting an appropriate angle of incidence of the primary beam, with simultaneous knowledge of the linear absorption coefficient of investigated material, one can set desired penetration depth, which is particularly important for the investigation of only several microns thick coatings.

Special goniometers – Eulerian cradle

For the measurements of inhomogeneous materials, or quantities, which can vary

depending on the direction in the specimen (as for example lattice strains, or preferred orientation of crystallites) in general, it is necessary to use a goniometer that allows additional rotations of the sample with respect to the goniometer plane. For that purposes the κ -goniometer or the diffractometer equipped with an Eulerian cradle can be used. A schematic sketch of the Eulerian cradle defining additional rotation axes is shown in Fig. 5. The Eulerian cradle allows tilt of the sample (the normal to the sample surface does not need to lie in the diffraction plane) χ - axis, and simultaneously the rotation of the specimen around its normal is possible ϕ - axis.

Modern Eulerian cradle equipped goniometers additionally allow (x, y, z) translations, which permits exact adjustment of arbitrary position in the sample and together with the use of thin diameter capillary, spatially resolved diffraction measurements. While performing measurement with varying χ - tilts it is necessary to work with spatially restricted primary beam, because higher χ - tilts significantly broaden the beam spot on the sample.

The use of divergent X-ray beam together with χ - tilts, for the measurement, can lead to a whole variety of the aberrations. The whole irradiated volume of the specimen does not coincide with χ rotation axis and out of axis lying irradiated sample volume moves away from the ideal focusing position. For each individual potential aberration it is possible to derive an analytical equation, however simultaneous combination of all aberrations together makes the analytical description difficult. Consequently, for exact X-ray measurements (measurements of the lattice strains for example) it is necessary to work with an appropriate standard and to correct measured data precisely. If we employ the parallel beam (ideal is the goniometer equipped with polycapillary optics), the majority of possible aberrations are negligible and the only important error of the measurement can be, as it was already discuss, wrong setting of the zero position of the goniometer.

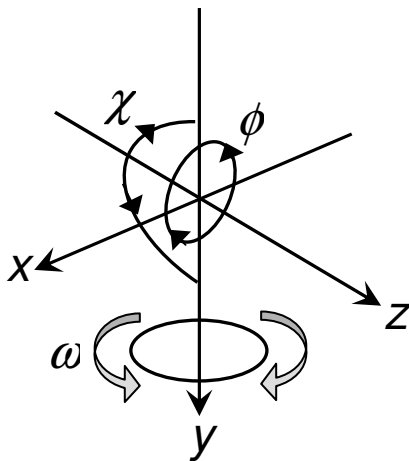


Fig. 5. Sketch of an Eulerian cradle. In the scheme, the axes x , y , z , and goniometer circles ω , χ a ϕ are shown. The rotation axis ω coincides with y axis and rotation axis (tilt axis) χ with axis x .

In the case of thin coatings, or materials containing depth gradients measurement, we have to keep in mind, that the penetration depth depends on the χ - tilt (it is decreasing with increasing χ - tilt), as well.

X-ray diffraction geometries used for the experiments

For the X-ray measurements present in this work, the next goniometers were used.

GAXRD measurements with a constant angle of incidence of the primary beam were done using a D8 diffractometer (Bruker, AXS) equipped with a parabolic Göbel mirror in the primary beam and a Soller collimator with acceptance angle of 0.12° and with a flat LiF monochromator in the diffracted beam. The texture measurements (pole figures measurements) were done on a PTS 3000 diffractometer (Seifert, FPM) equipped with the Eulerian cradle and a point focus monocapillary optics. The lattice strains were measured on a X'Pert MRD diffractometer (Pananalytical) equipped with the Eulerian cradle, polycapillary optics in the primary beam and with a Soller collimator having the acceptance angle of 0.27° and flat graphite monochromator in the diffracted beam or on the D8 Advance diffractometer (Bruker, AXS) equipped with the Eulerian cradle and polycapillary optics located in the primary beam and with flat graphite monochromator in the diffracted beam. For all measurements the $\text{CuK}\alpha$ radiation ($\lambda = 1.5418 \text{ \AA}$) was used.

2.4. TEM and HRTEM investigations

Transmission electron microscopy (TEM) and high-resolution transmission electron microscopy (HRTEM) were done on a 200 kV analytical high-resolution transmission electron microscope JEM 2010 FEF (from Jeol) equipped by an ultra-high-resolution objective lens ($C_s = 0.5 \text{ mm}$) and an in-column energy filter. The latter was used to select only the elastic electrons for the HRTEM micrograph recording. The specimens for TEM were prepared in the plane-view orientation, which is more convenient for a direct comparison of the XRD and HRTEM results. The coatings were first removed from the substrates, mechanically pre-thinned and etched by ion beam. The final step in the specimen preparation was a plasma cleaning procedure.

2.5. Hardness measurements

The hardness of the coatings was obtained from the nanoindentation experiments performed on three different equipments. Continuous stiffness measurements were done with a computer-controlled Nano Indenter XP (MTS) using the sinus mode [41] to obtain the hardness as a function of the penetration depth. Twenty indentations were done at each sample and the hardness was calculated from the values obtained in indentation depths from 50 to 100 nm, where the hardness was affected neither by the surface roughness nor by the substrate hardness. These measurements were complemented by standard nanoindentation measurements performed using a computer controlled Fischerscope H100 microhardness tester and a Nano Hardness tester (CSM). The maximum load of 70 mN, which was recommended for super-hard coatings in [41], was reached in 20 s. The unloading time was 20 s as well. The maximum indentation depth ranged between 0.3 and 0.4 μm , which are below 10% of the thickness in most coatings (compare thickness of the coatings given in Table 2). For all measurements, the Berkovich indenter was used.

3. Results and discussion

3.1. Phase composition

The analysis of the phase composition was done using the glancing angle X-ray diffraction (GAXRD) data. The conventional qualitative phase analysis consisting of comparison of measured diffraction patterns with tabulated peak positions was complemented by precise determination of the stress-free lattice parameters. Later procedure is, due to an extremely high sensitivity of the stress-free lattice parameter of the fcc phase to the aluminium and silicon contents dissolved in the lattice, very important. From deviations of expected Vegard-like dependence of the stress free lattice parameter, one can immediately reveal the formation of a new phase, even for low phase concentrations, which could not be visible in the diffraction pattern yet, and especially in the case of development of an amorphous Si_xN_y phase, which does not contribute to the measured diffraction pattern with Bragg's maximums.

Depending on the sample stoichiometry, three regions with different phase compositions exist in the coatings. In the transition metal (Cr, Ti or Zr) richest samples, a single face centered cubic (fcc) $\text{M}_{1-x-y}\text{Al}_x\text{Si}_y\text{N}$ phase exists in the coating (hereinafter referred to as fcc phase, only). With increasing Al content, wurtzitic AlN (hereinafter referred to as w-AlN, only) starts to develop as a second crystalline phase, whereas in this region both phases, fcc and w-AlN, coexist. Finally, at the highest Al concentrations only w-AlN phase exists in the coatings. In samples containing silicon, the silicon atoms are dissolved in the fcc phase in coatings with low Si concentration and with increasing Si content they build a third phase, which is amorphous Si_xN_y . The phase composition and the limits of the phases coexistence depends strongly on the transition metal type. The sketch of the phase evolution in M-Al-N and M-Al-Si-N coatings with increasing Al content and structures of the fcc and w-AlN phases are shown in Fig. 6.

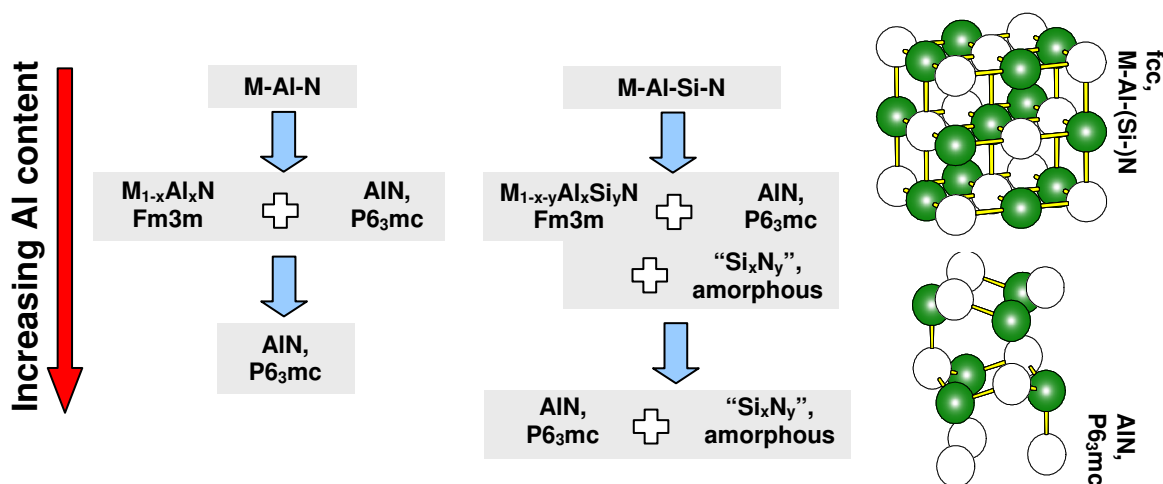


Fig. 6. Sketch of the phase evolution in M-Al-N and M-Al-Si-N coatings with increasing Al content and structures of the fcc phase and wurtzitic AlN.

The maximum solubility of AlN into transition metal nitrides with the fcc structure predicted by the two band parameters, based on the pseudopotential approach and the bond orbital model, and structural map was calculated to be 77 at. %, 65 at. % and 33 at. % for Cr, Ti and Zr, respectively [14, 15].

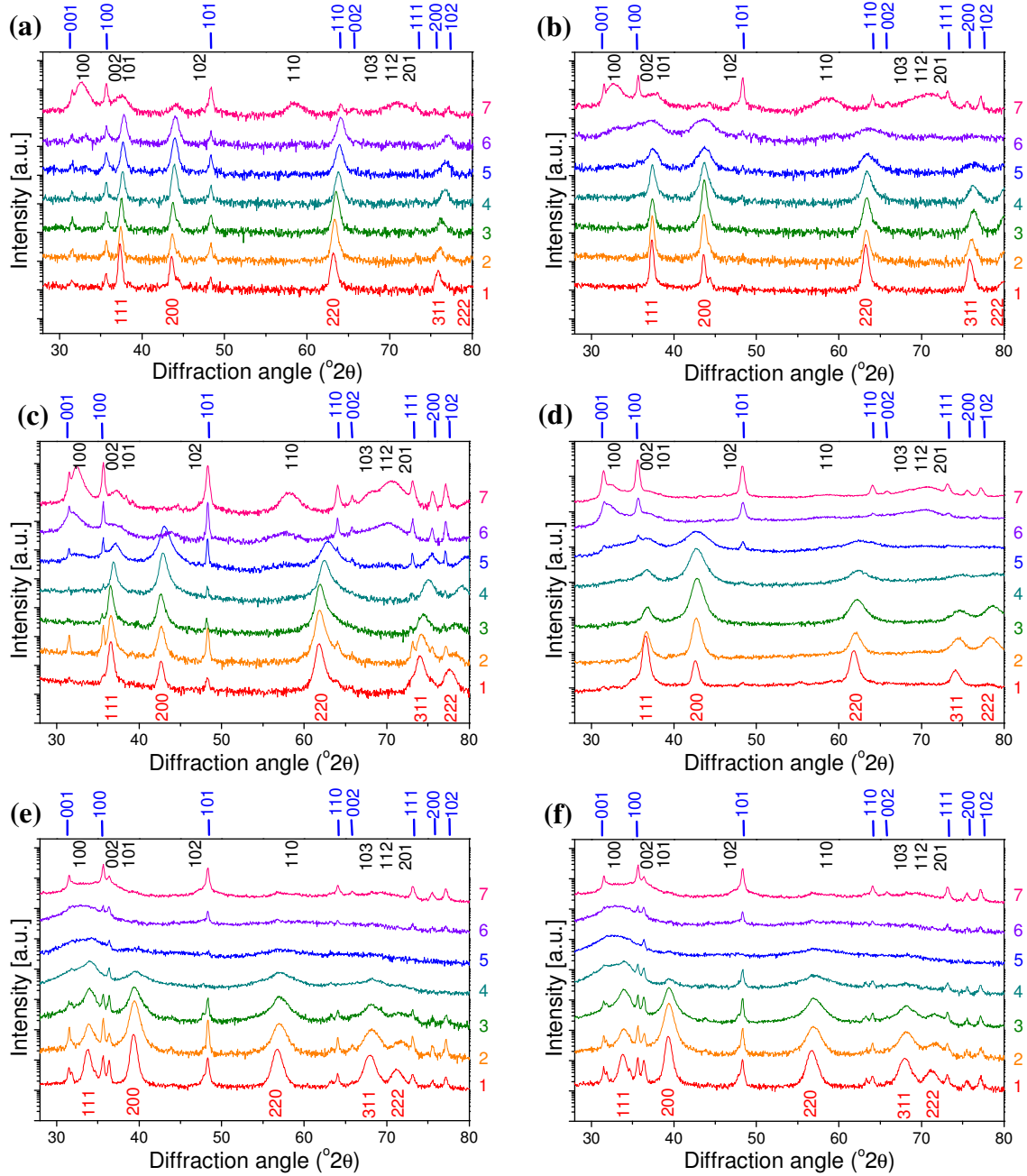


Fig. 7. Fragments of the diffraction patterns taken for the Cr-Al-N (a), Cr-Al-Si-N (b), Ti-Al-N (c), Ti-Al-Si-N (d), Zr-Al-N (e) and Zr-Al-Si-N (f) coatings. The intensity scale in arbitrary units is logarithmic. In each figure bottom diffraction pattern corresponds to the coating with highest transition metal concentration and in the following diffraction patterns, the concentration of Al (or Al+Si) is increasing in accordance with the coatings composition given in Table 1. Diffraction lines from fcc phase are labelled by corresponding diffraction indices at the bottom (red coloured indices), diffraction lines from the w-AlN at the top of figures (black coloured indices). Reflections corresponding to the substrate are labelled with blue line and diffraction indices at the top of figures (blue coloured indices).

In Figs. 7 fragments of the measured diffraction patterns of the samples under study are shown with labelled diffraction lines corresponding to the fcc $M_{1-x-y}Al_xSi_yN$ and w-AlN phases of coatings as well as the reflections from the substrate. In the Zr-Al-(Si)-N coatings droplets of hexagonal Zr, were present in the coatings. Peaks from the hexagonal zirconium droplets are clearly visible in the Zr-Al-(Si)-N diffraction patterns – see the unindexed peaks in Figs. 7e, f.

In silicon free M-Al-N coatings at the lowest aluminium contents, all samples contained only fcc. In the single-phase regions, the stress-free lattice parameters decreased linearly with increasing Al contents (Fig. 8). These Vegard-like dependences were approximated by the following functions: $a(Cr_{1-x}Al_xN)=[0.41486(2)-0.00827(1) \cdot x]$ nm, $a(Ti_{1-x}Al_xN)=[0.42418(2)-0.01432(2) \cdot x]$ nm and $a(Zr_{1-x}Al_xN)=[0.458(1)-0.026(1) \cdot x]$ nm (the lattice parameters for the stoichiometric binary nitrides shown in Fig. 8 were taken from the ICSD database [16]). The decrease of the stress-free lattice parameters with increasing Al contents becomes faster with increasing intrinsic lattice parameter of the respective binary transition metal nitride. In the dual-phase coatings, the stress free lattice parameters of fcc were larger than the lattice parameters predicted from the respective Vegard-like dependence for the “overall” chemical composition of the coatings as revealed by EPMA/WDX. The reason is that a part of Al atoms segregates from the host structure of the fcc phase. Thus, the fcc phase contains less Al than the mixture of fcc phase and w-AlN, which chemical composition was analyzed using EPMA/WDX. The segregation of Al from fcc phase is responsible for the apparent increase of the lattice parameter in the cubic phases.

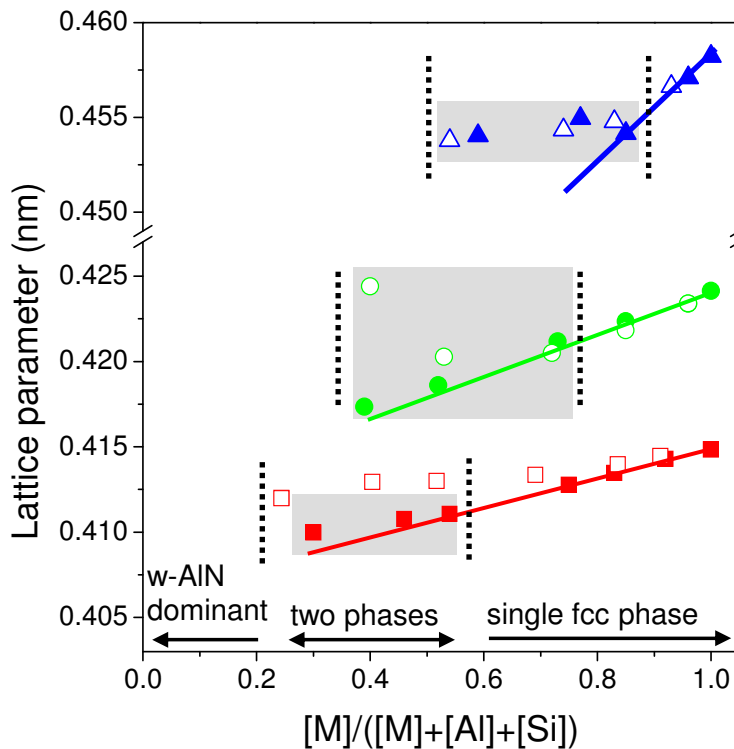


Fig. 8. Dependence of the stress-free lattice parameters on the transition metal contents in fcc-(Cr, Al, Si) N (red boxes), fcc-(Ti, Al, Si) N (green circles) and fcc-(Zr, Al, Si) N coatings (blue triangles) as measured in the samples, in which fcc-(M, Al, Si) N was the dominating phase. Solid symbols are used for Si-free coatings, open symbols for coatings containing Si. Error bars of determined stress-free lattice parameters are smaller than the symbols. Solid lines indicate the hypothetical Vegard-like dependences for $Cr_{1-x}Al_xN$, $Ti_{1-x}Al_xN$ and $Zr_{1-x}Al_xN$. Grey rectangles mark the composition ranges of the maximum hardness from Fig. 23. Vertical dotted lines separate single fcc phase, dual phase (fcc + w-AlN) region and region, where the w-AlN is dominant (from right to left), respectively.

Accordingly, the composition ranges, in which the stress-free lattice parameters of fcc phase deviate from the hypothetical Vegard-like dependence, match well with the composition ranges, in which the presence of two crystalline phases and the increase of the hardness were observed (compare with Fig. 22). For the silicon-free coatings, the phase decomposition starts at $\text{Cr}_{0.54}\text{Al}_{0.46}\text{N}$, $\text{Ti}_{0.72}\text{Al}_{0.28}\text{N}$ and $\text{Zr}_{0.85}\text{Al}_{0.15}\text{N}$ as determined from the respective overall chemical composition of the coatings, for which the stress-free lattice parameters start to deviate from the Vegard-like dependence. The maximum Al contents in the fcc phases of the samples under study were $\text{Cr}_{0.44}\text{Al}_{0.56}\text{N}$, $\text{Ti}_{0.48}\text{Al}_{0.52}\text{N}$ and $\text{Zr}_{0.85}\text{Al}_{0.15}\text{N}$ as calculated back from the minimum lattice parameters and from the Vegard-like dependences shown above. As Si present in the Cr-Al-Si-N, Ti-Al-Si-N and Zr-Al-Si-N coatings segregates from the host structure of fcc $\text{M}_{1-x-y}\text{Al}_x\text{Si}_y\text{N}$ by forming amorphous silicon nitride [1, 17], the segregation of Si could not be confirmed directly using the XRD phase analysis. Nevertheless, it was concluded from the comparison of the stress-free lattice parameters of fcc $\text{M}_{1-x}\text{Al}_x\text{N}$ and fcc $\text{M}_{1-x-y}\text{Al}_x\text{Si}_y\text{N}$ in samples containing a single crystalline phase (Fig. 8) that fcc $\text{Cr}_{1-x}\text{Al}_x\text{N}$ can accommodate more Si than fcc $\text{Ti}_{1-x-y}\text{Al}_x\text{N}$. In fcc $\text{Cr}_{1-x-y}\text{Al}_x\text{Si}_y\text{N}$, silicon inflates the stress-free lattice parameter as described in [18]. In the Ti-Al-Si-N coatings, superfluous Si causes a complete segregation of Ti, Al and Si into fcc-TiN, w-AlN and amorphous silicon nitride [19], as it can also be seen on the increase of the stress-free lattice parameter of fcc $\text{Ti}_{1-x-y}\text{Al}_x\text{Si}_y\text{N}$ towards stoichiometric TiN. In Zr-Al-Si-N coatings the presence of silicon affects the lattice parameter of the fcc phase similarly as in the Cr-Al-Si-N, we observed slight increase of the lattice parameter in first two zirconium richest samples. Exact quantification of the influence of silicon on the lattice parameter of the fcc phase in M-Al-Si-N coatings is a rather difficult task, because it is not clear when the silicon is dissolved in the crystal lattice yet, and when it starts to segregate while building the amorphous Si_xN_y phase. Nevertheless, other consequences of silicon addition on the microstructure of the M-Al-Si-N coatings are discussed in the next sections.

3.2. Residual stresses and elastic anisotropy

In next section we focus on the residual stress determination of the fcc phase in M-Al-(Si-)N coatings using the GAXRD data and data obtained from measurements on a goniometer equipped with an Eulerian cradle, using the classical $\sin^2\psi$ and the Crystallite Group methods. Other procedures suitable for the residual stress determination from the X-ray measurements in thin films are shown in closer details, on the example of titanium nitride coatings, in chapter 8.

On the basis of the GAXRD measurements performed at several different angles of incidence of the primary beam (i.e. different information depth of diffracted intensity), we can conclude that no depth gradients were observed in our coatings, as can be seen from nearly identical slopes of the $\sin^2\psi$ dependences constructed from these measurements (Fig. 9b). Rather high errors of the slopes determined from the linear function fit come from the scatter of measured lattice parameters caused by the pronounced crystal anisotropy present in our coatings, whereas the biggest error calculated for measurement at the lowest angle of incidence ($\gamma=1^\circ$) is caused solely by the quality of measured diffraction pattern.

Equation 2 describes the relation between the measured lattice deformation and the stress tensor. Lattice deformations measured at three different angles ϕ and at several tilts ψ allow due to equation 2 all stress tensor components to be determined [13]. As it is clearly apparent from Fig 9c, the coatings are under the state of biaxial, (rotationally symmetrical - $\sigma_{11} = \sigma_{22} = \sigma$) stress, because data measured for different angles ϕ are identical. No shear stresses ($\sigma_{13} = \sigma_{23} = 0$) are present in our samples that can be demonstrated by similar behaviour of lattice parameters measured for positive and negative ψ tilts i.e. no ψ splitting is observable [13] (see Fig. 9d).

$$\begin{aligned} \varepsilon_{\phi,\psi}^{hkl} = & \frac{1}{2} s_2^{hkl} [(\sigma_{11} \cos^2 \phi + \sigma_{12} \sin 2\phi + \sigma_{22} \sin^2 \phi - \sigma_{33}) \sin^2 \psi + \sigma_{33}] + \\ & + \frac{1}{2} s_2^{hkl} (\sigma_{13} \cos \phi + \sigma_{23} \sin \phi) \sin 2\psi + s_1^{hkl} (\sigma_{11} + \sigma_{22} + \sigma_{33}) \end{aligned} \quad (2)$$

Under the assumptions of biaxial, rotationally symmetrical state of stress, without shear stresses and normal stress component (σ_{33}) equal to zero, equation 2 reduces to a formula, which predicts the linear dependence of ε^{hkl} vs. $\sin^2\psi$ – equation 3.

$$\varepsilon_{\phi,\psi}^{hkl} = \left(2s_1^{hkl} + \frac{1}{2} s_2^{hkl} \sin^2 \psi \right) \sigma = 2s_1^{hkl} \sigma + \frac{1}{2} s_2^{hkl} \sigma \sin^2 \psi \quad (3)$$

From data measured using the classical $\sin^2\psi$ method, the elastic anisotropy factor A , defined by equation 4, can be derived [20]. The elastic anisotropy factor is given by the ratio between the slopes (ζ) of the dependences ε^{hkl} versus $\sin^2\psi$ measured on $(00h)$ and (hhh) lattice planes. Elastic anisotropy factor quantifies the effect of the residual stress on the strain, whereas the isotropy condition requires $A = 1$. The larger is the deviation from one the higher is the crystal anisotropy.

$$A = \frac{\zeta^{00h}}{\zeta^{hhh}} = \frac{1/2s_2^{00h}\sigma}{1/2s_2^{hhh}\sigma} = \frac{s_2^{00h}}{s_2^{hhh}} \quad (4)$$

The measured dependences of lattice deformations vs. $\sin^2\psi$ were approximated with a linear function (equation 3). We have to mention that there occur deviations from the expected linear behaviour even for $00h$ and hhh reflections (see Fig. 9c at low ψ tilts). We suppose that this effect comes from the plastic deformation of highly stressed lattice planes parallel to sample surface. The plastic deformation was recently demonstrated by the presence of screw dislocations in our coatings [18, 21].

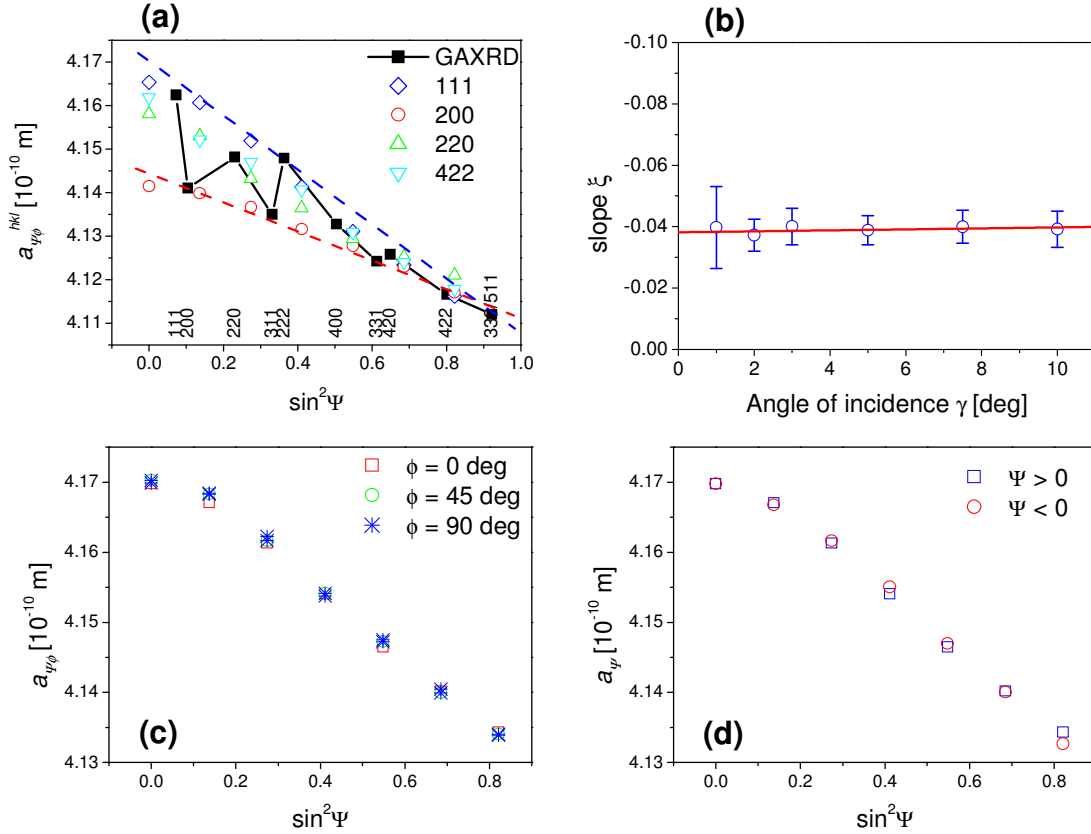


Fig. 9. Lattice parameters of the fcc phase calculated from the GAXRD measurements and lattice parameters calculated from the interplanar spacings of the lattice planes (111), (200), (220) and (422) measured at different inclinations of the sample ψ from the symmetrical position ($\psi = 0$) in sample $\text{Cr}_{0.69}\text{Al}_{0.28}\text{Si}_{0.03}\text{N}$ (a). Slopes of the $\sin^2\psi$ plots calculated from GAXRD measurements obtained for different angles of incidence γ for sample $\text{Cr}_{0.54}\text{Al}_{0.46}\text{N}$ (b). Plot of the lattice parameters obtained from the interplanar spacing of the lattice planes (111) versus $\sin^2\psi$ measured for three different ϕ angles (c), measured for positive and negative ψ tilts (d) for sample $\text{Cr}_{0.91}\text{Al}_{0.08}\text{Si}_{0.01}\text{N}$.

In Fig. 9a lattice parameters of the fcc phase calculated from the GAXRD measurements and lattice parameters calculated from the interplanar spacings of the lattice planes (111), (200), (220) and (422) measured at different inclinations of the sample ψ from the symmetrical position ($\psi = 0$) in the sample $\text{Cr}_{0.69}\text{Al}_{0.28}\text{Si}_{0.03}\text{N}$ are shown. Large scatter of the lattice parameters calculated from the GAXRD data indicates strong crystal anisotropy of the lattice deformation, which implies a strong anisotropy of the X-ray elastic constants in the fcc

phase. As observed also for other nitrides crystallizing with the NaCl type structure, and comparing the lattice parameters calculated from the interplanar spacings measured at the lattice planes (200) and (111), the hard deformation direction is $\langle 100 \rangle$ and easy deformation direction $\langle 111 \rangle$ [22-24].

For highly textured materials, the Crystallite Group method (CGM) [13] is usually applied. The benefit of this method is the possibility of getting information on specially chosen crystallites set, taking into account the angular relations between individual crystallite planes. Using the CGM method, the residual stresses in crystallites families having orientation mostly incorporated in our samples, i.e. for the crystallites corresponding to the strongest texture component present in the coating, were derived.

Cr-Al-N and Cr-Al-Si-N coatings

The anisotropy factor A was smaller than 1 in all cases, i.e. $s_2^{hhh} > s_2^{h00}$. The dependence of the anisotropy factor on aluminium contents was much weaker than the dependence of the anisotropy factor on silicon contents in the Cr-Al-(Si-)N coatings (Fig. 10a). The strongest anisotropy ($A = 0.4$) was observed in the sample $\text{Cr}_{0.69}\text{Al}_{0.28}\text{Si}_{0.03}\text{N}$. The slopes of the dependences of ε versus $\sin^2\psi$, which were used for the calculation of the anisotropy factors, were obtained with a very high accuracy unlike the residual stresses, which would be affected by the difficulties and uncertainties in the determination of the elastic constants. In Figs. 10c and 10d, the slopes ζ^{111} and ζ^{200} are plotted as functions of the chemical compositions of the Cr-Al-(Si-)N coatings. The slope of the ε versus $\sin^2\psi$ dependences is negative for all investigated samples, whereas it is nearly constant or slowly decreasing with increasing Al concentration in Cr-Al-N system and increasing with Al and Si concentration for Cr-Al-Si-N coatings. The magnitudes of the slopes obtained using CGM (slopes of the ε vs. $\sin^2\psi$ dependences measured on crystallite family corresponding to strongest texture component) – Fig. 10b, lies between the boundary values calculated using the classical method for (111) and (200) lattice planes (compare Figs. 10b and 10c, 10d). Slight differences between the slopes obtained from the classical method and from CGM occur since both methods apply different types of averaging. Data obtained from the classical method are averaged over crystallites having different orientation with respect to the sample surface measured on certain lattice planes, whereas CGM results are averaged over different (hkl) , but the results correspond to the crystallites having distinct orientation (in our case crystallites corresponding to the major texture component).

Adopting elastic constants given in [25] ($\nu = 0.214$ and $E = 520$ GPa) and taking into account relations between the Young's modulus and Poisson's ratio and XECs $s_1 = -\nu/E$ and $1/2 s_2 = (\nu + 1)/E$ [13], one can calculate the values of the residual stress. However, these results can be understood as a very rough approximation as the possible dependence of the elastic constants on the chemical composition was neglected. Residual stress determined using CGM in both types of coatings is compressive, whereas its magnitude is significantly

higher for samples without Si (approximately two times for the first four samples richest in the chromium), and it is decreasing in Si free samples and increasing in coatings containing Si with increase of [Al] (or [Al]+[Si]) concentration. For the fifth samples - $\text{Cr}_{0.46}\text{Al}_{0.54}\text{N}$ and $\text{Cr}_{0.40}\text{Al}_{0.52}\text{Si}_{0.08}\text{N}$, the residual stress magnitude is similar, around -6 GPa for both coating series. Residual stresses determined using the classical $\sin^2\psi$ method exhibit the same trend as described for CGM results, moreover the dependences of residual stress on the composition are slightly smoother than in the CGM results.

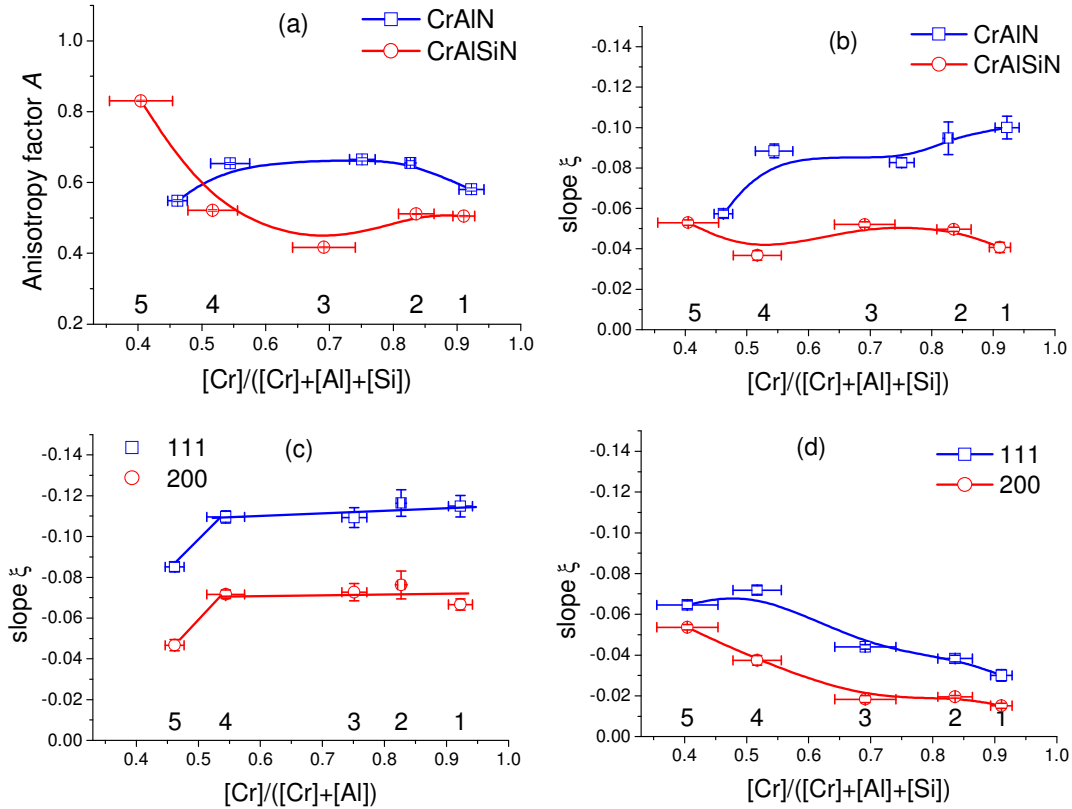


Fig. 10. Plot of the anisotropy factor A (a), slopes of the ε vs. $\sin^2\psi$ dependences measured on crystallite family corresponding to strongest texture component (CGM) (b), and slopes of the ε vs. $\sin^2\psi$ dependences measured on (111) and (200) lattice planes ((c) - for Cr-Al-N , (d) - for Cr-Al-Si-N), versus amount of chromium in Cr-Al-(Si)-N coatings.

Ti-Al-N and Ti-Al-Si-N coatings

The anisotropy factor A is increasing with increasing Al and Si content and it can be well described by functions $y = 0.79(7) \cdot c[\text{Al}] + 0.58(3)$, $y = 0.99(9) \cdot c([\text{Al}] + [\text{Si}]) + 0.56(9)$ for Ti-Al-N and Ti-Al-Si-N coatings respectively (Fig. 11a), where $c[\text{Al}]$ or $c([\text{Al}] + [\text{Si}])$ represent Al, or Al+Si concentration. The anisotropy relaxation is slightly faster in the samples containing Si.

The slopes of the ε versus $\sin^2\psi$ dependences obtained using the classical method are negative for both Ti-Al-N and Ti-Al-Si-N, and increase linearly with increasing Al and Si concentration up to the $[\text{Ti}]/([\text{Ti}] + [\text{Al}] + [\text{Si}]) \sim 0.7$. The dependences show saturation at approximately -0.07 and -0.055 for Ti-Al-N and Ti-Al-Si-N coatings, respectively – Figs. 11c

and 11d, whereas the values are, in the bounds of errors, similar for (111) and (200) lattice planes (corresponding to the anisotropy relaxation for these samples).

Using the elastic constants $\nu = 0.295$ and $E = 640$ GPa from [20], the residual stress can be calculated from slope of the ε versus $\sin^2\psi$ dependence. Because of the uncertainty in the dependence of elastic constants on composition, the elaborated values of residual stress can again be understood as a rough approximation. Residual stress determined using CGM shows an increase from approximately -5.5 GPa or -4.3 GPa to -8.5 GPa or -7.3 GPa with increasing Al and Si concentration for Ti-Al-N or Ti-Al-Si-N samples respectively. The stress determined for samples without Si is higher than in samples containing silicon, and reach its maximum at -9 GPa for the third sample. Comparison of data obtained from CGM and the classical $\sin^2\psi$ methods show that the residual stress determined from the classical $\sin^2\psi$ method (i.e. averaged over all crystallites orientation) is slightly smaller than its value from CGM. It denotes that preferentially oriented crystallites (crystallites belonging to the main texture component present in coatings) are in a state of higher compressive residual stress.

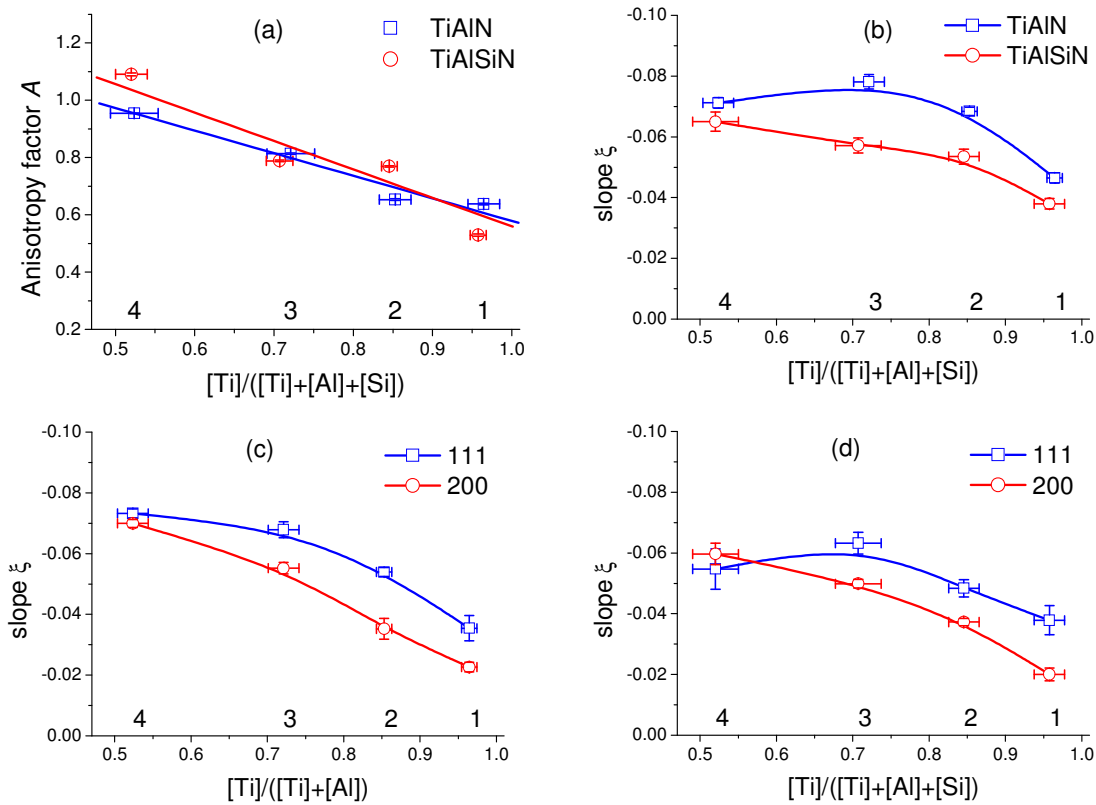


Fig. 11. Plot of the anisotropy factors A , lines correspond to the linear fit (a) Slopes of the ε vs. $\sin^2\psi$ dependences measured on crystallite family corresponding to strongest texture component (CGM) (b), and slopes of the ε vs. $\sin^2\psi$ dependences measured on (111) and (200) lattice planes ((c) - for Ti-Al-N, (d) - for Ti-Al-Si-N), versus amount of titanium in Ti-Al-(Si)-N coatings.

Zr-Al-N and Zr-Al-Si-N coatings

More complicated situation, concerning the residual stress determination, occurred in Zr-Al-(Si)-N coatings. Due to extremely small crystallite sizes (discussed in next chapters) the peaks profiles were enormously broadened, moreover the reflections from the fcc phase were

superimposed with peaks from hexagonal zirconium, coming from the droplets present in the coatings (see Figs. 7e and 7f), which slightly complicated the peaks refinement. Furthermore, measured dependencies of lattice strain ε versus $\sin^2\psi$ exhibited pronounced non-linear behaviour, which was true namely for (200) lattice planes measured at low ψ tilts. This fact prevents linear fitting of all measured data, moreover the CGM yield no plausible results. Only the linear parts of $\sin^2\psi$ plots were used for the anisotropy factor A and residual stress determination. The results, affected by a huge error, therefore can be understand just as a very rough approximation of the true sample state.

The anisotropy in Zr-Al-(Si-)N samples, containing high zirconium concentrations, is highest from all investigated M-Al-(Si-)N coatings. The anisotropy factors A start at 0.25 and 0.23 for specimens $\text{Zr}_{0.96}\text{Al}_{0.04}\text{N}$ and $\text{Zr}_{0.93}\text{Al}_{0.06}\text{Si}_{0.01}\text{N}$, respectively (see Fig. 12a). With increasing Al and Si concentration, the elastic anisotropy of the fcc crystallites decreases. In the Zr-Al-N coatings the anisotropy saturates at a value of approximately $A = 0.5$ in sample $\text{Zr}_{0.85}\text{Al}_{0.15}\text{N}$ and further increase of the aluminium concentration does not significantly influence the anisotropy factor A . Increase of the silicon concentration in the Zr-Al-Si-N coatings cause pronounced decay of the elastic anisotropy, whereas in sample $\text{Zr}_{0.54}\text{Al}_{0.41}\text{Si}_{0.05}\text{N}$ the anisotropy factor A nearly approaches 1, which means no elastic anisotropy (e.g. fcc crystallites appear to be isotropic). The elastic anisotropy in the Zr-Al-(Si-)N coatings depends strongly on the silicon than on the aluminium concentration, similarly as it was observed in the Cr-Al-(Si-)N samples.

The slopes of ε versus $\sin^2\psi$ dependences, obtained using the classical method, slightly increase its magnitude with increasing aluminium content, approach its maximum in sample $\text{Zr}_{0.85}\text{Al}_{0.15}\text{N}$ and saturate for higher aluminium concentration. The Zr-Al-Si-N coatings follow a similar trend, however the addition of silicon significantly emphasizes the evolution of a maximum in sample $\text{Zr}_{0.83}\text{Al}_{0.15}\text{Si}_{0.02}\text{N}$ (compare Figs. 12b and 12c) and has in consequence faster decay of the 111 slopes magnitude with further aluminium and silicon increase.

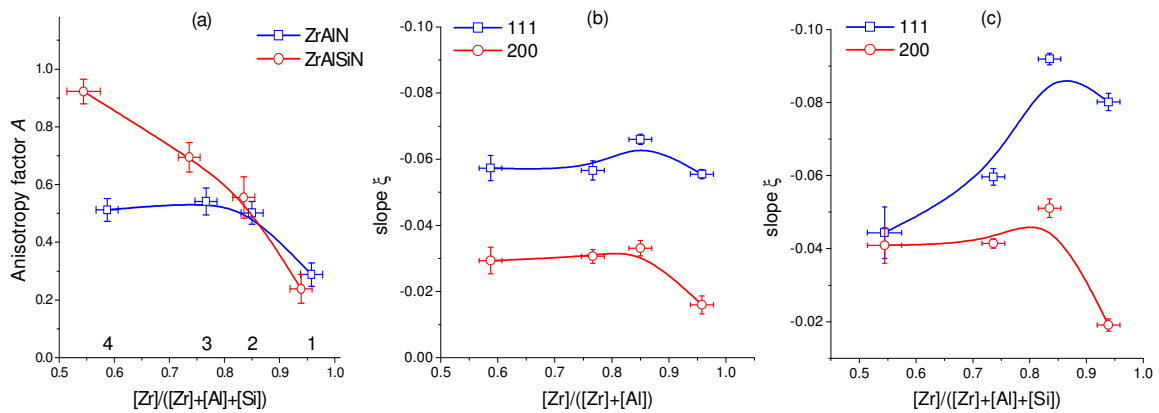


Fig. 12. Plot of the anisotropy factor A (a), slopes of the ε vs. $\sin^2\psi$ dependences measured on (111) and (200) lattice planes ((b) - for Zr-Al-N , (c) - for Zr-Al-Si-N), versus the amount of zirconium in Zr-Al-(Si-)N coatings.

Adopting elastic constants $\nu = 0.19$ and $E = 460$ GPa published in [20, 26], the residual stress can be derived from the slopes of ε versus $\sin^2\psi$ dependences. Similarly as it was discussed in previous sections for Cr-Al-(Si)-N and Ti-Al-(Si)-N coatings there exist huge uncertainty in the values of the elastic constants as well as unknown dependences of elastic constants on the composition (aluminium and/or silicon contents), therefore determined values of the residual stresses are only a first rough approximation. All Zr-Al-(Si)-N samples under study are in state of compressive residual stress. Quantification yields the residual stress of about -5 GPa and -2 GPa for (111) and (200) lattice planes respectively in Zr-Al-N coatings, and residual stress varying from approximately -7 GPa to -4 GPa and from -1.5 GPa to -4 GPa for (111) and (200) lattice planes in the case of Zr-Al-Si-N samples

In all M-Al-(Si)-N coatings under study, no residual stress and lattice parameter depth gradients as well as no shear stresses and only biaxial rotationally symmetrical compressive state of stress were observed. The elastic anisotropy of the fcc crystallites decreased generally with increasing Al and Si concentration for all samples, except of the Cr-Al-N coatings. In the Ti-Al-(Si)-N samples the anisotropy decreased linearly with increasing Al and Si concentration, whereas in coatings containing Si the anisotropy decay was slightly faster. In samples with composition $\text{Ti}_{0.52}\text{Al}_{0.48}\text{N}$ and $\text{Ti}_{0.52}\text{Al}_{0.43}\text{Si}_{0.05}\text{N}$ the elastic anisotropy factor A approached 1 and fcc crystallites become elastically isotropic. In the Cr-Al-(Si)-N and Zr-Al-(Si)-N coatings significantly higher influence of the Si addition on the elastic anisotropy factor relaxation and thus transition from the elastically anisotropic to elastically isotropic state of the fcc crystallites was observed. The elastic anisotropy factor A remains around approximately 0.5 for coatings with composition $\text{Cr}_{0.46}\text{Al}_{0.54}\text{N}$ and $\text{Zr}_{0.59}\text{Al}_{0.41}\text{N}$ (the fcc crystallites are still highly anisotropic), while in samples containing Si the elastic anisotropy factor approaches 1 in samples $\text{Cr}_{0.40}\text{Al}_{0.52}\text{Si}_{0.08}\text{N}$ and $\text{Zr}_{0.54}\text{Al}_{0.41}\text{Si}_{0.05}\text{N}$ (the fcc crystallites appears elastically isotropic).

The highest residual stress was observed in the Cr-Al-N coatings in which samples the residual stress is nearly constant or slightly decreases with increasing Al contents. The fine decay of the residual stress is probably caused by the fact that the initial value of the residual stress is too high and highly strained fcc crystallites try to relax. Significant reduction of the residual stress is obvious in sample with composition $\text{Cr}_{0.40}\text{Al}_{0.52}\text{Si}_{0.08}\text{N}$ in which the second w-AlN phase develops. Therefore, we can deduce that initial residual stress in the fcc crystallites was too high and relaxed (probably on the grain boundaries between the fcc and w-AlN crystallites) when the w-AlN occurred in the coating. Similar evolution of the residual stress with composition and residual stress magnitude was observed for both types of averaging – e.g. CGM and classical method in Cr-Al-N coatings. In chromium richest Cr-Al-(Si)-N coatings the residual stress is approximately two times smaller than in the samples without silicon, whereas slightly different results yield the CGM and classical method. The residual stress determined using the classical method is modestly increasing with

increasing Al and Si contents, while it is constant as calculated using the CGM. In sample $\text{Cr}_{0.40}\text{Al}_{0.52}\text{Si}_{0.08}\text{N}$ both methods yield similar values of the residual stress that are moreover similar to the residual stress value calculated in the Cr-Al-N samples with analogous Cr contents.

In the Ti-Al-(Si-)N specimens the residual stress exhibit a pronounced increase with increasing Al and Si contents in both sample series without and with silicon, whereas the residual stress is higher in the coatings without silicon. Both types of averaging – the CGM and classical method yield similar results for the Ti-Al-(Si-)N coatings. In the Zr-Al-(Si-)N coatings the residual stress reach the maximum value for the samples with compositions $\text{Zr}_{0.85}\text{Al}_{0.15}\text{N}$ and $\text{Zr}_{0.83}\text{Al}_{0.15}\text{Si}_{0.02}\text{N}$, whereas with additional increase of Al and Si the residual stress is approximately constant in the Zr-Al-N and smoothly decreases in the Zr-Al-Si-N coatings, respectively.

3.3. Preferred orientation of crystallites

Preferred orientation of crystallites (texture) is the microstructural parameter that has fundamental influence on the mechanical properties of coatings, particularly in highly anisotropic materials. Perry and Schoenes [27] have shown in their review that the deposition parameters, such as the composition of the working gas, the gas pressure, the deposition rate, the bias voltage, can affect texture in thin films of transition nitrides significantly.

In our investigated coatings, a strong three-dimensional preferred orientation of crystallites mainly in the fcc transition metal nitride phase was observed, which was described by coexisting out-of-plane and in-plane texture [28, 29]. We correlated the texture development in the coatings with other microstructural features (the chemical and phase composition, the crystallite size, the degree of the partial coherence of neighbouring crystallites and the lattice strain) and with the geometry of the deposition process - different distances between the samples and the cathodes that affected the flux of the deposited particles [28, 29]. The texture development was described in terms of the inclination of the main texture component from the sample surface perpendicular direction and in terms of the degree of the out-of-plane and the in-plane preferred orientation of crystallites in the coatings.

Cr-Al-N and Cr-Al-Si-N coatings

Examples of the pole figures measured on the fcc phase in the Cr-Al-N and Cr-Al-Si-N coatings are shown in Figs. 13 and 14, respectively. The cubic crystallites in all Cr-Al-N coatings under study were preferentially oriented with their direction $\langle 111 \rangle$ nearly perpendicular to the sample surface and showed additionally a pronounced in-plane texture. Only a slight inclination of the $\{111\}$ out-of-plane texture from the samples surface perpendicular direction was observed with decreasing chromium and increasing aluminium contents (Fig. 15a). The maximum inclination of the texture direction was approximately 5° .

In the fcc phase of the Cr-Al-Si-N coatings, the combination of the out-of-plane and in-plane texture was also observed similarly to the Cr-Al-N samples. However, the $\langle 111 \rangle$ texture direction inclined more rapidly from the sample surface perpendicular direction with increasing silicon and aluminium contents in the Cr-Al-Si-N coatings, than with increasing aluminium contents in the Cr-Al-N coatings (see Figs. 14 and 15a). In the coatings with the overall chemical composition of $\text{Cr}_{0.40}\text{Al}_{0.52}\text{Si}_{0.08}\text{N}$, the fcc crystallites were nearly preferentially oriented with their direction $\langle 110 \rangle$ perpendicularly to the sample surface. This orientation of crystallites corresponds to the angle between the $\langle 111 \rangle$ direction and the sample surface perpendicular direction of 35° (see Fig. 15a).

The degree of the out-of-plane preferred orientation changed both with the chemical composition of the samples (Fig. 16a) and with their position in the deposition apparatus (Fig. 16b). In Figs. 16a, b, the degree of the out-of-plane preferred orientation is represented by the full width at the half maximum (FWHM) of a central pole that was fitted by a two-dimensional Gaussian function.

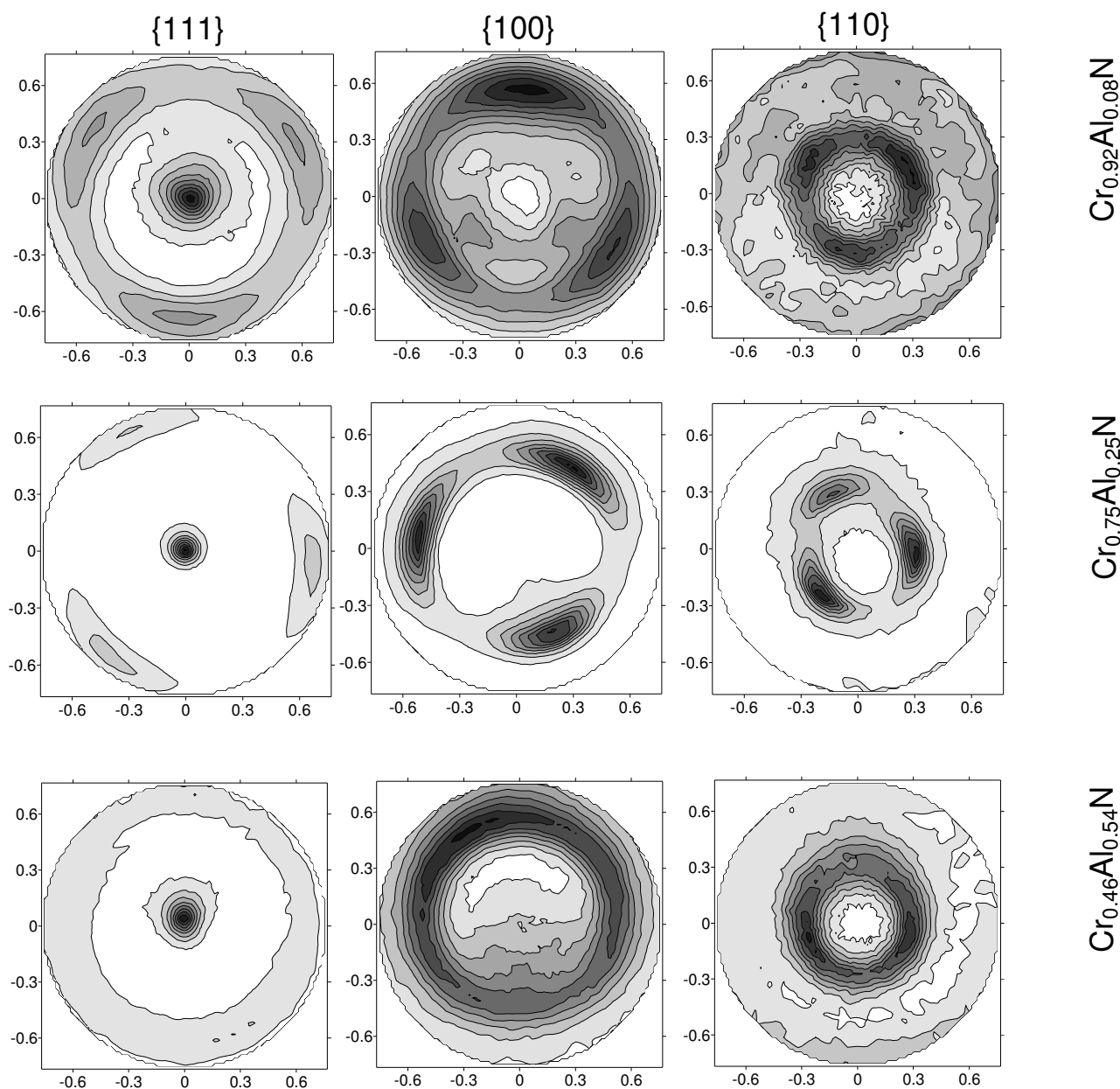


Fig. 13. Pole figures {111}, {100} and {110} (from the left to the right) of the fcc phase measured in the samples with the overall chemical composition $\text{Cr}_{0.92}\text{Al}_{0.08}\text{N}$, $\text{Cr}_{0.75}\text{Al}_{0.25}\text{N}$ and $\text{Cr}_{0.46}\text{Al}_{0.54}\text{N}$ (from the top to the bottom) recalculated into the stereographic projection.

For the determination of the degree of the out-of-plane preferred orientation in the Cr-Al-N samples, the central pole (111) was selected in all coatings. In the samples of the Cr-Al-Si-N series, the central pole (111) was only used for the chromium-richest samples $\text{Cr}_{0.91}\text{Al}_{0.08}\text{Si}_{0.01}\text{N}$ and $\text{Cr}_{0.84}\text{Al}_{0.15}\text{Si}_{0.01}\text{N}$. In the samples $\text{Cr}_{0.69}\text{Al}_{0.28}\text{Si}_{0.03}\text{N}$ and $\text{Cr}_{0.52}\text{Al}_{0.43}\text{Si}_{0.05}\text{N}$, the solitary and nearly central pole (100) was used for determination of the texture degree. For the description of the sample positions in the deposition apparatus in Fig. 16b, the middle position between the cathodes was used, which was almost identical with the position of the anode tip in this experimental setup (see Fig. 1a).

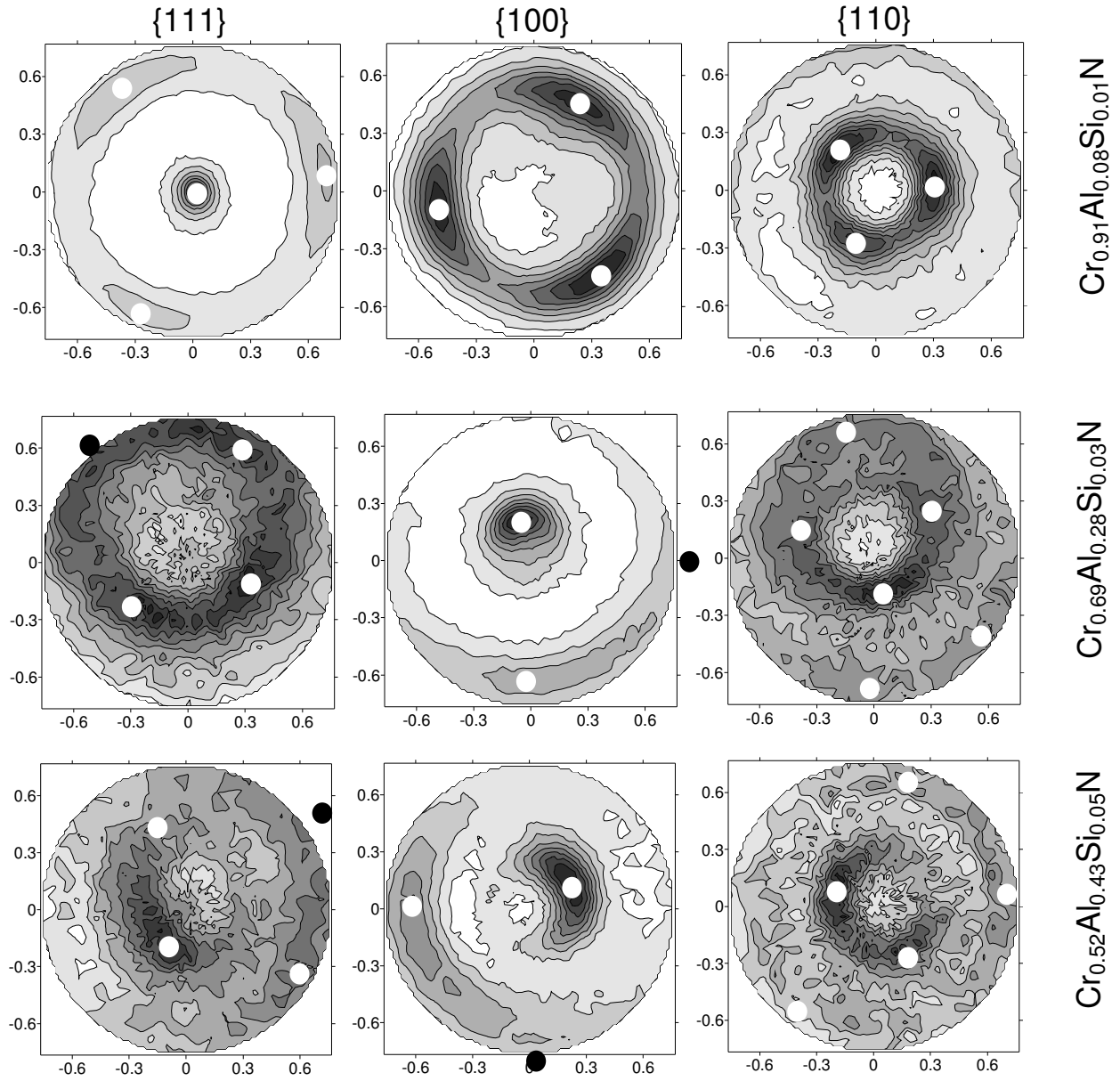


Fig. 14. Pole figures $\{111\}$, $\{100\}$ and $\{110\}$ (from the left to the right) of the fcc phase measured in the samples with the overall chemical composition $\text{Cr}_{0.91}\text{Al}_{0.08}\text{Si}_{0.01}\text{N}$, $\text{Cr}_{0.69}\text{Al}_{0.28}\text{Si}_{0.03}\text{N}$ and $\text{Cr}_{0.52}\text{Al}_{0.43}\text{Si}_{0.05}\text{N}$ (from the top to the bottom) re-calculated into the stereographic projection. The dots show the positions of the poles as obtained for an fcc single-crystal in the same orientation as for the respective sample.

From the comparison of both dependencies (Figs. 16a and 16b), it is apparent that in the fcc phase of the Cr-Al-N coatings the FWHM of the out-of-plane texture is controlled rather by the distance between the samples and the middle position of the cathodes than by the aluminium contents. The larger is the distance, the weaker is the out-of-plane texture. In the Cr-Al-Si-N system, the degree of the preferred orientation of cubic crystallites increases apparently with increasing distance of the samples from the middle position between the cathodes. On the other hand, the out-of-plane texture in the Cr-Al-Si-N coatings gets weaker with increasing aluminium and silicon contents. Thus, we can assume that the increasing silicon concentration causes an obvious decay of the out-of-plane preferred orientation of the fcc crystallites in the Cr-Al-Si-N coatings.

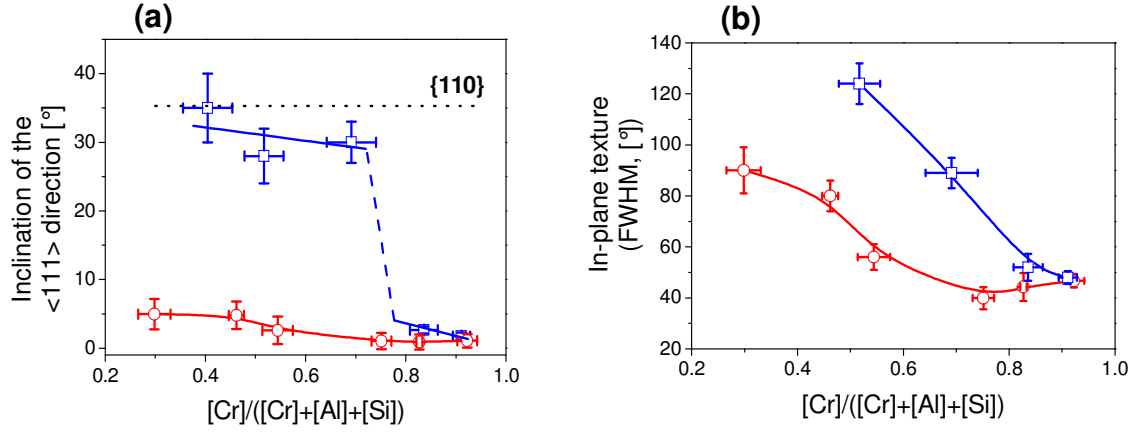


Fig. 15. Inclination of the $\langle 111 \rangle$ texture direction from the sample surface perpendicular direction as observed for the cubic phase in Cr-Al-N (○) and Cr-Al-Si-N (□) thin films. The angle of 35° shown by the dotted line is the angle between the directions $\langle 111 \rangle$ and $\langle 110 \rangle$ in cubic system (a). Degree of the in-plane texture in the Cr-Al-N (○) and Cr-Al-Si-N (□) thin films in dependence on the chemical composition of the coatings (b).

The in-plane texture shows a similar behaviour like the out-of-plane preferred orientation of the fcc crystallites (compare Figs. 15b and 16a). At low Al concentrations in the Cr-Al-N coatings, the in-plane texture becomes more pronounced with decreasing distance from the “anode” in the deposition apparatus. At higher Al concentrations starting with $Cr_{0.54}Al_{0.46}N$, the weakening of the in-plane texture is obviously caused both by the increasing distances from the “anode” and by the increasing aluminium contents. The in-plane texture in the Cr-Al-Si-N coatings gets monotonously weaker with increasing aluminium and silicon contents. The same tendency was observed for the out-of-plane texture in the Cr-Al-Si-N coatings. The similar trends observed for the out-of-plane and in-plane textures in both sample series (without and with Si) indicate that the physical processes behind the preferred orientation of crystallites are similar in all macroscopic directions.

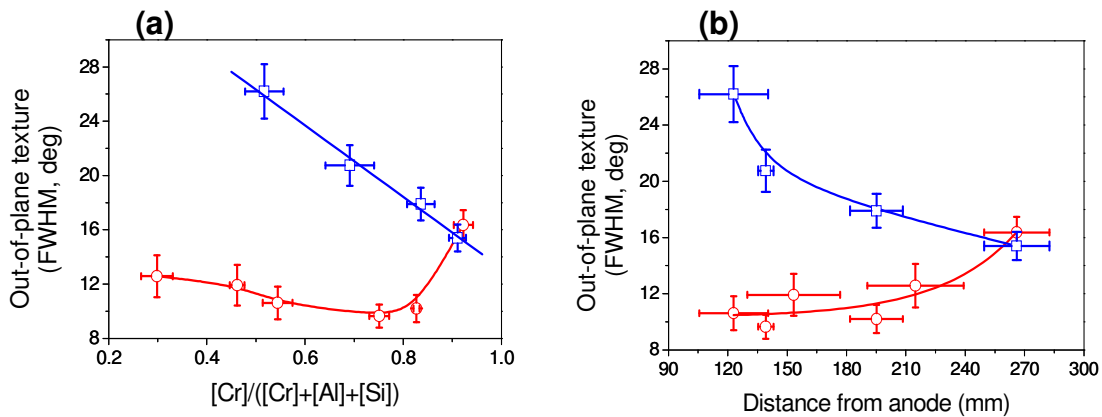


Fig. 16. Degree of the out-of-plane texture of the cubic phase in Cr-Al-N (○) and Cr-Al-Si-N (□) coatings shown in dependence on the chemical composition of the coatings (a) and in dependence on the sample position in the deposition apparatus (b).

It follows from the comparison of results obtained for the Cr-Al-N and Cr-Al-Si-N coatings that the silicon present in the Cr-Al-N coatings has a huge influence on the preferred

orientation of the fcc crystallites. It substantially contributes to the inclination of the preferred orientation direction $\langle 111 \rangle$ away from the sample surface perpendicular direction and to the loss of both, the out-of-plane and the in-plane preferred orientation of the fcc crystallites.

Ti-Al-N and Ti-Al-Si-N coatings

Analogous situation to the preferred orientation of crystallites evolution in the fcc phase of Cr-Al-N and Cr-Al-Si-N coatings described in previous paragraphs occurred in the Ti-Al-N and Ti-Al-Si-N coatings. The fcc Ti-Al-N and Ti-Al-Si-N crystallites grew with a strong preferred orientation of crystallites. In the Ti-Al-N coatings, the fcc crystallites were additionally strongly preferentially oriented in the plane of the films - three-dimensional texture (similar as found in Cr-Al-N coatings) contrary to the Ti-Al-Si-N coatings, where the in-plane preferred orientation of fcc crystallites was quite weak.

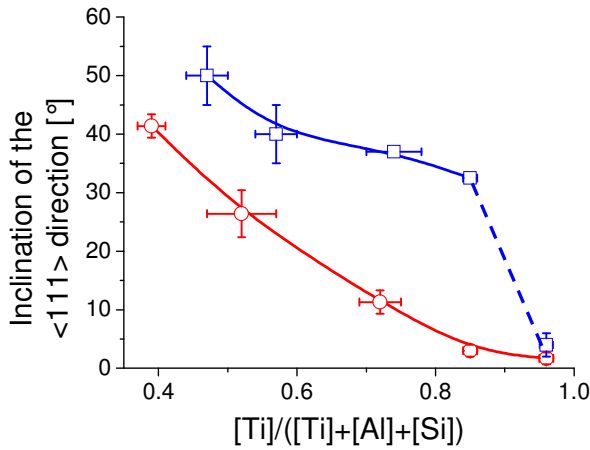


Fig. 17. Inclination of the $\langle 111 \rangle$ texture direction from the sample surface perpendicular direction as observed for the cubic phase in the Ti-Al-N (open red circles - \circ) and Ti-Al-Si-N (open blue squares - \square) coatings.

In the Ti-Al-N coating, the cubic crystallites in the sample with the highest titanium content were oriented with the $\langle 111 \rangle$ crystallographic direction perpendicular to the sample surface (the deviation of the $\langle 111 \rangle$ direction from the sample normal was less than 2° , which is in fact accuracy of positioning of the sample in the deposition apparatus). With increasing aluminium contents, the $\langle 111 \rangle$ crystallographic direction inclined from the sample surface perpendicular direction towards the in-plane direction (see Fig. 17). In the sample $\text{Ti}_{0.39}\text{Al}_{0.61}\text{N}$ the cubic crystallites were oriented with the crystallographic direction $\langle 100 \rangle$ nearly perpendicular to the sample surface. The in-plane texture development in the Ti-Al-N coatings follows the evolution described in the Cr-Al-N, and similarly as in the Cr-Al-N coatings, the maximum of the in-plane preferred orientation was found in the sample located in front of the pure metal (titanium) cathode.

Addition of the silicon in the Ti-Al-Si-N coatings changed the texture evolution dramatically. In the sample $\text{Ti}_{0.96}\text{Al}_{0.04}\text{Si}_{0.00}\text{N}$, specimen containing highest titanium fraction and less than 0.1 at.% of silicon, the $\langle 111 \rangle$ crystallographic direction was preferentially oriented perpendicular to the sample surface like in the titanium richest sample in the Ti-Al-N coatings. Approximately 0.4 at.% of silicon in the sample $\text{Ti}_{0.85}\text{Al}_{0.14}\text{Si}_{0.01}\text{N}$ changed the

texture direction significantly. The angle between the crystallographic direction $\langle 111 \rangle$ and the normal direction was about 32.5° , which corresponds to the crystallographic direction $\langle 110 \rangle$ being nearly perpendicular to the sample surface. With increasing aluminium and silicon content, the $\langle 111 \rangle$ direction was progressively inclined into the plane of the film (see Fig. 17). Besides, the presence of silicon blocked up the formation of the three-dimensional preferred orientation of crystallites since the in-plane texture component did not form in the Ti-Al-Si-N coatings.

Zr-Al-N and Zr-Al-Si-N coatings

Completely different evolution of the preferred orientation of fcc crystallites occurred in Zr-Al-N and Zr-Al-Si-N coatings, compared to the Cr and Ti samples. Contrary to the Cr and Ti based coatings, where we observed the $\{111\}$ texture in transition metal richest samples in the Zr-Al-N and Zr-Al-Si-N coatings with highest zirconium concentration the fcc crystallites preferentially oriented with the $\langle 100 \rangle$ crystallographic direction parallel to the sample normal direction. With increasing aluminium and silicon contents the $\langle 100 \rangle$ crystallographic direction rapidly inclines towards the sample surface.

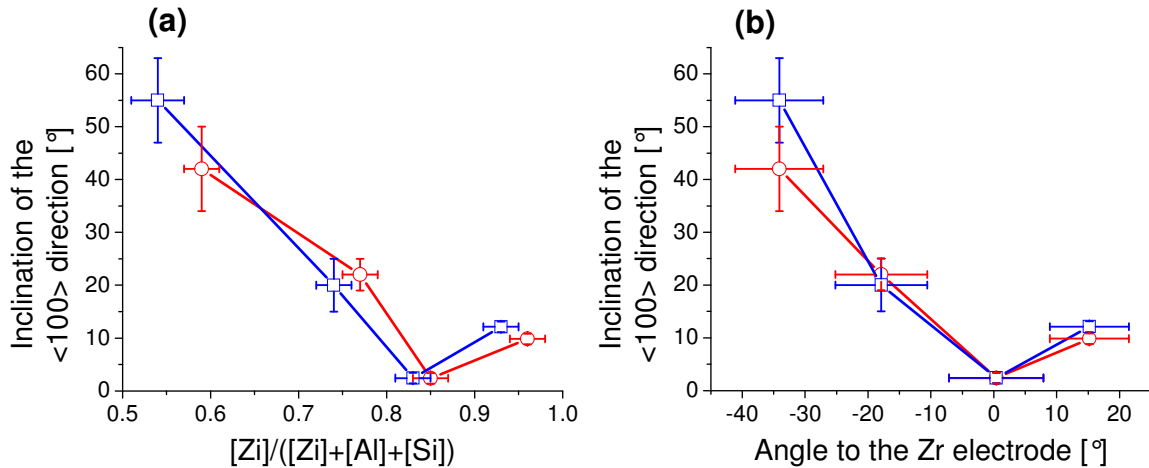


Fig. 18. Inclination of the $\langle 100 \rangle$ texture direction from the sample surface perpendicular direction as observed for the cubic phase in the Zr-Al-N (open red circles - \circ) and Zr-Al-Si-N (open blue squares - \square) thin films as a function of the zirconium contents (a), and as a function of the angle between the sample normal direction and the direction from the substrate to the Zr cathode (b).

The inclination of the $\langle 100 \rangle$ preferred orientation direction of fcc crystallites perpendicular to the sample normal towards the sample surface was independent on the silicon content as it can be clearly seen from Fig. 18a, where the inclination of the $\langle 100 \rangle$ texture direction for samples with and without silicon underwent similar evolution. The degree of the out-of-plane texture, derived from the FWHM of the central texture peak was in both cases strongest for samples containing highest zirconium concentration and with increasing aluminium and silicon contents the degree of the out-of-plane texture decreased rapidly. The three-dimensional preferred orientation of fcc crystallites was not observed in the

Zr-Al-N and Zr-Al-Si-N coatings – the in-plane texture did not form in the zirconium based coatings.

In Fig. 18b the inclination of the $\langle 100 \rangle$ crystallographic direction of the fcc crystallites from the sample surface perpendicular direction as a function of the angle between the surface normal direction and the direction from the substrate to the zirconium cathode in Zr-Al-(Si-)N coatings is shown. It is obvious from the Fig. 18b that the inclination of the $\langle 100 \rangle$ crystallographic direction strongly correlates with the angle between the sample normal and sample-cathode direction. For the first three zirconium richest samples in both Zr-Al-N and Zr-Al-Si-N coatings series the correlation is nearly perfect. The correlation is less pronounced in the samples with composition $\text{Zr}_{0.59}\text{Al}_{0.41}\text{N}$ and $\text{Zr}_{0.54}\text{Al}_{0.41}\text{Si}_{0.05}\text{N}$, however in these coatings, the intensity maximum in the measured pole figures was weak and highly broadened besides so that the determined value of the maximum suffers from a high error. Therefore, we suppose that the deposition geometry plays the most important role in the preferred orientation of the fcc crystallites development in the Zr-Al-(Si-)N coatings.

Comparison of the preferred orientation of crystallites in the fcc phase of M-Al-(Si-)N coatings under study, allows us to draw the next conclusions. For the texture evolution in the CAE M-Al-(Si-)N coatings the next parameters are highly important: a) the deposition geometry, b) chemical and phase composition of coatings and c) residual stress and elastic anisotropy.

In the cubic phase of all M-Al-(Si-)N coatings under study, we observed one main texture component preferentially oriented perpendicular to the sample surface in samples with high transition metal contents. In the Cr-Al-(Si-)N and Ti-Al-(Si-)N coatings the $\langle 111 \rangle$ crystallographic direction, and in the Zr-Al-(Si-)N samples the $\langle 100 \rangle$ crystallographic direction were preferentially oriented perpendicular to the sample surface. With increasing Al and Si contents, the main texture direction significantly inclined from the sample surface perpendicular direction, except the Cr-Al-N coatings, where the inclination was only moderate. Besides, in the Cr-Al-(Si-)N and Ti-Al-(Si-)N coatings a pronounced three-dimensional preferred orientation of the fcc crystallites, described by the coexistence of the out-of-plane and in-plane texture, was observed.

The strongest influence on the degree and formation of the in-plane preferred orientation has the deposition geometry, i.e. the position of the specimen in the deposition chamber. The samples situated in front of the transition metal cathode exhibited strongest in-plane texture, whereas with increasing distance from this cathode the in-plane texture significantly weakened. However, the degree of the in-plane texture is also influenced by the chemical composition of the coatings. In the Cr-Al-N and Ti-Al-N coatings, the neighbouring crystallites were in contact and grew coherently with a pronounced preferred in-plane orientation. The addition of silicon led to a separation of the crystallites by amorphous Si_xN_y phase in which the lateral coherence of crystallites and the in-plane texture were lost.

The inclination of the main texture direction from the normal to the sample surface (inclination of the out-of-plane texture) is controlled mainly by the chemical composition of coatings. With increasing aluminium and silicon contents, we observed obvious inclination of the out-of-plane texture in all Cr-Al-(Si)-N and Ti-Al-(Si)-N coatings under study, whereas the effect of silicon addition is stronger as in the samples containing silicon the inclination of the out-of-plane texture is more pronounced. The out-of-plane texture inclination in the Cr-Al-N samples is only moderate in comparison to the Cr-Al-Si-N and Ti-Al-(Si)-N coatings. This effect can be explained taking into account high residual stresses that are present in the Cr-Al-N samples.

It was shown by several authors that the preferred orientation of the fcc crystallites in thin films of transition metal nitrides is controlled by the competition between the surface energy and the strain energy [30-34]. In the transition metal nitrides with the fcc structure, the {001} lattice planes possess the lowest surface energy, thus the {100} texture is expected in very thin films with none or very low lattice strain. Because of the strong crystallographic anisotropy of the elastic constants in the M-Al-(Si)-N coatings, which results in the anisotropy of the Young modulus with $E_{001} > E_{111}$, the {111} texture should dominate for increasing compressive residual stress. The strain energy increases with increasing thickness of the coatings, thus the preferred orientation changes during the layer growth as it was observed, e.g., in [31, 32, 34].

This consideration fully explains the texture evolution in the Cr-Al-N coatings where we observed only a slight inclination of the out-of-plane {111} texture. In the Cr-Al-N coatings, the strain energy prevails over the surface energy because the Cr-Al-N samples exhibit highest residual stresses from all coatings under study, and in addition high elastic anisotropy that does not relax with increasing aluminium contents. Vice versa, the lower residual stresses and significant reduction of the elastic anisotropy with increasing aluminium contents is the reason for the out-of-plane texture inclination in the Ti-Al-N coatings.

To explain the effect of silicon that speeds up the $\langle 111 \rangle$ out-of-plane texture direction inclination and additionally causes decay of both (in-plane and out-of-plane) texture components in the Cr-Al-Si-N and Ti-Al-Si-N coatings we have to consider the phase development as well. As it was already mentioned in previous chapters, the superfluous silicon creates amorphous Si_xN_y phase, which surrounds the crystallites. Primarily the formation of amorphous Si_xN_y causes a steep increase of the local disorientation of neighbouring fcc crystallites because the transfer of the preferred orientation of crystallites between neighbouring crystallites is interrupted by the amorphous silicon nitride, which cause the decay of both texture components degree. Moreover, the fcc nanocrystallites growing on the amorphous phase build in fact very thin slabs, which thickness is comparable with the crystallite size. Thus, the texture of small fcc crystallites will consequently be controlled rather by the surface energy of the crystallites than by their strain energy, or in other words the out-of-plane texture component tilts from the {111} into the {100} texture. As the strain

energy depends on the thickness of the crystalline slabs, the size of crystallites in the M-Al-(Si-)N nanocomposite coatings that are separated by the amorphous phase can be one of the microstructure parameters, which control the inclination of the texture direction.

In Zr-Al-(Si-)N coatings we did not observe the three dimensional preferred orientation of the fcc crystallites and only the {100} out-of-plane texture was observed. Based on the surface and strain energy considerations, we suppose that the formation of the {100} texture is the consequence of relatively small residual stresses and mainly the small crystallites sizes in the Zr-Al-(Si-)N coatings (which in combination prefer the formation of the {100} over the {111} texture). A dominant influence on the $\langle 100 \rangle$ texture direction inclination has the deposition geometry as the angle of the $\langle 100 \rangle$ texture direction inclination correlates well with the angle between the sample surface normal and the sample-cathode direction. We can deduce that in the Zr-Al-(Si-)N coatings the {100} texture forms in the fcc phase, independently on the specimens chemical and phase composition, in the plane perpendicular to the incoming zirconium particles direction. The inclination of the $\langle 100 \rangle$ texture direction is than only a virtual artefact coming from the orientation of the angle between the sample normal and the metal cathode direction.

3.4. Crystallite size and partial coherence of crystallites

High hardness, which is one of the most important parameter for the industrial applications of the hard coatings, is significantly influenced by the crystallite size. The idea to exploit the small crystallite size for the improvement of the hardness is based on the work of Hall and Petch [3,4], who have shown the increase of hardness in metallic materials with decreasing grain size.

The fundamental technique that was used in this work for the determination of the crystallite size was the analysis of the XRD line broadening. The results obtained from the XRD profile analysis were confirmed and complemented by HRTEM and TEM investigation. The dependence of the integral line broadening on the sine of the diffraction angle that was observed in all CAE M-Al-(Si)-N coatings under study is shown in Figs. 19 a, b on the example of the fcc crystallites in Zr-Al-N (Fig. 19a) and Zr-Al-Si-N (Fig. 19b) samples with different Al and Si contents.

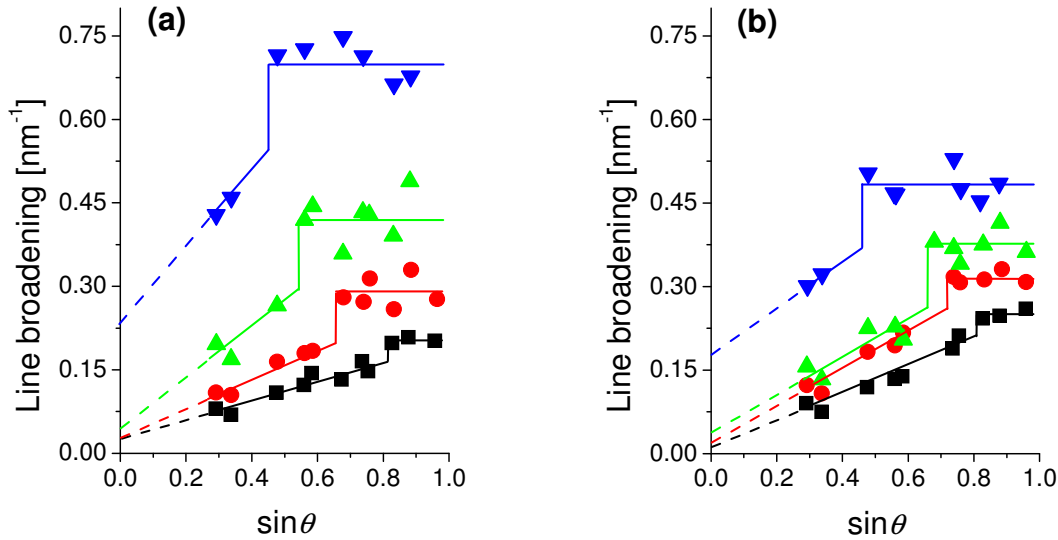


Fig. 19. Dependence of the integral line broadening on sine of the Bragg angle as observed for the fcc phase of the Zr-Al-N coatings (a); $Zr_{0.96}Al_{0.04}N$ - black boxes, $Zr_{0.85}Al_{0.15}N$ - red circles, $Zr_{0.77}Al_{0.23}N$ - green triangles and $Zr_{0.59}Al_{0.41}N$ - blue bottom up triangles, and Zr-Al-Si-N samples (b); $Zr_{0.93}Al_{0.06}Si_{0.01}N$ - black boxes, $Zr_{0.83}Al_{0.15}Si_{0.02}N$ - red circles, $Zr_{0.74}Al_{0.23}Si_{0.03}N$ - green triangles and $Zr_{0.54}Al_{0.41}Si_{0.05}N$ - blue bottom up triangles. Horizontal solid lines show the saturated XRD line broadening that was used for calculation of the crystallite size. Dashed lines show the extrapolation of the XRD line broadening from partially coherent crystallites to $\sin\theta = 0$ that was used for the estimation of the cluster size.

As described in details in [35-37] and in chapter 9, this dependence can be divided into two parts. At low diffraction angles, an increase of the XRD line broadening with increasing diffraction angle is observed similarly to the classical Williamson-Hall plot [38]. Within the classical kinematical diffraction theory, the extrapolation of the linear dependence of the XRD line broadening to $\sin\theta = 0$ yields the reciprocal size of crystallites, i.e. the reciprocal size of coherent domains that can contain structure defects, e.g. dislocations. These structure defects are responsible for the increase of the XRD line broadening with increasing diffraction angle [39]. In nanocrystalline materials and in nanocomposites with a strong preferred orientation of

the neighbouring nanocrystallites, the extrapolation of the linear dependence of the XRD line broadening to $\sin\theta = 0$ (dashed lines in Fig. 19) yields the reciprocal size of domains (clusters), which parts are partially coherent for X-rays. The effect of the partial coherence disappears at a certain diffraction angle [35] that is observed as a steep increase of the XRD line broadening (Fig. 19). The position of the steep increase of the XRD line broadening was used for determination of the mutual disorientation of the parts of the domains. In the second part of the modified Williamson–Hall plot, where the partial coherence of the nanocrystallites within the clusters is absent, a constant XRD line broadening is typically observed. This maximum line broadening corresponds to the reciprocal size of nearly defect-free nanocrystallites as it is often calculated using the classical Scherrer formula [40].

The size of clusters consisting of partially coherent nanocrystallites was (47 ± 8) nm in the Cr-Al-N and Cr-Al-Si-N coatings, (26 ± 6) nm in the Ti-Al-N and Ti-Al-Si-N coatings and (50 ± 9) nm in the Zr-Al-N and Zr-Al-Si-N coatings as calculated from the extrapolation of the XRD line broadening to $\sin\theta = 0$. A TEM micrograph of the cluster is shown in Fig. 20a for the sample $\text{Cr}_{0.91}\text{Al}_{0.08}\text{Si}_{0.01}\text{N}$. The cluster size obtained from the XRD line broadening did not change significantly with the Al and Si contents. However, the accuracy of the cluster size determination decreased rapidly with increasing Al and Si contents, because the range of the constant XRD line broadening shifted to smaller diffraction angles. Thus, only few experimental points could be used for the extrapolation of the line broadening within the region of the partial coherence (Fig. 19). The TEM micrograph from Fig. 20a indicates an internal structure of the clusters, which was proven by HRTEM and quantified by XRD. In this particular sample with the overall chemical composition $\text{Cr}_{0.91}\text{Al}_{0.08}\text{Si}_{0.01}\text{N}$, XRD revealed the cluster size of (47 ± 8) nm, which matches well with the TEM micrograph.

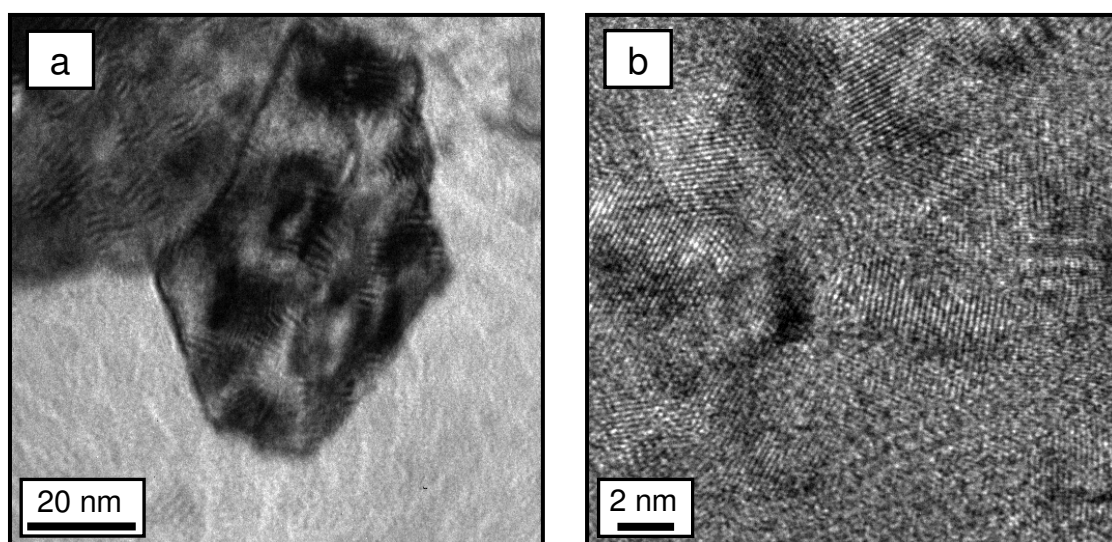


Fig. 20. TEM micrograph of the sample $\text{Cr}_{0.91}\text{Al}_{0.08}\text{Si}_{0.01}\text{N}$ showing the object, which was identified using XRD as a nanostructured cluster with the size of (47 ± 8) nm consisting of partially coherent nanocrystallites having the size of (11.0 ± 0.5) nm and the mutual disorientation of $(0.47 \pm 0.05)^\circ$ (a). HRTEM micrograph of the sample $\text{Cr}_{0.40}\text{Al}_{0.52}\text{Si}_{0.08}\text{N}$. The crystallite size calculated from the XRD line broadening was (4.5 ± 0.3) nm, and the neighbouring crystallites were non-coherent for XRD (b).

Furthermore, XRD resolved the internal structure of the clusters in this sample and found out that they consist of partially coherent nanocrystallites having the size of (11.0 ± 0.5) nm and the mutual disorientation of $(0.47 \pm 0.05)^\circ$. The presence of individual nanocrystallites gives obviously rise to the occurrence of the diffraction contrast within the clusters in Fig. 20a. The existence of nanocrystallites within the clusters can much better be seen in the HRTEM micrograph of the sample $\text{Cr}_{0.40}\text{Al}_{0.52}\text{Si}_{0.08}\text{N}$ (Fig. 20b). According to the results of XRD, this sample contains non-coherent nanocrystallites having the size of (4.5 ± 0.3) nm. This crystallite size agrees well with the size of the nanocrystallites seen by HRTEM. The mutual disorientation of the non-coherent nanocrystallites in this sample was sufficiently high in order to be able to recognize their boundaries using HRTEM - more than 1.45° as obtained from XRD. The size of the fcc crystallites and their mutual disorientation within the clusters are plotted in Figs. 21a and 21b, respectively, as functions of the chemical composition of the coatings.

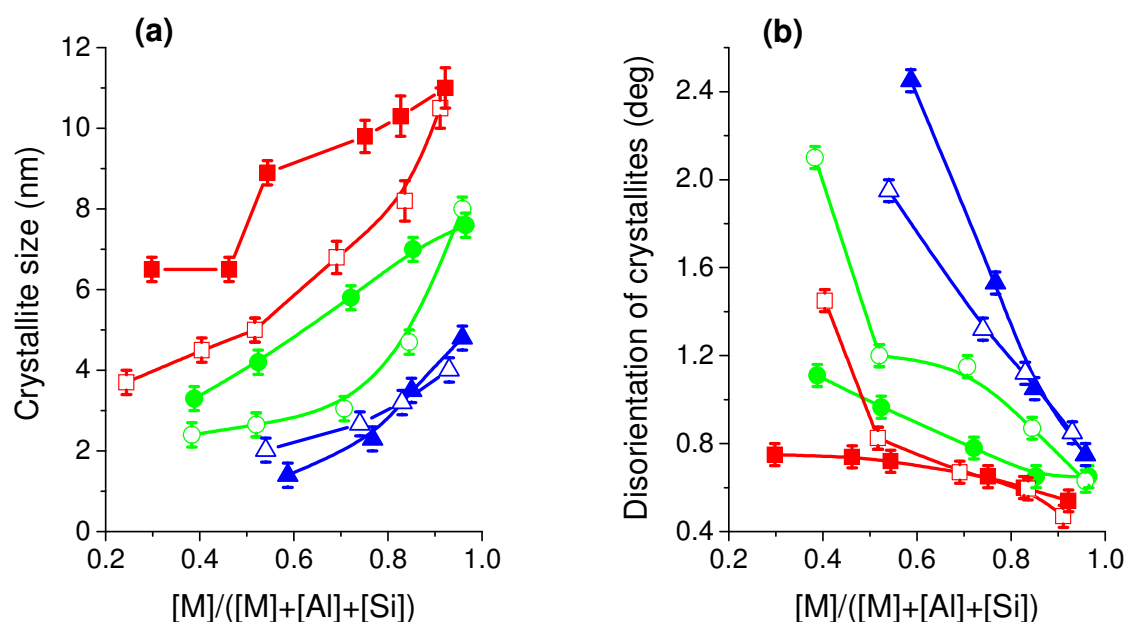


Fig. 21. The size of the fcc crystallites in the Cr-Al-N (red solid boxes), Cr-Al-Si-N (red open boxes), Ti-Al-N (green solid circles), Ti-Al-Si-N (green open circles) Zr-Al-N (blue solid triangles) and Zr-Al-Si-N (blue open triangles) nanocomposites as a function of the transition metal contents (a). Dependence of the mutual disorientation of partially coherent fcc nanocrystallites on the transition metal contents in the Cr-Al-N (red solid boxes), Cr-Al-Si-N (red open boxes), Ti-Al-N (green solid circles), Ti-Al-Si-N (green open circles), Zr-Al-N (solid triangles) and Zr-Al-Si-N (blue open triangles) nanocomposites (b). The fcc crystallites in the coatings with the overall chemical compositions $\text{Cr}_{0.40}\text{Al}_{0.52}\text{Si}_{0.08}\text{N}$ and $\text{Ti}_{0.38}\text{Al}_{0.54}\text{Si}_{0.08}\text{N}$ were non-coherent for X-ray diffraction; thus their mutual disorientations could only be estimated to exceed 1.45° and 2.1° , respectively.

In all coatings under study, the crystallite size was much smaller than the cluster size and decreased with increasing Al and Si contents. In the transition-metal-rich Cr-Al-(Si)-N and Ti-Al-(Si)-N coatings, the size of crystallites was approximately 4 times smaller than the cluster size. In the Zr-rich Zr-Al-(Si)-N coatings, this ratio was larger than 10. In the Si-free M-Al-N coatings, the fastest decrease of the crystallite size was observed at the beginning of the phase decomposition, i.e. below $\text{Cr}_{0.54}\text{Al}_{0.46}\text{N}$, $\text{Ti}_{0.72}\text{Al}_{0.28}\text{N}$ and $\text{Zr}_{0.85}\text{Al}_{0.15}\text{N}$. The mutual

disorientation of the neighbouring nanocrystallites increased in all M-Al-N coatings with increasing Al contents. In the Cr-Al-N coatings, the increase of the crystallite disorientation with increasing Al contents was faster in the single-phase region than in the two-phase region. The Ti-Al-N and Zr-Al-N coatings behaved conversely to the Cr-Al-N coatings: the increase of the disorientation of neighbouring nanocrystallites was faster in the two-phase region than in the single-phase region. The addition of Si speeded up the reduction of the crystallite size both in the Cr-Al-Si-N and Ti-Al-Si-N coatings. In Zr-Al-Si-N coatings, the addition of silicon accelerated the crystallite size reduction only in the single phase region. The mutual disorientation of crystallites was affected by the addition of Si mainly in the Ti-Al-Si-N coatings. In the Cr-Al-Si-N coatings, a larger disorientation of neighbouring nanocrystallites as compared to the Cr-Al-N coatings was only observed at the highest Si contents. In both sample series, Cr-Al-Si-N and Ti-Al-Si-N, the disorientation of crystallites exceeded the limit for their partial coherence at the Si concentration of 4 at.%. The influence of increasing Al contents on the increase of the mutual disorientation of crystallites is most pronounced in the Zr-Al-N and Zr-Al-Si-N samples comparing to the chromium and titanium containing coatings. Simultaneously, the addition of silicon in the Zr-Al-Si-N samples acts conversely in comparison to the chromium and titanium based coatings.

On the basis of above results, we can conclude that the development of the crystallite size and mutual disorientation of crystallites in the M-Al-(Si-)N coatings is driven mainly by the element and phase composition. Increasing aluminium contents in the coatings caused a reduction of the fcc nanocrystallites size and an increase of their mutual disorientation. More pronounced increase of the crystallite disorientations was observed after w-AlN appeared in the coatings that is caused by a larger lattice misfit between the fcc and w-AlN with increasing volume fraction of the w-AlN crystallites. Moreover, the increasing volume fraction of the w-AlN crystallites accelerated the reduction of the fcc crystallites. The addition of silicon speeded up the reduction of the size of the fcc crystallites in the Cr-Al-Si-N and Ti-Al-Si-N coatings, which effect was only insignificant in the Zr-Al-Si-N samples. In the Ti-Al-Si-N coatings, the addition of Si led additionally to a larger disorientation of the fcc crystallites in comparison with the Ti-Al-N coatings. At the Si contents higher than approximately 4 at.%, the mutual disorientation of fcc crystallites exceeded the limit of their partial coherence for X-rays both in the Cr-Al-Si-N and in the Ti-Al-Si-N coatings. The fcc nanocrystallites in the Cr-Al-Si-N and Ti-Al-Si-N coatings were not partially coherent for the X-rays any more, contrary to the Zr-Al-Si-N coating which remained partially coherent even for such high silicon contents.

3.5. Mechanical properties – hardness

The hardness of coatings is the parameter having one of the highest importance for coatings industrial applications. The hardness of the coatings was obtained from the nanoindentation experiments performed on three different equipments, as it is in details described in chapter 2.5. In the bounds of errors, all three measurements performed on different equipments yielded similar results.

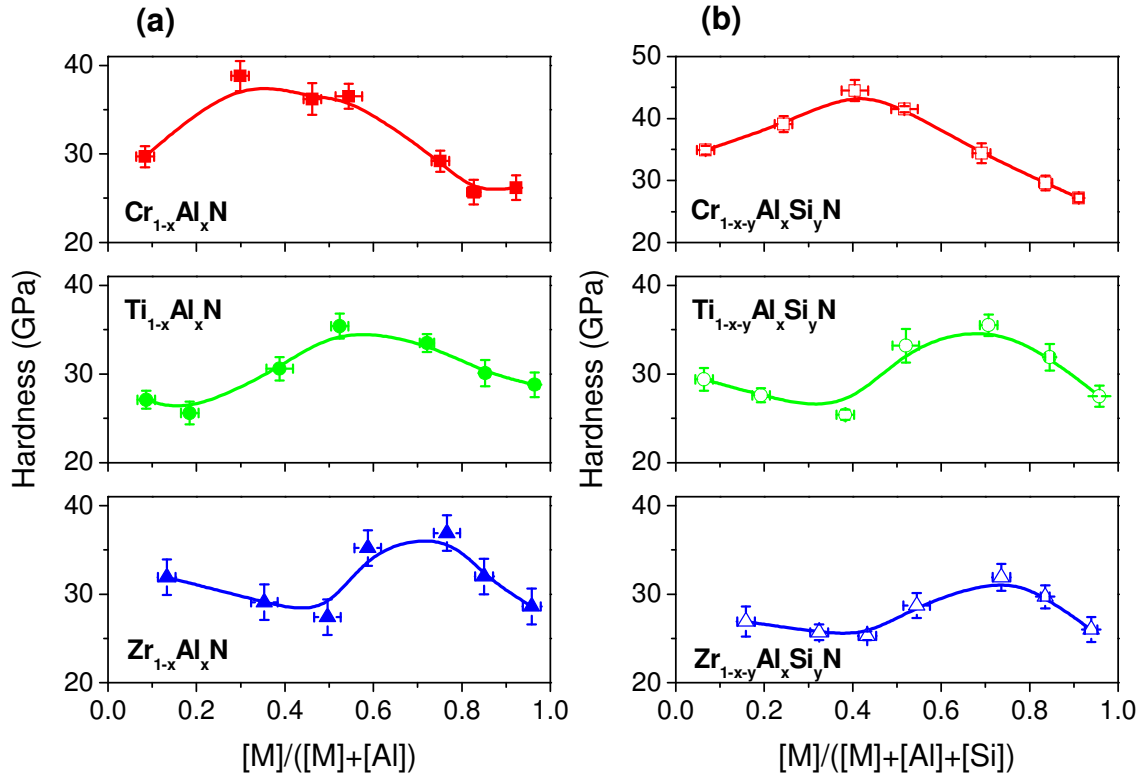


Fig. 22. Hardness of the Cr-Al-N, Ti-Al-N, Zr-Al-N (a) and Cr-Al-Si-N, Ti-Al-Si-N, Zr-Al-Si-N (b) coatings as a function of the transition metal contents.

In all M-Al-(Si-)N samples under study, the hardness of the coatings increased with the addition of Al until a maximum was reached that was followed by a decrease of the hardness with further increasing Al contents (Fig. 22). The Al contents, for which the maximum hardness was observed, decreased with increasing intrinsic lattice parameter of the respective binary nitride. In the silicon free coatings the hardness maximum was observed at 35 at.% Al in $\text{Cr}_{0.30}\text{Al}_{0.70}\text{N}$, 24 at.% Al in $\text{Ti}_{0.52}\text{Al}_{0.48}\text{N}$ and 12 at.% Al in $\text{Zr}_{0.77}\text{Al}_{0.23}\text{N}$. The addition of silicon shifted the maximum of hardness slightly to lower Al concentration region in Cr-Al-Si-N and Ti-Al-Si-N coatings, while the Al concentration of the hardness maximum in Zr-Al-Si-N was nearly similar as in Zr-Al-N coatings. The samples with the maximum hardness consisted of two crystalline phases, fcc phase and w-AlN, having approximately the same volume ratio (compare Figs. 22 and 8).

The highest hardness in all M-Al-(Si-)N coatings under study was observed in the Cr-Al-Si-N coatings in general, whereas the maximum hardness reached the sample

$\text{Cr}_{0.40}\text{Al}_{0.52}\text{Si}_{0.08}\text{N}$ with hardness of (44.5 ± 1.7) GPa. The maximum hardness in the silicon free Cr-Al-N and Ti-Al-N series was in both cases slightly lower than in samples containing silicon. Contrary, in the Zr based coatings the hardness was higher in the sample series without silicon. Besides, in the M-Al-Si-N coatings, we can observe a significant evolution of the maximum hardness – decrease from Cr-Al-Si-N over Ti-Al-Si-N to Zr-Al-Si-N coatings, while in the Si-free samples the maximum hardness in all three M-Al-N coatings is, in the bounds of errors, similar (see Figs. 23a, b).

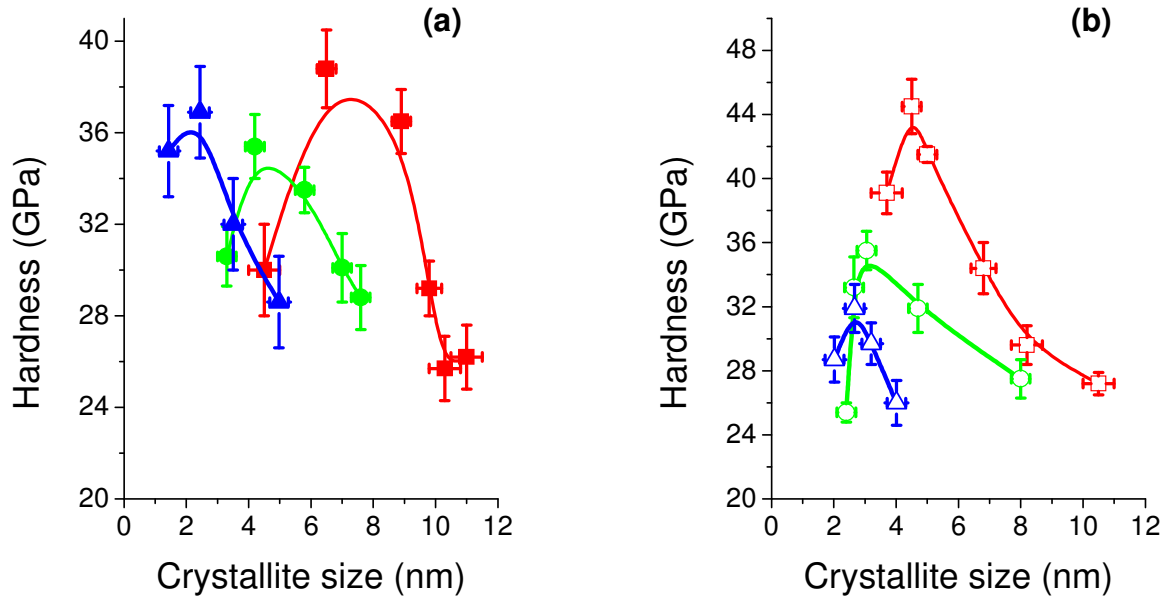


Fig. 23. Hardness of the Cr-Al-N (solid red squares), Ti-Al-N (solid green circles), Zr-Al-N (solid blue triangles) (a) and Cr-Al-Si-N (open red squares), Ti-Al-Si-N (open green circles), Zr-Al-Si-N (open blue triangles) (b) coatings plotted as a function of the fcc phase crystallite size.

In Figs. 23a, b the hardness of the coatings plotted as a function of the fcc phase crystallite size is shown. In all M-Al-(Si-)N systems studied, the hardness of the coatings increases with decreasing crystallite size until a maximum is reached and consequently the hardness is decreasing with further decrease of the crystallite size. The crystallite size of the fcc phase at which the maximum is achieved decreases with increasing intrinsic lattice parameter of corresponding binary nitride i.e. Zr-Al-(Si-)N coatings reach the maximum hardness at lowest crystallite size, followed by the Ti-Al-(Si-)N and finally the hardness maximum in Cr-Al-(Si-)N coatings developed at the largest size of the crystallites. The maximum hardness is achieved for the crystallite size of about 6.5 nm for Cr-Al-N, 4.2 nm for Ti-Al-N and 2.4 nm for Zr-Al-N. Addition of silicon decreases furthermore the crystallite size of the fcc phase, at which the maximum of hardness is achieved in Cr-Al-Si-N and Ti-Al-Si-N to approximately 4.5 nm and 3.1 nm, respectively. In the Zr-Al-Si-N coatings, the addition of silicon does not play any significant role and the crystallite size of the highest hardness is, in the bounds of errors, similar to Zr-Al-N.

Correlating the results of the preceding paragraphs with the hardness measurements we can summarize the all microstructural parameters discussed in the previous chapters, i.e. the elementary and the phase composition, residual stress, preferred orientation of crystallites and the size and partial coherence of nanocrystallites influence significantly the mechanical properties of the M-Al-(Si-)N coatings. The fundamental role play the elementary and implicitly the phase composition as we saw that the highest hardness developed in coatings containing two crystalline phases (fcc phase and w-AlN) in which the fcc crystallites were partially coherent. In samples with partially coherent cubic crystallites the crystallites of the fcc phase and w-AlN phases are intertwined, which is needed for the transfer of the local crystallographic orientation in the coatings that is necessary for the partial coherence of cubic crystallites and that contributes concurrently to the development of the intrinsic lattice strain. The intrinsic lattice strain (and intrinsic residual stress), that improves the hardness of coatings, necessarily results from a mismatch of the interplanar spacings in both structures (fcc phase and w-AlN) if the crystallites have an appropriate mutual orientation. In samples with non-coherent crystallites, the crystallites are separated by amorphous phase, which can neither transfer the crystallographic orientation between neighbouring crystallites nor assist in the development of the intrinsic lattice deformation at the crystallite boundaries. However, a small amount of amorphous Si_xN_y , in samples where the fcc crystallites are still partially coherent, is beneficial for the higher hardness of the coatings as well, since the amorphous phase can “absorb” the local strain (and deformation) changes that could otherwise lead to the creation and propagation of cracks in the crystalline phases. This phenomenon was found to be responsible for increase of the hardness in the Cr-Al-Si-N and Ti-Al-Si-N coatings in comparison to the samples without silicon. Finally, the influence of decreasing crystallite size on the increase of hardness was obvious in all M-Al-(Si-)N coatings under study.

Therefore we can conclude that for the high hardness development in the M-Al-(Si-)N coatings the dual-phase composition (with small amount of amorphous Si_xN_y , eventually), the partially coherent crystallites, high compressive residual stresses and small crystallites are highly important. The M-Al-(Si-)N coatings reveal the highest hardness after simultaneous satisfaction of all above mentioned conditions.

3.6. Microstructural model

The following model of the microstructure formation and evolution in the Cr-Al-(Si)-N, Ti-Al-(Si)-N and Zr-Al-(Si)-N nanocomposite coatings deposited using cathodic arc evaporation can be suggested from the above results. During the cathodic arc evaporation, the coatings were built up from clusters of the respective fcc phase, which had the size of several tens of nanometers. The size of the clusters was different in the coatings containing Cr, Ti and Zr, but for the particular transition metal, it did not change significantly with the addition of Al and Si within the experimental accuracy of the XRD line profile analysis. The clusters consisted of fcc nanocrystallites that had very small mutual disorientations and that were partially coherent for XRD in the most cases.

The increasing Al contents in the coatings caused a further reduction of the size of the fcc nanocrystallites and an increase of their mutual disorientation. A more pronounced increase of the crystallite disorientations was observed after w-AlN appeared in the coatings that can be explained by a lattice misfit between fcc and w-AlN. With increasing volume of the w-AlN crystallites the disorientation of the fcc crystallites increases as well (Fig. 21b). The appearance and increasing amount of the w-AlN nanocrystallites accelerated the reduction of the size of fcc crystallites. Although the mutual disorientation of the fcc crystallites increased with increasing Al contents, it was below 2.5° in all M-Al-N coatings that contained fcc phase as the dominant phase. This small disorientation of crystallites implies that w-AlN forms during the segregation of Al from the fcc phase. Furthermore, the transfer of the preferred orientation of crystallites during the deposition process, concluded from the partial coherence of the fcc crystallites, was confirmed by the presence of a pronounced three-dimensional macroscopic texture in the Cr-Al-(Si)-N and Ti-Al-(Si)-N coatings. Schematic models of the cluster of crystallites in the single-phase region in M-Al-Si-N coatings, cluster in dual-phase region in M-Al-N and three-phase region in M-Al-Si-N coatings are shown in Fig. 24.

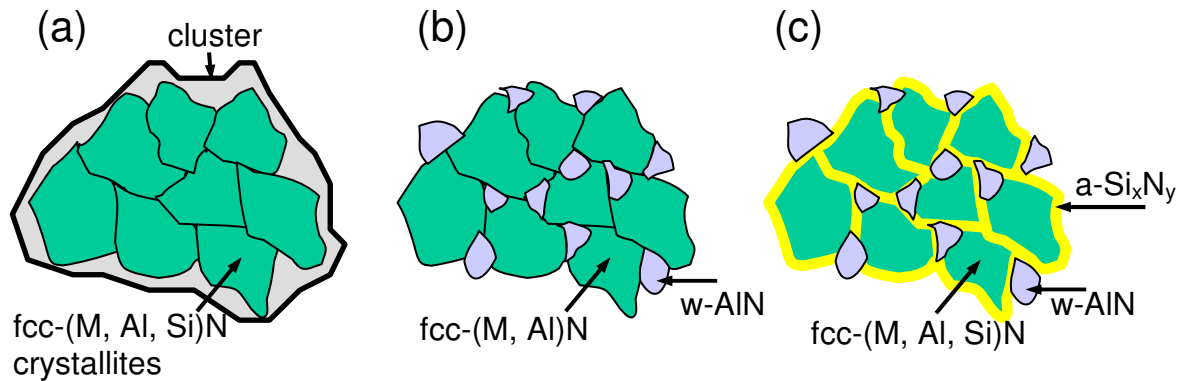


Fig. 24. Schematic model of the cluster of nanocrystallites in single-phase region in M-Al-Si-N coatings (a), cluster in two-phase region in M-Al-N (b) and three-phase region with 4 at.% of silicon in M-Al-Si-N (c) coatings. Green grains represent the fcc crystallites, light blue grains stand for the wurtzitic AlN crystallites and yellow colour symbolizes the amorphous Si_xN_y .

The maximum hardness was observed in the dual-phase M-Al-N coatings, in which the internal lattice strain developed at the interfaces between fcc and w-AlN. The increase of the hardness of the Ti-Al-N coatings due to the segregation of AlN was also reported in [42].

The addition of Si in the Cr-Al-Si-N and Ti-Al-Si-N coatings speeded up the reduction of the size of the fcc crystallites; however, this effect was only insignificant in the Zr-Al-Si-N samples. In the Ti-Al-Si-N coatings, the addition of Si led additionally to a larger disorientation of the fcc crystallites in comparison with the Ti-Al-N coatings. In the Cr-Al-Si-N coatings, a rapid increase of the disorientation of the fcc crystallites was first observed at Si contents exceeding 2.5 at.%. At Si contents higher than approximately 4 at.%, the mutual disorientation of the fcc crystallites exceeded the limit of their partial coherence for X-rays both in the Cr-Al-Si-N and in the Ti-Al-Si-N coatings. In both, Zr-Al-N and Zr-Al-Si-N coatings, the disorientation of the fcc crystallites increased linearly with increasing Al and Si contents. Surprisingly, this effect was slightly more pronounced in coatings without silicon.

Because of the observed gradual decrease of the size of the fcc crystallites (Fig. 21a) that was accompanied by the gradual increase of their mutual disorientation (Fig. 21b), we can assume that the superfluous elements (Al and Si) segregate at the existing microstructure defects, i.e. at the boundaries of the partially coherent fcc nanocrystallites, which are defined by dislocation networks [21, 43]. The segregation of the superfluous elements at the crystallite or grain boundaries in the ternary nitride thin films was described in [5, 44]. The segregation of Al and Si is followed by the growth of “bulky” w-AlN and amorphous Si_xN_y at higher Al and Si concentrations. The segregation of Al from the fcc phase host structure and the growth of w-AlN were directly confirmed by the analysis of the stress-free lattice parameters and by the XRD phase analysis, respectively (Figs. 7 and 8). Additional information about the growth of w-AlN and amorphous Si_xN_y at the present microstructure defects was obtained from the XRD analysis of the mutual disorientation of fcc crystallites. The very small mutual disorientation of neighbouring fcc nanocrystallites in the transition-metal-rich samples confirmed that the nanocrystallites are partially coherent and that they originate from the same cluster. The strong local preferred orientation of the fcc nanocrystallites in M-Al-N coatings containing w-AlN as a second phase supports the theory that w-AlN forms during the deposition process as a consequence of the segregation of elements or as a consequence of the spinodal decomposition of M-Al-N as suggested in [15, 45-49]. On the other hand, the transfer of the local preferred orientation between fcc crystallites through w-AlN is supported by the orientation relationship between the fcc phases and w-AlN and by similar interplanar spacings of certain lattice plains in both compounds [50]. Consequently, the mutual disorientation of fcc crystallites is larger for a larger lattice parameter of the respective fcc $\text{M}_{1-x}\text{Al}_x\text{N}$ phase that causes a larger lattice misfit between fcc $\text{M}_{1-x}\text{Al}_x\text{N}$ and w-AlN. The different mutual disorientations of fcc crystallites in the Cr-Al-(Si)-N, Ti-Al-(Si)-N and Zr-Al-(Si)-N coatings were illustrated in Fig. 21b. A small amount of Si influences the microstructure of the Cr-Al-Si-N and the Ti-Al-Si-N coatings differently. The decrease of the crystallite size

and the increase of the mutual disorientation of the partially coherent nanocrystallites are faster with increasing Si contents in the Ti-Al-Si-N coatings than in the Cr-Al-Si-N coatings. At higher Si contents, both systems behave similarly. The Zr-Al-N and Zr-Al-Si-N samples evolved similarly and we can conclude that the addition of silicon acts only a negligible role in these coatings.

Another questionable issue is the mechanism of the amorphous Si_xN_y phase formation. Based on the observed increase of the mutual disorientation of neighbouring fcc crystallites with increasing silicon contents, we suppose that for small silicon contents the superfluous silicon segregates at the crystallite or grain boundaries, forming small clusters of amorphous Si_xN_y phase. In this range of the silicon concentration, the amorphous Si_xN_y clusters increase the mutual disorientation of the fcc crystallites, however the fcc crystallites in the whole sample are still partially coherent. The reason is that the local preferred orientation of crystallites is controlled by the prevailing interfaces between the fcc crystallites, between which the local orientation can be transferred through. After the silicon contents exceed some critical concentration (in our samples it was approximately 4 at.%) a continuous amorphous layer, which surrounds the crystallites, forms rather than isolated amorphous clusters. The continuous amorphous layer surrounding the crystallites interrupts the transfer of the local preferred orientation of crystallites, which has in consequence the loss of the partial coherence of crystallites as we observed in the Cr-Al-Si-N and Ti-Al-Si-N coatings. A similar model of the amorphous phase development was published by Merics et al. [51], as well. However, only indirect validation of this hypothesis is possible from the experimental results. Very thin amorphous Si_xN_y layer surrounding the crystallites is neither detectable in the HRTEM nor it produces X-ray diffraction pattern. Therefore, the only indication of such amorphous Si_xN_y layer comes from the mutual disorientation of neighbouring crystallites and from the loss of the partial coherence of crystallites.

4. Conclusions

In this work, microstructure and properties of M-Al-(Si-)N nanocrystalline hard coatings and thin film nanocomposites deposited by cathodic arc evaporation (CAE) process at different positions of substrates in the deposition apparatus were investigated using the combination of electron probe microanalysis, X-ray diffraction, transmission electron microscopy with high resolution and hardness measurement.

The essential microstructural parameters; the chemical and phase composition, the residual stress, preferred orientation of crystallites, crystallite size and mutual disorientation of crystallites were determined in all coatings under study. The derived microstructural parameters were correlated with the hardness of coatings. Finally, the microstructural model of the nanocrystalline hard coatings and thin film nanocomposites formation was developed.

Depending on the sample chemical composition, three regions with different phase compositions exist in the coatings. In the transition metal richest samples, a single fcc $M_{1-x-y}Al_xSi_yN$ phase exists in the coating. With increasing Al content, w-AlN starts to develop as a second crystalline phase, whereas in this region both phases, fcc and w-AlN, coexist. Finally, at the highest Al concentrations only w-AlN phase exists in the coatings. In samples containing silicon, the silicon atoms are dissolved in the fcc phase in coatings with low Si concentration and with increasing Si content they form a third, amorphous Si_xN_y , phase. The phase composition and the limits of the phases coexistence depends strongly on the transition metal type.

In all coatings under study, no residual stress and lattice parameter depth gradients as well as no shear stresses and only biaxial rotationally symmetrical compressive state of stress were observed. The elastic anisotropy of the fcc crystallites decreased generally with increasing Al and Si concentration for all samples, whereas in the Ti-Al-(Si-)N coatings the anisotropy decay was linear with increasing Al and Si and the elastic anisotropy factor A approached one and the fcc crystallites became elastically isotropic. In the Cr-Al-(Si-)N and Zr-Al-(Si-)N coatings a significantly higher influence of the Si addition on the elastic anisotropy factor relaxation and thus transition from the elastically anisotropic to elastically isotropic state of the fcc crystallites was observed. The elastic anisotropy of the fcc crystallites remained high even for coatings with higher w-AlN phase fraction (the fcc crystallites are still highly anisotropic), while in samples containing Si the elastic anisotropy factor approached 1 in samples with prevailing w-AlN contents and the fcc crystallites appears elastically isotropic.

In all studied M-Al-(Si-)N coatings, a strong preferred orientation of crystallites was observed. In the fcc crystallites of the Cr-Al-(Si-)N and Ti-Al-(Si-)N coatings the $\langle 111 \rangle$ crystallographic direction, and in the Zr-Al-(Si-)N samples the $\langle 100 \rangle$ crystallographic direction was preferentially oriented perpendicular to the sample surface. With increasing Al and Si contents, the main texture direction of the fcc crystallites significantly inclined from

the sample surface perpendicular direction, except the Cr-Al-N coatings, where the inclination was only moderate. Besides, in the Cr-Al-(Si)-N and Ti-Al-(Si)-N coatings a pronounced three-dimensional preferred orientation of the fcc crystallites, described by coexistence of the out-of-plane and in-plane texture, was observed. The texture evolution in the fcc crystallites of studied coatings was described on basis of the deposition geometry, phase composition and residual stress and elastic anisotropy.

The cluster and the crystallite size of the investigated M-Al-(Si)-N coatings were determined from the analysis of the XRD line broadening and confirmed by the TEM and HRTEM investigations. The size of the clusters was (47 ± 8) nm in the Cr-Al-N and Cr-Al-Si-N coatings, (26 ± 6) nm in the Ti-Al-N and Ti-Al-Si-N coatings and (50 ± 9) nm in the Zr-Al-N and Zr-Al-Si-N coatings and the cluster size obtained from the XRD line broadening did not change significantly with the Al and Si contents. Increasing aluminium contents in the coatings caused a reduction of the fcc crystallites size and an increase of their mutual disorientation. More pronounced increase of the fcc crystallite disorientations was observed after w-AlN appeared in the coatings. Moreover, the increasing volume fraction of the w-AlN crystallites accelerated the reduction of the fcc crystallites. The addition of silicon speeded up the reduction of the size of the fcc crystallites in the Cr-Al-Si-N and Ti-Al-Si-N coatings, which effect was only insignificant in the Zr-Al-Si-N samples. At the Si contents higher than approximately 4 at.%, the mutual disorientation of fcc crystallites exceeded the limit of their partial coherence for X-rays both in the Cr-Al-Si-N and in the Ti-Al-Si-N coatings. The fcc crystallites in the Cr-Al-Si-N and Ti-Al-Si-N coatings were not partially coherent for the X-rays any more, contrary to the Zr-Al-Si-N coating which remained partially coherent even for such high silicon contents.

In all M-Al-(Si)-N samples under study, the hardness of the coatings increased with the addition of Al until a maximum was reached that was followed by a decrease of the hardness with further increasing Al contents. The Al contents, for which the maximum hardness was observed, decreased with increasing intrinsic lattice parameter of the respective binary transition metal nitride. In the silicon free coatings the hardness maximum was observed at 35 at.% Al in $\text{Cr}_{0.30}\text{Al}_{0.70}\text{N}$, 24 at.% Al in $\text{Ti}_{0.52}\text{Al}_{0.48}\text{N}$ and 12 at.% Al in $\text{Zr}_{0.77}\text{Al}_{0.23}\text{N}$. The addition of silicon shifted the maximum of hardness slightly to lower Al concentration region in Cr-Al-Si-N and Ti-Al-Si-N coatings, while the Al concentration of the hardness maximum in Zr-Al-Si-N was nearly similar as in Zr-Al-N coatings. The samples with the maximum hardness consisted of two crystalline phases, fcc phase and w-AlN, having approximately the same volume ratio, which confirmed that the formation of the nanocomposites is responsible for high hardness of the M-Al-(Si)-N coatings deposited using CAE.

It was shown that the elementary and the phase composition, residual stress, preferred orientation of crystallites and the size and partial coherence of nanocrystallites significantly influence the hardness of coatings. A fundamental role play the elementary and implicitly the phase composition as we saw that highest hardness developed in coatings containing two crystalline phases (fcc phase and w-AlN) in which the fcc crystallites were partially coherent.

In samples with partially coherent cubic crystallites the crystallites of the fcc phase and w-AlN phases are intertwined, which is needed for the transfer of the local crystallographic orientation in the coatings that is necessary for the partial coherence of cubic crystallites and that contributes concurrently to the development of the intrinsic lattice strain. The intrinsic lattice strain (and intrinsic residual stress), that improves the hardness of coatings, necessarily results from a mismatch of the interplanar spacings in both structures (fcc phase and w-AlN) if the crystallites have an appropriate mutual orientation. In samples with non-coherent crystallites, the crystallites are separated by amorphous phase, which can neither transfer the crystallographic orientation between neighbouring crystallites nor assist in development of the intrinsic lattice deformation at the crystallite boundaries. However, a small amount of amorphous Si_xN_y , in the samples where the fcc crystallites are still partially coherent, is beneficial for the higher hardness of the coatings as well, since the amorphous phase can “absorb” the local strain (and deformation) changes that could otherwise lead to the creation and propagation of cracks in crystalline phases. This phenomenon was found to be responsible for increase of the hardness in the Cr-Al-Si-N and Ti-Al-Si-N coatings in comparison to samples without silicon. Finally, the influence of decreasing crystallite size on the hardness increase was obvious in all M-Al-(Si-)N coatings under study.

5. References

- [1] S. Veprek, S. Reiprich, Li Shizhi, *Appl. Phys. Lett.*, **66**, (1995), 2640.
- [2] S. Veprek, S. Reiprich, *Thin Solid Films*, **268**, (1995), 64.
- [3] E. O. Hall, *Proc. Phys. Soc. Lond.*, **B 64**, (1951), 747.
- [4] N. J. Petch, *J. Iron Steel Inst.*, **174**, (1953), 25.
- [5] C. S. Sandu, R. Sanjinés, M. Benkahoul, F. Medjani, F. Lévy, *Surf. Coat. Technol.*, **201**, (2006), 4083.
- [6] P. H. Mayrhofer, G. Tischler, C. Mitterer, *Surf. Coat. Technol.*, **142-144**, (2001), 78.
- [7] P. H. Mayrhofer, C. Mitterer, J. Musil, *Surf. Coat. Technol.*, **174-175**, (2003), 725.
- [8] S. Veprek, M.G.J. Veprek-Heijman, *Surf. Coat. Technol.*, **201**, (2007), 6064.
- [9] P. Holubář, M. Jílek, M. Šíma, *Surf. Coat. Technol.*, **133-134**, (2000), 145.
- [10] DIN V ENV 1071-2:1993-11.
- [11] W. Parrish and M. Mack, *Acta Cryst.*, **23**, (1967), 687.
- [12] D. Rafaja, V. Valvoda, *Powder Diffraction*, **6 (4)**, (1991), 200.
- [13] V. Hauk, *Structural and Residual Stress Analysis by Nondestructive Methods*, Amsterdam, Elsevier, (1997).
- [14] Sugishima, A., Kajioka, H. & Makino, Y., *Surf. Coat. Technol.*, **97**, (1997), 590.
- [15] P. H. Mayrhofer, D. Music, J. M. Schneider, *Appl. Phys. Lett.*, **88**, (2006), 071922.
- [16] ICSD Database, Version 2007-2, FIZ Karlsruhe & NIST (2007).
- [17] P. J. Martin, A. Bendavid, J. M. Cairney, M. Hoffman, *Surf. Coat. Technol.*, **200**, (2005), 2228.
- [18] D. Rafaja, C. Wüstefeld, M. Dopita, M. Růžicka, V. Klemm, G. Schreiber, D. Heger, M. Šíma, *Surf. Coat. Technol.*, **201**, (2007), 9476.
- [19] D. Rafaja, A. Poklad, V. Klemm, G. Schreiber, D. Heger, M. Šíma, M. Dopita, *Thin Solid Films*, **514**, (2006), 240.
- [20] A. J. Perry, *Thin Solid Films*, **193/194**, (1990), 463.
- [21] Ch., Wüstefeld, D. Rafaja, M. Dopita, V. Klemm, *Z. Kristallographie*, **27**, (2008), 159.
- [22] D. Rafaja, M. Šíma, V. Klemm, G. Schreiber, D. Heger, L. Havela, R. Kužel, *J. Alloys Compd.*, **378**, (2004), 107.
- [23] D. Rafaja, V. Valvoda, R. Kužel, A.J. Perry, J.R. Treglio, *Surf. Coat. Technol.*, **86-87**, (1996), 302.
- [24] M. Dopita, D. Rafaja, *Z. Kristallographie*, **23**, (2006), 67.
- [25] F. Attar, and T. Johannesson, *Thin Solid Films*, **258**, (1995), 205.
- [26] A. J. Perry, V. Valvoda, D. Rafaja, *Thin Solid Films*, **214**, (1992), 169.
- [27] A. J. Perry, J. Schoenes, *Vacuum*, **36**, (1986), 149.
- [28] D. Rafaja, A. Poklad, G. Schreiber, V. Klemm, D. Heger, M. Šíma, *Z. Metallkd.*, **96**, (2005), 736.

- [29] M. Dopita, D. Rafaja, C. Wüstefeld, M. Růžicka, V. Klemm, D. Heger, G. Schreiber, M. Šíma, *Surf. Coat. Technol.*, **202**, (2008), 3199.
- [30] C.-H. Ma, J.-H. Huang, H. Chen, *Thin Solid Films*, **446**, (2004), 184.
- [31] J. Pelleg, L. Z. Zevin, S. Lungo, *Thin Solid Films*, **197**, (1991), 117.
- [32] U. C. Oh, J. H. Je, *J. Appl. Phys.*, **74**, (1993), 1692.
- [33] C. V. Falub, A. Karimi, M. Ante, W. Kalss, *Surf. Coat. Technol.*, **201**, (2007), 5891.
- [34] C. Quaeys, G. Knuyt, J. D'Haen, L.M. Stals, *Thin Solid Films*, **258**, (1995), 170.
- [35] D. Rafaja, V. Klemm, G. Schreiber, M. Knapp, R. Kužel, *J. Appl. Crystallogr.*, **37**, (2004), 613.
- [36] D. Rafaja, V. Klemm, C. Wüstefeld, M. Motylenko, M. Dopita, *Materials Structure*, **14**, no.2, (2007), 67.
- [37] D. Rafaja, V. Klemm, C. Wüstefeld, M. Motylenko, M. Dopita, M. Schwarz, T. Barsukova, E. Kroke, *Z. Kristallographie*, **27**, (2008), 15.
- [38] G. K. Williamson, A. H. Hall, *Acta Metall. Mater.*, **1**, (1953), 22.
- [39] M. A. Krivoglaz, *X-ray and Neutron Diffraction in Non-ideal Crystals*, Springer, Berlin, (1996), 357.
- [40] P. Scherrer, *Nachr. Ges. Wiss. Göttingen*, **2**, (1918), 96.
- [41] W. C. Oliver, and G. M. Pharr, *J. Mater. Res.*, **7** (4), (1992), 1564.
- [42] A. Escudeiro Santana, A. Karimi, V. H. Derflinger, A. Schütze, *Thin Solid Films*, **469-470**, (2004), 339.
- [43] D. Rafaja, C. Wüstefeld, M. Dopita, V. Klemm, M. Růžicka, V. Klemm, G. Schreiber, D. Heger, M. Šíma, *Surf. Coat. Technol.*, **201**, (2007), 9476.
- [44] C. S. Sandu, R. Sanjinés, M. Benkahoul, M. Parlinska-Wojtan, A. Karimi, F. Lévy, *Thin Solid Films*, **496**, (2006), 336.
- [45] P. H. Mayrhofer, A. Hörling, L. Karlsson, J. Sjöln, T. Larsson, C. Mitterer, L. Hultman, *Appl. Phys. Lett.*, **83**, (2003), 2049.
- [46] R. F. Zhang, S. Veprék, *Acta Mater.*, **55**, (2007), 4615.
- [47] R. F. Zhang, S. Veprék, *Phys. Rev.*, **B 76**, (2007), 174105.
- [48] R. F. Zhang, S. Veprék, *Mat. Sci. Eng.*, **A 448**, (2007), 111.
- [49] P. H. Mayrhofer, F. D. Fischer, H.J. Böhm, C. Mitterer, J. M. Schneider, *Acta Mater.*, **55**, (2007), 1441.
- [50] D. Rafaja, T. Markewitz, C. Polzer, V. Klemm, G. Schreiber, P. Polcik, M. Kathrein, *Proceedings of the 17th Plansee seminar*, Vol 2, (2009), HM38.
- [51] D. Mercs, N. Bonasso, S. Naamane, J.-M. Bordes, C. Coddet, *Surf. Coat. Technol.*, **200**, (2005), 403.

6. List of figures

Fig. 1.	Sketch of the deposition chamber from the top view (a), picture of the deposition apparatus (b) and photograph of the samples positioned in the samples holder (c).	8
Fig. 2.	Illustration of several crystallites of a polycrystalline material satisfying the diffraction condition for different families of lattice planes (different diffraction angles 2θ) – normal directions to respective diffracting lattice planes have different angle with respect to the sample surface (a). Schematic sketch of the parallel beam geometry (b).	10
Fig. 3.	Two possible methods for the production of the parallel X-ray beam from a divergent monochromatic beam emitted by a conventional laboratory X-ray tube. Scheme of the multilayered parabolic mirror (a). Sketch of the polycapillary optics (b).	11
Fig. 4.	Penetration depth x_e as a function of diffraction angle 2θ calculated for the GAXRD due to the equation 1 for material having linear absorption coefficient $\mu = 580 \text{ cm}^{-1}$ and angles of incidence of primary beam $\gamma = 1, 2, 3, 5, 7$ and 10°	12
Fig. 5.	Sketch of an Eulerian cradle. In the scheme, the axes x, y, z , and goniometer circles ω, χ, ϕ are shown. The rotation axis ω coincides with y axis and rotation axis (tilt axis) χ with axis x	13
Fig. 6.	Sketch of the phase evolution in M-Al-N and M-Al-Si-N coatings with increasing Al content and structures of the fcc phase and wurtzitic AlN.	15
Fig. 7.	Fragments of the diffraction patterns taken for the Cr-Al-N (a), Cr-Al-Si-N (b), Ti-Al-N (c), Ti-Al-Si-N (d), Zr-Al-N (e) and Zr-Al-Si-N (f) coatings. The intensity scale in arbitrary units is logarithmic. In each figure bottom diffraction pattern corresponds to the coating with highest transition metal concentration and in the following diffraction patterns, the concentration of Al (or Al+Si) is increasing in accordance with the coatings composition given in Table 1. Diffraction lines from fcc phase are labelled by corresponding diffraction indices at the bottom (red coloured indices), diffraction lines from the w-AlN at the top of figures (black coloured indices). Reflections corresponding to the substrate are labelled with blue line and diffraction indices at the top of figures (blue coloured indices).	16
Fig. 8.	Dependence of the stress-free lattice parameters on the transition metal contents in fcc-(Cr, Al, Si) N (red boxes), fcc-(Ti, Al, Si) N (green circles) and fcc-(Zr, Al, Si) N coatings (blue triangles) as measured in the samples, in which fcc-(M, Al, Si) N was the dominating phase. Solid symbols are used for Si-free coatings, open symbols for coatings containing Si. Error bars of determined stress-free lattice parameters are smaller than the symbols. Solid lines indicate the hypothetical Vegard-like dependences for $\text{Cr}_{1-x}\text{Al}_x\text{N}$, $\text{Ti}_{1-x}\text{Al}_x\text{N}$ and $\text{Zr}_{1-x}\text{Al}_x\text{N}$. Grey rectangles mark the composition ranges of the maximum hardness from Fig. 23. Vertical dotted lines separate single fcc phase, dual phase (fcc + w-AlN) region and region, where the w-AlN is dominant (from right to left), respectively.	17
Fig. 9.	Lattice parameters of the fcc phase calculated from the GAXRD measurements and lattice parameters calculated from the interplanar spacings of the lattice planes (111), (200), (220) and (422) measured at different inclinations of the sample ψ from the symmetrical position ($\psi = 0$) in sample $\text{Cr}_{0.69}\text{Al}_{0.28}\text{Si}_{0.03}\text{N}$ (a). Slopes of the $\sin^2\psi$ plots calculated from GAXRD measurements obtained for different angles of incidence γ for sample $\text{Cr}_{0.54}\text{Al}_{0.46}\text{N}$ (b). Plot of the lattice parameters obtained from the interplanar spacing of the lattice planes (111) versus $\sin^2\psi$ measured for three different ϕ angles (c), measured for positive and negative ψ tilts (d) for sample $\text{Cr}_{0.91}\text{Al}_{0.08}\text{Si}_{0.01}\text{N}$	20
Fig. 10.	Plot of the anisotropy factor A (a), slopes of the ε vs. $\sin^2\psi$ dependences measured on crystallite family corresponding to strongest texture component (CGM) (b), and slopes of the ε vs. $\sin^2\psi$ dependences measured on (111) and (200) lattice planes ((c)- for Cr-Al-N, (d)- for Cr-Al-Si-N), versus amount of chromium in Cr-Al-(Si)-N coatings.	22
Fig. 11.	Plot of the anisotropy factors A , lines correspond to the linear fit (a). Slopes of the ε vs. $\sin^2\psi$ dependences measured on crystallite family corresponding to strongest texture component (CGM) (b), and slopes of the ε vs. $\sin^2\psi$ dependences measured on (111) and (200) lattice planes ((c) - for Ti-Al-N, (d) - for Ti-Al-Si-N), versus amount of titanium in Ti-Al-(Si)-N coatings.	23

Fig. 12.	Plot of the anisotropy factor A (a), slopes of the ε vs. $\sin^2\psi$ dependences measured on (111) and (200) lattice planes ((b) - for Zr-Al-N, (c) - for Zr-Al-Si-N), versus amount of zirconium in Zr-Al-(Si)-N coatings.	24
Fig. 13.	Pole figures {111}, {100} and {110} (from the left to the right) of the fcc phase measured in the samples with the overall chemical composition $\text{Cr}_{0.92}\text{Al}_{0.08}\text{N}$, $\text{Cr}_{0.75}\text{Al}_{0.25}\text{N}$ and $\text{Cr}_{0.46}\text{Al}_{0.54}\text{N}$ (from the top to the bottom) recalculated into the stereographic projection.	28
Fig. 14.	Pole figures {111}, {100} and {110} (from the left to the right) of the fcc phase measured in the samples with the overall chemical composition $\text{Cr}_{0.91}\text{Al}_{0.08}\text{Si}_{0.01}\text{N}$, $\text{Cr}_{0.69}\text{Al}_{0.28}\text{Si}_{0.03}\text{N}$ and $\text{Cr}_{0.52}\text{Al}_{0.43}\text{Si}_{0.05}\text{N}$ (from the top to the bottom) re-calculated into the stereographic projection. The dots show the positions of the poles as obtained for an fcc single-crystal in the same orientation as for the respective sample.	29
Fig. 15.	Inclination of the $\langle 111 \rangle$ texture direction from the sample surface perpendicular direction as observed for the cubic phase in Cr-Al-N (\odot) and Cr-Al-Si-N (\square) thin films. The angle of 35° shown by the dotted line is the angle between the directions $\langle 111 \rangle$ and $\langle 110 \rangle$ in cubic system (a). Degree of the in-plane texture in the Cr-Al-N (\odot) and Cr-Al-Si-N (\square) thin films in dependence on the chemical composition of the coatings (b).	30
Fig. 16.	Degree of the out-of-plane texture of the cubic phase in Cr-Al-N (\odot) and Cr-Al-Si-N (\square) coatings shown in dependence on the chemical composition of the coatings (a) and in dependence on the sample position in the deposition apparatus (b).	30
Fig. 17.	Inclination of the $\langle 111 \rangle$ texture direction from the sample surface perpendicular direction as observed for the cubic phase in the Ti-Al-N (open red circles) and Ti-Al-Si-N (open blue squares) coatings.	31
Fig. 18.	Inclination of the $\langle 100 \rangle$ texture direction from the sample surface perpendicular direction as observed for the cubic phase in the Zr-Al-N (open red circles) and Zr-Al-Si-N (open blue squares) thin films as a function of the zirconium contents (a), and as a function of the angle between the sample normal direction and the direction from the substrate to the Zr cathode (b).	32
Fig. 19.	Dependence of the integral line broadening on sine of the Bragg angle as observed for the fcc phase of the Zr-Al-N coatings (a); $\text{Zr}_{0.96}\text{Al}_{0.04}\text{N}$ - black boxes, $\text{Zr}_{0.85}\text{Al}_{0.15}\text{N}$ - red circles, $\text{Zr}_{0.77}\text{Al}_{0.23}\text{N}$ - green triangles and $\text{Zr}_{0.59}\text{Al}_{0.41}\text{N}$ - blue bottom up triangles, and Zr-Al-Si-N samples (b); $\text{Zr}_{0.93}\text{Al}_{0.06}\text{Si}_{0.01}\text{N}$ - black boxes, $\text{Zr}_{0.83}\text{Al}_{0.15}\text{Si}_{0.02}\text{N}$ - red circles, $\text{Zr}_{0.74}\text{Al}_{0.23}\text{Si}_{0.03}\text{N}$ - green triangles and $\text{Zr}_{0.54}\text{Al}_{0.41}\text{Si}_{0.05}\text{N}$ - blue bottom up triangles. Horizontal solid lines show the saturated XRD line broadening that was used for calculation of the crystallite size. Dashed lines show the extrapolation of the XRD line broadening from partially coherent crystallites to $\sin\theta = 0$ that was used for the estimation of the cluster size.	36
Fig. 20.	TEM micrograph of the sample $\text{Cr}_{0.91}\text{Al}_{0.08}\text{Si}_{0.01}\text{N}$ showing the object, which was identified using XRD as nanostructured cluster with the size of (47 ± 8) nm consisting of partially coherent nanocrystallites having the size of (11.0 ± 0.5) nm and the mutual disorientation of $(0.47 \pm 0.05)^\circ$ (a). HRTEM micrograph of the sample $\text{Cr}_{0.40}\text{Al}_{0.52}\text{Si}_{0.08}\text{N}$. The crystallite size calculated from the XRD line broadening was (4.5 ± 0.3) nm, and the neighbouring crystallites were non-coherent for XRD (b).	37
Fig. 21.	The size of the fcc crystallites in the Cr-Al-N (red solid boxes), Cr-Al-Si-N (red open boxes), Ti-Al-N (green solid circles), Ti-Al-Si-N (green open circles) Zr-Al-N (blue solid triangles) and Zr-Al-Si-N (blue open triangles) nanocomposites as a function of the transition metal contents (a). Dependence of the mutual disorientation of partially coherent fcc nanocrystallites on the transition metal contents in the Cr-Al-N (red solid boxes), Cr-Al-Si-N (red open boxes), Ti-Al-N (green solid circles), Ti-Al-Si-N (green open circles), Zr-Al-N (solid triangles) and Zr-Al-Si-N (blue open triangles) nanocomposites (b).	38
Fig. 22.	Hardness of the Cr-Al-N, Ti-Al-N, Zr-Al-N (a) and Cr-Al-Si-N, Ti-Al-Si-N, Zr-Al-Si-N (b) coatings as a function of the transition metal contents.	40
Fig. 23.	Hardness of the Cr-Al-N (solid red squares), Ti-Al-N (solid green circles), Zr-Al-N (solid blue triangles) (a) and Cr-Al-Si-N (open red squares), Ti-Al-Si-N (open green circles), Zr-Al-Si-N (open blue triangles) (b) coatings plotted as a function of the fcc phase crystallite size.	41
Fig. 24.	Schematic model of the cluster of nanocrystallites in single-phase region in M-Al-Si-N coatings (a), cluster in two-phase region in M-Al-N (b) and three-phase region in M-Al-Si-N (c) coatings. Green grains represent the fcc crystallites, light blue grains stand for the wurtzitic AlN crystallites and yellow colour symbolizes the amorphous Si_xN_y	43

Chapter 2

Dopita M., Rafaja D., Wüstefeld Ch., Růžička M., Klemm V., Heger D.,
Schreiber G. and Šíma M.,
*Interplay of microstructural features in $Cr_{1-x}Al_xN$ and $Cr_{1-x-y}Al_xSi_yN$
nanocomposite coatings deposited by cathodic arc evaporation,*
Surface and Coatings Technology, **202**, (2008), 3199-3207

Interplay of microstructural features in $\text{Cr}_{1-x}\text{Al}_x\text{N}$ and $\text{Cr}_{1-x-y}\text{Al}_x\text{Si}_y\text{N}$ nanocomposite coatings deposited by cathodic arc evaporation

M. Dopita ^{a,b}, D. Rafaja ^{a,*}, Ch. Wüstefeld ^a, M. Růžicka ^c, V. Klemm ^a,
D. Heger ^a, G. Schreiber ^a, M. Šíma ^c

^a Institute of Materials Science, TU Bergakademie Freiberg, Gustav-Zeuner-Str. 5, D-09599 Freiberg, Germany

^b Department of Condensed Matter Physics, Faculty of Mathematics and Physics, Charles University, Ke Karlovu 5, CZ-121 16 Prague, Czech Republic

^c SHM Ltd., Průmyslová 3, CZ-787 01 Šumperk, Czech Republic

Received 14 September 2007; accepted in revised form 26 November 2007

Available online 3 December 2007

Abstract

The interplay between the deposition geometry, the chemical and phase composition, the crystallite size, the lattice strain and the direction and the degree of the preferred orientation of crystallites was investigated in the $\text{Cr}_{1-x}\text{Al}_x\text{N}$ and $\text{Cr}_{1-x-y}\text{Al}_x\text{Si}_y\text{N}$ nanocrystalline coatings and nanocomposites, which were deposited in cathodic arc evaporation process at different positions of substrates in the deposition apparatus. The different positions of the substrates affected primarily the distance between the samples and the cathodes and consequently the chemical and phase composition of the coatings, the crystallite size, the lattice strain and the preferred orientation of crystallites. In the $\text{Cr}_{1-x}\text{Al}_x\text{N}$ coatings, the dominating cubic crystallites were preferentially oriented with their $\langle 111 \rangle$ direction perpendicular to the sample surface; this out-of-plane preferred orientation of crystallites was accompanied by a strong in-plane texture. In the $\text{Cr}_{1-x-y}\text{Al}_x\text{Si}_y\text{N}$ coatings, a strong inclination of the $\{111\}$ texture from the normal direction and a decay of the in-plane preferred orientation were observed in cubic crystallites with increasing silicon (and aluminium) contents.

© 2007 Elsevier B.V. All rights reserved.

Keywords: Chromium aluminium silicon nitrides; Cathodic arc evaporation; Texture; XRD

1. Introduction

Preferred orientation of crystallites belongs to the microstructural parameters, which are frequently investigated in the protective coatings, as it contains important information about the deposition process. In 1986, Perry and Schoenes [1] have shown in their review that the deposition parameters, such as the composition of the working gas, the gas pressure, the deposition rate, the bias voltage, can affect preferred orientation of crystallites in thin films of transition metal nitrides significantly. On the other hand, a strong texture can influence considerably the properties of the coatings, particularly in highly anisotropic materials. In the Cr–Al–Si–N coatings, the explanation of the relationship between the preferred orientation of crystallites and the deposition parameters was the main task of many studies.

For CrN coatings, Bull and Rickerby [2] investigated the effect of the nitrogen partial pressure on the texture direction; they observed a change of the texture from $\{100\}$ to $\{111\}$ with increasing partial pressure of nitrogen. Attar and Johannesson [3] found the $\{110\}$ texture in PVD CrN coatings deposited on steel substrates at the deposition pressure of 0.2 Pa, at the substrate temperature of 200 °C and at the bias voltage of –150 V. The effect of the bias voltage on the texture development in cathodic arc evaporated CrN coatings was described by Odén et al. [4]. For –200 V, they observed a $\{110\}$ fibre texture. A decrease of the bias voltage from –200 V to –50 V caused a weakening of the $\{110\}$ texture and a development of other texture components. In CrN coatings deposited on silicon substrates using the ion beam assisted deposition, Ma et al. [5] observed a strong correlation between the texture direction and the deposition parameters like the ion beam energy, the flux of the incoming metal particles and the nitrogen ions, the sputtering geometry and the deposition temperature. By

* Corresponding author. Tel.: +49 3731 39 2299; fax: +49 3731 39 3657.

E-mail address: Rafaja@ww.tu-freiberg.de (D. Rafaja).

changing the above deposition parameters, the out-of-plane texture, which direction was related to the sample surface normal direction in this case, changed from $\{111\}$ to $\{100\}$. Furthermore, several types of the in-plane texture were reported in [5].

In the $\text{Cr}_{1-x}\text{Al}_x\text{N}$ layers deposited by reactive magnetron sputtering from Cr and Al targets in the Ar/N_2 atmosphere, Banakh et al. [6] and Pulugurtha and Bhat [7] observed the $\{111\}$ texture. In the (Cr, Al) N layers deposited both on steel and cemented carbide substrates using the arc ion plating, Lugscheider et al. [8] observed predominantly also the $\{111\}$ texture in arc PVD coatings. Lin et al. [9] described the change of the texture direction with variable aluminium contents in the $\text{Cr}_{1-x}\text{Al}_x\text{N}$ coatings prepared using pulsed closed field unbalanced magnetron sputtering. They observed $\{100\}$ texture for samples with Al concentration below 58.5at.% and both $\{111\}$ and $\{100\}$ texture components for higher aluminium contents.

In the $\text{Cr}_{1-x-y}\text{Al}_x\text{Si}_y\text{N}$ nanocomposite coatings deposited using the cathodic arc evaporation from two cathodes, a three-dimensional preferred orientation of crystallites was observed, which was described by coexisting out-of-plane and in-plane texture [10]. In the chromium-richest coatings, the crystallites were oriented with their $\langle 111 \rangle$ direction perpendicularly to the sample surface. With increasing chromium contents, the $\langle 111 \rangle$ direction inclined towards the plane of the coatings. Besides the macroscopic preferred orientation of nanocrystallites, their local texture was observed in the $\text{Cr}_{1-x-y}\text{Al}_x\text{Si}_y\text{N}$ nanocomposites. The theoretical approach for determination of the local preferred orientation of nanocrystallites from the X-ray diffraction pattern is based on the theory of partial coherence of neighbouring nanocrystallites [11]. Some applications of this approach were illustrated in Refs. [10] and [12–14].

In this contribution, we correlate the texture development in the $\text{Cr}_{1-x}\text{Al}_x\text{N}$ and $\text{Cr}_{1-x-y}\text{Al}_x\text{Si}_y\text{N}$ coatings deposited using the cathodic arc evaporation from two cathodes with the microstructure features and with the geometry of the deposition process. The texture development is described in terms of the inclination of the texture direction $\langle 111 \rangle$ from the sample surface perpendicular direction and in terms of the degree of the out-of-plane and the in-plane preferred orientation of crystallites in the coatings. As microstructure features important for the texture development, the chemical and phase composition, the crystallite size, the degree of the partial coherence of neighbouring crystallites and the lattice strain are considered. The influence of the geometry of the arc deposition process on the microstructure development was through the different distances between the samples and the cathodes that affected the flux of the deposited particles.

2. Experimental

Two series of coatings, $\text{Cr}_{1-x}\text{Al}_x\text{N}$ and $\text{Cr}_{1-x-y}\text{Al}_x\text{Si}_y\text{N}$, were deposited using cathodic arc evaporation (CAE) in nitrogen atmosphere with the working pressure of 1.3Pa using two laterally rotating arc cathodes (π -80 from PLATIT) [15]. One

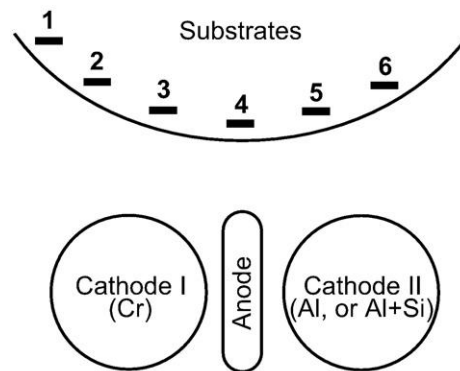


Fig. 1. Schematic drawing of the positions of the samples (shown by horizontal bars) in the deposition apparatus.

cathode was made of chromium; the second cathode consisted either of pure aluminium or of aluminium with 11at.% Si in case of the $\text{Cr}_{1-x}\text{Al}_x\text{N}$ and $\text{Cr}_{1-x-y}\text{Al}_x\text{Si}_y\text{N}$ coatings, respectively. Polished plates of cemented carbide having random orientation of crystallites were used as substrates. The positions of the samples in the deposition apparatus are shown schematically in Fig. 1. In contrast to the commercially produced coatings, our samples were not rotated during the deposition process. Thus, the preferred orientation of crystallites was not superimposed by the sample rotation. The following parameters of the deposition process were kept constant in order to avoid their additional influence on the development of the preferred orientation of crystallites: the arc current on the Cr cathode at 80A, the arc current on the Al and/or Al–Si cathode at 120A, the bias voltage at -75V , the base pressure at $5 \times 10^{-3}\text{Pa}$ and the deposition temperature at approximately 450°C .

The overall chemical composition of the coatings was determined using the electron probe microanalysis with wavelength-dispersive spectroscopy (EPMA/WDS) in 40 points randomly distributed across each sample. The nitrogen concentration was 50at.% within the experimental accuracy in all samples under study. The maximum oxygen concentration in the coatings was estimated from the detection limit of the ESMA/WDS to be lower than 0.1at.% as no oxygen signal was registered. Texture measurements were done on a PTS 3000 X-ray diffractometer from Seifert equipped with an Eulerian cradle and with a mono-capillary in the primary beam. For the fcc phase, the pole figures $\{111\}$, $\{100\}$ and $\{110\}$ were measured for each sample on the diffraction lines 111, 200 and 220. After the background intensity correction, the measured pole figures were re-calculated to the stereographic projections using the equations (see e.g. [16]):

$$x = \frac{\sin \psi}{1 + \cos \psi} \cdot \cos \varphi \quad \text{and} \quad y = \frac{\sin \psi}{1 + \cos \psi} \cdot \sin \varphi \quad (1)$$

In Eq. (1), ψ is the inclination of the sample from the symmetrical position and φ the sample rotation around the

Table 1

Basic characteristics of the $\text{Cr}_{1-x}\text{Al}_x\text{N}$ coatings deposited using cathodic arc evaporation as taken from Ref. [14]

Sample no.	Distance from cathodes (mm)	Layer thickness (μm)	Chemical composition	Phase composition	Crystallite size (nm)	Partial coherence
1	266	3.3 ± 0.2	$\text{Cr}_{0.92}\text{Al}_{0.08}\text{N}$	fcc	11.0 ± 0.4	Yes
2	195	5.0 ± 0.2	$\text{Cr}_{0.83}\text{Al}_{0.17}\text{N}$	fcc	10.3 ± 0.6	Yes
3	139	5.6 ± 0.2	$\text{Cr}_{0.75}\text{Al}_{0.25}\text{N}$	fcc	9.8 ± 0.3	Yes
4	123	7.2 ± 0.2	$\text{Cr}_{0.54}\text{Al}_{0.46}\text{N}$	fcc	8.9 ± 0.2	Yes
5	153	6.3 ± 0.2	$\text{Cr}_{0.46}\text{Al}_{0.54}\text{N}$	fcc + w-AlN	6.5 ± 0.3	Yes
6	215	5.4 ± 0.2	$\text{Cr}_{0.30}\text{Al}_{0.70}\text{N}$	fcc + w-AlN	6.5 ± 0.6	Yes

sample surface perpendicular direction. For the quantification of the degree of the out-of-plane preferred orientation of crystallites, central poles in the pole figures were fitted by two-dimensional Gaussian functions. For the quantification of the degree of the out-of-plane preferred orientation of crystallites, selected azimuthal scans in the pole figures were fitted by one-dimensional Gaussian functions.

Lattice strain was measured on an X'Pert MRD diffractometer from PANalytical, which was equipped with an Eulerian cradle, with a poly-capillary optics in the primary beam, and with a Soller collimator having the acceptance angle of 0.27° and with a flat graphite monochromator in the diffracted beam. All XRD experiments were performed using the $\text{CuK}\alpha$ radiation ($\lambda = 0.15418\text{nm}$).

3. Results and discussion

3.1. Basic characteristics of the $\text{Cr}_{1-x}\text{Al}_x\text{N}$ and $\text{Cr}_{1-x-y}\text{Al}_x\text{Si}_y\text{N}$ coatings

Basic characteristics of the $\text{Cr}_{1-x}\text{Al}_x\text{N}$ and $\text{Cr}_{1-x-y}\text{Al}_x\text{Si}_y\text{N}$ coatings under study are summarised in Tables 1 and 2, respectively. The sample numbers given in Tables 1 and 2 correspond to the sample numbers shown in Fig. 1. The mean distance between the cathodes and the samples given in the tables has the meaning of the arithmetic mean of the distances between the respective sample and the centre of the respective cathode. With respect to the deposition geometry used for the deposition, it is not straightforward to define the “uncertainty” of the mean distance from the cathodes. Therefore, the mean distances are given without “error bars”. The phase composition, the crystallite size and the partial coherence of crystallites were taken from reference [14]. In both systems, the thickness of the coatings increased nearly linearly with decreasing distance from the cathodes (Fig. 2). In the first approximation, the thickness of the coatings can be understood as a measure

of the flux of the deposited particles if the re-sputtering of the coatings is neglected. In the $\text{Cr}_{1-x}\text{Al}_x\text{N}$ coatings, either a single fcc phase of (Cr, Al) N or a mixture of fcc-(Cr, Al) N and wurtzitic AlN was observed depending on the overall chemical composition. In the sample $\text{Cr}_{0.40}\text{Al}_{0.52}\text{Si}_{0.08}\text{N}$, two crystalline phases, fcc-(Cr, Al) N and w-AlN, and an amorphous phase were found. The amorphous phase was a silicon nitride [17–19].

3.2. Preferred orientation of crystallites

Examples of the pole figures measured on the fcc phase in the $\text{Cr}_{1-x}\text{Al}_x\text{N}$ and $\text{Cr}_{1-x-y}\text{Al}_x\text{Si}_y\text{N}$ coatings are shown in Figs. 3 and 4, respectively. The cubic crystallites in all $\text{Cr}_{1-x}\text{Al}_x\text{N}$ coatings under study were preferentially oriented with their direction $\langle 111 \rangle$ nearly perpendicular to the sample surface and showed additionally a pronounced in-plane texture (Fig. 3). Only a slight inclination of the $\{111\}$ out-of-plane texture from the samples surface perpendicular direction was observed at the highest aluminium contents (Fig. 5). The maximum inclination of the texture direction was approximately 5° .

In the $\text{Cr}_{1-x-y}\text{Al}_x\text{Si}_y\text{N}$ coatings, the combination of the out-of-plane and in-plane texture was also observed similarly to the $\text{Cr}_{1-x}\text{Al}_x\text{N}$ samples. However, the preferred orientation direction $\langle 111 \rangle$ inclined much more rapidly from the sample surface perpendicular direction with increasing silicon (and aluminium) contents in the $\text{Cr}_{1-x-y}\text{Al}_x\text{Si}_y\text{N}$ coatings than with increasing aluminium contents in the $\text{Cr}_{1-x}\text{Al}_x\text{N}$ coatings (see Figs. 4 and 5). In the coatings with the overall chemical composition of $\text{Cr}_{0.40}\text{Al}_{0.52}\text{Si}_{0.08}\text{N}$, the fcc crystallites were nearly preferentially oriented with their direction $\langle 110 \rangle$ perpendicularly to the sample surface. This orientation of cubic crystallites corresponds to the angle between the $\langle 111 \rangle$ direction and the sample surface perpendicular direction of 35° (see Fig. 5).

Table 2

Basic characteristics of the $\text{Cr}_{1-x-y}\text{Al}_x\text{Si}_y\text{N}$ coatings deposited using cathodic arc evaporation as taken from Ref. [14]

Sample no.	Distance from cathodes (mm)	Layer thickness (μm)	Chemical composition	Phase composition	Crystallite size (nm)	Partial coherence
1	266	4.5 ± 0.2	$\text{Cr}_{0.91}\text{Al}_{0.08}\text{Si}_{0.01}\text{N}$	fcc	10.5 ± 1.0	Yes
2	195	6.3 ± 0.2	$\text{Cr}_{0.84}\text{Al}_{0.15}\text{Si}_{0.01}\text{N}$	fcc	8.2 ± 0.5	Yes
3	139	7.9 ± 0.3	$\text{Cr}_{0.69}\text{Al}_{0.28}\text{Si}_{0.03}\text{N}$	fcc	6.8 ± 0.5	Yes
4	123	8.7 ± 0.3	$\text{Cr}_{0.52}\text{Al}_{0.43}\text{Si}_{0.05}\text{N}$	fcc	5.0 ± 0.5	Yes
5	153	8.6 ± 0.3	$\text{Cr}_{0.40}\text{Al}_{0.52}\text{Si}_{0.08}\text{N}$	fcc + w-AlN	4.5 ± 0.5	No

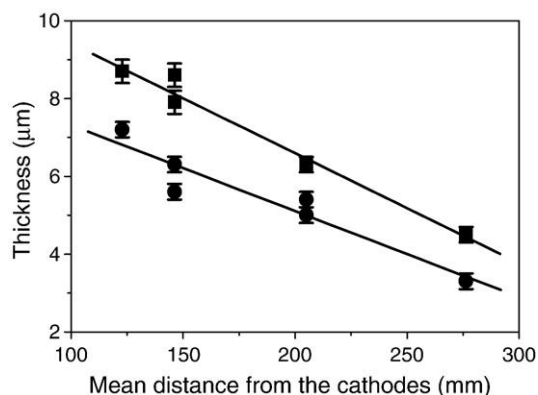


Fig. 2. Dependence of the thickness of the $\text{Cr}_{1-x}\text{Al}_x\text{N}$ (●) and $\text{Cr}_{1-x-y}\text{Al}_x\text{Si}_y\text{N}$ (■) coatings on the mean distance between the samples and the cathodes.

The comparison of the experimental results obtained for the $\text{Cr}_{1-x}\text{Al}_x\text{N}$ and $\text{Cr}_{1-x-y}\text{Al}_x\text{Si}_y\text{N}$ coatings has shown that the inclination of the texture direction is controlled predominantly by the concentration of silicon in the $\text{Cr}_{1-x-y}\text{Al}_x\text{Si}_y\text{N}$ coatings. Only a negligible inclination of the texture direction was observed in the $\text{Cr}_{1-x}\text{Al}_x\text{N}$ coatings even if they were deposited at different deposition fluxes and if they contained different amounts of aluminium. Indirectly, the results obtained on the $\text{Cr}_{1-x}\text{Al}_x\text{N}$ coatings have shown that the angle between the samples and the cathodes has no significant effect on the inclination of the texture direction (compare Figs. 1 and 5).

An enhanced inclination of the texture direction due to the increasing silicon contents was also observed in the Ti–Al–Si–N coatings as compared with the Ti–Al–N coatings [20]. The effect of the angle between the samples and the cathodes was studied comprehensively in [20] on the TiN coatings deposited both from a single Ti cathode and from two Ti cathodes using the same deposition geometry like here. In these TiN coatings, no changes of the texture direction with varying deposition flux and/or with varying angle between the samples and the cathodes were observed. Thus, our results that are obtained on “stationary”, i.e. non-rotated samples, can, to a certain extent, be extended to the standard deposition processes, in which the samples are rotated during deposition.

The degree of the out-of-plane preferred orientation changed both with the chemical composition of the samples (Fig. 6a) and with their mean distance from the cathodes (Fig. 6b). In Fig. 6, the degree of the out-of-plane preferred orientation is represented by the full width at the half maximum (FWHM) of a central pole that was fitted by a two-dimensional Gaussian function. For determination of the degree of the out-of-plane preferred orientation in the $\text{Cr}_{1-x}\text{Al}_x\text{N}$ samples, the central pole (111) was selected in all cases. For the samples of the $\text{Cr}_{1-x-y}\text{Al}_x\text{Si}_y\text{N}$ series, the central pole (111) was only used for the chromium-richest samples $\text{Cr}_{0.91}\text{Al}_{0.08}\text{Si}_{0.01}\text{N}$ and $\text{Cr}_{0.84}\text{Al}_{0.15}\text{Si}_{0.01}\text{N}$. In the samples $\text{Cr}_{0.69}\text{Al}_{0.28}\text{Si}_{0.03}\text{N}$ and $\text{Cr}_{0.52}\text{Al}_{0.43}\text{Si}_{0.05}\text{N}$, the solitary and nearly central pole (100) was used for determination of the texture degree.

The differences in the degree of the out-of-plane texture observed for the $\text{Cr}_{1-x}\text{Al}_x\text{N}$ and $\text{Cr}_{1-x-y}\text{Al}_x\text{Si}_y\text{N}$ systems

(Fig. 6a) yield valuable information about the effect of the chemical composition on the preferred orientation of crystallites, especially if they are complemented by the dependence of the degree of the out-of-plane texture on the distance of the samples from the cathodes (Fig. 6b). In the $\text{Cr}_{1-x}\text{Al}_x\text{N}$ system, the degree of the out-of-plane texture is controlled rather by the mean distance of the samples from the cathodes than by the aluminium contents. The larger is the distance of the samples from the cathodes, the weaker the out-of-plane texture as it can be seen from Fig. 6b. According to Fig. 2, the flux of incoming particles decreased with increasing distance between the cathodes and the samples. Thus, in the $\text{Cr}_{1-x}\text{Al}_x\text{N}$ system the out-of-plane texture gets weaker with decreasing flux of incoming particles. The effect of the aluminium contents on the degree of the out-of-plane texture can be deduced from the differences in the FWHM of the out-of-plane texture in samples with different chemical compositions and with the same distance from the cathodes (Fig. 6a and b). A weaker out-of-plane texture in Fig. 6b was found in the samples with higher aluminium contents. In the $\text{Cr}_{1-x-y}\text{Al}_x\text{Si}_y\text{N}$ system, the out-of-plane texture gets weaker mainly with increasing silicon contents. In comparison with the effect of silicon, the distance between the cathodes and the samples and thus the flux of incoming particles play a minor role in this system. Also the influence of the aluminium contents on the degree of the out-of-plane preferred orientation of crystallites is very weak.

The in-plane texture of the fcc crystallites shows a similar behaviour like their out-of-plane texture (compare Figs. 6a and 7). At low Al concentrations in the $\text{Cr}_{1-x}\text{Al}_x\text{N}$ coatings, the in-plane texture becomes more pronounced with decreasing distance from the cathodes, i.e. with increasing flux of incoming particles. At higher Al concentrations starting with $\text{Cr}_{0.54}\text{Al}_{0.46}\text{N}$, the decay of the in-plane texture is obviously caused both by the increasing distances from the cathodes and by the increasing aluminium contents. The in-plane texture in the $\text{Cr}_{1-x-y}\text{Al}_x\text{Si}_y\text{N}$ coatings gets monotonously weaker with increasing silicon (and aluminium) contents. The similar trends observed for both texture types, i.e. for the out-of-plane and in-plane textures indicate that the physical processes behind the preferred orientation of crystallites are very similar in all macroscopic directions.

3.3. Effect of the lattice strain

Several authors, e.g. Pelleg et al. [21], Oh and Je [22] and later Ma et al. [5] and Falub et al. [23], supposed that the preferred orientation of the fcc crystallites in the PVD thin films of the transition metal nitrides is controlled by the competition between the surface energy and the strain energy [24]. In the transition metal nitrides with the fcc structure, the {001} lattice planes possess the lowest surface energy, thus the {100} texture is expected in very thin films with none or very low lattice strain. Because of the strong crystallographic anisotropy of the elastic constants in the $\text{Cr}_{1-x-y}\text{Al}_x\text{Si}_y\text{N}$ coatings, which results in the anisotropy of the Young modulus with $E_{001} > E_{111}$ [10], the {111} texture should dominate for increasing compressive residual stress. Often, the compressive residual stress increases

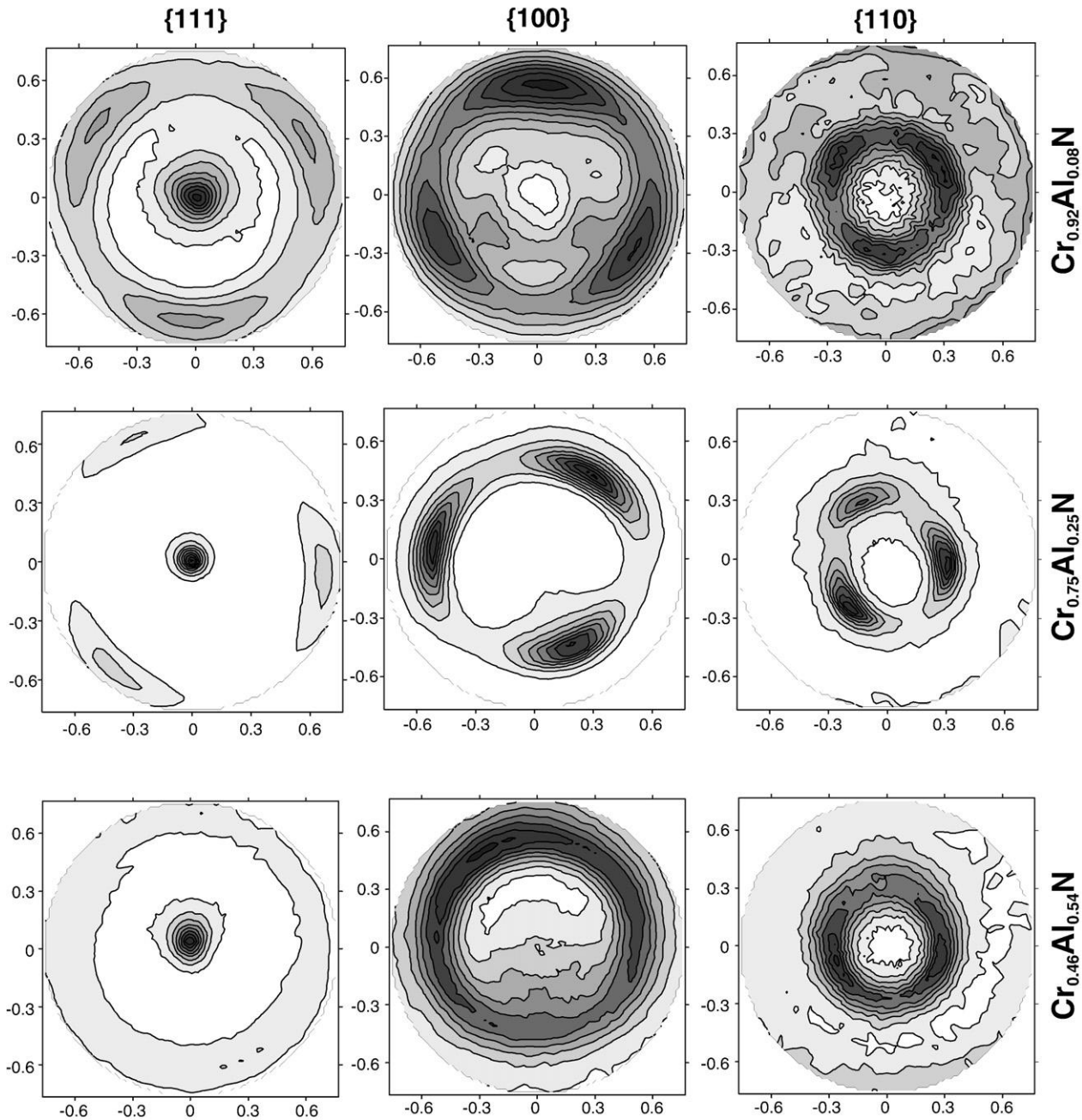


Fig. 3. Pole figures $\{111\}$, $\{100\}$ and $\{110\}$ measured on the fcc phase in the samples with the overall chemical composition $\text{Cr}_{0.92}\text{Al}_{0.08}\text{N}$, $\text{Cr}_{0.75}\text{Al}_{0.25}\text{N}$ and $\text{Cr}_{0.46}\text{Al}_{0.54}\text{N}$ and re-calculated into the stereographic projection using Eq. (1).

with increasing thickness of the coatings, thus the preferred orientation changes during the layer growth as it was observed, e.g., in [21,22,25].

The lattice strain in the fcc phase of the $\text{Cr}_{1-x}\text{Al}_x\text{N}$ and $\text{Cr}_{1-x-y}\text{Al}_x\text{Si}_y\text{N}$ coatings that is shown in Fig. 8 was obtained from the linear dependence of the lattice parameters a_ψ^{111} measured on the $\{111\}$ lattice planes on $\sin^2\psi$ (see, e.g. [10,26]):

$$a_\psi^{111} = (a_{\parallel}^{111} - a_{\perp}^{111}) \sin^2\psi + a_{\perp}^{111} \quad (2)$$

In Eq. (2), ψ is the inclination of the sample from the symmetrical position; a_{\parallel}^{111} and a_{\perp}^{111} have the meaning of the in-plane and out-of-plane lattice parameters measured on the lattice planes $\{111\}$ that correspond to $\psi=90^\circ$ and $\psi=0^\circ$, respectively. The lattice strain ε^{111} in Fig. 8 was calculated from these lattice parameters and from the stress-free lattice parameter a_0 using:

$$\varepsilon^{111} = \frac{a_{\parallel}^{111} - a_{\perp}^{111}}{2a_0}, \quad (3)$$

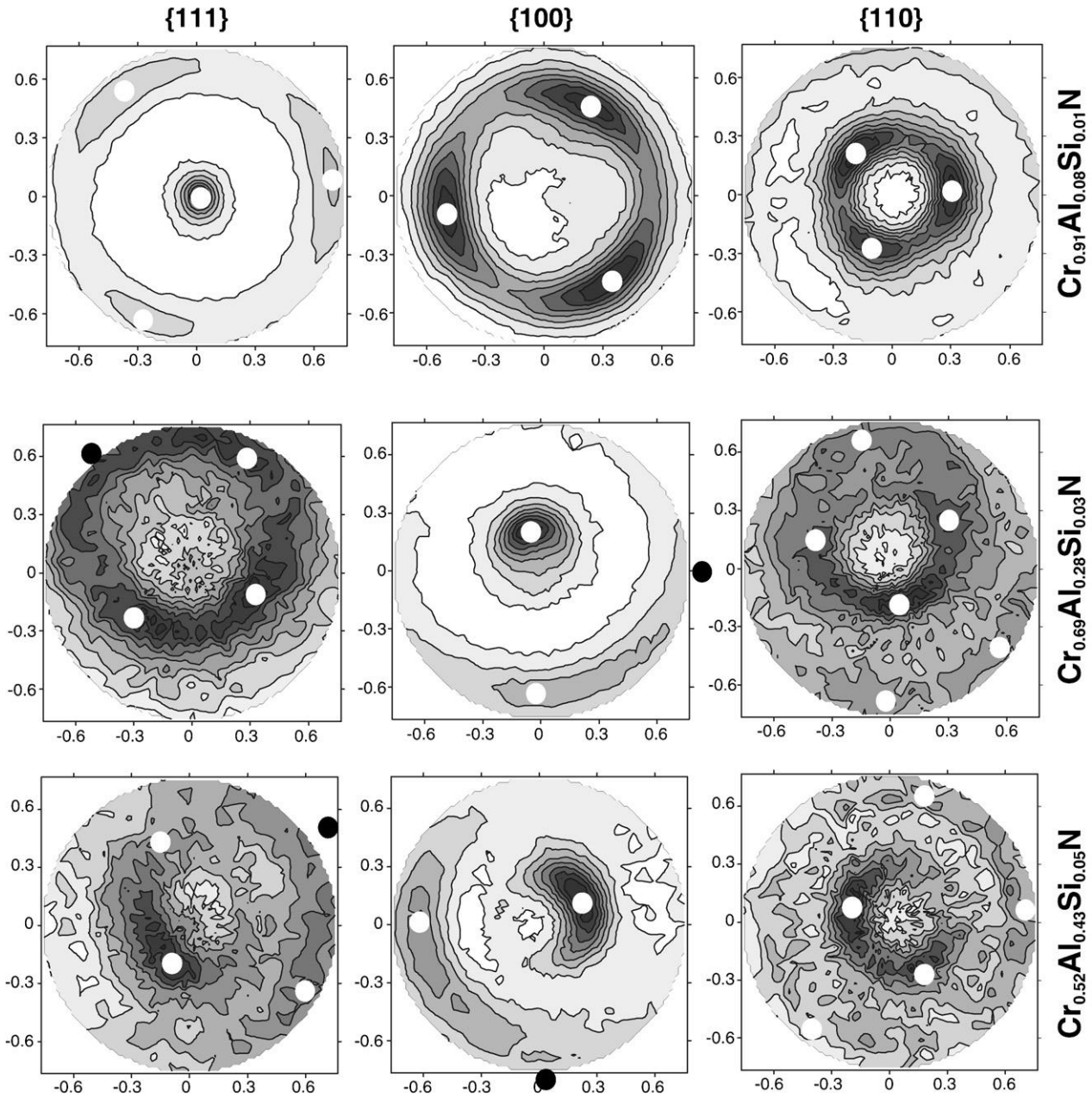


Fig. 4. Pole figures $\{111\}$, $\{100\}$ and $\{110\}$ measured on the fcc phase in the samples with the overall chemical composition $\text{Cr}_{0.91}\text{Al}_{0.08}\text{Si}_{0.01}\text{N}$, $\text{Cr}_{0.69}\text{Al}_{0.28}\text{Si}_{0.03}\text{N}$ and $\text{Cr}_{0.52}\text{Al}_{0.43}\text{Si}_{0.05}\text{N}$ and re-calculated into the stereographic projection using Eq. (1). The dots show the positions of the poles as obtained for an fcc single-crystal in the same orientation as for the respective sample.

The stress-free lattice parameter a_0 was calculated using Eq. (2) for [26]:

$$\sin^2 \psi = \frac{2\nu^{111}}{\nu^{111} + 1}, \quad (4)$$

i.e. from

$$a_0 = \left(a_{\parallel}^{111} - a_{\perp}^{111} \right) \cdot \frac{2\nu^{111}}{\nu^{111} + 1} + a_{\perp}^{111} \quad (5)$$

In Eqs. (4) and (5), ν is the Poisson ratio. Regarding the definition of the lattice strains:

$$\varepsilon_{\parallel} = \frac{a_{\parallel} - a_0}{a_0} \quad \text{and} \quad \varepsilon_{\perp} = \frac{a_0 - a_{\perp}}{a_0}, \quad (6)$$

Eq. (3) is equivalent to:

$$\varepsilon^{111} = \frac{1}{2} \left(\varepsilon_{\parallel}^{111} + \varepsilon_{\perp}^{111} \right) \quad (7)$$

Eq. (7) shows that ε^{111} in Eq. (3) and in Fig. 8 has the meaning of the average lattice strain as calculated from the elastic lattice

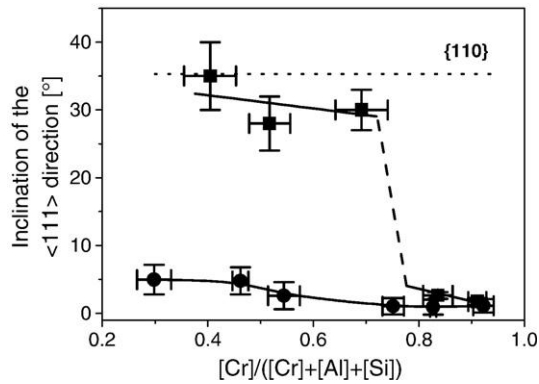


Fig. 5. Inclination of the $\langle 111 \rangle$ texture direction from the sample surface perpendicular direction as observed in the $\text{Cr}_{1-x}\text{Al}_x\text{N}$ (●) and $\text{Cr}_{1-x-y}\text{Al}_x\text{Si}_y\text{N}$ (■) thin films. The angle of 35° shown by the dotted line is the angle between the directions $\langle 111 \rangle$ and $\langle 110 \rangle$ in cubic systems.

distortions in the plane of the coating and in the sample surface perpendicular direction. Positive values of the average lattice strain indicate tensile residual stress; negative average lattice strain indicates compressive residual stress in the coatings.

In the $\text{Cr}_{1-x}\text{Al}_x\text{N}$ coatings except the sample with the lowest Al concentration, the lattice strain increased linearly with increasing aluminium contents (filled circles in Fig. 8a). Up to the overall chemical composition $\text{Cr}_{0.54}\text{Al}_{0.46}\text{N}$, the increase of the lattice strain correlated with the increase of the layer thickness (open circles in Fig. 8a). In the $\text{Cr}_{1-x-y}\text{Al}_x\text{Si}_y\text{N}$ coatings, the lattice strain increased slightly with the increasing

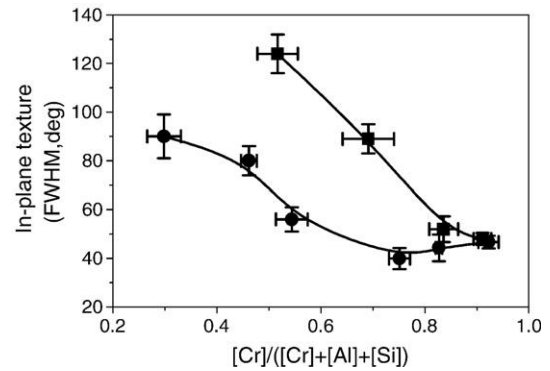


Fig. 7. Degree of the in-plane texture in the $\text{Cr}_{1-x}\text{Al}_x\text{N}$ (●) and $\text{Cr}_{1-x-y}\text{Al}_x\text{Si}_y\text{N}$ (■) thin films in dependence on the chemical composition of the coatings.

aluminium and silicon contents up to $\text{Cr}_{0.69}\text{Al}_{0.28}\text{Si}_{0.03}\text{N}$ (filled boxes in Fig. 8b). This increase of the lattice strain correlated again with the increase of the layer thickness (open boxes in Fig. 8b). Between $\text{Cr}_{0.52}\text{Al}_{0.43}\text{Si}_{0.05}\text{N}$ and $\text{Cr}_{0.69}\text{Al}_{0.28}\text{Si}_{0.03}\text{N}$, a steep increase of the lattice strain was observed that was followed by a slight decrease of the lattice strain in the samples with $[\text{Cr}]/([\text{Cr}] + [\text{Al}] + [\text{Si}]) \leq 0.52$, in which the layer thickness also decreased with increasing aluminium and silicon contents.

3.4. Interplay of microstructure features

In addition to the lattice strain that can affect the texture development as discussed in the previous section, we observed correlations between other microstructure features that could help in explaining the inclination of the texture direction and the degree of the out-of-plane and the in-plane texture in the CAE $\text{Cr}_{1-x}\text{Al}_x\text{N}$ and $\text{Cr}_{1-x-y}\text{Al}_x\text{Si}_y\text{N}$ coatings under study. The additional microstructural features that were considered to be responsible for the texture development are the phase composition of the coatings and the size and partial coherence of crystallites in the coatings that are summarised in Tables 1 and 2.

In the $\text{Cr}_{1-x}\text{Al}_x\text{N}$ coatings, the high degree (Fig. 6) and the very small inclination of the $\{111\}$ out-of-plane texture from the normal direction (Fig. 5) were supported by the high lattice strain (Fig. 8a), by the presence of the single fcc phase until $\text{Cr}_{0.54}\text{Al}_{0.46}\text{N}$ (Table 1) and by a high degree of the local preferred orientation of neighbouring nanocrystallites that led to their partial coherence (Table 1). The strong local preferred orientation of neighbouring nanocrystallites supported also the development of the in-plane texture (Fig. 7). The highest inclination of the out-of-plane texture direction, a slight decay of the out-of-plane texture and an evident decay of the in-plane texture were observed in two $\text{Cr}_{1-x}\text{Al}_x\text{N}$ coatings with the highest aluminium concentrations, in which w-AlN developed as a second crystalline phase. Apparently, w-AlN influences the transfer of the preferred orientation between neighbouring fcc crystallites. Furthermore, the development of w-AlN in the $\text{Cr}_{1-x}\text{Al}_x\text{N}$ coatings caused a rapid decrease of the crystallite size (Table 1) and a further increase of the lattice strain. In the single-phase $\text{Cr}_{1-x}\text{Al}_x\text{N}$ coatings, the lattice strain increased monotonously with increasing layer thickness (Fig. 8a). In the

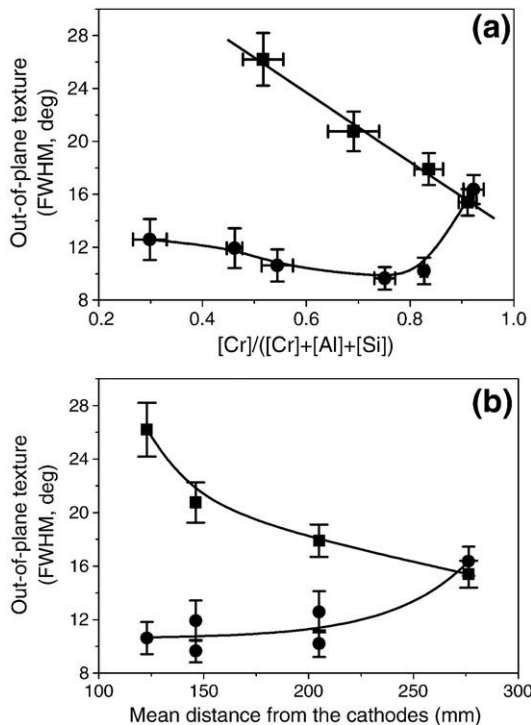


Fig. 6. Degree of the out-of-plane texture in the $\text{Cr}_{1-x}\text{Al}_x\text{N}$ (●) and $\text{Cr}_{1-x-y}\text{Al}_x\text{Si}_y\text{N}$ (■) thin films shown in dependence on the chemical composition of the coatings (a) and in dependence on the mean distance of the samples from the cathodes (b).

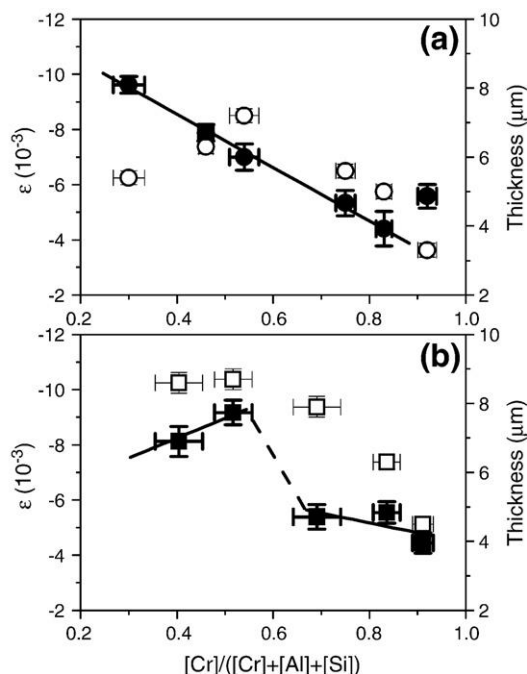


Fig. 8. Macroscopic lattice strain as measured for the fcc phase (filled symbols) and layer thickness (open symbols) of the $Cr_{1-x}Al_xN$ (a) and $Cr_{1-x-y}Al_xSi_yN$ (b) thin films. The lattice strain was measured on the lattice planes {111}.

$Cr_{1-x}Al_xN$ coatings containing two phases, the lattice strain increased although their thickness decreased with increasing aluminium contents (Fig. 8a). One reason for the further increase of the lattice strain in the $Cr_{1-x}Al_xN$ coatings containing two phases can be the development of intrinsic residual stresses at the semi-coherent interfaces between fcc-(Cr, Al) N and w-AlN crystallites. This phenomenon was already described in Ti–Al–N coatings containing fcc-(Ti, Al) N and w-AlN [12,13]. Another reason for the increase of the lattice strain could be a larger molar volume of AlN against CrN (~18% according to [27]). However, the differences in the molar volumes are directly related to the differences in the lattice parameters and interplanar spacings that are responsible for development of the intrinsic residual stresses at the semi-coherent interfaces.

As discussed in Section 3.2, the addition of silicon caused the strongest inclination of the {111} texture from the sample surface perpendicular direction (Fig. 5) and the decay of the out-of-plane (Fig. 6) and the in-plane texture (Fig. 7). The reason for this is the development of amorphous silicon nitride in the $Cr_{1-x-y}Al_xSi_yN$ coatings [14,17–19] in addition to the fcc and w-AlN phases. Primarily, the formation of the amorphous silicon nitride caused a steep increase of the local disorientation of neighbouring fcc crystallites that was observed as a decay of their partial coherence. At the silicon contents $[Si]/([Cr]+[Al]+[Si]) \geq 0.08$, the neighbouring crystallites were non-coherent, as the transfer of the preferred orientation between the neighbouring crystallites was interrupted by the amorphous silicon nitride. Furthermore, the formation of the amorphous silicon nitride caused the fast decay of the global in-plane and out-of-plane textures in the $Cr_{1-x-y}Al_xSi_yN$ coatings.

At the silicon contents $[Si]/([Cr]+[Al]+[Si])$ between 0.03 and 0.05, a steep increase of the lattice strain in the $Cr_{1-x-y}Al_xSi_yN$ coatings was observed. This increase of the lattice strain is responsible for the increase of the hardness of the $Cr_{1-x-y}Al_xSi_yN$ coatings, which typically reaches its maximum between $[Si]/([Cr]+[Al]+[Si]) = 0.06$ and 0.08 [14,19]. The steep increase of the lattice strain preceded both the observable segregation of Al and Si from the fcc phase of $Cr_{1-x-y}Al_xSi_yN$ and the loss of the strong local preferred orientation of crystallites. On the other hand, the steep increase of the lattice strain was observed later than the onset of the strong inclination of the out-of-plane texture, which was already observed between $Cr_{0.84}Al_{0.15}Si_{0.01}N$ and $Cr_{0.69}Al_{0.28}Si_{0.03}N$. From this point of view, the inclination of the out-of-plane texture direction is the most sensitive parameter that indicates the effect of silicon on the microstructure of the $Cr_{1-x-y}Al_xSi_yN$ coatings, e.g. the development of the amorphous silicon nitride that was discussed in [17–19]. The fcc-(Cr, Al, Si) N nanocrystallites growing on the amorphous phase build in fact very thin slabs, which thickness is comparable with the crystallite size. Thus, the texture of very small fcc crystallites will consequently be controlled rather by the surface energy of the crystallites than by their (bulk) strain energy. As the strain energy depends on the thickness of the crystalline slabs, the size of crystallites in the $Cr_{1-x-y}Al_xSi_yN$ nanocomposite coatings that are separated by the amorphous phase can be one of the microstructure parameters, which control the inclination of the texture direction. Another consequence of the development of amorphous silicon nitride at the crystallites boundaries is the decay of the out-of-plane and in-plane texture, which started already at low silicon concentrations in the $Cr_{1-x-y}Al_xSi_yN$ coatings.

4. Conclusions

In chromium-rich $Cr_{1-x}Al_xN$ and $Cr_{1-x-y}Al_xSi_yN$ nanocrystalline coatings deposited using cathodic arc evaporation, the {111} out-of-plane texture was observed that was perpendicular to the sample surface. The out-of-plane texture was accompanied by a pronounced in-plane texture. The combination of the out-of-plane and in-plane texture was a consequence of the transfer of the preferred orientation between crystallites during the deposition process. In the $Cr_{1-x}Al_xN$ coatings, a slight inclination of the out-of-plane texture was found only at the highest aluminium contents. The related samples contained two crystalline phases, fcc-(Cr, Al) N and w-AlN. The degree of the out-of-plane texture in the silicon-free samples was controlled mainly by the mean distance between the samples and the cathodes. The effect of the aluminium contents and phase composition on the degree of the out-of-plane texture was weaker. The degree of the in-plane texture in the $Cr_{1-x}Al_xN$ coatings was controlled both by the mean distance from the cathodes and by the chemical and phase composition.

Silicon present in the $Cr_{1-x-y}Al_xSi_yN$ coatings caused large inclination of the out-of-plane texture direction and a fast decay of the out-of-plane and in-plane texture already for small silicon

concentrations. The strong effect of silicon on the microstructure of the $\text{Cr}_{1-x-y}\text{Al}_x\text{Si}_y\text{N}$ coatings was explained by the development of the amorphous silicon nitride that interrupted the growth of the crystalline phases and in such a way obstructed the transfer of the preferred orientation between neighbouring crystallites. Additionally, the development of the amorphous phase led to a decrease of the crystallite size and to the loss of their partial coherence.

Acknowledgements

The authors thank the German Scientific Council (DFG) for financial support of the project # RA-1050/9-1. The work is a part of the research program MSM 0021620834. HRTEM Jeol 2010 FEF was purchased from the funds of the DFG Priority Programme # 1062.

References

- [1] A.J. Perry, J. Schoenes, *Vacuum* 36 (1986) 149.
- [2] S.J. Bull, D.S. Rickerby, *Surf. Coat. Technol.* 43/44 (1990) 732.
- [3] F. Attar, T. Johannesson, *Thin Solid Films* 258 (1995) 205.
- [4] M. Odén, C. Ericsson, G. Håkansson, H. Ljungerantz, *Surf. Coat. Technol.* 114 (1999) 39.
- [5] C.-H. Ma, J.-H. Huang, H. Chen, *Thin Solid Films* 446 (2004) 184.
- [6] O. Banakh, P.E. Schmid, R. Sanjinés, F. Lévy, *Surf. Coat. Technol.* 163–164 (2003) 57.
- [7] S.R. Pulugurtha, D.G. Bhat, *Surf. Coat. Technol.* 201 (2006) 4411.
- [8] E. Lugscheider, K. Bobzin, Th. Hornig, M. Maes, *Thin Solid Films* 420–421 (2002) 318.
- [9] J. Lin, B. Mishra, J.J. Moore, W.D. Sproul, *Surf. Coat. Technol.* 201 (2006) 4329.
- [10] D. Rafaja, M. Dopita, M. Růžicka, V. Klemm, D. Heger, G. Schreiber, M. Šíma, *Surf. Coat. Technol.* 201 (2006) 2835.
- [11] D. Rafaja, V. Klemm, G. Schreiber, M. Knapp, R. Kužel, *J. Appl. Cryst.* 37 (2004) 613.
- [12] D. Rafaja, A. Poklad, V. Klemm, G. Schreiber, D. Heger, M. Šíma, M. Dopita, *Thin Solid Films* 514 (2006) 240.
- [13] D. Rafaja, A. Poklad, V. Klemm, G. Schreiber, D. Heger, M. Šíma, *Mat. Sci. Eng. A* 462 (2007) 279.
- [14] D. Rafaja, C. Wüstefeld, M. Dopita, M. Růžicka, V. Klemm, G. Schreiber, D. Heger, M. Šíma, *Surf. Coat. Technol.* 201 (2007) 9476.
- [15] P. Holubář, M. Jilek, M. Šíma, *Surf. Coat. Technol.* 133/134 (2000) 145.
- [16] H.S.M. Coxeter, *Introduction to Geometry*, 2nd edition, John Wiley & Sons, Inc., New York, 1969.
- [17] C.S. Sandu, R. Sanjinés, M. Benkahoul, F. Medjani, F. Lévy, *Surf. Coat. Technol.* 201 (2006) 4083.
- [18] C.S. Sandu, M. Benkahoul, R. Sanjinés, F. Lévy, *Surf. Coat. Technol.* 201 (2006) 2897.
- [19] L. Castaldi, D. Kurapov, A. Reiter, V. Shklover, P. Schwaller, J. Patscheider, *Surf. Coat. Technol.* 202 (2007) 781.
- [20] D. Rafaja, A. Poklad, G. Schreiber, V. Klemm, D. Heger, M. Šíma, *Z. Metallkunde* 96 (2005) 736.
- [21] J. Pelleg, L.Z. Zevin, S. Lungo, *Thin Solid Films* 197 (1991) 117.
- [22] U.C. Oh, J.H. Je, *J. Appl. Phys.* 74 (1993) 1692.
- [23] C.V. Falub, A. Karimi, M. Ante, W. Kalss, *Surf. Coat. Technol.* 201 (2007) 5891.
- [24] An example of the computer simulation of the competition between the strain, surface and interface energy and the influence of these energies on the grain growth in metallic thin films was shown in: R. Carel, C.V. Thompson, H.J. Frost, *Acta Mater.* 44 (1996) 2479.
- [25] C. Quaeysaegens, G. Knuyt, J. D'Haen, L.M. Stals, *Thin Solid Films* 258 (1995) 170.
- [26] A.J. Perry, V. Valvoda, D. Rafaja, *Thin Solid Films* 214 (1992) 169.
- [27] *Inorganic Structure Crystal Database (ICSD)*, FIZ Karlsruhe, 2007.

Chapter 3

Rafaja D., Dopita M., Růžička M., Klemm V., Heger D., Schreiber G., Šíma M.,
*Microstructure development in Cr-Al-Si-N nanocomposites deposited by
cathodic arc evaporation,*
Surface and Coatings Technology, **201**, (2006), 2835-2843.

Microstructure development in Cr–Al–Si–N nanocomposites deposited by cathodic arc evaporation

D. Rafaja^{a,*}, M. Dopita^b, M. Růžicka^c, V. Klemm^a, D. Heger^a, G. Schreiber^a, M. Šíma^c

^a Institute of Materials Science, TU Bergakademie Freiberg, Gustav-Zeuner-Str. 5, D-09599 Freiberg, Germany

^b Department of Electronic Structures, Faculty of Mathematics and Physics, Charles University, Ke Karlovu 5, CZ-121 16 Prague, Czech Republic

^c SHM Ltd., Průmyslová 3, CZ-787 01 Šumperk, Czech Republic

Received 21 April 2006; accepted in revised form 26 May 2006

Available online 17 July 2006

Abstract

Phase and texture analysis using X-ray diffraction, analysis of the diffraction line broadening, analysis of the lattice parameters and high-resolution transmission electron microscopy were employed to characterize the microstructure development in the Cr–Al–Si–N thin film nanocomposites with a variable $[\text{Cr}]/([\text{Al}] + [\text{Si}])$ ratio deposited by cathodic arc evaporation. At the highest chromium contents, a single face centered cubic phase formed in the coatings. Below $[\text{Cr}]/([\text{Cr}] + [\text{Al}] + [\text{Si}]) \approx 0.52$, a second crystalline phase developed that was identified as hexagonal AlN. The size of the fcc crystallites decreased with increasing aluminum and silicon contents until it reached 5 nm in the sample with the overall chemical composition $\text{Cr}_{0.40}\text{Al}_{0.52}\text{Si}_{0.08}\text{N}$. The small crystallite size and the presence of two crystalline phases were found to be responsible for a high hardness of the Cr–Al–Si–N nanocomposites. Analysis of the lattice parameters revealed strong crystal anisotropy of the elastic constants in the cubic phase that decreased with increasing aluminum and silicon contents.

© 2006 Elsevier B.V. All rights reserved.

PACS: 61.10.Nz; 61.46.-w; 61.82.Rx; 62.20.Dc; 68.37.-d; 68.37.Lp; 68.55.-a; 68.55.Jk; 68.65.-k

Keywords: Cathodic arc evaporation; Cr–Al–Si–N; Nanocomposites; XRD; HRTEM

1. Introduction

Chromium nitride coatings are regarded as an alternative to the ultra-hard coatings based on titanium nitride. The industrial applications of the CrN-based coatings exploit excellent wear and hardness properties of CrN, which are accompanied by its very good corrosion resistance and thermal stability [1–5]. For some applications, it is advantageous that CrN possesses low residual stress, thus relatively thick coatings can be deposited [6]. Because of their properties, CrN-based coatings are primarily used for special tools like hobs for automotive industry, sliding parts or molding dies [7]. Various physical vapor deposition (PVD) processes can be used for the deposition of the CrN coatings as summarized in Ref. [8]. The cathodic arc evaporation (CAE) [9–11] is one of them. During the last years, the technical importance

of the thin films nanocomposites proposed in Ref. [12] increased rapidly. This trend is also evident for nanocomposites based on chromium nitride [13–16]. In the Ti–Al–N and Ti–Al–Si–N systems, the formation of nano-sized domains was explained by a spinodal decomposition process [17–24] producing a face-centered cubic (fcc) phase of $\text{Ti}_{1-x}\text{Al}_x\text{N}$ and a hexagonal phase of AlN. The third phase in the coatings containing silicon is amorphous Si_3N_4 [25]. Regarding an analogy between the Ti–Al–Si–N and Cr–Al–Si–N systems, the phase stability of the Cr–Al–Si–N coatings should be one of the parameters controlling their microstructure and properties like for the Ti–Al–Si–N coatings. The fcc- $\text{Cr}_{1-x}\text{Al}_x\text{N}$ phase having the NaCl-type crystal structure was found to be stable up to the stoichiometry ratio $x = 0.67$ – 0.80 [26,27]; the critical stoichiometry ratio did depend on the nature of the deposition process.

Recently, we have shown on the example of the Ti–Al–N and Ti–Al–Si–N coatings that the dependence of the stress-free lattice parameter in the fcc phase on the overall chemical composition of the coatings can be used to recognize the decomposition of these

* Corresponding author. Tel.: +49 3731 39 2299; fax: +49 3731 39 3657.

E-mail address: Rafaja@ww.tu-freiberg.de (D. Rafaja).

systems into two crystalline phases, fcc-Ti_{1-x}Al_xN and h-AlN [28]. Although only the Poisson ratio is needed for calculation of the stress-free lattice parameters in cubic thin films [29], the calculation of the stress-free lattice parameters in Cr–Al–Si–N nanocomposites from the X-ray diffraction (XRD) data is not straightforward, because the dependence of the Poisson ratio on the chemical composition is not known. Besides, CrN belongs to materials with a strong crystal anisotropy of the elastic constants [8,30–33], which complicates the calculation of the stress-free lattice parameters in the Cr–Al–Si–N nanocomposites additionally. In anisotropic materials, the complete set of the X-ray elastic constants (XECs) must be known to be able to calculate the stress-free lattice parameters. XECs can be calculated from the single-crystalline elastic constants using the famous models [34–38] if the single-crystalline elastic constants are known, which is not true for the Cr–Al–Si–N system. Other ways of determining the XECs in coatings were proposed in Refs. [8,30,33]. However, these experimental techniques work only for coatings containing a single phase, not for composites.

In Ti–Al–Si–N nanocomposites, nanocrystallites with a very small mutual disorientation, i.e. with a high degree of the local preferred orientation, and thus with a high degree of the partial crystallographic coherence were found [28,39]. The partial crystallographic coherence was recognized from the dependence of the XRD line broadening on the size of the diffraction vector as it reduces the diffraction line broadening at small diffraction vectors [39]. In Ti–Al–Si–N coatings, the partial crystallographic coherence of nanocrystalline domains supported the development of intrinsic residual stresses [28], which improved the hardness of the coatings. The high local preferred orientation of crystallites was accompanied by a three-dimensional global texture, i.e. the preferred orientation of crystallites in the plane and normal to the plane of the coatings. The preferred orientation of crystallites reported for the CrN thin films in Ref. [40] is very similar to the texture observed in the Ti–Al–N and Ti–Al–Si–N coatings deposited using CAE [41].

2. Experimental details

The Cr–Al–Si–N coatings were deposited using CAE in nitrogen atmosphere at the working pressure of 1.3 Pa using two laterally rotating arc cathodes (π -80 from PLATIT) [42]. One cathode was made of chromium, the second one from aluminum containing 11 at.% Si. The ion current on the Cr cathode was 80 A, on the Al–Si cathode 120 A. The bias voltage was –75 V. Polished plates of cemented carbide were used as substrates. The base pressure was 5×10^{-3} Pa; the deposition temperature was approximately 450 °C. In contrast to commercial coatings, the samples were not rotated during the deposition process, which offers the following advantages for microstructure studies. The expected preferred orientation of crystallites is not superimposed by the sample rotation. A series of coatings with different chemical compositions can be obtained in one deposition process, as the chemical composition depends on the distance from the respective cathode. The deposition geometry was shown in Ref. [41]. Finally, the phase composition of the coatings is not primarily controlled by macroscopic chemical inhomogeneities caused by the sample rotation [43].

Table 1

The overall chemical composition of the Cr–Al–Si–N coatings as measured using EPMA with WDS, their thickness and hardness

Chemical composition	Thickness [μ m]	Hardness [GPa]
Cr _{0.91} Al _{0.08} Si _{0.01} N	4.5 \pm 0.2	27.7 \pm 0.7
Cr _{0.84} Al _{0.15} Si _{0.01} N	6.3 \pm 0.2	29.6 \pm 1.2
Cr _{0.69} Al _{0.28} Si _{0.03} N	7.9 \pm 0.3	34.4 \pm 1.6
Cr _{0.52} Al _{0.43} Si _{0.05} N	8.7 \pm 0.3	41.5 \pm 0.5
Cr _{0.40} Al _{0.52} Si _{0.08} N	8.6 \pm 0.3	44.5 \pm 1.7
Cr _{0.24} Al _{0.65} Si _{0.10} N	7.5 \pm 0.3	39.1 \pm 1.3
Cr _{0.07} Al _{0.81} Si _{0.12} N	3.6 \pm 0.2	34.9 \pm 0.7

The overall chemical composition of the coatings was determined using the electron probe microanalysis with wavelength-dispersive spectroscopy (EPMA/WDS) in 40 points across each sample. In each point, the signals from Cr, Al, Si, N, O and W were registered in the maximum of the respective spectral line. Cr, Al, Si and N are contained in the coatings, oxygen is an expected impurity contained in the coatings and W is the main component contained in the substrates. The background coming predominantly from *bremsstrahlung* was measured before and behind each spectral line and subtracted from the maximum intensity. The net intensities from the analyzed samples were compared to the net intensities measured on standard samples with a known chemical composition to obtain the concentrations of the elements in mass percent. The sum over concentrations of all analyzed elements (the analytical total) yielded (104 \pm 3) wt.%, which means that the standardization procedure and the microstructure model used for correction of the absorption of the individual spectral lines in the coatings were successful. The concentrations of individual elements were recalculated from the measured mass percent to the atomic percent (and finally to the stoichiometry ratio that is shown in Table 1) assuming that the sum over atomic percent is equal to 100%. The maximum spread in the concentration of Cr, Al and Si calculated over the 40 points in individual samples was below 2 at.%. The nitrogen concentrations were (54 \pm 3) at.% in all samples under study, which can be regarded as 50 at.% within the statistical spread in the experimental data. As no oxygen spectral signal exceeding the background was registered, the maximum oxygen concentration in the Cr–Al–Si–N coatings could only be estimated from the detection limit of the ESMA/WDS, which was calculated from the background intensity, to be lower than 0.1 at.%.

Microstructure of the Cr–Al–Si–N nanocomposites was investigated using X-ray diffraction (XRD) and high-resolution transmission electron microscopy (HRTEM). XRD experiments were performed using several diffraction geometries. Glancing-angle X-ray diffraction (GAXRD) measurements with a constant angle of incidence of the primary beam (3°) were done on a D8 diffractometer (Bruker, AXS) in order to analyze the phase composition of the coatings, the degree of the partial crystallographic coherence of the fcc crystallites, their size and lattice parameters. The D8 diffractometer was equipped by a parabolic Göbel mirror in the primary beam and by a Soller collimator with the acceptance angle of 0.12° and a flat LiF monochromator in the diffracted beam. Using GAXRD, the lattice parameters in cubic structures are measured on different lattice planes, i.e. on lattice planes with different diffraction indices hkl , that is advantageous for a direct evaluation of the crystal anisotropy. Complementary measurements of the lattice

parameters in the cubic phase were performed on a MRD diffractometer (PANalytical) equipped with an Eulerian cradle, a polycapillary optics in the primary beam, a Soller collimator having the acceptance angle of 0.27° and a flat graphite monochromator in the diffracted beam. These measurements were done on identical lattice planes, i.e. on the lattice planes with the same hkl , and used for an alternative calculation of the stress-free lattice parameters with the aid of the classical $\sin^2\psi$ method and for the determination of the degree of the crystal anisotropy in the cubic phase. The capability of both diffraction methods is described in Section 3 in more details. Texture measurements were performed on a PTS diffractometer (Seifert) equipped with an Eulerian cradle. All XRD experiments were performed using the $\text{CuK}\alpha$ radiation.

HRTEM was applied to visualize the amorphous component in the coatings and to verify the crystallite size and the mutual disorientation of adjacent crystallites obtained from XRD. HRTEM was performed with a 200 kV analytical high-resolution transmission electron microscope JEM 2010 FEF (Jeol) equipped by ultra-high-resolution objective lens ($C_s=0.5$ mm) and in-column energy filter. The latter was used to select only the elastic electrons for the HRTEM image formation. The specimens for HRTEM were prepared in the plane-view orientation, which is more convenient for comparison of the XRD and HRTEM results. The coatings were

first mechanically pre-thinned and etched by an ion beam. The final step in the specimen preparation was a plasma cleaning procedure.

Mechanical properties of the coatings were characterized by their hardness, which was calculated from the indentation load-displacement curve [44] measured in 10 points per sample using a computer-controlled Fischerscope H100 micro-hardness tester. The maximum load of 70 mN, which was recommended for superhard coatings in Ref. [45], was reached in 20 s. The unloading time was 20 s as well. The maximum indentation depth ranged between 0.3 and 0.4 μm , which are certainly below 10% of the coatings thickness (s. Table 1).

3. Results and discussion

3.1. Phase composition of the coatings and preferred orientation of crystallites

XRD phase analysis has shown that the samples up to the overall chemical composition $\text{Cr}_{0.52}\text{Al}_{0.43}\text{Si}_{0.05}\text{N}$ contain only one fcc phase. At higher aluminum and silicon contents, hexagonal AlN with the wurtzite type structure was detected as the second crystalline phase. Its amount increased with increasing aluminum contents as shown in Fig. 1. Still, the fcc phase prevailed up to the overall chemical composition $\text{Cr}_{0.24}\text{Al}_{0.65}\text{Si}_{0.10}\text{N}$ that is comparable with the maximum aluminum contents in the fcc- $\text{Cr}_{1-x}\text{Al}_x\text{N}$ reported in Refs. [26] and [27]. As we have shown recently [28], the existence of two crystalline phases is an important factor influencing the hardness of the thin film nanocomposites. The hardness of the Cr–Al–Si–N coatings is given in Table 1 together with their thickness and overall chemical compositions.

In order to improve the sensitivity and reliability of the XRD phase analysis, the individual diffraction lines were fitted by the Pearson VII function. The results of the diffraction line fitting were also used for calculation of the lattice parameters from the positions of the diffraction lines and for calculation of the crystallite size from the diffraction line broadening [39]. Texture analysis done on chromium-rich Cr–Al–Si–N coatings has confirmed that the fcc crystallites are strongly preferred oriented. A “three-dimensional” texture was observed like for the Ti–Al–N coatings [41], which were deposited at similar deposition conditions. The pole figures shown in Fig. 2 illustrate the changes in the preferred orientation of the fcc crystallites with increasing aluminum and silicon contents. In the sample with the overall chemical composition $\text{Cr}_{0.91}\text{Al}_{0.08}\text{Si}_{0.01}\text{N}$ that contains only fcc crystallites, the texture direction $\langle 111 \rangle$ is perpendicular to the sample surface (Fig. 2a). The pole figure (100) illustrates the in-plane orientation of the crystallites. With increasing aluminum and silicon contents, the $\langle 111 \rangle$ texture direction in the fcc crystallites inclines away from the normal direction as it can be seen from the shift of the intensity maxima in the pole figures taken in the samples $\text{Cr}_{0.84}\text{Al}_{0.15}\text{Si}_{0.01}\text{N}$ (Fig. 2b) and $\text{Cr}_{0.69}\text{Al}_{0.28}\text{Si}_{0.03}\text{N}$ (Fig. 2c).

3.2. Partial crystallographic coherence of neighboring crystallites

Analysis of the XRD line broadening revealed a high degree of the crystallographic coherence between fcc crystallites up to the overall chemical composition of $\text{Cr}_{0.52}\text{Al}_{0.43}\text{Si}_{0.05}\text{N}$. The partial

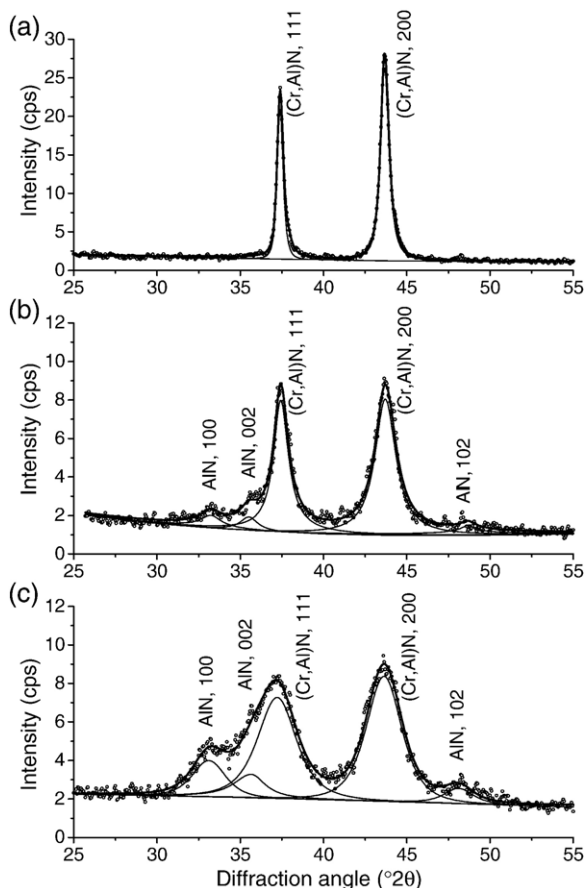


Fig. 1. Parts of the diffraction patterns measured on the samples $\text{Cr}_{0.52}\text{Al}_{0.43}\text{Si}_{0.05}\text{N}$ (a), $\text{Cr}_{0.40}\text{Al}_{0.52}\text{Si}_{0.08}\text{N}$ (b) and $\text{Cr}_{0.24}\text{Al}_{0.65}\text{Si}_{0.10}\text{N}$ (c) showing the development of hexagonal AlN with increasing aluminum and silicon contents. The small circles are the experimental data, the thin solid lines the individual diffraction lines and the wide solid lines the sum over the individual diffraction lines.

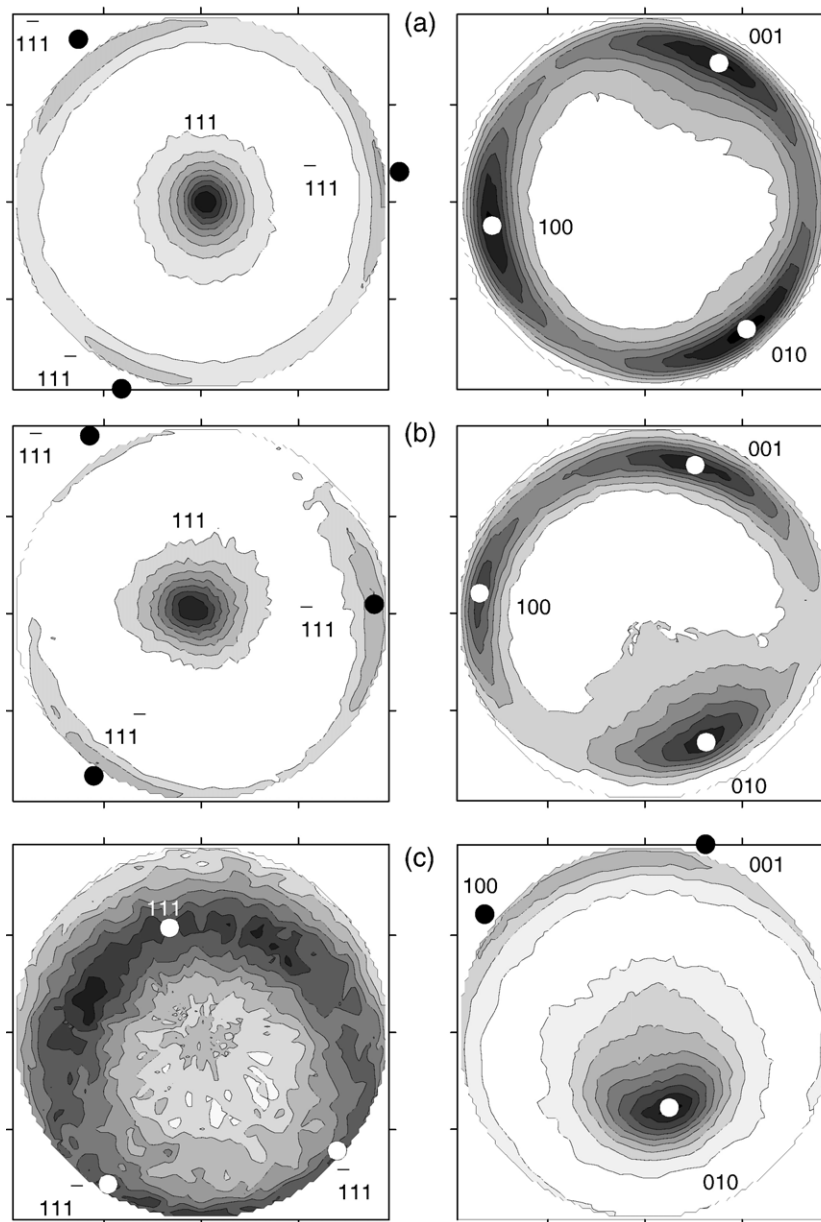


Fig. 2. Pole figures of the samples $\text{Cr}_{0.91}\text{Al}_{0.08}\text{Si}_{0.01}\text{N}$ (a), $\text{Cr}_{0.84}\text{Al}_{0.15}\text{Si}_{0.01}\text{N}$ (b) and $\text{Cr}_{0.69}\text{Al}_{0.28}\text{Si}_{0.03}\text{N}$ (c) measured on the diffraction lines 111 and 200. The poles corresponding to a perfect crystal orientation are indicated by circles and labeled by Miller indices.

crystallographic coherence was concluded from a slight increase of the line broadening with increasing diffraction angle up to $\sin\theta \approx 0.6$ (see the examples for the samples $\text{Cr}_{0.91}\text{Al}_{0.08}\text{Si}_{0.01}\text{N}$ and $\text{Cr}_{0.52}\text{Al}_{0.43}\text{Si}_{0.05}\text{N}$ shown in Fig. 3) that was followed by a steep increase and finally by a saturation of the diffraction line broadening at the highest diffraction angles. These phenomena were explained theoretically in Ref. [39], where it was shown that the partial crystallographic coherence of slightly disoriented nanocrystallites is equivalent to a partial overlap of their reciprocal lattice points. In the reciprocal space, the disorientation of adjacent crystallites corresponds to the rotation of their reciprocal lattices around the common origin of both reciprocal lattices. As the diffraction line broadening is independent of diffraction angle for small crystallites, which is well known as the “size effect”, a small disorientation of nanocrystallites causes a departure of their re-

ciprocal lattice points that increases with increasing distance of the reciprocal lattice points from their origin, i.e. with increasing diffraction angle. Consequently, the partial crystallographic coherence of crystallites causes a reduction of the diffraction line broadening at small and medium diffraction angles, where the reciprocal lattice points overlap each other. At large diffraction angles, the reciprocal lattice points of disoriented crystallites are too far from each other to be able to overlap and thus the diffraction line broadening remains constant as it is described by the Scherrer formula. In the coatings with $[\text{Cr}]/([\text{Cr}] + [\text{Al}] + [\text{Si}]) \leq 0.4$, no crystallographic coherence were observed experimentally as the diffraction line broadening was saturated for all accessible diffraction angles.

From the dependence of the line broadening on $\sin\theta$ in Fig. 3, two microstructure parameters were concluded: the size of the fcc

crystallites and their local disorientation. The crystallite size was calculated from the saturated line broadening, their local disorientation from the diffraction angle, for which the line broadening saturated [39]. The crystallite size decreased with decreasing chromium contents in the coatings (Fig. 4). HRTEM confirmed the small crystallite size; Fig. 5 illustrates a good match between the crystallite size calculated from the XRD line broadening and the crystallite size observed using HRTEM on the example of the $\text{Cr}_{0.40}\text{Al}_{0.52}\text{Si}_{0.08}\text{N}$ coating. The disorientations of the partially coherent crystallites increased with decreasing chromium contents from 0.6° in $\text{Cr}_{0.91}\text{Al}_{0.08}\text{Si}_{0.01}\text{N}$ to 1.3° in $\text{Cr}_{0.52}\text{Al}_{0.43}\text{Si}_{0.05}\text{N}$ as calculated from the XRD line broadening. This high local preferred orientation of partially coherent crystallites supported the formation of pronounced three-dimensional texture as confirmed by the pole figures shown in Fig. 2. The disorientation of the fcc crystallites in the coating with the overall chemical composition $\text{Cr}_{0.40}\text{Al}_{0.52}\text{Si}_{0.08}\text{N}$ exceeded 3° as calculated for a destroyed partial coherence (Fig. 3). The disorientation of non-coherent nanocrystallites in $\text{Cr}_{0.40}\text{Al}_{0.52}\text{Si}_{0.08}\text{N}$ was also apparent from the HRTEM micrographs shown in Figs. 5 and 6. From the distances between the fringes in the moiré pattern (Fig. 6), the minimum disorientation of the non-coherent nanocrystallites was calculated according to Ref. [46] to be $(7.8 \pm 0.1)^\circ$.

3.3. Crystal anisotropy of the lattice deformation

Large scatter of the cubic lattice parameters calculated from the GAXRD data indicated strong crystal anisotropy of the lattice

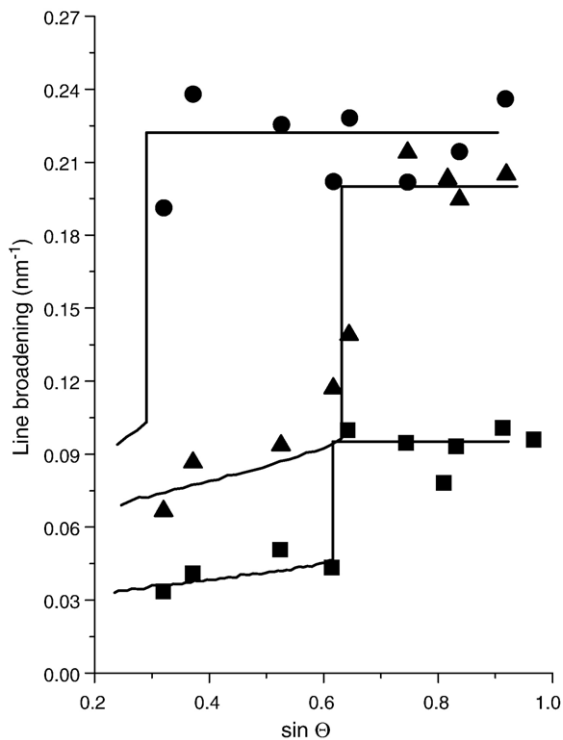


Fig. 3. Dependence of the XRD line broadening on $\sin\theta$ as measured for coatings with the overall chemical compositions $\text{Cr}_{0.91}\text{Al}_{0.08}\text{Si}_{0.01}\text{N}$ (boxes), $\text{Cr}_{0.52}\text{Al}_{0.43}\text{Si}_{0.05}\text{N}$ (triangles) and $\text{Cr}_{0.40}\text{Al}_{0.52}\text{Si}_{0.08}\text{N}$ (circles). The lines show the diffraction line broadening calculated according to Ref. [32].

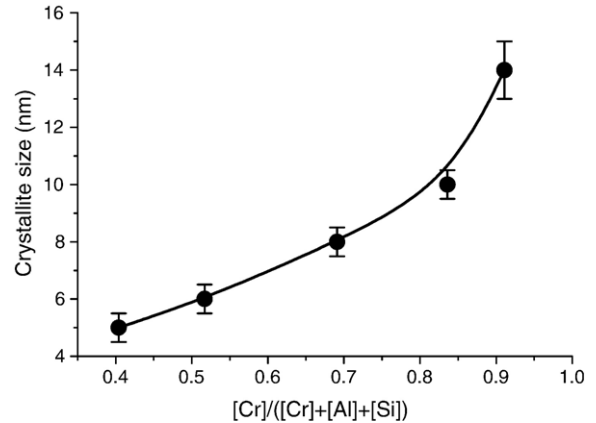


Fig. 4. Dependence of the crystallite size on the chromium contents in the Cr–Al–Si–N nanocomposites.

deformation, which implies a strong anisotropy of the X-ray elastic constants (XECs) in the fcc phase. As observed also for other nitrides that crystallize with the NaCl-type structure [22,47,48], the easy deformation direction is $\langle 111 \rangle$, the hard deformation direction $\langle 100 \rangle$. An example of the crystal anisotropy of the lattice deformation is shown in Fig. 7 for the $\text{Cr}_{0.91}\text{Al}_{0.08}\text{Si}_{0.01}\text{N}$ coating. The cubic lattice parameters calculated from GAXRD were compared with the lattice parameters obtained from the interplanar spacing of the lattice planes (111) and (200), which were measured at different inclinations of the sample (ψ) from the symmetrical position ($\psi=0^\circ$). In cubic materials under uniaxial residual stress, the lattice parameter depends linearly on $\sin^2\psi$:

$$a_{\psi}^{hkl} = (a_{\parallel}^{hkl} - a_{\perp}^{hkl}) \sin^2\psi + a_{\perp}^{hkl} \quad (1)$$

a_{\parallel}^{hkl} and a_{\perp}^{hkl} are the in-plane lattice parameter ($\psi=90^\circ$) and the lattice parameter normal to the sample surface ($\psi=0^\circ$),

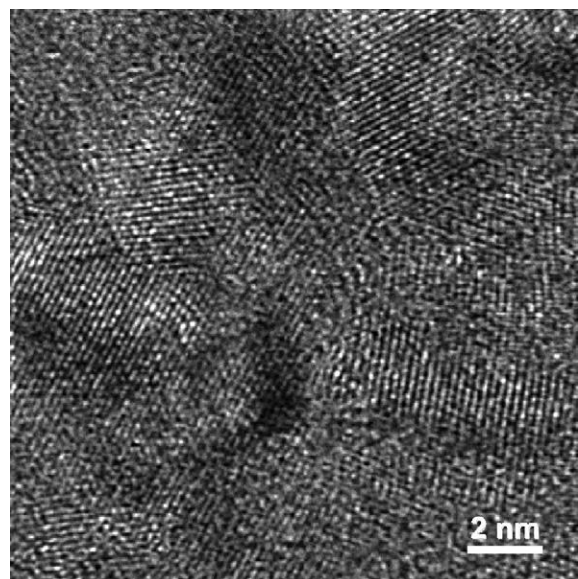


Fig. 5. HRTEM micrograph of the nanocrystallites in the sample $\text{Cr}_{0.40}\text{Al}_{0.52}\text{Si}_{0.08}\text{N}$.

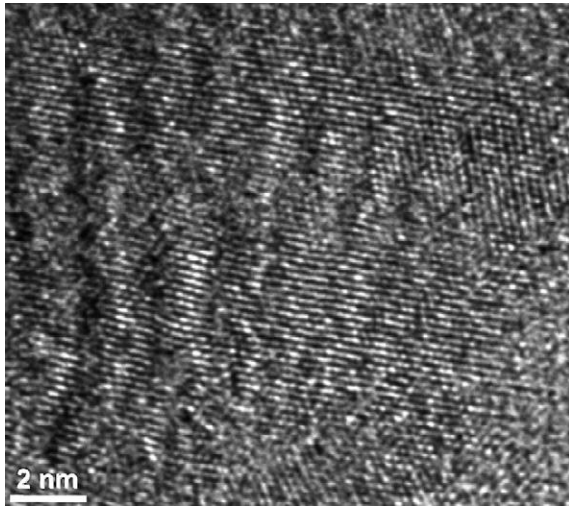


Fig. 6. HRTEM micrograph of the coating $\text{Cr}_{0.40}\text{Al}_{0.52}\text{Si}_{0.08}\text{N}$ showing moiré pattern due to a small mutual rotation of nanocrystallites.

respectively. They can be employed for calculation of the stress-free lattice parameter a_0 if the Poisson ratio $\nu^{hk\ell}$ is known [29]:

$$a_0 = (a_{\parallel}^{hk\ell} - a_{\perp}^{hk\ell}) \frac{2\nu^{hk\ell}}{\nu^{hk\ell} + 1} + a_{\perp}^{hk\ell} \quad (2)$$

Eqs. (1) and (2) were used for calculation of the stress-free lattice parameter in the sample $\text{Cr}_{0.91}\text{Al}_{0.08}\text{Si}_{0.01}\text{N}$ from the dependence of the lattice parameter a^{200} on $\sin^2\psi$. The Poisson ratio $\nu^{200} = 0.214$ taken from Ref. [30] yielded the stress-free lattice parameter of (0.41446 ± 0.00009) nm. The uniaxial residual stress calculated from

$$\sigma = \frac{a_0 - a_{\perp}^{hk\ell}}{a_0} \cdot \frac{E^{hk\ell}}{2\nu^{hk\ell}} \quad (3)$$

for the Young modulus $E^{200} = 520$ GPa [30] was $-(1.81 \pm 0.06)$ GPa. Unfortunately, this straightforward calculation of the

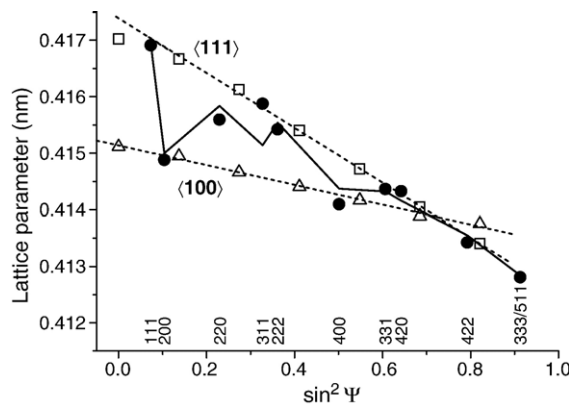


Fig. 7. $\sin^2\psi$ -plot for the cubic lattice parameters measured in the sample $\text{Cr}_{0.91}\text{Al}_{0.08}\text{Si}_{0.01}\text{N}$. Open boxes and triangles show the lattice parameters obtained from the interplanar spacing of the lattice planes (111) and (200), respectively, filled circles for the lattice parameters measured using GAXRD on different lattice planes. For the GAXRD method, the diffraction indices are given at the bottom of the plot. Dashed lines are the linear fits of a_{ψ}^{111} and a_{ψ}^{200} vs. $\sin^2\psi$; the broken line is the fit of $a_{\psi}^{hk\ell}$ vs. $\sin^2\psi$ using Eq. (7).

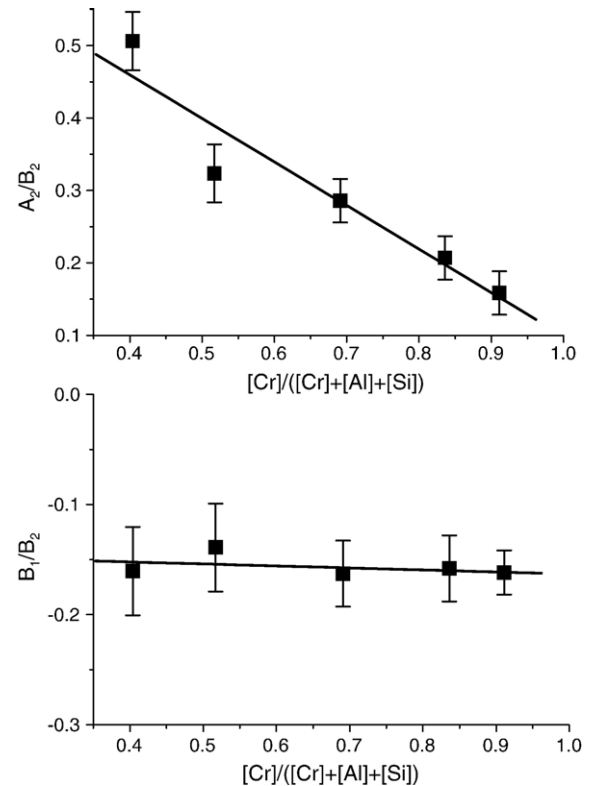


Fig. 8. Changes in the elastic anisotropy of fcc crystallites as a function of the chromium contents in the Cr–Al–Si–N nanocomposites. The meaning of the parameters is explained in text.

stress-free lattice parameter cannot be employed for compounds like Cr–Al–Si–N, in which a dependence of the XECs on the chemical composition is anticipated and the Poisson ratio unknown.

Using the linear dependence of the XECs, $s_1^{hk\ell}$ and $s_2^{hk\ell}$, on the orientation factor Γ [35–38]:

$$s_1^{hk\ell} = -\frac{\nu^{hk\ell}}{E^{hk\ell}} = A_1 + B_1\Gamma \quad \text{and} \quad s_2^{hk\ell} = 2 \cdot \frac{1 + \nu^{hk\ell}}{E^{hk\ell}} = A_2 + B_2\Gamma, \quad (4)$$

where

$$\Gamma = \frac{h^2k^2 + k^2\ell^2 + \ell^2h^2}{(h^2 + k^2 + \ell^2)^2} \quad (5)$$

and A_1 , A_2 , B_1 and B_2 are constants describing the crystal anisotropy of the respective compound, the well-known dependence of the cubic lattice parameters on $\sin^2\psi$ for coatings under uniaxial residual stress σ (see, e.g. [29]),

$$a_{\psi}^{hk\ell} = a_0 \left[\sigma \left(\frac{1}{2} s_2^{hk\ell} \sin^2\psi + 2s_1^{hk\ell} \right) + 1 \right], \quad (6)$$

can be rewritten into the form

$$a_{\psi}^{hk\ell} = \frac{1}{2} A_2 a_0 \sigma \sin^2\psi + \frac{1}{2} B_2 a_0 \sigma \Gamma \sin^2\psi + 2A_1 a_0 \sigma + 2B_1 a_0 \sigma \Gamma + a_0 \quad (7)$$

Eq. (7) can be used to get information on the crystal anisotropy of XECs from the GAXRD data, because the lattice parameters

obtained using GAXRD are measured on different crystallographic planes and at different inclinations of the sample from the symmetrical position, i.e., they depend both on $I(hk\ell)$ and ψ . The result of the GAXRD data fitting using the least-square method is shown for the sample $\text{Cr}_{0.91}\text{Al}_{0.08}\text{Si}_{0.01}\text{N}$ by the broken line in Fig. 7. The differences between the measured data (filled circles) and the fit (broken line) are caused by the strong preferred orientation of crystallites as described in Refs. [49–53].

In coatings with known stress-free lattice parameters (a_0) and residual stress (σ), Eq. (7) can be used to calculate the constants A_1 , A_2 , B_1 and B_2 , i.e. to obtain the complete set of the XECs $s_1^{hk\ell}$ and $s_2^{hk\ell}$ from Eq. (4). In coatings with unknown stress-free lattice parameters and/or residual stresses, only the relations between the constants A_1 , A_2 , B_1 and B_2 can be obtained. As it follows from Eq. (4), the ratio A_2/B_2 can be understood as a measure of the crystal anisotropy of $s_2^{hk\ell}$; B_1/B_2 describes the relation between the crystal anisotropy of $s_1^{hk\ell}$ and $s_2^{hk\ell}$. The dependencies of A_2/B_2 and B_1/B_2 on the chromium contents in the Cr–Al–Si–N coatings are shown in Fig. 8. The ratio A_2/B_2 increases with decreasing chromium contents, which means that the degree of crystal anisotropy of the fcc phase decreases with increasing aluminum and silicon contents. The ratio B_1/B_2 remains nearly constant with variable chromium contents, which means that the crystal anisotropy of both XECs changes very similarly with the chemical composition of Cr–Al–Si–N.

3.4. Stress-free lattice parameters of the fcc phase

As described above, the stress-free lattice parameter of a cubic phase can be calculated from the dependence $a_{\psi}^{hk\ell}$ vs. $\sin^2\psi$ if the Poisson ratio is known for the respective crystallographic directions. To eliminate the relatively strong anisotropy of XECs and the dependence of the degree of the crystallographic anisotropy of XECs on the chemical composition in the Cr–Al–Si–N system, the lattice parameters a^{200} measured at different inclinations of the samples from the symmetrical direction were used for calculation of the stress-free lattice parameters like in the “classical” $\sin^2\psi$ method. According to Eq. (5), $I(hk\ell)$ is equal to zero for $h00$, thus the effect of the crystal anisotropy disappears for the diffraction line 200. In a complementary calculation of the stress-free lattice

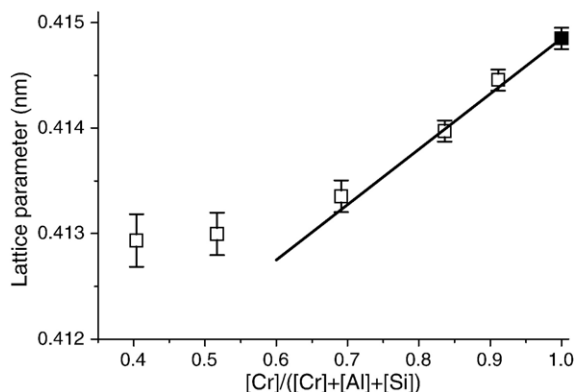


Fig. 9. Dependence of the stress-free lattice parameter on the chromium contents in the Cr–Al–Si–N nanocomposites (open boxes). The filled box indicates the lattice parameter of CrN taken from the PDF-2 database [54].

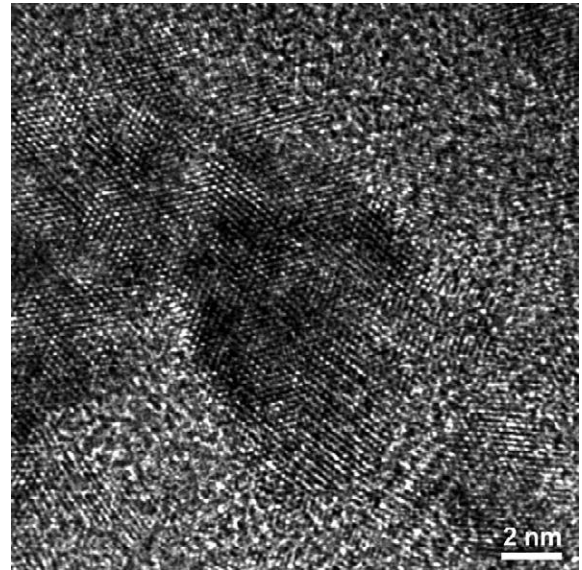


Fig. 10. HRTEM micrograph of the coating with the overall chemical composition $\text{Cr}_{0.52}\text{Al}_{0.43}\text{Si}_{0.05}\text{N}$ shows the typical distribution of crystalline and amorphous phases in the Cr–Al–Si–N system. Nanocrystallites are surrounded by amorphous regions and/or embedded in amorphous matrix.

parameters, the crystallographic anisotropy of XECs was “subtracted” from the GAXRD data using Eq. (7). This routine yielded, within the experimental accuracy, the same results as the fitting of the dependence a^{200} vs. $\sin^2\psi$. However, the separation of the crystal anisotropy from the measured lattice parameters does not solve the problem with unknown dependence of the Poisson ratio on the chemical composition in the Cr–Al–Si–N coatings. In order to be able to calculate the stress-free lattice parameters shown in Fig. 9, we assumed that the isotropic part of the Poisson ratio does not change substantially with the chemical composition of the coatings. Thus, the value of $\nu^{200}=0.214$ reported for CrN in Ref. [30] was used for all samples shown in Fig. 9. Although the assumption of a concentration-independent Poisson ratio is just a rough estimation, the stress-free lattice parameters from Fig. 9 are affected only marginally by the possibly incorrect value of the Poisson ratio. The reason is the low lattice strain observed in the $\langle 100 \rangle$ direction for all samples and thus a small slope of the dependence a^{200} vs. $\sin^2\psi$, from which the stress-free lattice parameters were calculated. An example of this dependence was shown by the lower dashed line in Fig. 7. For a departure of $\pm 10\%$ from a correct Poisson ratio, the difference in the stress-free lattice parameter would be below ± 0.0001 nm for the current lattice strains that is comparable with the size of the error bars in Fig. 9 that were obtained from the regression analysis.

At the highest chromium contents in the Cr–Al–Si–N coatings, the stress-free lattice parameter of the fcc phase decreases linearly with increasing aluminum and silicon contents as expected for a single cubic phase according to the Vegard rule. For $[\text{Cr}]/([\text{Cr}]+[\text{Al}]+[\text{Si}]) < 0.7$, a strong departure from the linear dependence was observed. The relatively high stress-free lattice parameter in the sample with the overall chemical composition $\text{Cr}_{0.40}\text{Al}_{0.52}\text{Si}_{0.08}\text{N}$ can be explained by formation of two crystalline phases in this sample as illustrated in Fig. 1 and discussed in Section 3.1. The formation of h-AlN as the second phase in the coating causes an

effective decrease of the amount of aluminum in the fcc phase in comparison with the overall chemical composition, which increases the stress-free lattice parameter of the fcc phase as aluminum is known to decrease the lattice parameter of CrN [26,27,55,56]. An analogous behavior of the stress-free lattice parameter was observed during the decomposition of the Ti–Al–Si–N coatings into fcc-(Ti, Al) N, h-AlN and a-Si₃N₄ [28]. However, the high stress-free lattice parameter of the sample Cr_{0.52}Al_{0.43}Si_{0.05}N cannot be explained by the concurrent formation of the cubic and hexagonal phases, because no h-AlN was revealed by the XRD phase analysis in this sample (Fig. 1). Thus, the increase of the stress-free lattice parameter as compared to its value expected for the [Cr]/([Cr]+[Al]+[Si]) ratio could be explained either by a slight disappearance of aluminum from the fcc phase that must not be accompanied by a detectable formation of h-AlN, or by a disappearance of silicon from the quaternary Cr–Al–Si–N system. For the latter, the additional phase would be amorphous. Presence of an amorphous phase was confirmed by HRTEM (see Fig. 10). In analogy with the Ti–Al–Si–N system [25], amorphous Si₃N₄ is expected.

3.5. Microstructure of the Cr–Al–Si–N nanocomposites and their hardness

The maximum hardness was reached for the overall chemical composition between Cr_{0.52}Al_{0.43}Si_{0.05}N and Cr_{0.40}Al_{0.52}Si_{0.08}N (Table 1). In this concentration range, the superfluous aluminum present in the coatings creates hexagonal AlN as a second crystalline phase (Fig. 1). The superfluous silicon creates an amorphous phase (Figs. 5 and 10), which disturbs the crystallographic coherence of adjacent crystallites in samples with [Cr]/([Cr]+[Al]+[Si]) ≤ 0.4 as shown for the Cr_{0.40}Al_{0.52}Si_{0.08}N coating in Fig. 3. The relationship between the formation of large amorphous domains and the disappearance of the crystallographic coherence of the fcc crystallites was discussed on the example of the Ti–Al–Si–N nanocomposites in Ref. [28], where it was shown that nanocrystallites surrounded by amorphous phase lose their high mutual orientation and consequently their partial crystallographic coherence. The partial crystallographic coherence of nanocrystallites was regarded as an efficient indicator of their intertwining, which is one of the factors improving the hardness of such nanocomposites [28]. An analogous conclusion can be drawn for the Cr–Al–Si–N system, in which the formation of nanocomposites with partially coherent crystallites can also be regarded as one of the reasons for their high hardness, particularly in the range of the chemical composition between Cr_{0.52}Al_{0.43}Si_{0.05}N and Cr_{0.40}Al_{0.52}Si_{0.08}N, where two nanocrystalline phases form and the fcc nanocrystallites are partially coherent.

Another very important factor that is responsible for the high hardness of the nanocomposites is the small crystallite size [12]. In the Cr–Al–Si–N coatings, the size of the fcc crystallites decreased with increasing aluminum and silicon contents up to the overall chemical composition Cr_{0.40}Al_{0.52}Si_{0.08}N (Fig. 4). In the coatings with the highest hardness, the mean crystallite size was (5.0 ± 0.5) nm. The strong preferred orientation of adjacent fcc crystallites, which was deduced from their partial crystallographic coherence, supports the hypothesis that the nanocrystalline

microstructure could be formed in a spinodal decomposition process as suggested in Refs. [17–24]. However, this hypothesis must be confirmed by thermodynamic modeling and/or by annealing the samples at high temperatures. The mean disorientation of partially coherent fcc crystallites in these clusters as obtained from the XRD line broadening was between 0.6° and 1.3° in the coatings with the overall chemical composition between Cr_{0.91}Al_{0.08}Si_{0.01}N and Cr_{0.52}Al_{0.43}Si_{0.05}N, respectively. In the coating Cr_{0.40}Al_{0.52}Si_{0.08}N, the smallest disorientation of crystallites exceeded 3° as estimated from the missing crystallographic coherence of crystallites. This disorientation was determined more precisely from the moiré pattern observed in the HRTEM micrograph (Fig. 6) to be (7.8 ± 0.1)° as described in Section 3.2. The critical chromium concentration [Cr]/([Cr]+[Al]+[Si]) < 0.52, at which hexagonal AlN arises, is higher than the critical titanium contents in the Ti–Al–Si–N coatings [28]. As a reason, the smaller difference between the lattice parameters of CrN and AlN can be considered than between the lattice parameters TiN and AlN [55,56].

The strong local texture in the Cr–Al–Si–N coatings was accompanied by a pronounced three-dimensional global texture that was concluded from the pole figures (Fig. 2). Similarly to the Ti–Al–N and Ti–Al–Si–N coatings deposited by CAE [41], the texture direction in the Cr–Al–Si–N coatings inclined with changing chemical composition and with changing angle between the substrate and the cathodes. A similar nature of the global texture was reported in Ref. [40] for CrN deposited using the ion-beam assisted deposition at different energies of the ion beam bombardment.

4. Conclusions

It was confirmed that the formation of the nanocomposites is responsible for high hardness of the Cr–Al–Si–N coatings deposited using cathodic arc evaporation. Formation of an amorphous phase surrounding fcc nanocrystallites of Cr–Al(Si)–N was concluded from the combination of GAXRD and HRTEM for [Cr]/([Cr]+[Al]+[Si]) < 0.7. In this concentration range, GAXRD revealed a higher stress-free lattice parameter than expected for the amount of aluminum and silicon obtained from the EPMA/WDS analysis. HRTEM visualized the amorphous phase in these samples. For [Cr]/([Cr]+[Al]+[Si]) < 0.52, formation of two nanocrystalline phases, fcc-Cr_{1-x}Al_xN with the NaCl-type structure and hexagonal AlN with the wurtzite-type structure, was observed. The size of the fcc crystallites decreased with decreasing chromium contents from 14 nm in Cr_{0.91}Al_{0.08}Si_{0.01}N to 5 nm in Cr_{0.40}Al_{0.52}Si_{0.08}N. Pronounced three-dimensional texture (a combination of the in-plane and the out-of-plane preferred orientation of crystallites) was observed; the texture direction perpendicular to the sample surface changed with increasing aluminum and silicon contents from <111> to <100>. The global texture was accompanied by a strong local preferred orientation of the fcc crystallites that was detected via their partial crystallographic coherence in chromium-rich samples up to the overall chemical composition Cr_{0.52}Al_{0.43}Si_{0.05}N. For lower chromium contents, the crystallographic coherence of the fcc crystallites disappeared, which was caused by their increasing disorientation due to the excess of the amorphous phase in the coatings.

The analysis of the lattice parameters in the fcc phase confirmed a strong crystallographic anisotropy of the X-ray elastic constants; the degree of the anisotropy decreased with increasing aluminum and silicon contents. Comparison of the “classical” $\sin^2\psi$ method that is usually performed on a single diffraction line with the modified $\sin^2\psi$ method that employs all diffraction lines measured using GAXRD has shown an equivalence of both approaches. The advantage of GAXRD is that it offers the same information contents within one diffraction pattern like the “classical” $\sin^2\psi$ method performed on the whole set of lattice planes.

Acknowledgements

The financial support of this work due to the DFG (German Research Foundation) under project # RA-1050/9 is highly appreciated. The HRTEM JEM 2010 FEF was financed through DFG in the frame of the Priority program # 1062. This work is a part of the research program MSM 0021620834 financed by the Ministry of Education of the Czech Republic.

References

- [1] B. Navinsek, P. Panjan, *Surf. Coat. Technol.* 59 (1993) 244.
- [2] J.A. Sue, T.P. Chang, *Surf. Coat. Technol.* 76–77 (1995) 61.
- [3] R. Gahlin, M. Bromark, P. Hedenqvist, S. Hogmark, G. Hakansson, *Surf. Coat. Technol.* 76–77 (1995) 174.
- [4] G. Bertrand, H. Mahdjoub, C. Meunier, *Surf. Coat. Technol.* 126 (2000) 199.
- [5] P. Carlsson, M. Olsson, *Surf. Coat. Technol.* 200 (2006) 4654.
- [6] H.C. Barshilia, N. Selvakumar, B. Deepthi, K.S. Rajam, *Surf. Coat. Technol.* 201 (2006) 2193, doi:10.1016/j.surfcoat.2006.03.037.
- [7] M. Brizuela, A. Garcia-Luis, I. Bracerias, J.I. Oñate, J.C. Sánchez-López, D. Martínez-Martínez, C. López-Cartes, A. Fernández, *Surf. Coat. Technol.* 200 (2005) 192.
- [8] J.A. Sue, A.J. Perry, J. Vetter, *Surf. Coat. Technol.* 68–69 (1994) 126.
- [9] E. Erturk, H.-J. Heuvel, H.-G. Dederichs, *Surf. Coat. Technol.* 39–40 (1989) 435.
- [10] O. Knotek, F. Löffler, H.-J. Scholl, *Surf. Coat. Technol.* 45 (1991) 53.
- [11] R.R. Aharonov, B.F. Coll, R.P. Fontana, *Surf. Coat. Technol.* 61 (1993) 223.
- [12] S. Veprek, S. Reiprich, Li Shizhib, *Appl. Phys. Lett.* 66 (1995) 2640.
- [13] E. Martinez, R. Sanjinés, O. Banakh, F. Lévy, *Thin Solid Films* 447–448 (2004) 332.
- [14] D. Mercs, N. Bonasso, S. Naamane, J.-M. Bordes, C. Coddet, *Surf. Coat. Technol.* 200 (2005) 403.
- [15] K. Yamamoto, S. Kujime, K. Takahara, *Surf. Coat. Technol.* 200 (2005) 1383.
- [16] A. Thobor-Keck, F. Lapostolle, A.S. Dehlinger, D. Pilloud, J.F. Pierson, C. Coddet, *Surf. Coat. Technol.* 200 (2005) 264.
- [17] S. Veprek, *J. Vac. Sci. Technol.*, A 17 (1999) 2401.
- [18] A. Hörling, J. Sjöln, L. Karlsson, M. Odén, L. Hultman, *J. Vac. Sci. Technol.*, A 20 (2002) 1815.
- [19] P.H. Mayrhofer, A. Hörling, L. Karlsson, J. Sjöln, T. Larsson, C. Mitterer, L. Hultman, *Appl. Phys. Lett.* 83 (10) (2003) 2049.
- [20] M. Parlinska-Wojtan, A. Karimi, O. Coddet, T. Cselle, M. Morstein, *Surf. Coat. Technol.* 188–189 (2004) 344.
- [21] S. Veprek, H.D. Männling, M. Jílek, P. Holubář, *Mater. Sci. Eng., A Struct. Mater.: Prop. Microstruct. Process.* 366 (2004) 202.
- [22] D. Rafaja, M. Šima, V. Klemm, G. Schreiber, D. Heger, L. Havela, R. Kužel, *J. Alloys Compd.* 378 (2004) 107.
- [23] P.H. Mayrhofer, H. Clemens, C. Mitterer, *Z. Met.kd.* 96 (2005) 468.
- [24] A. Hörling, L. Hultman, M. Odén, J. Sjöln, L. Karlsson, *Surf. Coat. Technol.* 191 (2005) 384.
- [25] S. Veprek, A. Niederhofer, K. Moto, T. Bolom, H.-D. Männling, P. Nesládek, G. Dollinger, A. Bergmaier, *Surf. Coat. Technol.* 133–134 (2000) 152.
- [26] A. Sugishima, H. Kajioka, Y. Makino, *Surf. Coat. Technol.* 97 (1997) 590.
- [27] Y. Makino, K. Nogi, *Surf. Coat. Technol.* 98 (1998) 1008.
- [28] D. Rafaja, A. Poklad, V. Klemm, G. Schreiber, D. Heger, M. Šima, M. Dopita, *Thin Solid Films* (2006), doi:10.1016/j.tsf.2006.02.092.
- [29] A.J. Perry, V. Valvoda, D. Rafaja, *Thin Solid Films* 214 (1992) 169.
- [30] F. Attar, T. Johannesson, *Thin Solid Films* 258 (1995) 205.
- [31] L. Cunha, M. Andritschky, K. Pischow, Z. Wang, *Thin Solid Films* 355–356 (1999) 465.
- [32] G. Wei, A. Rar, J.A. Barnard, *Thin Solid Films* 398–399 (2001) 460.
- [33] H.-Y. Chen, Ch.-J. Tsai, F.-H. Lu, *Surf. Coat. Technol.* 184 (2004) 69.
- [34] W. Voigt, *Lehrbuch der Kristallphysik*, Teubner-Verlag, Leipzig – Berlin, 1928.
- [35] A. Reuss, *Z. Angew. Math. Mech. Solids* 9 (1929) 49.
- [36] H. Neerfeld, *Mitt. Kaiser-Wilhelm-Inst. Eisenforsch. Dusseld.* 24 (1942) 61.
- [37] E. Kröner, *Z. Phys.* 151 (1958) 504.
- [38] R.W. Vook, F. Witt, *J. Appl. Phys.* 36 (1965) 2169.
- [39] D. Rafaja, V. Klemm, G. Schreiber, M. Knapp, R. Kužel, *J. Appl. Crystallogr.* 37 (2004) 613.
- [40] C.-H. Ma, J.-H. Huang, H. Chen, *Thin Solid Films* (2000) 184.
- [41] D. Rafaja, A. Poklad, G. Schreiber, V. Klemm, D. Heger, M. Šima, *Z. Met.kd.* 96 (2005) 736.
- [42] P. Holubář, M. Jílek, M. Šima, *Surf. Coat. Technol.* 133/134 (2000) 145.
- [43] H.A. Jehn, B. Rother, *Surf. Coat. Technol.* 112 (1999) 103.
- [44] W.C. Oliver, G.M. Pharr, *J. Mater. Res.* 7 (4) (1992) 1564.
- [45] J. Musil, F. Kunc, H. Zeman, H. Poláková, *Surf. Coat. Technol.* 154 (2002) 304.
- [46] D.B. Williams, C.B. Carter, *Transmission Electron Microscopy III — Imaging*, Plenum Press, New York, 1996.
- [47] D. Rafaja, V. Valvoda, R. Kužel, A.J. Perry, J.R. Treglio, *Surf. Coat. Technol.* 86–87 (1996) 302.
- [48] D. Rafaja, L. Havela, R. Kužel, F. Wastin, E. Colineau, T. Gouder, *J. Alloys Compd.* 386 (2005) 87.
- [49] H. Dölle, *J. Appl. Crystallogr.* 12 (1979) 489.
- [50] M. Barral, J.L. Lebrun, J.M. Sprauel, G. Maeder, *Metall. Trans., A, Phys. Metall. Mater. Sci.* 18 (1987) 1229.
- [51] M. Humbert, J. Diz, *J. Appl. Crystallogr.* 24 (1991) 978.
- [52] J. Diz, M. Humbert, *J. Appl. Crystallogr.* 25 (1992) 756.
- [53] M. Leoni, U. Welzel, P. Lamparter, E.J. Mittemeijer, J.-D. Kamminga, *Philos. Mag.*, A 81 (2001) 597.
- [54] PDF-2, Powder Diffraction File on CD-ROM, ICDD, Philadelphia, PA, 1997.
- [55] K. Yamamoto, T. Sato, K. Takahara, K. Hanaguri, *Surf. Coat. Technol.* 174–175 (2003) 620.
- [56] Y. Sun, Y.H. Wang, H.P. Seow, *J. Mater. Sci.* 39 (2004) 7369.

Chapter 4

Dopita M., Wüstefeld Ch., Klemm V., Schreiber G., Heger D., Růžička M.,
Rafaja D.,
*Residual stress and elastic anisotropy in the Ti-Al-(Si-)N and Cr-Al-(Si-)N
nanocomposites deposited by cathodic arc evaporation,*
Zeitschrift für Kristallographie, **27**, (2008), 245-252.

Residual stress and elastic anisotropy in the Ti-Al-(Si-)N and Cr-Al-(Si-)N nanocomposites deposited by cathodic arc evaporation

M. Dopita^{1,2,*}, Ch. Wüstefeld¹, V. Klemm¹, G. Schreiber¹,
D. Heger¹, M. Růžicka³, D. Rafaja¹

¹ Institute of Materials Science, TU Bergakademie Freiberg, D-09599 Freiberg, Germany

² Department of Condensed Matter Physics, Faculty of Mathematics and Physics, Charles University, Ke Karlovu 5, CZ-121 16 Prague, Czech Republic

³ SHM Ltd., Průmyslová 3, CZ-787 01 Šumperk, Czech Republic

* dopita@gmail.com

Keywords: thin coatings, nanocomposites, residual stress, elastic anisotropy, texture

Abstract. The elastic anisotropy of the Cr-Al-(Si-)N and Ti-Al-(Si-)N thin film nanocomposites with different aluminium and silicon contents deposited by the cathodic arc evaporation was investigated using complementary X-ray diffraction methods. Glancing angle X-ray diffraction (GAXRD) was employed to get the first information about the anisotropy of the elastic constants. The measurements done on an X-ray diffractometer equipped with an Eulerian cradle were used for calculation of the lattice strain and residual stress using the Crystallite Group Method and for determination of the preferred orientation of crystallites. In most samples, the degree of the elastic anisotropy decreased with increasing aluminium and silicon contents. Still, depending on the transition metal (Cr and/or Ti), different dependences of the elastic anisotropy on the aluminium and silicon contents were observed that could be related to the phase stability regions of the cubic phase in the Cr-Al-(Si-)N and Ti-Al-(Si-)N thin film nanocomposites.

1. Introduction

Protective coatings deposited by various PVD techniques are used for decades to improve the mechanical and tribological properties of cutting tools. During the last years, the importance of nanocomposite coatings has increased rapidly, because of their significantly improved hardness. Nowadays, the addition of a certain amount of aluminium and silicon into the chromium and titanium nitrides is a well-established method for the production of nanocrystalline coatings in which the cubic face-centred (fcc) phase dominates. As shown in [1], the solubility of aluminium in the fcc chromium and titanium nitrides is 77 at % for Cr and 65 at % for Ti. For higher aluminium concentrations, the wurtzitic AlN forms in the

coatings as a second crystalline phase that supports the development of the nanocomposites. The phase decomposition of the nano-scale is further supported by the segregation of superfluous silicon from the host structure of the chromium and titanium nitrides.

Besides the small crystallite size, one of the most important parameters which influences the hardness of the coatings significantly is the magnitude of the residual stress. For a correct determination of the residual stress in polycrystalline samples, the choice of a correct crystallite interaction model and the knowledge of the elastic constants are necessary. Unfortunately, rather deficient information about the elastic properties of nanocomposites is available in the literature. The main problems are the unknown dependence of X-ray elastic constants (XECs) on composition, unknown anisotropy of XECs and the unknown dependence of the anisotropy of XECs on composition, i.e. on the aluminium and silicon contents in the fcc Cr-Al-(Si)-N and Ti-Al-(Si)-N compounds. A strong anisotropy of the XECs in the systems under study was already indicated by our previous results [2]. Therefore, the main goal of this contribution is to describe the anisotropy of XECs in the Ti-Al-(Si)-N and Cr-Al-(Si)-N nanocomposites as a function of their chemical composition.

2. Experimental details

2.1 Sample preparation

Four series of coatings, Cr-Al-N, Cr-Al-Si-N, Ti-Al-N and Ti-Al-Si-N, were deposited using cathodic arc evaporation (CAE) in nitrogen atmosphere from two laterally rotating arc cathodes (π -80 from PLATIT) [3]. One cathode was made from the transition metal (Cr or Ti), the second one from aluminium for the sample series without silicon, i.e. Cr-Al-N and Ti-Al-N, and from aluminium containing approximately 11 at. % of silicon for the sample series containing silicon, i.e. Cr-Al-Si-N and Ti-Al-Si-N, respectively. To eliminate the influence of the parameters of the deposition process on the microstructure of the samples, the working pressure, ion current, bias voltage, base pressure and deposition temperature were kept identical for all samples. The working pressure was 1.3 Pa. The ion current on the transition metal cathode (Cr or Ti) was 80 A, and the ion current on the Al or Al-Si cathode was 120 A. The bias voltage was -75 V. The base pressure was 5×10^{-3} Pa and the deposition temperature was approximately 450°C. Polished plates of cemented carbide having random orientation of crystallites were used as substrates. In contrast to the commercially produced coatings, the samples were not rotated during the deposition process. Thus, the preferred orientation of crystallites was not superimposed by the sample rotation. Moreover, a set of coatings with different chemical compositions can be obtained in one deposition run, as the chemical composition of the individual samples depends on the position of the substrate with respect to both cathodes. For each sample series, seven samples differing in composition were prepared. However, only four Ti-Al-(Si)-N and five Cr-Al-(Si)-N coatings containing the cubic nitrides as the dominant phase were selected for a detailed microstructure investigation. As we showed recently [2, 10], the samples with the dominant fcc phase possess the highest hardness and are most important for industrial applications.

2.2 Investigation methods

The overall chemical composition of the coatings was determined using electron probe microanalysis with wavelength-dispersive spectroscopy (EPMA/WDX) at 40 points randomly distributed across each sample surface. The nitrogen concentration was 50 at. % within the experimental accuracy (for Ti-Al-(Si)-N, this was also checked by the glow-

discharge optical emission spectroscopy) and the maximum oxygen concentration was below the detection limit of the EPMA/WDX (lower than 0.1 at %) in all coatings under study. The overall chemical composition of the samples under consideration is given in table 1.

XRD experiments were performed using several diffraction geometries. Glancing-angle X-ray diffraction (GAXRD) measurements with a constant angle of incidence of the primary beam were done using a D8 diffractometer (Bruker, AXS) equipped with a parabolic Göbel mirror in the primary beam and a Soller collimator with acceptance angle of 0.12° and with a flat LiF monochromator in the diffracted beam. Data from GAXRD measurements were used mainly for the phase analysis, for the determination of the crystallite size and for the determination of the strain-free lattice parameter. Moreover, GAXRD data are suitable for fast visualisation of two effects. First, because the lattice parameters are measured on different crystallographic planes and at different inclinations of the sample from the symmetrical position, one can immediately get information about the crystal anisotropy from one GAXRD scan. Second, varying the angle of incidence of the primary beam has in consequence different penetration depths of X-rays, and thus different information depth of diffracted data. GAXRD measurements with several different angles of incidence can provide information about the presence of residual stress gradients as well as the strain-free lattice parameter depth profile can be calculated.

Table 1. Numbers of the samples and the overall chemical compositions of the investigated coatings.

Sample	$\text{Cr}_{1-x}\text{Al}_x\text{N}$	$\text{Cr}_{1-x-y}\text{Al}_x\text{Si}_y\text{N}$	$\text{Ti}_{1-x}\text{Al}_x\text{N}$	$\text{Ti}_{1-x-y}\text{Al}_x\text{Si}_y\text{N}$
1	$\text{Cr}_{0.92}\text{Al}_{0.08}\text{N}$	$\text{Cr}_{0.91}\text{Al}_{0.08}\text{Si}_{0.01}\text{N}$	$\text{Ti}_{0.96}\text{Al}_{0.04}\text{N}$	$\text{Ti}_{0.96}\text{Al}_{0.04}\text{Si}_{0.00}\text{N}$
2	$\text{Cr}_{0.83}\text{Al}_{0.17}\text{N}$	$\text{Cr}_{0.84}\text{Al}_{0.15}\text{Si}_{0.01}\text{N}$	$\text{Ti}_{0.85}\text{Al}_{0.15}\text{N}$	$\text{Ti}_{0.85}\text{Al}_{0.14}\text{Si}_{0.01}\text{N}$
3	$\text{Cr}_{0.75}\text{Al}_{0.25}\text{N}$	$\text{Cr}_{0.69}\text{Al}_{0.26}\text{Si}_{0.03}\text{N}$	$\text{Ti}_{0.72}\text{Al}_{0.28}\text{N}$	$\text{Ti}_{0.71}\text{Al}_{0.26}\text{Si}_{0.03}\text{N}$
4	$\text{Cr}_{0.54}\text{Al}_{0.46}\text{N}$	$\text{Cr}_{0.52}\text{Al}_{0.43}\text{Si}_{0.05}\text{N}$	$\text{Ti}_{0.52}\text{Al}_{0.48}\text{N}$	$\text{Ti}_{0.52}\text{Al}_{0.43}\text{Si}_{0.05}\text{N}$
5	$\text{Cr}_{0.46}\text{Al}_{0.54}\text{N}$	$\text{Cr}_{0.40}\text{Al}_{0.52}\text{Si}_{0.08}\text{N}$		

The texture measurements were done on a PTS 3000 diffractometer (Seifert) equipped with an Eulerian cradle and a point focus monocapillary optics. For each sample, the pole figures (111), (200) and (220) of the face centred cubic phase were recorded. The strain measurements were performed on a D8 diffractometer equipped with an Eulerian cradle and polycapillary optics located in the primary beam. Selected reflections were measured at three different azimuthal angles ϕ . For each ϕ setting, θ - 2θ scans were recorded at different inclinations of the sample ψ from the symmetrical position ($\psi = 0$). To obtain the parameters of the line positions, measured data were fitted by pseudo-Voigt function by means of the least-squares refinement. A linear background was supposed. Estimated errors in the line position determination were used as weight factors for subsequent data reduction. For the GAXRD and texture measurements the $\text{CuK}\alpha$ radiation ($\lambda = 1.5418 \text{ \AA}$) was used, whereas for the strain measurements, the $\text{CoK}\alpha$ radiation ($\lambda = 1.7903 \text{ \AA}$) was used.

3. Results and discussion

On the basis of the GAXRD measurements performed at several different angles of incidence of the primary beam (i.e. different information depth of diffracted intensity), we can conclude that no depth gradients were observed in our coatings, as can be seen from the nearly constant slopes of the $\sin^2\psi$ dependences constructed from these measurements (figure 1a). Rather high errors of the slopes determined from the linear function fit come

from the scatter of measured lattice parameters caused by the pronounced crystal anisotropy present in our coatings, whereas the biggest error calculated for measurement at the lowest angle of incidence ($\gamma = 1^\circ$) is caused solely by the quality of measured diffraction pattern. Equation 1 describes the relation between the measured lattice deformation and the stress tensor. Lattice deformations measured at three different angles ϕ and at several tilts ψ allow us, due to equation 1, to determine all stress tensor components [4]. As it is clearly visible from figure 1b, the coatings are under the state of biaxial, (rotationally symmetrical - $\sigma_{11} = \sigma_{22} = \sigma$) stress, because data measured for different angles ϕ are identical. No shear stresses ($\sigma_{13} = \sigma_{23} = 0$) are present in our samples which can be demonstrated by similar behaviour of lattice parameters measured for positive and negative ψ tilts i.e. no ψ splitting is observable – see figure 1c.

$$\varepsilon_{\phi,\psi}^{hkl} = \frac{1}{2}s_2^{hkl} \left[(\sigma_{11} \cos^2 \phi + \sigma_{12} \sin 2\phi + \sigma_{22} \sin^2 \phi - \sigma_{33}) \sin^2 \psi + \sigma_{33} \right] + \frac{1}{2}s_2^{hkl} (\sigma_{13} \cos \phi + \sigma_{23} \sin \phi) \sin 2\psi + s_1^{hkl} (\sigma_{11} + \sigma_{22} + \sigma_{33}) \quad (1)$$

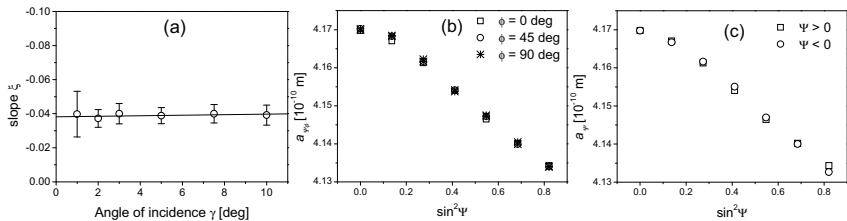
Under the assumptions of the biaxial, rotationally symmetrical state of stress, without shear stresses and normal stress component (σ_{33}) equal to zero, equation 1 reduces to a formula, which predicts the linear dependence of $\varepsilon_{\phi,\psi}^{hkl}$ vs. $\sin^2 \psi$ – equation 2.

$$\varepsilon_{\phi,\psi}^{hkl} = \left(2s_1^{hkl} + \frac{1}{2}s_2^{hkl} \sin^2 \psi \right) \sigma = 2s_1^{hkl} \sigma + \frac{1}{2}s_2^{hkl} \sigma \sin^2 \psi \quad (2)$$

From data measured using the classical $\sin^2 \psi$ method, the elastic anisotropy factor A can be derived – equation 3 [5]. Elastic anisotropy factor is given by the ratio between the slopes (ζ) of the dependences $\varepsilon_{\phi,\psi}^{hkl}$ versus $\sin^2 \psi$ measured on (00h) and (hhh) lattice planes.

$$A = \frac{\zeta^{00h}}{\zeta^{hhh}} = \frac{1/2s_2^{00h} \sigma}{1/2s_2^{hhh} \sigma} = \frac{s_2^{00h}}{s_2^{hhh}} \quad (3)$$

The measured dependences of lattice deformations vs. $\sin^2 \psi$ were approximated with a linear function (equation 2). We have to mention that there existed deviations from the expected linear behaviour even for 00h and hhh reflections (see figure 2b at low ψ tilts). We suppose that this effect comes from the plastic deformation of highly stressed lattice planes parallel to sample surface. The plastic deformation was recently demonstrated by the presence of screw dislocations in our coatings [6, 7].



Figures 1a, 1b and 1c. Slopes of the $\sin^2 \psi$ plots calculated from GAXRD measurements obtained for different angles of incidence γ for sample $\text{Cr}_{0.54}\text{Al}_{0.46}\text{N}$ (a). Plot of the lattice parameters obtained from the interplanar spacing of the lattice planes (111) versus $\sin^2 \psi$ measured for three different ϕ angles (b), measured for positive and negative ψ tilts (c) for sample $\text{Cr}_{0.91}\text{Al}_{0.08}\text{Si}_{0.01}\text{N}$.

For highly textured materials, the Crystallite Group Method (CGM) [4] is usually applied. The benefit of this method is, the possibility of getting information on specially chosen crystallite sets, taking into account the angular relations between individual crystallite planes. Using the CGM method the residual stresses for crystallite families having orientation widely incorporated in our samples, i.e. for the crystallites corresponding to the strongest texture component present in the coating, were derived.

3.1 Cr-Al-N and Cr-Al-Si-N system

The XRD phase analysis has show the presence of a single face centered cubic (fcc) phase up to chemical composition of $\text{Cr}_{0.54}\text{Al}_{0.46}\text{N}$ and $\text{Cr}_{0.52}\text{Al}_{0.43}\text{Si}_{0.05}\text{N}$. For higher Al contents in the samples, second – wurtzitic AlN phase was identified in coatings. The crystallite size decreases monotonously with increasing Al content from approximately 10 nm for the sample richest in chromium to 4.5 nm for sample #5 in the Cr-Al-Si-N coatings and from approx. 11 nm (sample #1) to 6.5 nm (sample #5) in the Cr-Al-N system. A detailed description of the evolution of microstructural parameters as a function of sample chemical composition are given in [2, 7]. All Cr-Al-N coatings under study were preferentially oriented with the $\langle 111 \rangle$ direction perpendicular to the sample surface. Only a slight inclination, less than 5° , of the $\langle 111 \rangle$ direction from the sample normal direction was observed. Moreover, all samples exhibit a strong in-plane texture. Similarly, the (111) texture was detected in the Cr-Al-Si-N samples. However, we observed a rapid inclination of the $\langle 111 \rangle$ direction from the sample surface perpendicular direction with increasing Al and Si content [8]. The “strength” of the in-plane texture gets weaker with increasing Al and Si concentration.

The anisotropy factor A was smaller than 1 in all cases, i.e. $s_2^{hhh} > s_2^{h00}$. The dependence of the anisotropy factor on aluminium content was much weaker than the dependence of the anisotropy factor on silicon content (figure 2a). The strongest anisotropy ($A = 0.4$) was observed in the sample $\text{Cr}_{0.69}\text{Al}_{0.28}\text{Si}_{0.03}\text{N}$. The slopes of the dependences of ε versus $\sin^2\psi$, which were used for calculation of the anisotropy factors, were obtained with a very high accuracy unlike the residual stresses, which would be affected by the difficulties and uncertainties in the determination of the elastic constants. In figures 2b, 2c and 2d, the slopes ζ^{111} and ζ^{200} are plotted as functions of the chemical compositions of the Cr-Al-(Si-)N coatings. The slope of the ε versus $\sin^2\psi$ dependences is negative for all investigated samples, whereas it is slowly decreasing with increasing Al concentration in Cr-Al-N system and increasing with Al and Si concentration for Cr-Al-Si-N coatings. The magnitude of the slope obtained using CGM lies between the boundary values calculated using the classical method for (111) and (200) lattice planes (compare figures 2b and 2c, 2d). Slight differences between the slopes obtained from the classical method and from CGM occur because these two methods apply different types of averaging. Data obtained from the classical method are averaged over crystallites having different orientation with respect to the sample surface measured on certain lattice planes, whereas CGM results are averaged over different (hkl), but the results correspond to the crystallites having distinct orientation (in our case crystallites corresponding to the major texture component).

Adopting elastic constants given in [9] ($\nu = 0.214$ and $E = 520$ GPa) and taking into account relations between the Young’s modulus and Poisson’s ratio and XECs $s_1 = -\nu/E$ and $\frac{1}{2}s_2 = (\nu+1)/E$ [4], one can calculate the values of the residual stress, but these results can

be understood as a very rough approximation as the possible dependence of the elastic constants on the chemical composition was neglected. Residual stress determined using CGM in both types of coatings is compressive, whereas its magnitude is significantly higher for samples without Si (approximately two times for the first four samples), and it is decreasing in Si free samples and increasing in coatings containing Si with increase of [Al] (or [Al]+[Si]) concentration. For the fifth samples - $\text{Cr}_{0.46}\text{Al}_{0.54}\text{N}$ and $\text{Cr}_{0.40}\text{Al}_{0.52}\text{Si}_{0.08}\text{N}$, the residual stress magnitude is similar, around -6 GPa for both coating series. Residual stresses determined using the classical $\sin^2\psi$ method exhibit the same trend as described for CGM results, moreover the dependences of residual stress on the composition are slightly smoother than in the CGM results.

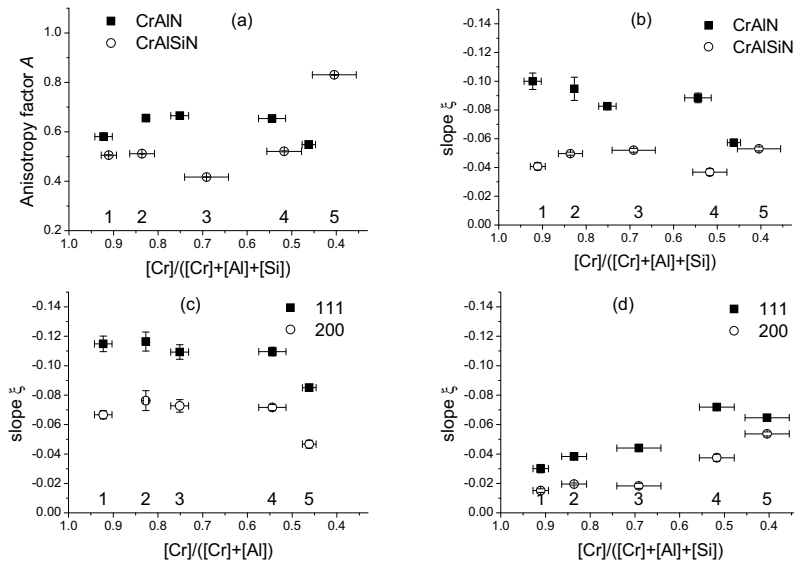


Figure 2a, 2b, 2c and 2d. Plot of the anisotropy factor A (a), slopes of the ϵ vs. $\sin^2\psi$ dependences measured on crystallite family corresponding to strongest texture component (CGM) (b), and slopes of the ϵ vs. $\sin^2\psi$ dependences measured on (111) and (200) lattice planes (c- for Cr-Al-N, d- for Cr-Al-Si-N), versus sample composition in chromium based coatings.

3.2 Ti-Al-N and Ti-Al-Si-N system

In Ti-Al-N and Ti-Al-Si-N coatings, the single fcc phase exists up to the chemical composition of $\text{Ti}_{0.72}\text{Al}_{0.28}\text{N}$ and $\text{Ti}_{0.71}\text{Al}_{0.26}\text{Si}_{0.03}\text{N}$. Then wurtzitic AlN phase starts to grow and for samples with higher Al and Si content ($([\text{Ti}]/[\text{Ti}]+[\text{Al}]+[\text{Si}]) < 0.4$) it becomes a dominant phase. The crystallite size decreases from 8 nm for sample #1 to approximately 4.2 nm for sample #4 in Ti-Al-N, and from 7 nm for sample #1 to roughly 2.7 nm for sample #4 in the Ti-Al-Si-N coatings. Crystallites with the highest Ti contents in Ti-Al-(Si)-N coatings are oriented with the $\langle 111 \rangle$ direction perpendicular to the sample surface. With increasing amount of Al the $\langle 111 \rangle$ crystallographic direction inclines towards the sample surface. In Si

free samples the crystallites are, additionally preferentially oriented in the plane of coatings. The crystallites in the Ti-Al-Si-N do not exhibit such in-plane texture [10, 11].

The anisotropy factor A is increasing with increasing Al and Si content and it can be well described by functions $y = 0.79(7) \cdot c_{[Al]} + 0.58(3)$, $y = 0.99(9) \cdot c_{([Al]+[Si])} + 0.56(9)$ for Ti-Al-N and Ti-Al-Si-N coatings respectively (figure 3a), where $c_{[Al]}$ or $c_{([Al]+[Si])}$ represent Al, or Al+Si concentration. The anisotropy relaxation is faster in the samples containing Si.

The slopes of the ε versus $\sin^2\psi$ dependences obtained using the classical method are negative for both Ti-Al-N and Ti-Al-Si-N as well, and increase linearly with increasing Al and Si concentration up to the $[Ti]/([Ti]+[Al]+[Si]) \sim 0.7$. The dependences show saturation at approximately -0.07 and -0.055 for Ti-Al-N and Ti-Al-Si-N, respectively – figures 3c and 3d, whereas the values are, in the bounds of errors, similar for (111) and (200) lattice planes (corresponding to the anisotropy relaxation for these samples).

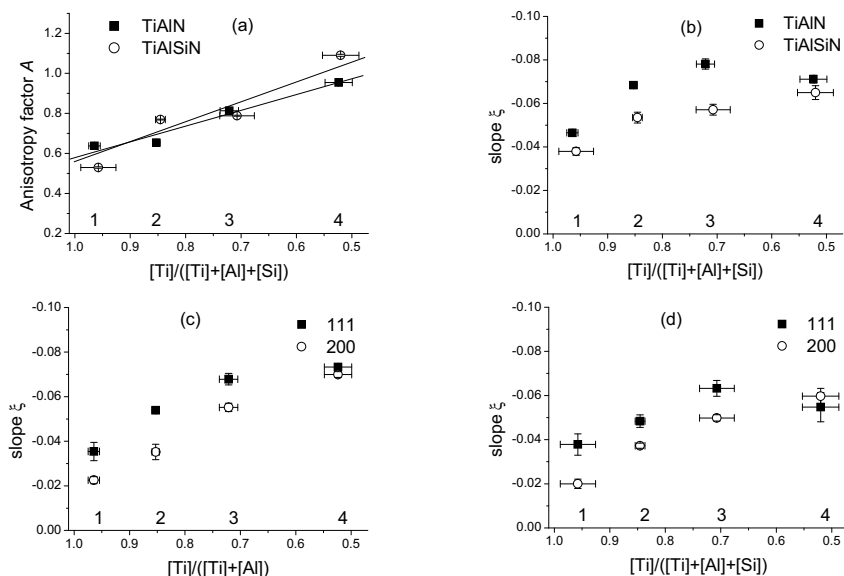


Figure 3a, 3b, 3c and 3d. Plot of the anisotropy factors A , lines correspond to the linear fit (a) Slopes of the ε vs. $\sin^2\psi$ dependences measured on crystallite family corresponding to strongest texture component (CGM) (b), and slopes of the ε vs. $\sin^2\psi$ dependences measured on (111) and (200) lattice planes (c- for Ti-Al-N, d- for Ti-Al-Si-N), versus sample composition in chromium based coatings.

Using the elastic constants $\nu = 0.295$ and $E = 640$ GPa from [5], the residual stress can be derived from the ε versus $\sin^2\psi$ dependence slopes. Because of the uncertainty in the dependence of elastic constants on composition, the elaborated values of residual stress can again be understood as a rough approximation. Residual stress determined using CGM shows an increase from approximately -5.5 GPa or -4.3 GPa to -8.5 GPa or -7.3 GPa with increasing Al and Si concentration for Ti-Al-N or Ti-Al-Si-N samples respectively. Stress determined for samples without Si is higher than in samples containing silicon, and reach its maximum at -9GPa for the third sample. Comparison of data obtained from CGM and the

classical $\sin^2\psi$ method shows that the residual stress determined from the classical $\sin^2\psi$ method (i.e. averaged over all crystallites orientation) is slightly smaller than its value from CGM, which means that preferentially oriented crystallites are in a state of higher compressive residual stress.

4. Conclusions

The Cr-Al-N, Cr-Al-Si-N, Ti-Al-N and Ti-Al-Si-N coatings deposited by CAE have been studied by X-ray diffraction. In all samples no residual stress or lattice parameter gradients as well no shear stresses and only biaxial rotationally symmetrical compressive state of stress were observed. Different types and degrees of preferred orientation of crystallites were found in the investigated samples. Applying the Crystallite Group Method, residual stresses for those families of crystallites having the majority orientation in our coatings were calculated. The anisotropy of the X-ray elastic constants decreased generally with increasing Al and Si concentration for all sample systems, except the case of Cr-Al-N coatings. In these samples rapid inclination of the $\langle 111 \rangle$ direction towards the sample surface were not observed. Anisotropy factors, slopes of ε versus $\sin^2\psi$ dependences and finally residual stresses as a function of sample composition were determined.

References

1. Sugishima, A., Kajioaka, H. & Makino, Y., 1997, *Surf. Coat. Technol.*, **97**, 590.
2. Rafaja, D., Dopita, M., Růžička, M., Klemm, V., Heger, D., Schreiber, G. & Šíma, M., 2006, *Surf. Coat. Technol.*, **201**, 2835.
3. Holubář, P., Jílek, M. & Šíma, M., 2000, *Surf. Coat. Technol.*, **133/134**, 145.
4. Hauk, V., 1997, *Structural and Residual Stress Analysis by Nondestructive Methods* (Amsterdam: Elsevier).
5. Perry, A.J., 1990, *Thin Solid Films*, **193/194**, 463.
6. Wüstefeld, Ch., Rafaja, D., Dopita, M. & Klemm, V., *Z. Kristallogr.*, this issue.
7. Rafaja, D., Wüstefeld, Ch., Dopita, M., Růžička, M., Klemm, V., Schreiber, G., Heger, D. & Šíma, M., 2007, *Surf. Coat. Technol.*, **201**, 9476.
8. Dopita, M., Rafaja, D., Wüstefeld, Ch., Růžička, M., Klemm, V., Heger, D., Schreiber, G. & Šíma, M., 2008, *Surf. Coat. Technol.*, **202**, 3199.
9. Attar, F. & Johannesson, T., 1995, *Thin Solid Films*, **258**, 205.
10. Rafaja, D., Poklad, A., Klemm, V., Schreiber, G., Heger, D., Šíma, M. & Dopita, M., 2006, *Thin Solid Films*, **514**, 240.
11. Rafaja, D., Poklad, A., Schreiber, G., Klemm, V., Heger, D. & Šíma, M., 2005, *Z. Metallkd.*, **96**, 736.

Acknowledgements. The authors thank the German Scientific Council (DFG) for financial support of the project # RA-1050/9-1. The work is a part of the research program MSM 0021620834 financed by the Ministry of Education of the Czech Republic.

Chapter 5

Rafaja D., Wüstefeld Ch., Dopita M., Ružička M., Klemm V., Schreiber G.,
Heger D. and Šíma M.,
*Internal structure of clusters of partially coherent nanocrystallites in Cr–Al–N
and Cr–Al–Si–N coatings,*
Surface and Coatings Technology, **201**, (2007), 9476-9484.

Internal structure of clusters of partially coherent nanocrystallites in Cr–Al–N and Cr–Al–Si–N coatings

David Rafaja^{a,*}, Christina Wüstefeld^a, Milan Dopita^{a,b}, Milan Růžička^c,
Volker Klemm^a, Gerhard Schreiber^a, Dietrich Heger^a, Michal Šíma^c

^a Institute of Materials Science, TU Bergakademie Freiberg, Gustav-Zeuner-Str. 5, D-09599 Freiberg, Germany

^b Department of Condensed Matter Physics, Faculty of Mathematics and Physics,
Charles University, Ke Karlovu 5, CZ-121 16 Prague, Czech Republic

^c SHM Ltd., Průmyslová 3, CZ-787 01 Šumperk, Czech Republic

Received 23 February 2007; accepted in revised form 2 April 2007

Available online 11 April 2007

Abstract

Nano-sized clusters consisting of strongly preferentially oriented, partially coherent nanocrystallites were observed in Cr–Al–N and Cr–Al–Si–N coatings deposited using cathodic arc evaporation. Microstructure analysis of the coatings, which was done using the combination of X-ray diffraction (XRD) and transmission electron microscopy with high resolution (HRTEM), revealed furthermore stress-free lattice parameters, size and local disorientation of crystallites within the nano-sized clusters in dependence on the aluminium and silicon contents, mean size of these clusters and the kind of structure defects. Within the face-centred cubic (fcc) $\text{Cr}_{1-x-y}\text{Al}_x\text{Si}_y\text{N}$ phase, the stress-free lattice parameter was described by the equation $a = (0.41486 - 0.00827 \cdot x + 0.034 \cdot y)$ nm. The size of individual crystallites decreased from ~ 11 nm in $\text{Cr}_{0.92}\text{Al}_{0.08}\text{N}$ to ~ 4 nm in $\text{Cr}_{0.24}\text{Al}_{0.65}\text{Si}_{0.10}\text{N}$. These nanocrystallites formed clusters with the mean size between 36 and 56 nm. The mutual disorientation of the partially coherent nanocrystallites forming the clusters increased with increasing aluminium and silicon contents from 0.5° to several degrees. The disorientation of neighbouring nanocrystallites was explained by the presence of screw dislocations and by presence of phase interfaces in coatings containing a single fcc phase and several phases, respectively.

© 2007 Elsevier B.V. All rights reserved.

Keywords: Cathodic arc evaporation; Nanocomposite; Partially coherent crystallites; Screw dislocations; XRD; HRTEM

1. Introduction

The relationship between the microstructure and properties of nanocrystalline coatings or thin film nanocomposites, which are based on nitrides of transition metals, is the main topic of many studies. This is also true for chromium nitride coatings, which contain additionally aluminium and silicon. The Cr–Al–N and Cr–Al–Si–N coatings are used with benefit in special industrial applications, e.g. for punching of perforated sheets [1], as super-elastic coatings for high end spindle bearings [2] or as thermal barriers redirecting the heat from the cutting tool into the chip [3]. In these applications, the microstructure and properties of the Cr–Al–N and Cr–Al–Si–N coatings are frequently tailored

by varying their chemical composition that influences primarily their phase composition [4–7]. For prediction of the phase composition in transition metal aluminium nitrides, Makino [6] published a theoretical approach that uses the band parameters method, which is based on the concept of the localized electron theory. For the face-centred cubic (fcc) $\text{Cr}_{1-x}\text{Al}_x\text{N}$, this approach yielded the maximum aluminium contents of $x = 0.772$. Experiments performed on the Cr–Al–N coatings deposited using magnetron sputtering [4] yielded the maximum aluminium contents between $x = 0.67$ and 0.75 . Cr–Al–N coatings deposited using rf-assisted magnetron sputtering [5] were composed of the single fcc phase up to $x = 0.7$ – 0.8 . The second phase, which forms above the solubility limit of aluminium in fcc $\text{Cr}_{1-x}\text{Al}_x\text{N}$, is AlN with the wurtzite crystal structure. Many applications of the CrN and Cr–Al–N coatings exploit their high oxidation resistance [3,8]. The onset of the oxidation in CrN is typically above 700°C ; the exact temperature of the beginning oxidation

* Corresponding author. Tel.: +49 3731 39 2299; fax: +49 3731 39 3657.

E-mail address: Rafaja@ww.tu-freiberg.de (D. Rafaja).

depends on the microstructure of the coatings [8]. Increasing aluminium contents improves the oxidation resistance of fcc (Cr, Al) N [9–12]. Reiter et al. [11] observed the onset of a rapid oxidation above 950 °C and 1000 °C for coatings with the chemical compositions $\text{Cr}_{0.79}\text{Al}_{0.21}\text{N}$ and $\text{Cr}_{0.54}\text{Al}_{0.46}\text{N}$, respectively.

As for other nanocomposites [13–15], the crystallite size and the morphology of the internal interfaces are the most important factors influencing the mechanical properties of Cr–Al–N and Cr–Al–Si–N nanocomposites. This is true particularly for their hardness, as the high hardness in nanocomposites is usually explained by a high elastic recovery of the material and by a high resistance against crack formation [16] or by prevention of the grain boundary sliding [17,18]. The relationship between crystallite size in stoichiometric CrN coatings and their hardness was described in detail by Mayrhofer et al. in [19], who has shown that the hardness of CrN coatings obeys the Hall–Petch relationship up to approximately 15 nm. In smaller crystallites, the hardness decreased. Like in the Ti–Al–Si–N system, the addition of silicon into Cr–Al–N improves the hardness of the nanocomposites. Approximately 9 at.% of Si was regarded as an optimum silicon concentration that increased the hardness of CrN from ~23 GPa to ~35 GPa and the hardness of Cr–Al–N from ~25 GPa to ~55 GPa [20]. Frequently, nanocomposites form during a decomposition process [6,21–28], which is anticipated to be accelerated by the presence of silicon, particularly in the Ti–Al–Si–N system. It was verified by first-principle calculations [29,30] that in Ti–Si–N the neighbouring TiN nanocrystallites can be connected by a slab of silicon nitride. An analogous inter-connection of neighbouring nanocrystallites of fcc-(Ti, Al) N and hexagonal AlN having similar inter-planar spacings was observed experimentally in Ti–Al–Si–N nanocomposites [31]. Such an inter-connection or inter-twinning of nanocrystallites was anticipated to be responsible for formation of local intrinsic stresses at the crystallites boundaries and thus for an additional increase of the hardness in these nanocomposites.

A very important experimental tool in description of the inter-twinning of neighbouring crystallites was the effect of the partial crystallographic coherence [32], which was exploited to determine small mutual disorientations of nanocrystallites. As discussed in [32], partially coherent nanocrystallites produce broad reciprocal lattice points. The size of the reciprocal lattice points that is related to the broadening of X-ray diffraction lines is reciprocally proportional to the crystallite size. Broad reciprocal lattice points overlap partially each other at small disorientations of the neighbouring crystallites. The overlap of the reciprocal lattice points from neighbouring crystallites is perfect at the origin of the reciprocal space, where the size of the diffraction vector

$$q = \frac{4\pi}{\lambda} \sin \theta \quad (1)$$

is equal to zero. With increasing length of the diffraction vector, the overlap of the reciprocal lattice points decreases until it disappears [31]. In Eq. (1), λ is the wavelength of X-rays and θ the diffraction angle. The partial overlap of the reciprocal lattice points corresponds to the coherence of X-rays scattered by the

related crystallites, thus it causes a “narrowing” of the broad diffraction lines from nanocrystallites (or it reduces the line broadening in nanocrystallites). An interpretation of this effect in the direct space is that the X-ray scattering cannot distinguish the partially coherent crystallites from each other. Therefore, partially coherent crystallites appear consequently larger than they are in a diffraction experiment. The apparent size of the crystallites varies with the size of the diffraction vector because the overlap of the reciprocal lattice points and the remaining XRD line broadening vary with the size of the diffraction vector. From the dependence of the diffraction line broadening on the size of the diffraction vector, two limiting quantities related to the apparent size of the crystallites can be calculated and assigned to the microstructure features, which can be verified by transmission electron microscopy (TEM): the size of individual nanocrystallites [32] and the size of clusters, which are composed of these nanocrystallites [33]. A requirement for the partial coherence of crystallites is that they have a similar crystallographic orientation. The maximum disorientation of partially coherent nanocrystallites is about 1° for the crystallite size of approximately 10 nm. Some examples are given in Section 3.

In this contribution, the phenomenon of the partial coherence of crystallites is employed to determine the size of clusters of partially coherent nanocrystallites, the average size of the nanocrystallites and their mutual disorientation in Cr–Al–N and Cr–Al–Si–N coatings containing a single phase or several phases, which are important parameters and features that can be used for a quantitative description of the microstructure of the coatings. In coatings containing several phases, the above features were used to describe quantitatively the microstructure of the coatings in terms of the models, which were derived or used, for instance, in Refs. [13–16,22,31,34–38]. These microstructure models assume the presence of at least two phases in the coatings and describe spatial distribution of the phases and/or the atomic ordering at the interfaces between different phases. In Cr–Al–N coatings containing a single phase, in which the same microstructure features were found like in the samples containing several phases, i.e. the clusters of partially coherent crystallites, the formation of these clusters was explained by the development of screw dislocations that were observed using TEM.

2. Experimental details

The Cr–Al–N and Cr–Al–Si–N coatings were deposited using cathodic arc evaporation (CAE) in nitrogen atmosphere at the working pressure of 1.3 Pa from two laterally rotating arc cathodes (π -80 from PLATIT) [39]. One cathode was made of chromium, the second one either from pure aluminium (for deposition of the Cr–Al–N coatings) or from aluminium containing 11 at.% Si (for deposition of the Cr–Al–Si–N coatings). The ion current on the Cr cathode was 80 A, the ion current on the Al or Al–Si cathode 120 A. The bias voltage was –75 V in all cases. Polished plates of cemented carbide were used as substrates. The base pressure was 5×10^{-3} Pa, the deposition temperature approximately 450 °C. In order to obtain a series of samples with a variable $[\text{Cr}]/[\text{Al}]$ or $[\text{Cr}]/([\text{Al}]+[\text{Si}])$ ratio in one deposition run, the positions of individual samples

did not change during the deposition process, i.e. the samples were not rotated unlike in technical deposition processes. The distance between the respective cathode and the respective substrate defined the chemical composition of individual coatings as discussed in Refs. [7,40].

The chemical composition of the Cr–Al–N and Cr–Al–Si–N coatings was determined using the electron probe microanalysis with wavelength-dispersive spectroscopy of characteristic X-rays (EPMA/WDS). Energy of the primary electrons in EPMA was 12 keV. High-purity Cr, Al and Si (99.999 %) were used as calibration standards together with BN, Fe₂N and Fe₄N. The stoichiometry ratios in individual samples are given in Tables 1 and 2 as averaged over 40 points measured across each sample. The maximum difference in the concentration of the analysed elements, i.e. Cr, Al, Si and N, within the individual samples was 2 at.%. The nitrogen contents was (54±3) at.% in all samples under study, which can be regarded as 50 at.% within the statistical spread in the experimental data. The stoichiometric composition of the samples regarding the nitrogen concentration was anticipated as based on the phase diagram of the Cr–N system [41] and confirmed by the electron probe microanalysis done on the Cr–Si–N thin films in [42]. The oxygen contents in the samples were below 0.1 at.% as discussed in [7]. Although aluminium and silicon were deposited from the same cathode, the [Si]/[Al] ratio in the coatings increased with decreasing chromium contents, i.e. with decreasing distance between the Al–Si cathode and the substrates in this deposition geometry. The hardness of the coatings, which is listed in Tables 1 and 2, was calculated from the indentation load–displacement curve [43] measured in 10 points per sample using a computer-controlled Fischerscope H100 microhardness tester. The maximum load of 70 mN, which was recommended for super-hard coatings in [44], was reached in 20 s. The unloading time was 20 s as well. The maximum indentation depth ranged between 0.3 and 0.4 µm, which are below 10% of the thickness in most coatings (compare thickness of the coatings given in Tables 1 and 2). The systematic variation of the thickness is caused by different distances between the cathodes and the substrates, which influences, besides the chemical composition, also the growth rate.

Phase composition of the coatings, stress-free lattice parameters, size of crystallites, size of clusters of partially coherent crystallites and the mutual disorientation of the partially coherent crystallites in the clusters were concluded from X-ray diffraction experiments that were performed in the glancing-angle X-ray

Table 2

Chemical composition, the [Si]/([Al]+[Si]) ratio, thickness and hardness of the Cr–Al–Si–N coatings

Chemical composition	[Si]/([Al]+[Si])	Thickness[µm]	Hardness [GPa]
Cr _{0.91(2)} Al _{0.08(1)} Si _{0.007(1)} N	(8.1±1.5) %	4.5±0.2	27.7±0.7
Cr _{0.84(3)} Al _{0.15(2)} Si _{0.013(3)} N	(8.1±2.1) %	6.3±0.2	29.6±1.2
Cr _{0.69(3)} Al _{0.28(3)} Si _{0.027(4)} N	(8.6±1.6) %	7.9±0.3	34.4±1.6
Cr _{0.52(3)} Al _{0.43(2)} Si _{0.049(3)} N	(10.1±0.8) %	8.7±0.3	41.5±0.5
Cr _{0.40(3)} Al _{0.52(3)} Si _{0.077(6)} N	(12.9±1.3) %	8.6±0.3	44.5±1.7
Cr _{0.24(2)} Al _{0.65(2)} Si _{0.102(8)} N	(13.5±1.2) %	7.5±0.3	39.1±1.3
Cr _{0.07(1)} Al _{0.81(3)} Si _{0.118(7)} N	(12.7±0.9) %	3.6±0.2	34.9±0.7

diffraction (GAXRD) geometry on a D8 diffractometer from Bruker AXS. In these diffraction experiments, copper radiation from a sealed X-ray tube was reflected by a parabolic Goebel mirror and directed to the sample surface. The angle of incidence was kept constant at 3°. Diffracted radiation was registered by a scintillation detector, which was preceded by a Soller collimator with the acceptance of 0.12° and by a flat LiF monochromator. The LiF monochromator located in the front of the detector changed the $K_{\alpha 2}/K_{\alpha 1}$ intensity ratio to 0.08. Additional measurements of the stress-free lattice parameter using the $\sin^2\psi$ method were carried out with an Eulerian cradle mounted on a PTS diffractometer from Seifert. High-resolution transmission electron microscopy (HRTEM) was done on a 200 kV analytical high-resolution transmission electron microscope JEM 2010 FEF from Jeol equipped by ultra-high-resolution objective lens ($C_s = 0.5$ mm) and in-column energy filter. The latter was used to select only the elastic electrons for the HRTEM image formation. The analysis of the dislocation structures was performed using the diffraction contrast in the bright field image. The specimens for TEM were prepared in the plane-view orientation, which is more convenient for a direct comparison of the XRD and HRTEM results. The coatings were first removed from the substrates, mechanically pre-thinned and etched by ion beam. The final step in the specimen preparation was a plasma cleaning procedure.

3. Experimental results

3.1. Phase stability and lattice parameters

Diffraction patterns of the Cr_{1-x}Al_xN and Cr_{1-x-y}Al_xSi_yN coatings shown in Figs. 1 and 2 confirmed that samples with the higher chromium contents than Cr_{0.46}Al_{0.54}N and Cr_{0.40}Al_{0.52}Si_{0.08}N, respectively, contain only one fcc phase. In samples with a lower chromium contents, wurtzitic AlN was identified as a second crystalline phase in the coatings. The third phase found in the XRD patterns was tungsten carbide from the substrate. Positions of the diffraction lines are marked in Figs. 1 and 2 for individual phases. The positions of the diffraction lines from the cubic phases, i.e. Cr_{1-x}Al_xN and Cr_{1-x-y}Al_xSi_yN, shift with the chemical composition of the samples that is due to the dependence of the lattice parameter on the stoichiometry in both systems. Because of the strong anisotropy of the elastic constants in the Cr–Al–N and Cr–Al–Si–N systems, the stress-free lattice parameters given in Fig. 3 were calculated using the

Table 1

Chemical composition, thickness and hardness of the Cr–Al–N coatings

Chemical composition	Thickness [µm]	Hardness [GPa]
Cr _{0.92(3)} Al _{0.08(1)} N	3.3±0.1	23.1±1.4
Cr _{0.83(3)} Al _{0.17(2)} N	5.0±0.1	25.7±1.4
Cr _{0.75(3)} Al _{0.25(3)} N	5.6±0.1	28.0±1.2
Cr _{0.54(3)} Al _{0.46(2)} N	7.2±0.1	36.3±1.4
Cr _{0.46(3)} Al _{0.54(2)} N	6.3±0.1	38.1±1.8
Cr _{0.30(2)} Al _{0.70(3)} N	5.4±0.1	38.3±1.7
Cr _{0.08(1)} Al _{0.91(3)} N	4.4±0.1	31.6±1.2

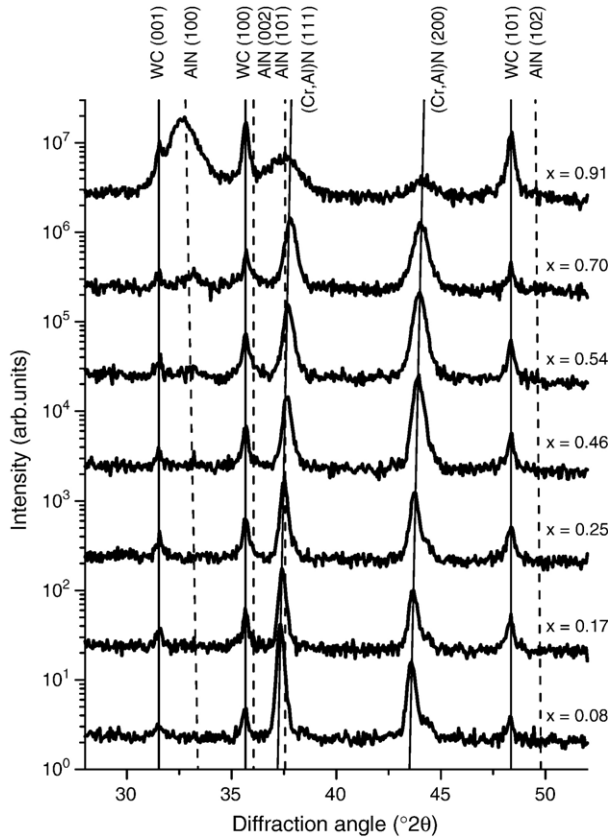


Fig. 1. Parts of the diffraction patterns of the $\text{Cr}_{1-x}\text{Al}_x\text{N}$ coatings with different chemical compositions. The vertical lines indicate the positions of individual XRD lines. Individual diffraction patterns were mutually shifted for clarity.

routine described in Ref. [7], which takes the well-known dependence of the elastic constants, e.g. [45–48], on the orientation factor

$$\Gamma = \frac{h^2k^2 + k^2\ell^2 + \ell^2h^2}{(h^2 + k^2 + \ell^2)^2} \quad (2)$$

into account. Results of this calculation were verified using the $\sin^2\psi$ method [49] applied on the lattice parameter a_{200} , for which is $\Gamma=0$. Dependence of the stress-free lattice parameters obtained from the XRD measurements on the chemical composition of the samples obtained using EPMA/WDX is shown by filled symbols in Fig. 3. Stress-free lattice parameter of CrN, i.e. for $[\text{Cr}]/([\text{Cr}]+[\text{Al}]+[\text{Si}])=1$, was taken from the ICSD database [50]. Solid lines connect lattice parameters that were calculated from the function:

$$a = [0.41486(2) - 0.00827(1) \cdot x + 0.034(1) \cdot y] \text{ nm} \quad (3)$$

for the chemical compositions of individual samples. The parameters x and y have the meaning of the stoichiometry ratios of aluminium and silicon in the fcc phase of $\text{Cr}_{1-x-y}\text{Al}_x\text{Si}_y\text{N}$. The numerical values in Eq. (3) were obtained from the linear regression that was done for the four chromium-richest samples in each series, which were found to contain a single crystalline phase. The first numerical coefficient in Eq. (3) has the meaning

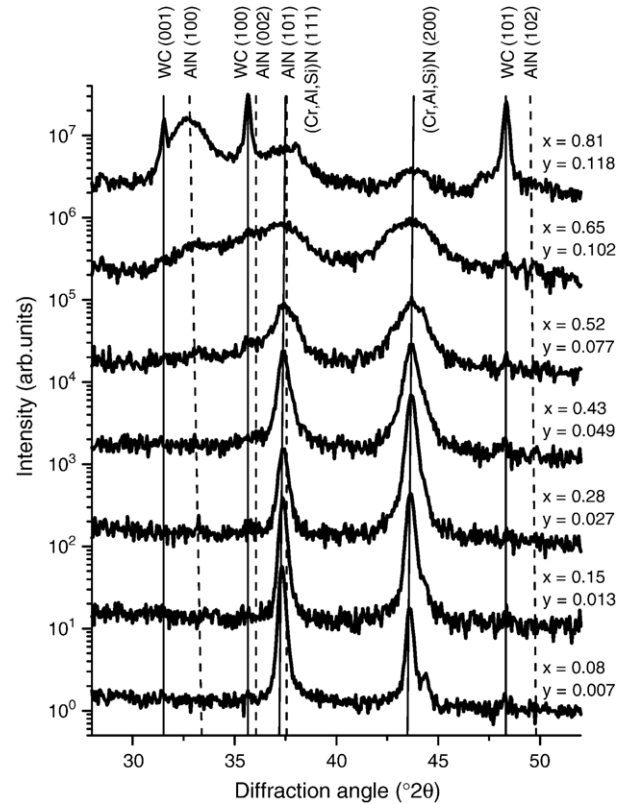


Fig. 2. Parts of the diffraction patterns of the $\text{Cr}_{1-x-y}\text{Al}_x\text{Si}_y\text{N}$ coatings with different chemical compositions. The vertical lines indicate the positions of individual XRD lines. Individual diffraction patterns were mutually shifted for clarity.

of the intrinsic lattice parameter of CrN. The second numerical coefficient quantifies the decrease of the lattice parameter in fcc Cr–Al–Si–N with increasing aluminium contents, the third one the increase of the lattice parameter with increasing silicon contents. Estimated standard deviations of the coefficients are given in parenthesis in Eq. (3).

The good match between the stress-free lattice parameters measured in chromium-rich samples up to $\text{Cr}_{0.54}\text{Al}_{0.46}\text{N}$ or

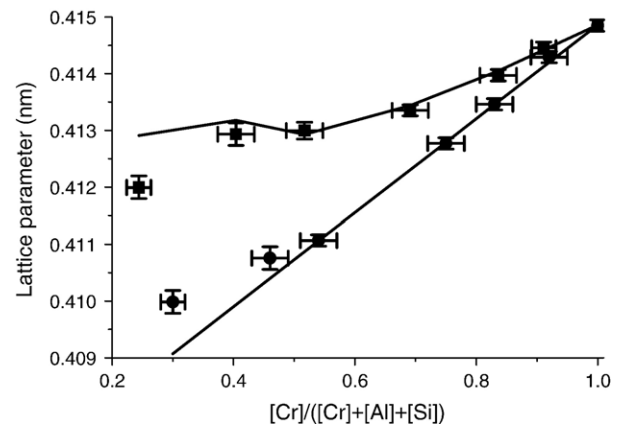


Fig. 3. Dependence of the stress-free lattice parameters on the chemical composition of the Cr–Al–N (●) and Cr–Al–Si–N (■) coatings. The solid lines show lattice parameters calculated according to Eq. (3).

$\text{Cr}_{0.52}\text{Al}_{0.43}\text{Si}_{0.05}\text{N}$ and the stress-free lattice parameters calculated using Eq. (3) confirmed the result of the XRD phase analysis that the samples contain a single fcc phase in this concentration range. At higher aluminium contents in the Cr–Al–N coatings, the measured stress-free lattice parameter of the fcc phase is larger than the calculated lattice parameters (Fig. 3). The reason is the segregation of aluminium from the host fcc crystal structure, which led to the development of AlN as observed by XRD phase analysis. In the Cr–Al–Si–N system, both Al and Si segregated from the host structure at lower chromium contents than $\text{Cr}_{0.52}\text{Al}_{0.43}\text{Si}_{0.05}\text{N}$. Segregation of aluminium was confirmed by XRD phase analysis, which recognized wurtzitic AlN. As it follows from Eq. (3), the increase of the stress-free lattice parameter with increasing silicon contents is larger than its decrease with increasing aluminium contents. Accordingly, the stress-free lattice parameter measured in the samples $\text{Cr}_{0.40}\text{Al}_{0.52}\text{Si}_{0.08}\text{N}$ and $\text{Cr}_{0.24}\text{Al}_{0.65}\text{Si}_{0.10}\text{N}$ is smaller than the value calculated from Eq. (3). Segregation of aluminium and silicon from the host structure of the fcc chromium nitride leads to the development of the nanocomposite microstructure as discussed below that is well-known to enhance the hardness of the coatings, see e.g. [13,14]. The highest hardness was observed in the Cr–Al–N and Cr–Al–Si–N coatings, in which the onset of AlN was found (see Tables 1 and 2). Increasing amount of the wurtzitic AlN caused a decrease of the hardness in both systems, Cr–Al–N and Cr–Al–Si–N. In the Cr–Al–N coatings, the maximum hardness correlates with the minimum crystallite size. In the Cr–Al–Si–N coatings, the maximum hardness was observed at the crystallite size of 4.5 nm. These results, particularly the correlation between the maximum of the hardness and the onset of the segregation of the AlN, confirm the hypothesis that the intrinsic stresses at the crystallites boundaries can additionally enhance the hardness.

3.2. Clusters of partially coherent crystallites

Size of individual crystallites, their mutual disorientation and the size of clusters consisting of partially coherent crystallites were obtained from the XRD line broadening [7,31–33] and verified by TEM and HRTEM. An example of the dependence of the XRD line broadening on sinus of the diffraction angle, $\sin \theta$, which is according to Eq. (1) proportional to the size of the diffraction vector, is shown in Fig. 4 for $\text{Cr}_{0.92}\text{Al}_{0.08}\text{N}$. As shown in [32], the saturated line broadening (for $\sin \theta > 0.75$ in Fig. 4) reveals the reciprocal crystallite size like the classical Scherrer equation or the Williamson–Hall approach [51] at zero microstrain. In the region of the diffraction angles, where the crystallites are partially coherent, the effect of the partial coherence of nanocrystallites causes a successive reduction of the XRD line broadening with decreasing diffraction angle [32]. Diffraction angle for which the effect of the partial coherence of nanocrystallites onsets depends on the mutual disorientation of partially coherent crystallites [7,32,33]. The smaller the mutual disorientation of crystallites, the higher is the diffraction angle, for which the crystallites are still partially coherent. For $\text{Cr}_{0.92}\text{Al}_{0.08}\text{N}$ (Fig. 4), the calculated mutual disorientation of partially

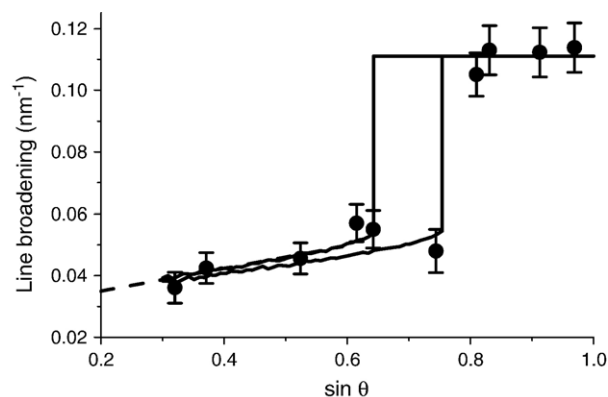


Fig. 4. Dependence of the XRD line broadening on $\sin \theta$ as measured for the $\text{Cr}_{0.92}\text{Al}_{0.08}\text{N}$ coating. The steep increase of the line broadening between $\sin \theta = 0.65$ and 0.75 indicates extinction of the partial coherence of crystallites. The solid lines show the XRD line broadening that was calculated according to [32] for two partially coherent crystallites having the size of 11 nm and the disorientation of 0.50° (lower curve) and 0.56° (upper curve) in each cluster. The dashed line shows extrapolation of the XRD line broadening in the partially coherent region to $q=0$.

coherent crystallites ranged between 0.50° (right-hand line) and 0.56° (left-hand line).

The size of crystallites and their mutual disorientations are plotted for individual samples in Figs. 5 and 6, respectively, as functions of the overall chemical composition. In the Cr–Al–N system, the increasing aluminium contents in the single fcc phase (up to $\text{Cr}_{0.54}\text{Al}_{0.46}\text{N}$) caused a moderate reduction of the crystallite size (solid circles in Fig. 5). Larger reduction of the crystallite size was observed in the samples, in which wurtzitic AlN developed. The mutual disorientation of neighbouring crystallites (solid circles in Fig. 6) increased slightly with increasing aluminium contents. The addition of silicon caused a further reduction of the crystallite size in comparison with the Cr–Al–N system; see solid boxes in Fig. 5. The decrease of the crystallite size with increasing aluminium and silicon contents could be described by a smooth function in contrast to the Cr–Al–N system. For low aluminium and silicon contents, the mutual disorientation of neighbouring crystallites in the Cr–Al–Si–N coatings followed the dependence found in the Cr–Al–N coatings. However, starting with $\text{Cr}_{0.52}\text{Al}_{0.43}\text{Si}_{0.05}\text{N}$ the disorientation of crystallites began to grow significantly with increasing silicon (and aluminium) contents. In $\text{Cr}_{0.40}\text{Al}_{0.52}\text{Si}_{0.08}\text{N}$, the disorientation of crystallites exceeded 1.4° , which is the maximum disorientation, for which the partial coherence of crystallites with the size of approximately 10 nm still could be observed. Such a loss of the partial crystallographic coherence of crystallites with increasing silicon contents was also observed in the Ti–Al–Si–N coatings [31], in which this phenomenon was related to the development of the amorphous Si_3N_4 phase.

A further microstructure parameter that was obtained from the XRD line broadening is the size of clusters, which consist of the partially coherent crystallites. As shown in the theory of XRD line broadening [52], the extrapolation of the XRD line width to the origin of the reciprocal space ($q=0$) yields the size of

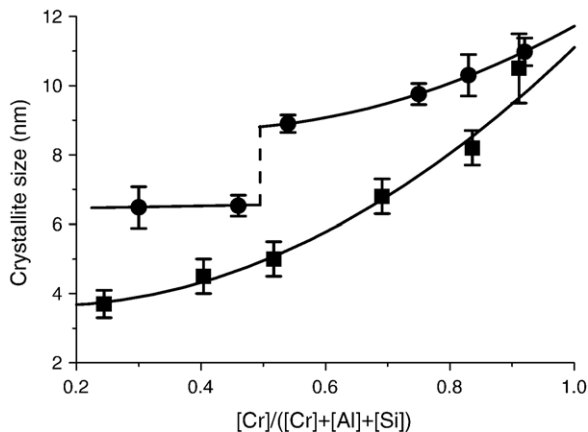


Fig. 5. Dependence of the crystallite size on the chemical composition in the Cr–Al–N (●) and Cr–Al–Si–N (■) coatings. The lines are guides for the eye.

coherently diffracting domains disregard their internal structure. In [32], it was shown that the coherence of partially coherent crystallites is enhanced at smaller diffraction vectors until the full coherence is reached at $q=0$. Thus for partially coherent crystallites, the extrapolation of the XRD line width to the origin of the reciprocal space should yield the size of clusters consisting of partially coherent crystallites instead of the size of individual crystallites. This hypothesis was confirmed by comparison of the results obtained from XRD and HRTEM. In the sample $\text{Cr}_{0.92}\text{Al}_{0.08}\text{N}$, the extrapolation of the XRD line broadening to $q=0$ (dashed line in Fig. 4) revealed that the size of clusters consisting of partially coherent crystallites is (36 ± 10) nm, which agrees well with their size obtained using HRTEM (compare with Fig. 7 for this particular sample). The low accuracy of the size of the clusters calculated from the extrapolation of the XRD line broadening is due to the fact that only the broadening of the diffraction lines affected by the partial coherence can be used for extrapolation. For this particular sample, just six diffraction lines were affected by the partial coherence. Size of the clusters consisting of partially coherent crystallites as obtained from the

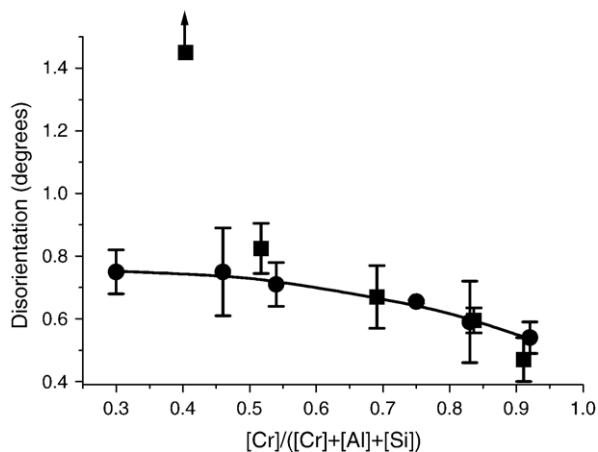


Fig. 6. Dependence of the mutual disorientation of partially coherent nanocrystallites on the chemical composition of the Cr–Al–N (●) and Cr–Al–Si–N (■) coatings. The solid line is guide for the eye.

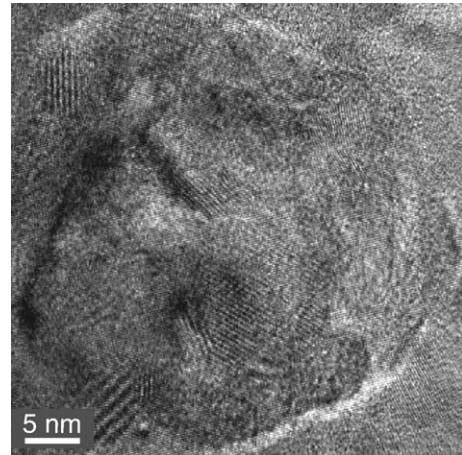


Fig. 7. HRTEM micrograph of the sample $\text{Cr}_{0.92}\text{Al}_{0.08}\text{N}$ showing a cluster consisting of partially coherent crystallites.

XRD line broadening in all samples under study ranged between 36 and 56 nm. Within the experimental accuracy, no systematic dependence of the cluster size on the chemical composition of the coatings was found.

3.3. Dislocation structures in the single-phase Cr–Al–N coatings

Small disorientations of neighbouring crystallites in nanocomposites, i.e. in materials containing more than one nano-sized phase, can be explained by the misfit of inter-atomic distances at the interfaces between individual phases [29–31]. Such an explanation of the crystallite's disorientation is applicable also for the aluminium- and silicon-rich Cr–Al–N and Cr–Al–Si–N coatings containing at least two phases as it can be seen from the steep increase of the disorientation of neighbouring crystallites in $\text{Cr}_{0.52}\text{Al}_{0.43}\text{Si}_{0.05}\text{N}$ and $\text{Cr}_{0.40}\text{Al}_{0.52}\text{Si}_{0.08}\text{N}$ (Fig. 6), where aluminium and silicon are leaving the host structure of chromium nitride (see Section 3.1 and Fig. 3). However, small disorientations of partially coherent neighbouring crystallites were also observed in the Cr–Al–N and Cr–Al–Si–N coatings with high chromium contents, which contained a single fcc phase. The fcc phase grew in clusters having the size between 36 and 56 nm as discussed in the previous section. The clusters in the single-phase coatings were composed from partially coherent crystallites having the size between 11 and 5 nm.

In analogy with the microstructure models used for description of the real structure in metallic materials and semiconductors, a possible explanation of the small disorientations of neighbouring crystallites in single-phase coatings is their disorientation due to dislocation structures. In materials containing complex dislocation structures, frequently defect-poor crystallites are observed that are separated by dislocation walls. In metallic materials, such a microstructure is usually described by Mughrabi's composite model [53]. Examples of analogous microstructural models can also be found in Refs. [54,55]. The disorientation of neighbouring crystallites that are separated by

a dislocation wall can be determined from the general formula given by Frank [56]:

$$\vec{B} = 2(\vec{r} \times \vec{\ell}) \sin \frac{\alpha}{2}, \quad (4)$$

where \vec{B} is the sum of Burgers vectors of the dislocations that are intersected by a vector \vec{r} , which lies in the dislocation wall. $\vec{\ell}$ is a unit vector, which also lies in the dislocation wall and is parallel to the tilt axis of the neighbouring crystallites. α is the disorientation of the crystallites. If the dislocation wall consists of pure edge dislocations, the tilt axis is located within the so-called tilt boundary; for dislocation walls containing only screw dislocations, the tilt axis is perpendicular to the so-called twist boundary [57].

An example of a dislocation wall in the sample $\text{Cr}_{0.92}\text{Al}_{0.08}\text{N}$ is shown in Fig. 8; the micrograph was taken in the two-beam diffraction condition [58]. In this particular case, the primary beam was parallel with the dislocation wall, which was perpendicular to the diffraction vector $(2\ 2\ 0)$. As the diffraction contrast does not change significantly in the neighbourhood of the dislocation wall, the sum of the Burgers vectors in the dislocation wall must be perpendicular to the diffraction vector, i.e. $\vec{q} \cdot \vec{B} = 0$. This means that the Burgers vector lies in the dislocation wall and that the tilt axis of neighbouring crystallites is perpendicular to the Burgers vector. The latter indicates that the excess dislocation of this dislocation wall is a screw dislocation. As the diffraction vector was $(2\ 2\ 0)$, the remaining dislocation resulting from the sum of the Burgers vectors of dislocations from the dislocation wall could be a complete screw dislocation with the Burgers vector $a/2 \langle 1\ 1\ 0 \rangle$, where a is the lattice parameter. In Fig. 9, the dislocation wall was slanted from the optical axis of the microscope, i.e. it was not parallel with the primary beam. Therefore the diffraction vector, which was $(\bar{2}\ 4\ 2)$ in this particular case, was not perpendicular to the Burgers vector of the dislocations; the dislocations become visible and their mutual distances can be estimated. Assuming that the dislocation wall is built from complete screw dislocations with the Burgers

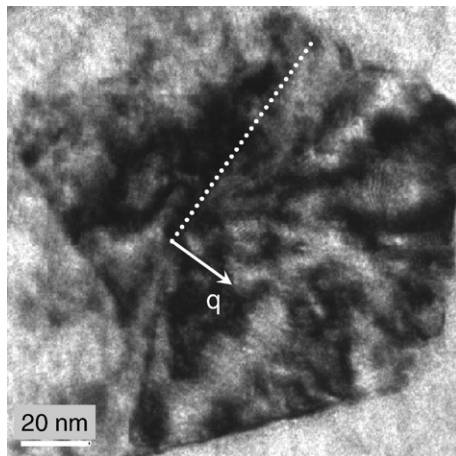


Fig. 8. A dislocation wall in the sample $\text{Cr}_{0.92}\text{Al}_{0.08}\text{N}$ (dotted line) that is perpendicular to the diffraction vector $\vec{q} = (2\ 2\ 0)$. The micrograph was taken in the two-beam diffraction condition.

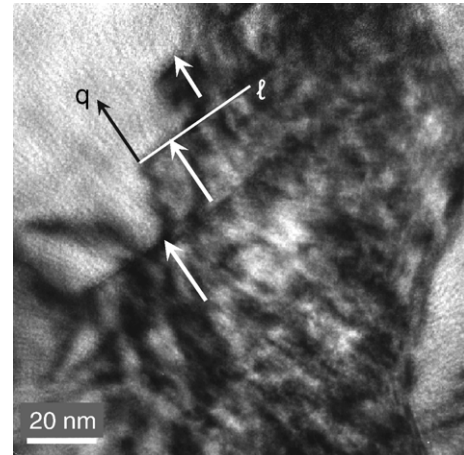


Fig. 9. A micrograph of three dislocation walls (marked by white arrows) taken at the diffraction vector $\vec{q} = (\bar{2}\ 4\ 2)$ in the sample $\text{Cr}_{0.92}\text{Al}_{0.08}\text{N}$. $\vec{\ell} = 1/\sqrt{2}(101)$ is a unit vector lying parallel to the tilt axis of the crystallites disorientation (marked by the white line).

vector $a/2 \langle 1\ 1\ 0 \rangle$, Eq. (4) can be rewritten into the following form:

$$|\vec{b}| = a \frac{\sqrt{2}}{2} = 2|\vec{r} \times \vec{\ell}| \sin \frac{\alpha}{2} \quad (5)$$

where \vec{b} is the Burgers vector of the complete screw dislocation and a the lattice parameter. According to Eq. (4), \vec{r} has the meaning of the distance between the screw dislocations in the dislocation wall; $|\vec{r} \times \vec{\ell}|$ stands for the projection of the distance between dislocations into the imaging plane of TEM. The disorientation of crystallites due to the screw dislocations is approximately 0.75° as calculated using Eq. (5) for $|\vec{r} \times \vec{\ell}| \approx 22\text{ nm}$, which was the visible distance between the dislocations in the sample $\text{Cr}_{0.92}\text{Al}_{0.08}\text{N}$ (see Fig. 9), and for $a = 0.4145\text{ nm}$ (see Fig. 3). This disorientation of crystallites is of the same order of magnitude like the disorientation of crystallites obtained from the XRD line broadening, which was 0.54° (see Fig. 6).

4. Summary and discussion

Nanocrystalline clusters were observed in all $\text{Cr}_{1-x}\text{Al}_x\text{N}$ and $\text{Cr}_{x-y}\text{Al}_x\text{Si}_y\text{N}$ coatings under study. The crystallite size decreased with increasing aluminium and silicon contents from $\sim 11\text{ nm}$ to $\sim 4\text{ nm}$. The decrease of the size of crystallites was accompanied by an increase of their mutual disorientation from 0.5° to several degrees. In the coatings without silicon ($\text{Cr}_{1-x}\text{Al}_x\text{N}$), generally larger crystallites with a smaller mutual disorientation were observed than in the coatings containing silicon ($\text{Cr}_{x-y}\text{Al}_x\text{Si}_y\text{N}$). A rapid decrease of the crystallite size was observed in the sample $\text{Cr}_{0.46}\text{Al}_{0.54}\text{N}$, in which wurtzitic AlN was found together with fcc (Cr, Al) N. In the coatings with silicon, the decrease of the crystallite size with increasing aluminium and silicon contents was faster than in the Cr–Al–N coatings. However, no rapid change of the crystallite size was observed in the sample $\text{Cr}_{0.40}\text{Al}_{0.52}\text{Si}_{0.08}\text{N}$, in which fcc-(Cr, Al)

N and wurtzitic AlN were observed concurrently. On the contrary, the mutual disorientation of crystallites increased rapidly with increasing aluminium and silicon contents in aluminium- and silicon-rich samples starting with the last “single-phase” sample $\text{Cr}_{0.52}\text{Al}_{0.43}\text{Si}_{0.05}\text{N}$. In the sample $\text{Cr}_{0.40}\text{Al}_{0.52}\text{Si}_{0.08}\text{N}$, the disorientation of crystallites exceeded the maximum disorientation, for which the phenomenon of the partial coherence of crystallites still can be observed. Thus, the disorientation of crystallites could not be calculated from the XRD line broadening; it could only be estimated to be larger than 1.4° . A similar effect was observed in the Ti–Al–Si–N coatings [31], where the loss of the crystallographic coherence of crystallites was explained by the development of amorphous Si_3N_4 between individual crystallites, which obstructed transfer of the preferred orientation between neighbouring crystallites.

The results of microstructure analysis indicated a substantial difference in the development of nanocrystallites in the Cr–Al–N and Cr–Al–Si–N coatings containing a single phase or several phases. Development of nanocrystallites in coatings containing more phases resulted from segregation of aluminium and silicon from the host structure of the fcc $\text{Cr}_{1-x-y}\text{Al}_x\text{Si}_y\text{N}$. Segregated aluminium builds nanocrystalline wurtzitic AlN, which splits fcc nanocrystallites without disturbing their partial coherence. A very strong local preferred orientation of fcc nanocrystallites with the size between 4 and 11 nm in clusters having the size between 36 and 56 nm, which is a requirement for the partial coherence of the nanocrystallites, supports the hypothesis that the nanocrystallites originate from the clusters in a decomposition process probably during the deposition process. Analogous microstructure models were discussed in numerous works, e.g. in Refs. [6,14,15,20,29–31,34,36,59–62].

The development of nanocrystallites in single-phase coatings can be illustrated on the sample $\text{Cr}_{0.92}\text{Al}_{0.08}\text{N}$. In this sample, XRD detected partially coherent nanocrystallites with the size of approximately 11 nm and with the average mutual disorientation of 0.54° . These nanocrystallites built clusters having the size of (36 ± 10) nm as obtained from XRD line broadening and confirmed by HRTEM. Using TEM, dislocations walls were found in this sample that consisted of screw dislocations with the Burgers vector $a/2 \langle 110 \rangle$, which had a distance larger than 22 nm. Assuming the above disorientation of crystallites (0.54°), the above Burgers vector of the screw dislocations ($a/2 \langle 110 \rangle$) and the vectors \vec{r} and $\vec{\ell}$ being perpendicular to each other, Eq. (5) yielded the distance between dislocations of 36 nm, which matches well with the mean size of the clusters in this particular sample. The last assumption that the vectors \vec{r} and $\vec{\ell}$ are perpendicular to each other means that the distance between dislocations is the real distance, no projection. It seems that each cluster contains typically a single screw dislocation. An issue for discussion is still the meaning of the individual partially coherent nanocrystallites, which build the nano-sized clusters. According to the experimental results, the partially coherent nanocrystallites are dislocation-free parts of the clusters that are mutually disoriented by the screw dislocations. As shown for instance in Refs. [53–55], XRD can only see the relatively undistorted core of the clusters, not the neighbourhood of dislocations or dislocation walls having an extremely high density

of microstructural defects. Therefore, the width of the regions that are strongly affected by the strain field of dislocations could be estimated from the difference between the cluster size and the sum of the crystallite sizes within individual clusters. For screw dislocations that are ideally located in the middle of the clusters, the total size of nanocrystallites per cluster would be equal to the double crystallite size. For the sample $\text{Cr}_{0.92}\text{Al}_{0.08}\text{N}$, the double crystallite size is equal to 22 nm, the size of the clusters 36 nm, thus the width of the regions that are strongly affected by the strain field of such dislocations is nearly 15 nm.

5. Conclusions

Microstructure analysis on Cr–Al–N and Cr–Al–Si–N coatings deposited using cathodic arc evaporation revealed information on their phase composition, stress-free lattice parameters, size of partially coherent nanocrystallites, their mutual disorientation in nano-sized clusters and the size of these clusters in dependence on the overall chemical composition of the coatings. In the Cr–Al–N system, a single fcc phase was stable between CrN and $\text{Cr}_{0.54}\text{Al}_{0.46}\text{N}$. Segregation of aluminium from the host structure of the fcc $\text{Cr}_{1-x}\text{Al}_x\text{N}$, which was accompanied by development of the hexagonal AlN, was observed at higher aluminium contents than $\text{Cr}_{0.54}\text{Al}_{0.46}\text{N}$. In the Cr–Al–Si–N system, the single fcc phase was stable between CrN and $\text{Cr}_{0.52}\text{Al}_{0.43}\text{Si}_{0.05}\text{N}$. At higher aluminium and silicon contents, aluminium and silicon escaped from $\text{Cr}_{1-x-y}\text{Al}_x\text{Si}_y\text{N}$. Consequently, hexagonal AlN and an amorphous phase were found. In the single-phase region, the stress-free lattice parameters were described by the function $a = [0.41486(2) - 0.00827(1) \cdot x + 0.034(1) \cdot y]$ nm, where x and y are the stoichiometric ratios of Al and Si in $\text{Cr}_{1-x-y}\text{Al}_x\text{Si}_y\text{N}$. Additional microstructural parameters were determined from the combination of XRD line broadening and TEM/HRTEM: the size of defect-free nanocrystallites, the mutual disorientation of partially coherent nanocrystallites, the size of clusters that are composed from partially coherent nanocrystallites, and the kind and distances of microstructural defects that split the clusters into the nanocrystallites.

Acknowledgements

The authors appreciate the financial support of the project # RA-1050/9 through the German Scientific Council (DFG). HRTEM Jeol 2010 FEF was purchased from the funds of the DFG Priority Programme # 1062.

References

- [1] E. Spain, J.C. Avelar-Batista, M. Letch, J. Housden, B. Lerga, Surf. Coat. Technol. 200 (2005) 1507.
- [2] C. Brecher, G. Spachtholz, K. Bobzin, E. Lugscheider, O. Knotek, M. Maes, Surf. Coat. Technol. 200 (2005) 1738.
- [3] H. Scheerer, T.H. Hoche, E. Broszeit, B. Schramm, E. Abele, C. Berger, Surf. Coat. Technol. 200 (2005) 203.
- [4] A. Sugishima, H. Kajioka, Y. Makino, Surf. Coat. Technol. 97 (1997) 590.
- [5] Y. Makino, K. Nogi, Surf. Coat. Technol. 98 (1998) 1008.
- [6] Y. Makino, Surf. Coat. Technol. 193 (2005) 185.
- [7] D. Rafaja, M. Dopita, M. Růžicka, V. Klemm, D. Heger, G. Schreiber, M. Šima, Surf. Coat. Technol. 201 (2006) 2835.

- [8] P.H. Mayrhofer, H. Willmann, C. Mitterer, *Surf. Coat. Technol.* 146–147 (2001) 222.
- [9] O. Banakh, P.E. Schmid, R. Sanjinés, F. Lévy, *Surf. Coat. Technol.* 163–164 (2003) 57.
- [10] M. Kawate, A.K. Hashimoto, T. Suzuki, *Surf. Coat. Technol.* 165 (2003) 163.
- [11] A.E. Reiter, V.H. Derflinger, B. Hanselmann, T. Bachmann, B. Sartory, *Surf. Coat. Technol.* 200 (2005) 2114.
- [12] S.R. Pulugurtha, D.G. Bhat, *Surf. Coat. Technol.* 201 (2006) 4411.
- [13] S. Veprek, S. Reiprich, *Thin Solid Films* 268 (1995) 64.
- [14] S. Veprek, A.S. Argon, *Surf. Coat. Technol.* 146147 (2001) 175.
- [15] S. Veprek, M.G.J. Veprek-Heijman, *Surf. Coat. Technol.* 201 (2007) 6064.
- [16] S. Veprek, A.S. Argon, *J. Vac. Sci. Technol., B* 20 (2002) 650.
- [17] J. Musil, *Surf. Coat. Technol.* 125 (2000) 322.
- [18] H.S. Myung, H.M. Lee, L.R. Shaginyan, J.G. Han, *Surf. Coat. Technol.* 163–164 (2003) 591.
- [19] P.H. Mayrhofer, G. Tischler, C. Mitterer, *Surf. Coat. Technol.* 142–144 (2001) 78.
- [20] I.-W. Park, D.S. Kang, J.J. Moore, S.C. Kwon, J.J. Rha, K.H. Kim, *Surf. Coat. Technol.* 201 (2006) 5223.
- [21] S. Veprek, *J. Vac. Sci. Technol., A, Vac. Surf. Films* 17 (1999) 2401.
- [22] A. Hörling, J. Sjöln, L. Karlsson, M. Odén, L. Hultman, *J. Vac. Sci. Technol., A, Vac. Surf. Films* 20 (2002) 1815.
- [23] P.H. Mayrhofer, A. Hörling, L. Karlsson, J. Sjöln, T. Larsson, C. Mitterer, L. Hultman, *Appl. Phys. Lett.* 83 (10) (2003) 2049.
- [24] M. Parlinska-Wojtan, A. Karimi, O. Coddet, T. Cselle, M. Morstein, *Surf. Coat. Technol.* 188–189 (2004) 344.
- [25] S. Veprek, H.D. Männling, M. Jílek, P. Holubář, *Mater. Sci. Eng., A Struct. Mater.: Prop. Microstruct. Process.* 366 (2004) 202.
- [26] D. Rafaja, M. Šíma, V. Klemm, G. Schreiber, D. Heger, L. Havela, R. Kužel, *J. Alloys Compd.* 378 (2004) 107.
- [27] P.H. Mayrhofer, H. Clemens, C. Mitterer, *Z. Met.kd.* 96 (2005) 468.
- [28] A. Hörling, L. Hultman, M. Odén, J. Sjöln, L. Karlsson, *Surf. Coat. Technol.* 191 (2005) 384.
- [29] S. Hao, B. Delley, C. Stampfl, *Phys. Rev. B* 74 (2006) 035402.
- [30] S. Hao, B. Delley, C. Stampfl, *Phys. Rev. B* 74 (2006) 035424.
- [31] D. Rafaja, A. Poklad, V. Klemm, G. Schreiber, D. Heger, M. Šíma, M. Dopita, *Thin Solid Films* 514 (2006) 240.
- [32] D. Rafaja, V. Klemm, G. Schreiber, M. Knapp, R. Kužel, *J. Appl. Crystallogr.* 37 (2004) 613.
- [33] D. Rafaja, V. Klemm, M. Dopita: Practical aspects of partial coherence of nanocrystalline domains, *CPD Newsletter* 34 (2006), Commission on Powder Diffraction, International Union of Crystallography, <http://www.mpi-stuttgart.mpg.de/cpd/html/newsletter.html>, in press.
- [34] D. Mercs, N. Bonasso, S. Naamane, J.-M. Bordes, C. Coddet, *Surf. Coat. Technol.* 200 (2005) 403.
- [35] P.H. Mayrhofer, C. Mitterer, L. Hultman, H. Clemens, *Prog. Mater. Sci.* 51 (2006) 1032.
- [36] P.H. Mayrhofer, D. Music, J.M. Schneider, *J. Appl. Phys.* 100 (2006) 094906.
- [37] J. Neidhardt, Z. Czigany, B. Sartory, R. Tessedri, M. O'Sullivan, C. Mitterer, *Acta Mater.* 54 (2006) 4193.
- [38] J. Neidhardt, M. O'Sullivan, A.E. Reiter, W. Rechberger, W. Grogger, C. Mitterer, *Surf. Coat. Technol.* 201 (2006) 2553.
- [39] P. Holubář, M. Jílek, M. Šíma, *Surf. Coat. Technol.* 133–134 (2000) 145.
- [40] D. Rafaja, A. Poklad, G. Schreiber, V. Klemm, D. Heger, M. Šíma, *Z. Met.kd.* 96 (2005) 736.
- [41] W. Mayr, W. Lengauer, P. Ettmayer, D. Rafaja, J. Bauer, M. Bohn, *J. Phase Equilib.* 20 (1) (1999) 35.
- [42] C.S. Sandu, R. Sanjinés, M. Benkahoul, F. Medjani, F. Lévy, *Surf. Coat. Technol.* 201 (2006) 4083.
- [43] W.C. Oliver, G.M. Pharr, *J. Mater. Res.* 7 (4) (1992) 1564.
- [44] J. Musil, F. Kunc, H. Zeman, H. Poláková, *Surf. Coat. Technol.* 154 (2002) 304.
- [45] A. Reuss, *Z. Angew. Math. Mech.* 9 (1929) 49.
- [46] H. Neerfeld, *Mitt. Kaiser-Wilhelm-Inst. Eisenforsch. Düsseld.* 24 (1942) 61.
- [47] E. Kröner, *Z. Phys.* 151 (1958) 504.
- [48] R.W. Vook, F. Witt, *J. Appl. Phys.* 36 (1965) 2169.
- [49] See, e.g., I.C. Noyan, J.B. Cohen: *Residual stresses, measurement by diffraction and interpretation*, Springer, New York, 1987.
- [50] *Inorganic Crystal Structure Database, ICSD on CD-ROM, Version 1.4.1, FIZ Karlsruhe*, 2006.
- [51] G.K. Williamson, W.H. Hall, *Acta Metall.* 1 (1953) 22.
- [52] See, e.g., M.A. Krivoglaz, *X-ray and neutron diffraction in nonideal crystals*, Springer, Berlin, Heidelberg, 1996.
- [53] H. Mughrabi, *Acta Metall.* 31 (1983) 1367.
- [54] R.E. Bolmaro, H.G. Brokmeier, J.W. Signorelli, A. Fourtz, M.A. Bertinetti, in: E.J. Mittemeijer, P. Scardi (Eds.), *Diffraction Analysis of the Microstructure of Materials*, Springer, Berlin, 2004, p. 391.
- [55] T. Ungár, G. Tichy, J. Gubicza, R.J. Hellmig, *Powder Diffr.* 20 (2005) 366.
- [56] F.C. Frank, *Report on the Symposium on Plastic Deformation of Crystalline Solids*, Carnegie Institute of Technology and Office of Naval Research, U.S. Government Printing Office, Washington, 1950, p. 150.
- [57] See, e.g., G. Gottstein, *Physical foundations of materials science*, Springer, Berlin, Heidelberg, 2004.
- [58] D.B. Williams, C.B. Carter, *Transmission Electron Microscopy III — Imaging*, Plenum Press, New York, 1996.
- [59] P.H. Mayrhofer, D. Music, J.M. Schneider, *Appl. Phys. Lett.* 88 (2006) 071922.
- [60] K. Ichijo, H. Hasegawa, T. Suzuki, *Surf. Coat. Technol.* 201 (2007) 5477.
- [61] H. Willmann, P.H. Mayrhofer, P.O.Å. Persson, A.E. Reiter, L. Hultman, C. Mitterer, *Scripta Mater.* 54 (2006) 1847.
- [62] K. Yamamoto, S. Kujime, K. Takahara, *Surf. Coat. Technol.* 200 (2005) 1383.

Chapter 6

Rafaja D., Poklad A., Klemm V., Schreiber G., Heger D., Šíma M., Dopita M.,
*Some consequences of the partial crystallographic coherence between
nanocrystalline domains in Ti-Al-N and Ti-Al-Si-N coatings,*
Thin Solid Films, **514**, (2006), 240-249.

Some consequences of the partial crystallographic coherence between nanocrystalline domains in Ti–Al–N and Ti–Al–Si–N coatings

D. Rafaja^{a,*}, A. Poklad^a, V. Klemm^a, G. Schreiber^a, D. Heger^a, M. Šíma^b, M. Dopita^c

^a Institute of Materials Science, TU Bergakademie Freiberg, Gustav-Zeuner-Str. 5, D-09599 Freiberg, Germany

^b SHM Ltd., Průmyslová 3, CZ-787 01 Šumperk, Czech Republic

^c Department of Electronic Structures, Faculty of Mathematics and Physics, Charles University, Ke Karlovu 5, CZ-121 16 Prague, Czech Republic

Received 4 October 2005; received in revised form 20 February 2006; accepted 20 February 2006

Available online 19 April 2006

Abstract

Formation of partially coherent nanocrystalline domains, development of intrinsic residual stresses and the relationship between the partial coherence of crystallites and the hardness of vacuum-arc-deposited Ti–Al–N and Ti–Al–Si–N nanocomposites were investigated for different chemical compositions of the nanocomposites using a combination of the electron probe microanalysis, X-ray diffraction, transmission electron microscopy with high resolution and hardness measurement. Partial coherence of nanocrystalline domains was found to be a very important microstructural feature, which is strongly related to the correlated orientation of neighbouring crystallites and to the atomic ordering at the crystallite boundaries. Appropriate mutual orientation of neighbouring crystallites and suitable atomic ordering at the crystallite boundaries facilitate the development of intrinsic residual stresses, which influence directly the hardness of the nanocomposites.

© 2006 Elsevier B.V. All rights reserved.

Keywords: Transmission electron microscopy; Nanostructures; X-ray diffraction; Hardness; Nitrides

1. Introduction

Nanocomposite coatings were proposed by Veprek et al. [1] about 10 years ago as novel promising super-hard materials. According to the Hall–Petch relationship [2,3], high density of grain boundaries was considered as the main reason for the extremely high hardness of these nanocomposites [4]. The optimum crystallite size was found to be approximately 3 nm [5–7], which is analogous to the optimum individual layer thickness observed in super-hard superlattices [8,9]. The best performance of the nanocomposites shall be reached if the nanocrystallites are covered by one monolayer of an amorphous substance, e.g., a-Si₃N₄ or a-BN [7,10,11]. For machining applications, high toughness and good chemical stability at temperatures exceeding 1000 °C are required besides the high hardness [12–14]. Thermal stability of the super-hard nanocomposites was investigated comprehensively in the past [11,15–20]. These studies together with the considerations

about the thermodynamics of the related systems yielded that the nanocomposites can be formed during a spinodal decomposition of immiscible or thermodynamically unstable substances [19,21–24].

The properties of nanocomposites can be explained only with the aid of detailed microstructure analysis. Therefore, the analysis of the crystallite size is an obligatory procedure in the studies of super-hard nanocomposites. It is usually performed through the analysis of the X-ray diffraction (XRD) line broadening. However, standard procedures based on the classical kinematical diffraction theory can yield quite unreliable results. This problem was discussed in [6], for instance. One source of this discrepancy is the decomposition process in immiscible or thermodynamically unstable or metastable systems [25], which, in nanocomposites, causes a partial coherence of neighbouring crystallites for X-ray diffraction [26]. This “crystallographic” coherence was described in [27] by a partial overlap of reciprocal lattice points for crystallites smaller than approximately 10 nm that causes a “narrowing” of XRD lines in nanocrystalline materials. Recently, our results on the partial coherence of crystallites [27] were supported by

* Corresponding author. Tel.: +49 3731 39 2299.

E-mail address: rafaja@ww.tu-freiberg.de (D. Rafaja).

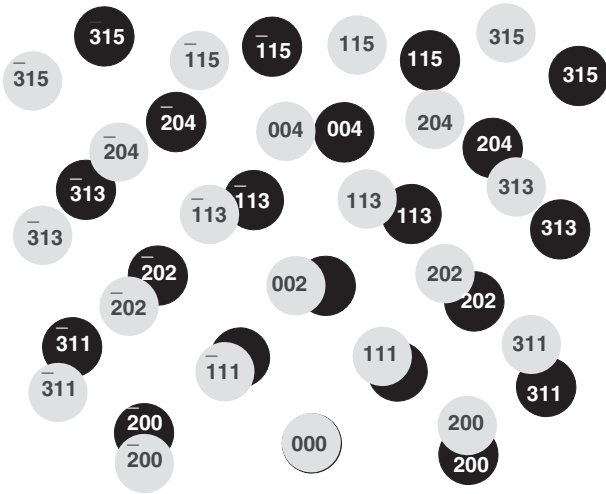


Fig. 1. Reciprocal lattice points of two mutually disoriented fcc crystallites (gray and black circles) projected into the x - y plane in the reciprocal space. The overlap of the reciprocal lattice points represents the degree of the partial coherence of the crystallites [27]. Numbers inside the circles are the diffraction indices.

Ribárik et al. [28] with results obtained on nanocrystalline powders.

In [27], we have shown that the “narrowing” of diffraction lines depends on the size of the diffraction vector, and thus on the diffraction angle, and on the mutual disorientation of crystallites having the same crystal structure. Most affected are diffraction lines measured at small diffraction angles. With increasing diffraction angle, the overlap of the reciprocal lattice points and thus the degree of the partial coherence of neighbouring crystallites decreases (Fig. 1). The diffraction lines broaden rapidly until the overlap of the reciprocal lattice points (the partial coherence of crystallites) disappears, which causes a rapid saturation of the diffraction line broadening. The saturated value of the line broadening corresponds to the true crystallite size [27]. The second parameter, which strongly influences the degree of the coherence of the neighbouring crystallites, is their mutual crystallographic orientation. The sharper the local texture, the smaller the disorientation of neighbouring crystallites and thus the stronger the effect of the partial coherence of crystallites on the XRD line broadening. In this contribution, we illustrate the relationship between the chemical composition of Ti–Al–N and Ti–Al–Si–N nanocomposites, their phase composition, crystallite size, global and local preferred orientation of crystallites, atomic ordering at the crystallite boundaries, partial coherence of neighbouring crystallites, amount of intrinsic residual stresses and hardness. The central issue of this contribution is discussion of the information contents of the partial coherence of crystallites.

2. Experimental details

Two series of samples were investigated in this study: one was based on the Ti–Al–N system and the second one on the Ti–Al–Si–N system. Each series consisted of seven samples

with different $[\text{Ti}]/([\text{Ti}]+[\text{Al}])$ or $[\text{Ti}]/([\text{Ti}]+[\text{Al}]+[\text{Si}])$ ratio. The samples were prepared by arc evaporation in nitrogen atmosphere with the working pressure of 1.3 Pa using two laterally rotating arc-cathodes (π -80 from PLATIT) [29]. The base pressure was 5×10^{-3} Pa and the deposition temperature 450 °C. One cathode consisted of titanium; the other was made either from aluminium (for the Ti–Al–N system) or from aluminium with addition of 11 at.% Si (for the Ti–Al–Si–N system). The ion current on the Ti cathode was 80 A and on the Al (or Al–Si) cathode 120 A. The bias voltage was -75 V. Variable stoichiometry of the coatings was achieved by different distances and angles between the substrates and the respective cathode [30]. Another consequence of the variable distance and variable angle between the substrates and the respective cathode was a variation in the thickness of the thin films, see Table 1. Polished plates of cemented carbide were used as substrates as usual for coatings considered for high-temperature applications. In contrast to commercial coatings, where the substrates are typically rotated in the deposition process, our substrates were not rotated during the deposition in order to be able to correlate the local and the global preferred orientation of crystallites to each other that is necessary for explanation of the coherence phenomena in these coatings.

Chemical composition of the samples (Table 1) was determined using a combination of the electron probe microanalysis with wavelength-dispersive spectroscopy (EPMA/WDS) and the glow-discharge optical emission spectroscopy (GDOES). The chemical analysis using EPMA/WDS was performed in 40 points across each sample to inspect the lateral homogeneity of the chemical composition. The maximum deviation in the concentration of Ti, Al and Si calculated over these 40 points was below 2 at.% in all samples. GDOES was primarily used to measure the nitrogen contents in the coatings, which cannot be achieved using EPMA/WDS with a sufficient reliability because of the overlap of the spectral line $K\alpha_1$ of nitrogen with the L1-line of titanium.

Microstructure of the samples was investigated using a combination of X-ray diffraction (XRD) and transmission electron microscopy with high resolution (HRTEM). HRTEM was performed with a 200 kV analytical high-resolution transmission electron microscope JEM 2010 FEF (Jeol) equipped by ultra-high-resolution objective lens ($C_s=0.5$ mm) and in-column energy filter to select only the elastic electrons

Table 1

Overall chemical composition, obtained from EPMA/WDS and GDOES, and thickness of the Ti–Al–N and Ti–Al–Si–N thin films under study

Chemical composition	Thickness (μm)	Chemical composition	Thickness (μm)
Ti _{0.96} Al _{0.04} N	2.7	Ti _{0.96} Al _{0.04} N	2.9
Ti _{0.85} Al _{0.15} N	4.7	Ti _{0.85} Al _{0.14} Si _{0.01} N	5.1
Ti _{0.73} Al _{0.27} N	5.8	Ti _{0.72} Al _{0.26} Si _{0.03} N	6.3
Ti _{0.52} Al _{0.48} N	6.1	Ti _{0.53} Al _{0.42} Si _{0.05} N	7.0
Ti _{0.38} Al _{0.62} N	5.5	Ti _{0.40} Al _{0.53} Si _{0.08} N	6.3
Ti _{0.17} Al _{0.83} N	5.2	Ti _{0.20} Al _{0.71} Si _{0.09} N	5.4
Ti _{0.09} Al _{0.91} N	3.7	Ti _{0.07} Al _{0.82} Si _{0.11} N	3.9

for the image recording. The specimens were prepared in the plane-view orientation. They were mechanically pre-thinned and etched by an ion beam. The final step in the specimen preparation was a plasma cleaning procedure. HRTEM was applied to visualize the distribution of the crystalline and amorphous phases in the coatings, the morphology of individual domains, the atomic ordering at the phase boundaries and the mutual orientations of neighbouring crystallites.

XRD was employed to obtain the phase composition of individual samples, the stress-free lattice parameters, the macroscopic deformation of the crystal lattice due to the residual stress, the average crystallite size, the preferred orientation of crystallites and the degree of the partial coherence of neighbouring crystallites. Most diffraction experiments were performed using glancing-angle X-ray diffraction (GAXRD) on a D8 diffractometer (Bruker AXS) equipped with a sealed X-ray tube with copper anode ($\lambda=0.15418\text{nm}$), with a Goebel mirror in the primary beam, and with a Soller collimator (divergence of 0.12°) and a flat LiF monochromator in the diffracted beam. Additional diffraction experiments were performed with synchrotron radiation at the wavelength of 0.11314nm (beamline B2 at HASYLAB/DESY). The synchrotron experiments were employed primarily to investigate the influence of the coherence length of the X-rays on the observed partial coherence of adjacent crystallites [27]. The angle of incidence of the primary beam was 3° in all GAXRD experiments (laboratory and synchrotron sources). Global preferred orientation of crystallites was concluded from pole figures taken on diffraction lines 111, 200 and 220 for the face-centered cubic phase, fcc-(Ti,Al)N, and on diffraction lines 100, 101, 110 and 102 for the hexagonal phase, h-AlN. The pole figure were measured at the Cu K_α radiation ($\lambda=0.15418\text{nm}$) on a diffractometer with Eulerian cradle (PTS from Seifert).

Hardness of the coatings was calculated from nanoindentation load–displacement data at a periodic loading and unloading of the samples at a successively increasing load [31]. The hardness was measured in 20 points per sample using the Nano Indenter XP from MTS equipped with a Berkovich indenter.

3. Results

3.1. Phase composition and stress-free lattice parameters

Results of GAXRD obtained on Ti–Al–N and Ti–Al–Si–N coatings confirmed limited solubility of aluminium in the NaCl-type host structure of TiN and negligible solubility of titanium in the Wurtzite-type host structure of AlN. In most samples under study, a mixture of fcc-(Ti,Al)N and h-AlN was found (Figs. 2 and 3). Diffraction maxima from substrate, especially those from h-WC that is the dominant phase in the substrate, became apparent in the diffraction patterns taken in samples with high aluminium contents. This is due to a much higher absorption of the Cu K_α radiation in TiN (with the linear absorption coefficient $\mu=876\text{cm}^{-1}$) than in $\text{Ti}_{0.06}\text{Al}_{0.82}\text{Si}_{0.12}\text{N}$ ($\mu=176\text{cm}^{-1}$). The penetration depths calculated according to [32] for these limiting chemical compositions and for the angle

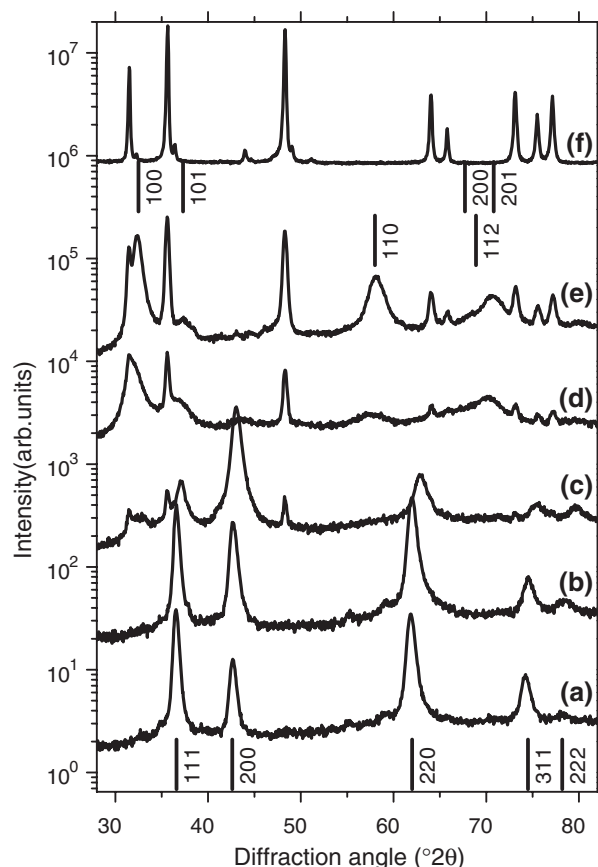


Fig. 2. Fragments of diffraction patterns of the nanocomposites with the overall chemical compositions $\text{Ti}_{0.85}\text{Al}_{0.15}\text{N}$ (a), $\text{Ti}_{0.73}\text{Al}_{0.27}\text{N}$ (b), $\text{Ti}_{0.38}\text{Al}_{0.62}\text{N}$ (c), $\text{Ti}_{0.17}\text{Al}_{0.83}\text{N}$ (d) and $\text{Ti}_{0.09}\text{Al}_{0.91}\text{N}$ (e). Diffraction lines from fcc-(Ti,Al)N are labelled by corresponding diffraction indices at the bottom, diffraction lines from h-AlN at the top of the figure. Figure (f) shows the corresponding part of the diffraction pattern taken on the virgin substrate.

of incidence of the primary beam of 3° are $0.6\mu\text{m}$ and $2.7\mu\text{m}$, respectively. The qualitative information on the phase composition must be obtained using the line profile analysis of the diffraction patterns as some diffraction lines were weak and overlapping each other.

The stress-free lattice parameters in the cubic phase a_0 shown in (Fig. 4) were calculated from the $\sin^2\psi$ -plot, i.e., from the linear dependence of the individual lattice parameters a_{ψ}^{hkl} on the function $\sin^2\psi$ (see [33], for instance), where ψ is the inclination of the diffraction vector from the normal direction.

$$a_0 = (a_{\parallel} - a_{\perp}) \frac{2\nu}{\nu + 1} + a_{\perp} \quad (1)$$

a_{\perp} and a_{\parallel} are the cubic lattice parameters perpendicular and parallel to the sample surface, which are directly obtained from the $\sin^2\psi$ -plot at $\sin^2\psi=0$ and $\sin^2\psi=1$, respectively. ν is the Poisson ratio of the cubic phase ($\nu=0.3$ [34]).

In the Ti–Al–N system, the stress-free lattice parameters in fcc- $\text{Ti}_{1-x}\text{Al}_x\text{N}$ decreased with increasing aluminium contents as anticipated (see, e.g., [35]). The calculated stress-free lattice parameters were compared with the anticipated Vegard-like dependence of the intrinsic lattice parameter on the overall

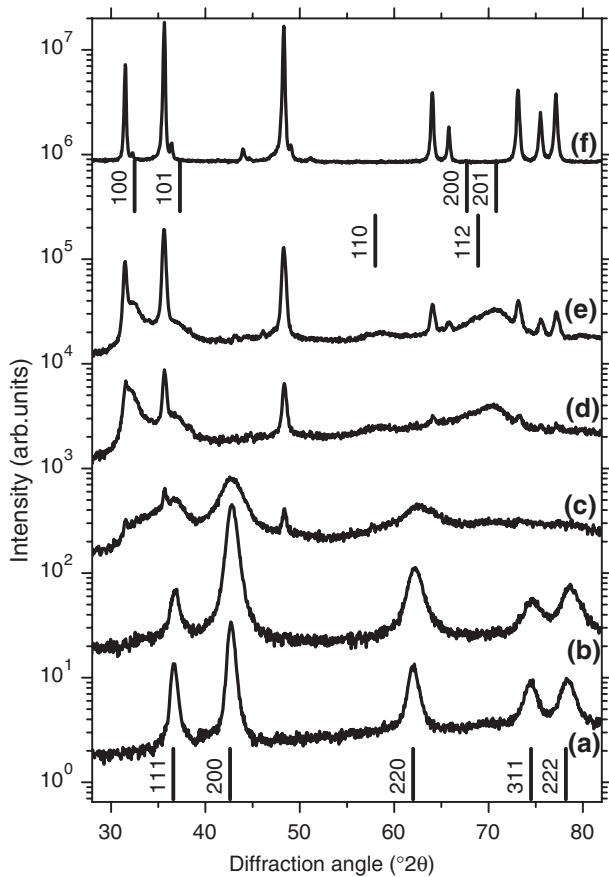


Fig. 3. Fragments of diffraction patterns of the nanocomposites with the overall chemical compositions $\text{Ti}_{0.85}\text{Al}_{0.14}\text{Si}_{0.01}\text{N}$ (a), $\text{Ti}_{0.72}\text{Al}_{0.26}\text{Si}_{0.03}\text{N}$ (b), $\text{Ti}_{0.40}\text{Al}_{0.53}\text{Si}_{0.08}\text{N}$ (c), $\text{Ti}_{0.20}\text{Al}_{0.71}\text{Si}_{0.09}\text{N}$ (d) and $\text{Ti}_{0.07}\text{Al}_{0.82}\text{Si}_{0.11}\text{N}$ (e). The bars at the top and at the bottom of the figure have the same meaning like in Fig. 2. A part of the diffraction pattern of the virgin substrate is shown in figure (f).

titanium contents in fcc-(Ti,Al)N, which is shown by the solid line in Fig. 4. The slope of the Vegard-like dependence was taken from Ref. [35], its intercept (the intrinsic lattice parameter of TiN) from the PDF-2 [36], because the data given in [35] are apparently afflicted by residual stress.

The lowest stress-free lattice parameter and thus the maximum aluminium contents in fcc-(Ti,Al)N was found in the sample with the overall chemical composition $\text{Ti}_{0.38}\text{Al}_{0.62}\text{N}$. The qualitative phase analysis of this sample (Fig. 2c) revealed that it consists of two crystalline phases, fcc-(Ti,Al)N and h-AlN. Therefore, some aluminium from the total aluminium contents measured using EPMA/WDS must also be contained in h-AlN and thus it must be missing in fcc-(Ti,Al)N. Consequently, fcc-(Ti,Al)N has higher titanium and lower aluminium contents, then it corresponds to the overall chemical composition of the individual samples obtained from EPMA/WDS and GDOES. The lower aluminium contents in fcc-(Ti,Al)N in comparison with the overall chemical composition results in a higher lattice parameter of this phase in comparison with the lattice parameter anticipated for the measured overall chemical composition as it can be seen in Fig. 4. In samples, where both phases are present, i.e., fcc-(Ti,Al)N and h-AlN, the departure of the stress-free lattice parameters from the anticipated Vegard-like dependence can be understood as a

measure of the degree of the decomposition of $\text{Ti}_{1-x}\text{Al}_x\text{N}$ into fcc-(Ti,Al)N and h-AlN.

In the Ti–Al–Si–N system, the stress-free lattice parameters were much higher than the anticipated values at the aluminium contents higher than $\text{Ti}_{0.72}\text{Al}_{0.26}\text{Si}_{0.03}\text{N}$. Still, the minimum lattice parameters and therefore the maximum aluminium contents in fcc-(Ti,Al)N was found in the sample with the overall chemical composition $\text{Ti}_{0.53}\text{Al}_{0.42}\text{Si}_{0.05}\text{N}$. In the sample with the overall chemical composition $\text{Ti}_{0.40}\text{Al}_{0.53}\text{Si}_{0.08}\text{N}$, the stress-free lattice parameters reached the intrinsic value for TiN ($a = 0.42418\text{ nm}$) [36], which indicates complete segregation of Ti, Al and Si into TiN, AlN and Si_3N_4 .

3.2. Macroscopic lattice deformation

The residual stress in super-hard nanocomposites is shown usually as an important parameter, which affects significantly the hardness of the coatings. In this study, macroscopic lattice deformation is given instead of the residual stress, because the Young moduli of individual phases, which are needed to recalculate the lattice deformations to the residual stress, can vary with the chemical composition and microstructure of the coatings, and cannot be obtained experimentally. In nanocomposites, the experimental methods, e.g., nanoindentation, yield just an averaged Young modulus. Thus, the macroscopic lattice deformation is the only reliable quantity that can be obtained from the XRD data for all crystalline phases contained in the samples. The maximum macroscopic lattice deformation (ϵ_{\perp}) in the cubic phase was calculated from a_{\parallel} and a_{\perp} obtained from the $\sin^2\psi$ -plot and from a_0 obtained from Eq. (1)

$$\epsilon_{\perp} = \frac{a_{\parallel} - a_{\perp}}{2a_0} \quad (2)$$

In GAXRD experiments, the individual lattice parameters, a_{ψ}^{hkl} , are typically measured on different lattice planes. Thus, the anisotropy of elastic constants causes a fan-like distribution of

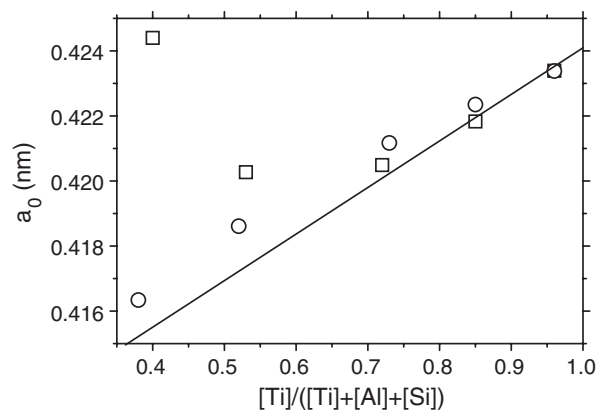


Fig. 4. Dependence of the stress-free lattice parameters of the fcc-(Ti,Al)N phase, a_0 , on the titanium stoichiometry ratio in $\text{Ti}_{1-x}\text{Al}_x\text{N}$ (○) and $\text{Ti}_{1-x-y}\text{Al}_x\text{Si}_y\text{N}$ (□) nanocomposites. a_0 was obtained from GAXRD, $[\text{Ti}]/([\text{Ti}]+[\text{Al}]+[\text{Si}])$ from EPMA/WDS and GDOES. Standard deviations of the stress-free lattice parameters are smaller than the size of the symbols. Solid line shows the anticipated Vegard-like dependence (see text).

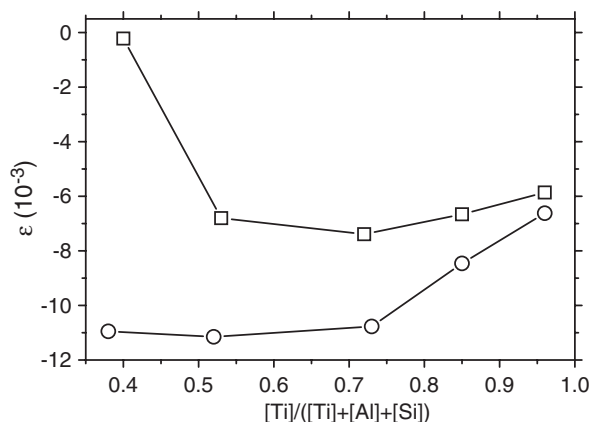


Fig. 5. Dependence of the macroscopic lattice deformation in the fcc-(Ti,Al)N phase on the titanium stoichiometry ratio in $Ti_{1-x}Al_xN$ (O) and $Ti_{1-x-y}Al_xSi_yN$ (□) nanocomposites. The standard deviations are comparable with the size of the symbols.

the individual lattice parameters [32]. To separate the influence of the elastic anisotropy on the calculated lattice deformation, the scattering of the individual lattice parameters was corrected using the routine described in [32].

The dependence of the macroscopic lattice deformation on the overall titanium contents in individual samples is shown for both series of samples in Fig. 5. The lattice deformation is substantially larger in the silicon-free samples than in the samples with silicon. In the Ti–Al–N system, the macroscopic lattice deformation is a monotonous function of the titanium contents up to $Ti_{0.38}Al_{0.62}N$. In the Ti–Al–Si–N system, the macroscopic lattice deformation has a similar functional dependence on the overall titanium contents like the corresponding stress-free lattice parameter (compare Figs. 4 and 5). The decomposition of Ti–Al–Si–N into fcc-(Ti,Al)N, h-AlN and a-Si₃N₄, which was indicated by the large departure of the stress-free lattice parameter from the anticipated Vegard-like dependence (Fig. 4), is related to a

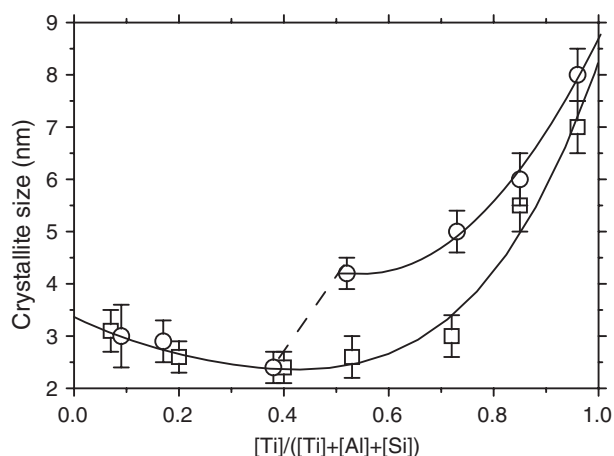


Fig. 6. Dependence of the crystallite size on the stoichiometry ratio of titanium in $Ti_{1-x}Al_xN$ (O) and $Ti_{1-x-y}Al_xSi_yN$ (□) nanocomposites. The crystallite size refers to the dominant phase in the samples, which is the fcc-(Ti,Al)N for $[Ti]/([Ti]+[Al]+[Si]) > 0.3$ and h-AlN for $[Ti]/([Ti]+[Al]+[Si]) < 0.3$. Lines are guides for eye.

relaxation of the macroscopic lattice deformation in the cubic phase (Fig. 5). In the sample $Ti_{0.40}Al_{0.53}Si_{0.08}N$, in which Ti, Al and Si were completely separated into TiN, AlN and a-Si₃N₄, the macroscopic deformation of the cubic lattice disappeared.

Macroscopic lattice deformation in the hexagonal phase was measured in the aluminium-rich samples, in which h-AlN was the dominant phase. The experimental values were -37×10^{-3} and -32×10^{-3} for the samples with the overall chemical composition of $Ti_{0.20}Al_{0.71}Si_{0.09}N$ and $Ti_{0.07}Al_{0.82}Si_{0.11}N$, respectively. The higher macroscopic lattice deformation in the hexagonal phase, as compared to the fcc phase, is due to its lower Young modulus. The macroscopic lattice deformation (ε_{\perp}) in the hexagonal phase was obtained from the linear dependence of the lattice deformation ε_{ψ}^{hkl} on $\sin^2\psi$.

$$\varepsilon_{\psi}^{hkl} = \frac{d_{\psi}^{hkl} - d_0^{hkl}}{d_0^{hkl}} = (\varepsilon_{\parallel} - \varepsilon_{\perp}) \sin^2\psi + \varepsilon_{\perp} \quad (3)$$

d_{ψ}^{hkl} and d_0^{hkl} are the measured and the stress-free interplanar distances, respectively. The intrinsic interplanar distances for h-AlN were taken from the PDF-2 [36]. Such a calculation of the lattice deformation is only possible for phases, in which the lattice parameters or the interplanar distances do not depend on the composition. This is true for h-AlN, which is a phase with extremely narrow homogeneity range.

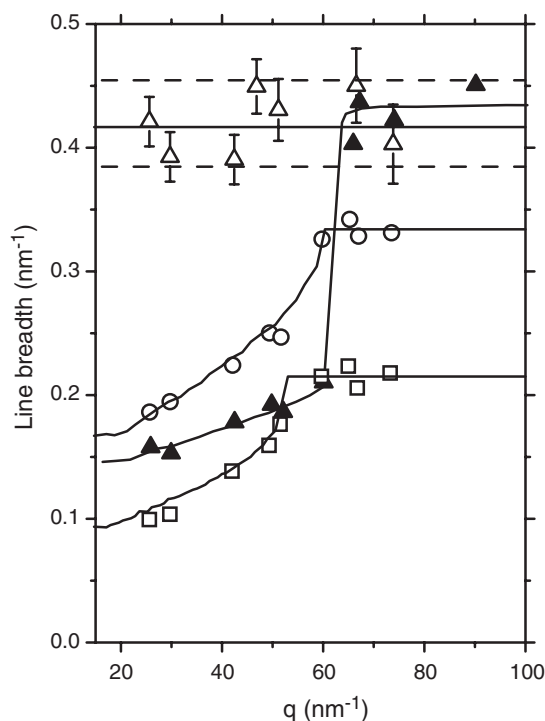


Fig. 7. Dependence of the XRD line broadening in the fcc phase on the size of the diffraction vector ($q=4\pi \sin \theta/\lambda$) as observed in the samples $Ti_{0.85}Al_{0.14}Si_{0.01}N$ (□), $Ti_{0.72}Al_{0.26}Si_{0.03}N$ (O), $Ti_{0.40}Al_{0.53}Si_{0.08}N$ (Δ) and $Ti_{0.38}Al_{0.62}N$ (▲). The last sample was measured using the synchrotron radiation. Solid lines show the dependence of the line broadening on the diffraction vector calculated according to Ref. [27]. Dashed lines show the maximum spread of the line breadths, which causes the experimental error in the crystallite size of ± 0.2 nm.

3.3. Atomic model of the Ti–Al–N and Ti–Al–Si–N nanocomposites

Average crystallite size and the degree of the partial coherence of neighbouring crystallites were determined from the dependence of the XRD line broadening on the size of the diffraction vector using the approach [27], which takes the partial coherence of crystallites into account. In all samples under study, the crystallite size was below 8 nm and decreased with increasing aluminium contents up to $[\text{Ti}]/([\text{Ti}]+[\text{Al}]+[\text{Si}]) \approx 0.4$ (Fig. 6). In the samples with $[\text{Ti}]/([\text{Ti}]+[\text{Al}]+[\text{Si}]) < 0.4$, in which h-AlN dominates, the crystallite size slightly increased with increasing aluminium contents. In the Ti–Al–N system, cubic crystallites were partially coherent in all samples. In the Ti–Al–Si–N system, cubic crystallites were partially coherent only up to the sample composition of $\text{Ti}_{0.53}\text{Al}_{0.42}\text{Si}_{0.05}\text{N}$. For higher silicon (and aluminium) contents, the crystallites are non-coherent as follows from the constant XRD line broadening observed for the sample $\text{Ti}_{0.40}\text{Al}_{0.53}\text{Si}_{0.08}\text{N}$ (Fig. 7). The comparison of both series of samples (with and without silicon), and particularly the comparison of the samples $\text{Ti}_{0.38}\text{Al}_{0.62}\text{N}$ and $\text{Ti}_{0.40}\text{Al}_{0.53}\text{Si}_{0.08}\text{N}$, clearly shows that high silicon content in the coatings hinders the mutual coherence of crystallites.

A requirement for the partial coherence of crystallites is their strong local preferred orientation (see Ref. [27] and Fig. 1).

Pronounced global texture in these Ti–Al–N and Ti–Al–Si–N nanocomposites was confirmed recently [30]. Cubic crystallites in the samples with the highest titanium contents were $\langle 111 \rangle$ -oriented perpendicularly to the sample surface (Fig. 8a,b). With increasing aluminium contents, the crystallographic direction $\langle 111 \rangle$ inclined towards the sample surface (Fig. 8c,d). In samples with $[\text{Ti}]/([\text{Ti}]+[\text{Al}]+[\text{Si}]) \approx 0.5$, the crystallographic direction $\langle 001 \rangle$ in cubic crystallites and the crystallographic direction $\langle 110 \rangle$ in hexagonal crystallites were nearly perpendicular to the sample surface (Fig. 9). In samples containing silicon, the inclination of the preferred oriented crystallographic direction $\langle 111 \rangle$ from the normal direction is similar like in the samples without Si [30]. However, the silicon contained in the samples influences strongly the development of in-plane texture. In silicon-free samples, the crystallites were preferentially oriented in the plane of the coatings, which can be seen from the inconstant angular intensity distribution in the pole figures (Figs. 8 and 9). From the pole figures taken in the fcc-(Ti,Al)N and h-AlN phases at the same macroscopic orientation of the sample (Fig. 9), we could conclude that the projections of the $\langle 111 \rangle$ direction in fcc-(Ti,Al)N into the lateral direction is parallel to the projection of the $\langle 100 \rangle$ direction in h-AlN. As the $\langle 111 \rangle$ direction in fcc-(Ti,Al)N is nearly perpendicular to the sample surface, the directions $\langle 100 \rangle$ and $\langle 010 \rangle$ are lying in the plane of the sample. In h-AlN, the preferred crystallographic

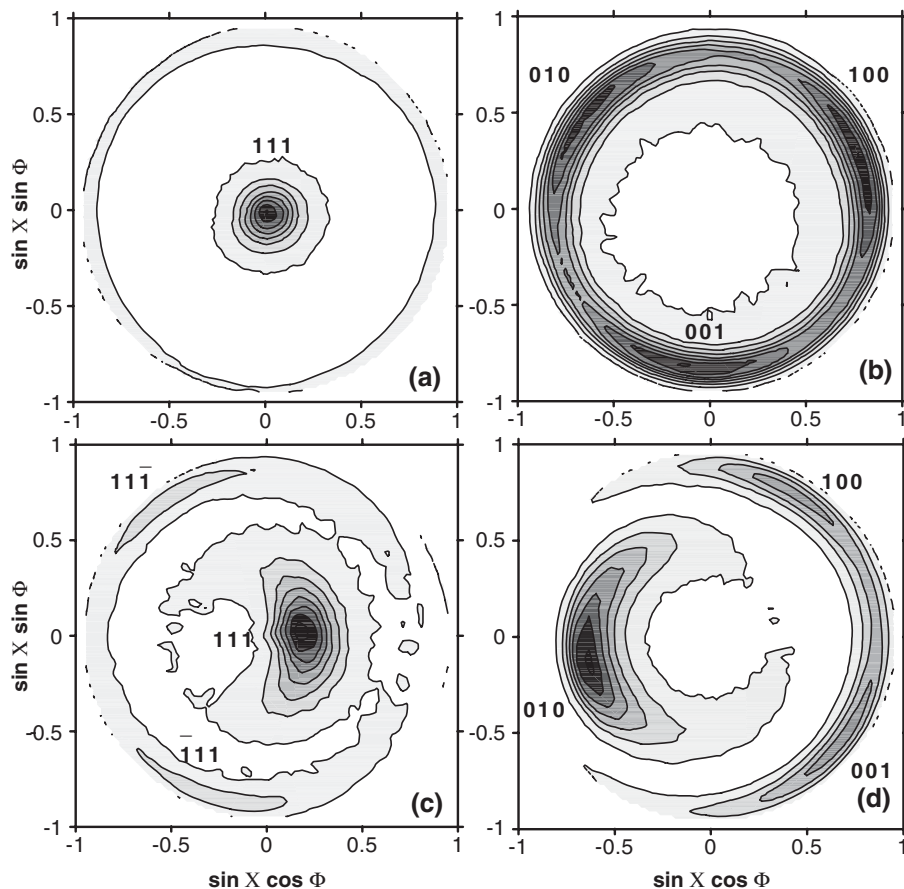


Fig. 8. Pole figures (111) and (001) measured for fcc-(Ti,Al)N in the samples $\text{Ti}_{0.96}\text{Al}_{0.04}\text{N}$ (a, b) and $\text{Ti}_{0.73}\text{Al}_{0.27}\text{N}$ (c, d). X is the inclination of the sample from the coplanar geometry and ϕ the rotation around the normal direction. Diffraction indices label the poles that are related to the observed intensity maxima.

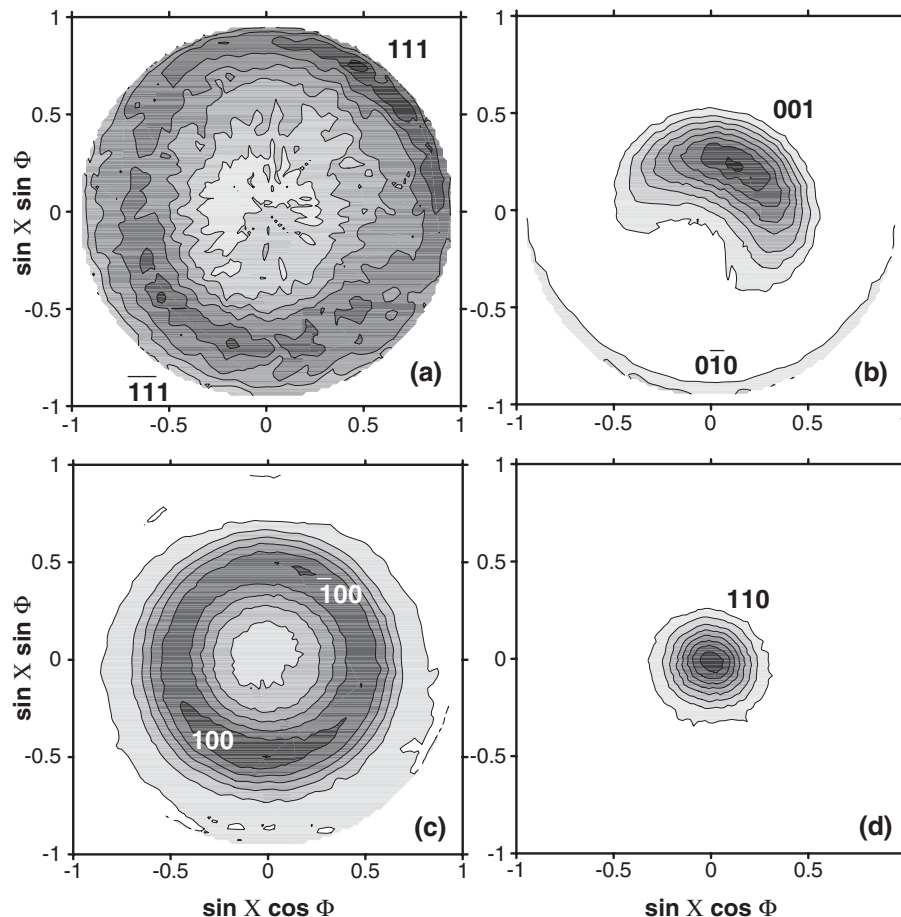


Fig. 9. Pole figures (111) (a) and (001) (b) measured for fcc-(Ti,Al)N and pole figures (100) (c) and (110) (d) measured for h-AlN in the sample $\text{Ti}_{0.52}\text{Al}_{0.48}\text{N}$. The meaning of the symbols (X , Φ , diffraction indices) is as for Fig. 8.

direction perpendicular to the sample surface is $\langle 110 \rangle$. The directions $\langle 001 \rangle$ and $\langle 1\bar{1}0 \rangle$ in h-AlN are consequently lying in the plane of the sample. The mutual in-plane orientation of the cubic and hexagonal crystallites can finally be concluded from the projections of the $\langle 111 \rangle$ and $\langle 1\bar{1}0 \rangle$ directions in fcc-(Ti,Al)N and h-AlN, respectively. The projection of the $\langle 111 \rangle$ direction in the cubic structure into the plane of the sample takes the angle of approximately 45° with both $\langle 010 \rangle$ and $\langle 100 \rangle$ directions (a slight deviation from 45° is due to the slight inclination of the $\langle 001 \rangle$ direction from the sample surface perpendicular direction), whereas the projection of $\langle 1\bar{1}0 \rangle$ direction in the hexagonal structure into the plane of the samples is parallel to the $\langle 1\bar{1}0 \rangle$ direction. Thus, the $\langle 001 \rangle$ direction in h-AlN takes the angle of approximately 45° with the $\langle 100 \rangle$ direction in fcc-(Ti,Al)N. Crystallites in the Ti–Al–Si–N samples did not exhibit such in-plane preferential orientation [30].

The development of the local preferential orientation of crystallites in the plane of the coatings, that is needed for the partial coherence of crystallites, was explained by a combination of GAXRD, pole figure measurements and HRTEM (Fig. 10). The in-plane orientation of crystallites of one phase (cubic or hexagonal) can be transferred over the crystallites of the other phase, if the crystalline phases are in a direct contact

and if the projections of the interplanar spacings of both adjacent crystalline phases to the phase boundary are similar. The atomic model of the interface between fcc-(Ti,Al)N and h-AlN shown in Fig. 11 was constructed from the HRTEM micrograph (Fig. 10) and from the pole figures (see above) using the phase composition (presence of fcc-(Ti,Al)N and h-AlN) and the stress-free lattice parameters obtained from GAXRD. The pole figure measurements, in particular, confirmed a strong preferred orientation of crystallites in the out-of-plane direction (Fig. 9b and d) in both crystalline phases, fcc-(Ti,Al)N and h-AlN, and showed the mutual orientation of the cubic and hexagonal crystallites (Fig. 9a and c) as explained above. The local texture, which is related to the disorientation of adjacent crystallites, is much stronger than the global texture as confirmed by the simulation of the dependence of the line broadening on the size of the diffraction vector [27] in Fig. 7. Amorphous regions (see the example in Fig. 12) blocks the transfer of the correlated crystallographic orientation between neighbouring crystallites that hinders the development of the in-plane texture and reduces substantially the degree of the partial coherence of neighbouring cubic crystallites (Fig. 7) in the Ti–Al–Si–N system. A very similar microstructure of the Ti–Al–Si–N coatings was shown in [37].

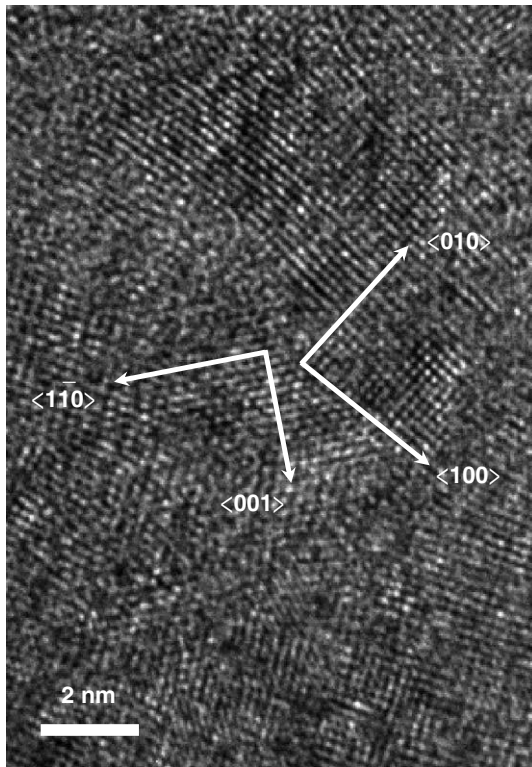


Fig. 10. HRTEM micrograph of the interface between h-AlN (left) and fcc-(Ti, Al)N (right) in the sample $\text{Ti}_{0.52}\text{Al}_{0.48}\text{N}$. Arrows show the crystallographic directions lying in the plane of the coating. The directions perpendicular to the plane of the film are $\langle 110 \rangle$ and $\langle 001 \rangle$ in h-AlN and fcc-(Ti, Al)N, respectively.

3.4. Hardness

Hardness of the Ti–Al–N and Ti–Al–Si–N nanocomposites increases with decreasing crystallite size up to approximately 3.5 nm and decreases in smaller crystallites (Fig. 13). In coatings with partially coherent cubic crystallites, the hardness follows the same functional dependence on the crystallite size

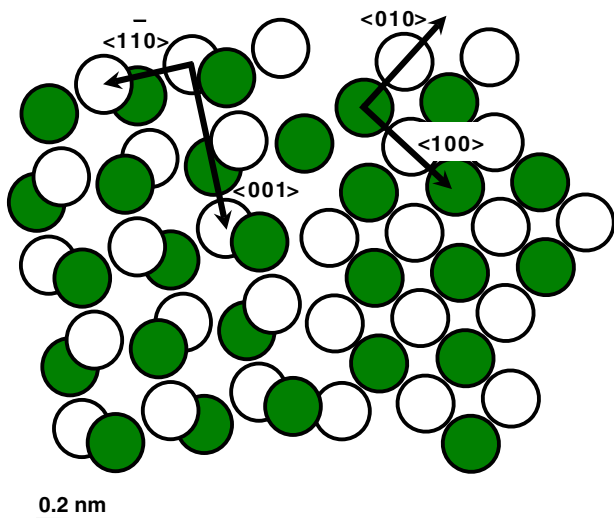


Fig. 11. Model of the atomic ordering at the interface between h-AlN (left) and fcc-(Ti, Al)N (right) shown in Fig. 10. White circles represent Al (left) and Ti (right) atoms; grey circles nitrogen.

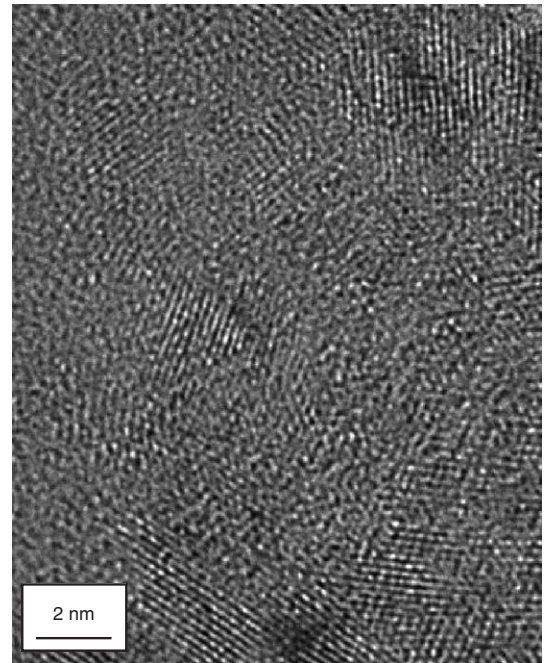


Fig. 12. HRTEM micrograph of the sample $\text{Ti}_{0.40}\text{Al}_{0.53}\text{Si}_{0.08}\text{N}$ shows crystalline domains surrounded by amorphous phase.

for both systems, Ti–Al–N and Ti–Al–Si–N, although the phase compositions, the Young moduli and the macroscopic lattice deformations differ generally in the samples with and without silicon. Particularly, the effect of the lattice deformation on the hardness is illustrated by different hardness of two samples (○#1 and □#1 in Fig. 13), which have practically the same chemical composition, $\text{Ti}_{0.96}\text{Al}_{0.04}\text{N}$, but different macroscopic lattice deformation in the cubic phase (Fig. 5).

The difference in the hardness of the samples $\text{Ti}_{0.52}\text{Al}_{0.48}\text{N}$ (○#5) and $\text{Ti}_{0.53}\text{Al}_{0.42}\text{Si}_{0.05}\text{N}$ (□#5) has a similar origin. Whereas the fcc phase in the silicon-free sample ($\text{Ti}_{0.52}\text{Al}_{0.48}\text{N}$) is under a large compressive residual stress (Fig. 5), the cubic phase in the sample containing silicon ($\text{Ti}_{0.53}\text{Al}_{0.42}\text{Si}_{0.05}\text{N}$) is

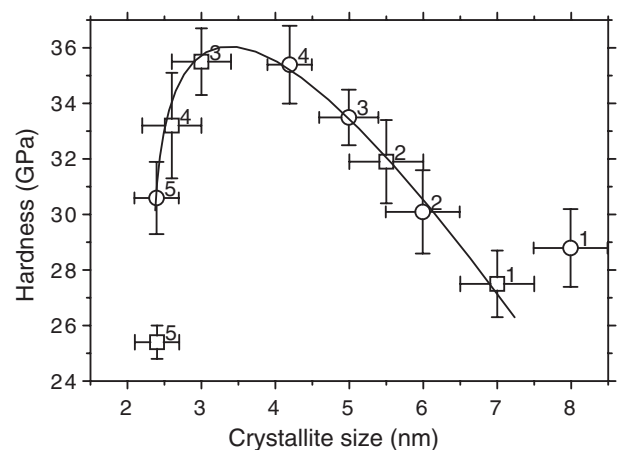


Fig. 13. Dependence of the hardness on the size of the fcc-(Ti, Al)N crystallites. The overall chemical compositions of the samples are $\text{Ti}_{0.96}\text{Al}_{0.04}\text{N}$ (○#1, □#1), $\text{Ti}_{0.85}\text{Al}_{0.15}\text{N}$ (○#2), $\text{Ti}_{0.85}\text{Al}_{0.14}\text{Si}_{0.01}\text{N}$ (□#2), $\text{Ti}_{0.73}\text{Al}_{0.27}\text{N}$ (○#3), $\text{Ti}_{0.72}\text{Al}_{0.26}\text{Si}_{0.03}\text{N}$ (□#3), $\text{Ti}_{0.52}\text{Al}_{0.48}\text{N}$ (○#4), $\text{Ti}_{0.53}\text{Al}_{0.42}\text{Si}_{0.05}\text{N}$ (□#4), $\text{Ti}_{0.38}\text{Al}_{0.62}\text{N}$ (○#5) and $\text{Ti}_{0.40}\text{Al}_{0.53}\text{Si}_{0.08}\text{N}$ (□#5).

completely relaxed and, according to the stress-free lattice parameter (Fig. 4), aluminium- and silicon-free. The different amount of the residual stress is related to the different degree of the partial coherence of the cubic crystallites. In samples with partially coherent cubic crystallites, the crystallites of the fcc-(Ti,Al)N and h-AlN phases are intertwined (Fig. 11), which is needed for the transfer of the in-plane crystallographic orientation in the coatings that is necessary for the partial coherence of cubic crystallites and that contributes concurrently to the development of the intrinsic lattice strain. The observed intrinsic lattice deformation that is related to the intrinsic lattice strain results from a mismatch of the interplanar spacings in both structures (fcc-(Ti,Al)N and h-AlN) if the crystallites have an appropriate mutual orientation (Figs. 9 and 11). In samples with non-coherent crystallites, the crystalline domains are separated by amorphous regions (see Fig. 12 and Ref. [37]), which can neither transfer the crystallographic orientation between adjacent crystallites nor assist in development of the intrinsic lattice deformation at crystallite boundaries.

4. Discussion

Combination of the phase analysis and the precise measurement of the stress-free lattice parameters in samples with different aluminium and silicon contents has shown differences between the Ti–Al–N and Ti–Al–Si–N systems. For the Ti–Al–N system, a substantially smaller lattice parameter and thus a larger maximum aluminium contents in the fcc-(Ti,Al)N phase were found than for the Ti–Al–Si–N system. This particular result might indicate a different phase stability of both systems under study. However, the comparison of the dependence of the stress-free lattice parameter on the overall chemical composition of the coatings with the dependence of the macroscopic lattice deformation on the overall chemical composition of the coatings has shown similarities in both systems. This comparison advised that the degree of the decomposition and the macroscopic lattice deformation are related to each other in both systems. In samples with higher macroscopic lattice deformation, the stress-free lattice parameter in fcc-(Ti,Al)N is lower and thus the aluminium content in this phase higher than in samples with lower macroscopic lattice deformation.

Our results confirmed that the crystallite size is a very important parameter that influence the hardness of nanocomposites. The maximum hardness was observed at the crystallite size of approximately 3.5 nm, which agrees with results of other authors [5–9]. The nanosized crystallites develop during decomposition of $\text{Ti}_{1-x}\text{Al}_x\text{N}$ or $\text{Ti}_{1-x-y}\text{Al}_x\text{Si}_y\text{N}$ into fcc-(Ti,Al)N, h-AlN and a- Si_3N_4 as reported in [19,21–24]. In samples without silicon as well as in samples with a low silicon contents, both crystalline phases, fcc-(Ti,Al)N and h-AlN, are in a direct contact and intertwined through the crystallographic planes with similar interplanar distances. The intertwining of nanocrystallites follows from their pronounced local preferred orientation, which was confirmed by the global texture (pole figures, XRD), by the partial coherence of cubic crystallites (line profile analysis, GAXRD) and by the ordering of individual atoms at

the crystallite boundaries (HRTEM). Consequently, intrinsic residual stresses formed at the crystallites boundaries as confirmed by large macroscopic lattice deformation (see Fig. 5). This can be illustrated on the sample with the overall chemical composition $\text{Ti}_{0.38}\text{Al}_{0.62}\text{N}$, which contains highly crystallographically coherent cubic crystallites that possess a high macroscopic lattice deformation.

In fcc-(Ti,Al)N, the distance between Ti (Al) and N atoms along the $\langle 100 \rangle$ and symmetrically equivalent directions ranges between 0.212 and 0.20825 nm (Fig. 11) for the lattice parameters between 0.424 and 0.4165 nm (Fig. 4). In h-AlN, the distances between Al and N atoms along the $\langle 001 \rangle$ direction are 0.189 nm and 0.309 nm. The shorter distances are more attractive for the correlated orientations of both crystal structures. The distances between Al and N atoms in h-AlN projected into the $\langle 1\bar{1}0 \rangle$ direction are 0.179 nm and 0.269 nm that are again the distances, to which the inter-atomic distances between Ti (Al) and N along the $\langle 100 \rangle$ direction in the fcc structure match roughly. Necessarily, the differences in the inter-atomic (and interplanar) distances between the cubic and the hexagonal phase lead to a development of intrinsic residual stresses that improves the hardness of the nanocomposites [16]. Appropriate mutual orientation of adjacent crystallites, which favours their partial coherence, plays a very important role in the development of the intrinsic residual stresses. Amorphous Si_3N_4 , which separates cubic and hexagonal crystallites in the silicon-rich Ti–Al–Si–N coatings, obstructs both the partial coherence and the development of the intrinsic residual stresses. This can be illustrated on the sample $\text{Ti}_{0.40}\text{Al}_{0.53}\text{Si}_{0.08}\text{N}$, in which no partial crystallographic coherence of cubic crystallites was observed and which had a nearly zero macroscopic lattice deformation.

5. Conclusions

Experimental results obtained on Ti–Al–N and Ti–Al–Si–N nanocomposites with the crystallite size below 8 nm have shown that formation of appropriately oriented and partially coherent crystallites supports the development of intrinsic residual stresses at the crystallites boundaries, which improve the hardness of the nanocomposites. The model of the atomic ordering at the crystallites boundaries was concluded from the combination of XRD and HRTEM experiments. It was shown that the partial coherence of nanocrystallites observed in the XRD experiments is an efficient tool for local texture analysis in nanocrystalline systems. Finally, a good correlation was found between the partial crystallographic coherence of cubic crystallites, their local preferred orientation, the mutual preferred orientation of cubic and hexagonal crystallites, the macroscopic lattice deformation in the cubic phase and the hardness of the Ti–Al–Si–N coatings.

Acknowledgements

The HRTEM JEM 2010 FEF was financed through Deutsche Forschungsgemeinschaft in frame of the Priority program # 1062. The financial support of this work due to the Grant

Agency of the Czech Republic (project # 106/03/0819) is highly acknowledged. We would like to thank Dr. T. Modes (FEP Dresden) for performing the hardness measurements.

References

- [1] S. Veprek, S. Reiprich, Li Shizhib, Appl. Phys. Lett. 66 (1995) 2640.
- [2] E.O. Hall, Proc. Phys. Soc., London, Sect. B 64 (1951) 747.
- [3] N.J. Petch, J. Iron Steel Inst. 174 (1953) 25.
- [4] S. Veprek, S. Reiprich, Thin Solid Films 268 (1995) 64.
- [5] S. Veprek, J. Vac. Sci. Technol., A 17 (1999) 2401.
- [6] A. Niederhofer, P. Nesládek, H.-D. Männling, K. Moto, S. Veprek, M. Jílek, Surf. Coat. Technol. 121 (1999) 173.
- [7] S. Veprek, A. Niederhofer, K. Moto, T. Bolom, H.-D. Männling, P. Nesládek, G. Dollinger, A. Bergmaier, Surf. Coat. Technol. 133 (2000) 152.
- [8] C.J. Tavares, L. Rebouta, E. Ribeiro, J.P. Riviere, J. Pacaud, M.F. Denanot, Surf. Coat. Technol. 174 (2003) 273.
- [9] S.Y. Lee, G.S. Kim, J.H. Hahn, Surf. Coat. Technol. 177 (2004) 426.
- [10] A. Niederhofer, T. Bolom, P. Nesládek, K. Moto, C. Eggs, D.S. Patil, S. Veprek, Surf. Coat. Technol. 146 (2001) 183.
- [11] P. Karvanková, M.G.J. Veprek-Heijman, O. Zindulka, A. Bergmaier, S. Veprek, Surf. Coat. Technol. 163 (2003) 149.
- [12] S. Zhang, D. Sun, Y.Q. Fu, J. Mater. Sci. Technol. 18 (2002) 485.
- [13] S. Zhang, D. Sun, Y.Q. Fu, H.J. Du, Surf. Coat. Technol. 167 (2003) 113.
- [14] H.Y. Zhao, Q.L. Fan, L.X. Song, E.W. Shi, X.F. Hu, J. Inorg. Mater. 19 (2004) 9.
- [15] H. Zeman, J. Musil, J. Vlček, P.H. Mayrhofer, C. Mitterer, Vacuum 72 (2003) 21.
- [16] S. Veprek, S. Mukherjee, P. Karvanková, H.D. Männling, J.L. He, K. Moto, J. Procházka, A.S. Argon, J. Vac. Sci. Technol., A 21 (2003) 532.
- [17] K. Moto, T. Bolom, S. Veprek, Adv. Mater. Process. II. Mat. Sci. Forum 437–4 (2003) 403.
- [18] M. Parlinska-Wojtan, A. Karimi, O. Coddet, T. Cselle, M. Morstein, Surf. Coat. Technol. 188 (2004) 344.
- [19] S. Veprek, H.-D. Männling, M. Jílek, Mater. Sci. Eng., A 366 (2004) 202.
- [20] S. Ma, J. Procházka, P. Karvanková, Q. Ma, X. Niu, X. Wang, D. Ma, K. Xu, S. Veprek, Surf. Coat. Technol. 194 (2005) 143.
- [21] H.-D. Männling, D.S. Patil, K. Moto, M. Jílek, S. Veprek, Surf. Coat. Technol. 146 (2001) 263.
- [22] F. Adibi, I. Petrov, L. Hultman, U. Wahlström, T. Shimizu, D. McIntyre, J.E. Greene, J.-E. Sundgren, J. Appl. Phys. 69 (1991) 6437.
- [23] A. Hörling, L. Hultman, M. Odén, J. Sjöln, L. Karlsson, J. Vac. Sci. Technol., A 20 (2002) 1815.
- [24] A. Hörling, L. Hultman, M. Odén, J. Sjöln, L. Karlsson, Surf. Coat. Technol. 191 (2005) 384.
- [25] O. Knotek, F. Löffler, L. Wolters, Surf. Coat. Technol. 8 (1994) 176.
- [26] D. Rafaja, M. Šíma, V. Klemm, G. Schreiber, D. Heger, L. Havela, R. Kužel, J. Alloys Compd. 378 (2004) 107.
- [27] D. Rafaja, V. Klemm, G. Schreiber, M. Knapp, R. Kužel, J. Appl. Crystallogr. 37 (2004) 613.
- [28] G. Ribárik, A. Audebrand, H. Palancher, T. Ungár, D. Louër, J. Appl. Crystallogr. 38 (2005) 912.
- [29] P. Holubář, M. Jílek, M. Šíma, Surf. Coat. Technol. 133/134 (2000) 145.
- [30] D. Rafaja, A. Poklad, G. Schreiber, V. Klemm, D. Heger, M. Šíma, Z. Metkd. 96 (2005) 736.
- [31] W.C. Oliver, G.M. Pharr, J. Mater. Res. 7 (1992) 1564.
- [32] D. Rafaja, V. Valvoda, R. Kužel, A.J. Perry, J.R. Treglio, Surf. Coat. Technol. 86/87 (1996) 302.
- [33] V. Valvoda, R. Kužel, R. Černý, D. Rafaja, J. Musil, S. Kadlec, A.J. Perry, Thin Solid Films 193/194 (1990) 401.
- [34] C. Kral, W. Lengauer, D. Rafaja, P. Ettmayer, J. Alloys Compd. 265 (1998) 215.
- [35] S. Inamura, K. Nobugai, K. Kanamaru, J. Solid State Chem. 68 (1987) 124.
- [36] PDF-2, Powder Diffraction File on CD-ROM, ICDD, Philadelphia, PA, 1997.
- [37] M. Parlinska-Wojtan, A. Karimi, T. Cselle, M. Morstein, Surf. Coat. Technol. 177–178 (2004) 376.

Chapter 7

Rafaja D., Wüstefeld Ch., Dopita M., Klemm V., Heger D., Schreiber G. and
Šíma M.:

Formation of defect structures in hard nanocomposites,
Surface and Coatings Technology, **203**, (2008), Pages 572-578.



Formation of defect structures in hard nanocomposites

D. Rafaja^{a,*}, C. Wüstefeld^a, M. Dopita^a, V. Klemm^a, D. Heger^a, G. Schreiber^a, M. Šíma^b

^a Institute of Materials Science, TU Bergakademie Freiberg, Gustav-Zeuner-Str. 5, D-09599 Freiberg, Germany

^b SHM Ltd., Průmyslová 3, CZ-787 01 Šumperk, Czech Republic

ARTICLE INFO

Available online 24 April 2008

Keywords:

Ti–Al–Si–N

Cr–Al–Si–N

Zr–Al–N

Thin film nanocomposites

Microstructure defects

XRD

TEM

ABSTRACT

Formation of structure defects and other microstructure phenomena in hard Cr–Al–(Si–)N, Ti–Al–(Si–)N and Zr–Al–N nanocomposite coatings with different aluminium and silicon contents deposited by using cathodic arc evaporation was investigated using a combination of X-ray diffraction and transmission electron microscopy. The subject of the microstructure studies was the analysis of the phase composition and, for the cubic phase, the determination of the stress-free lattice parameters, the crystallite size and the local disorientation of crystallites. It was found that the formation of structure defects starts with a fragmentation of the deposited clusters having the size of several tens of nanometers into nanocrystallites having the size below 12 nm. This fragmentation was driven by formation of dislocation networks. The formation of structure defects continued with the segregation of the excessive aluminium and silicon from the host structure of the transition metal nitrides that was followed by the growth of the wurtzitic AlN and an amorphous silicon nitride at higher aluminium and silicon concentrations. The microstructure of the coatings was correlated with their hardness. In all systems under study, an increase of the hardness with increasing density of the microstructure defects was observed. The maximum of the hardness was observed in the coatings containing both the cubic transition metal nitride (accommodating also aluminium and silicon) and the wurtzitic AlN.

© 2008 Elsevier B.V. All rights reserved.

1. Introduction

Small crystallite size and high residual stresses are two very important microstructure features that contribute to the increase of the hardness in super-hard nanocomposites [1]. The idea to use the small crystallite size for the improvement of the hardness is based on the work of Hall [2] and Petch [3]. High internal residual stresses are needed to reduce the sliding at the grain boundaries and thus to prevent a reduction of the hardness at small crystallite size. The relationship between the crystallite size, the residual stress and the hardness of nanocrystalline coatings and nanocomposites was the subject of numerous studies. For dual-phase CrN–Cr₂N, TiN–TiB₂ and TiC–TiB₂ coatings, the effect of the grain size and the effect of the residual stress on the hardness were illustrated in [4,5]; the authors have shown that the best performance of the ultra-hard coatings can be achieved with nanocrystalline dual-phase systems. For Ti–Al–N and Ti–Al–Si–N thin film nanocomposites, the Hall–Petch-like dependence of the hardness and the contribution of the internal residual stresses to the hardness were illustrated e.g. in [6] and [7], where also the role of silicon in the development of the residual stresses and hardness was discussed.

In the production of nanostructured coatings containing frequently high internal residual stresses, the formation of defect structures play a crucial role [8–19]. The most prominent processes are the segre-

gation of Si from the host structure of titanium nitrides [8,10], the defect-assisted segregation of Ti and Al in the Ti–Al–N system resulting in the decomposition of (Ti, Al) N into the coherent nano-sized domains of face-centred cubic (fcc) TiN and fcc-AlN [11], the spinodal decomposition in the Ti–Al–N [12–14] and Cr–Al–N [15] into fcc-TiN and/or fcc-CrN and wurtzite w-AlN and/or fcc-AlN, the three-dimensional preferred orientation of fcc crystallites in the Ti–Al–Si–N [16] and Cr–Al–Si–N systems [17], and the formation of dislocations in the Cr–Al–Si–N coatings [18]. Most of the above processes contribute to the development of nanocrystallites with coherent or semi-coherent interfaces that supports the development of the internal residual stresses [6,20–22].

In this contribution, the role of the formation of the defect structures and their impact on the hardness of the thin films nanocomposites is illustrated on the examples of the Cr–Al–(Si–)N, Ti–Al–(Si–)N and Zr–Al–N coatings. In particular, the fragmentation of grains having the size of several tens of nanometers into partially coherent nanocrystallites with the size below 12 nm and with the mutual disorientation below 2.5°, the formation of dislocation networks, the relationship between the nanocrystallite boundaries and the dislocation networks, the segregation of Al and Si from the host structure of M–Al–(Si–)N and the growth of AlN and Si_xN_y are discussed.

2. Experimental

Thin films of selected transition metal nitrides containing Al and Si were deposited using cathodic arc evaporation (CAE) in the deposition

* Corresponding author.

E-mail address: rafaja@www.tu-freiberg.de (D. Rafaja).

Table 1

Chemical composition of the Ti–Al–Si–N, Cr–Al–Si–N and Zr–Al–N coatings deposited using cathodic arc evaporation

Cr–Al–N	Cr–Al–Si–N	Ti–Al–N	Ti–Al–Si–N	Zr–Al–N
Cr _{0.92} Al _{0.08} N	Cr _{0.91} Al _{0.08} Si _{0.01} N	Ti _{0.96} Al _{0.04} N	Ti _{0.96} Al _{0.04} Si _{0.00} N	Zr _{0.96} Al _{0.04} N
Cr _{0.83} Al _{0.17} N	Cr _{0.84} Al _{0.15} Si _{0.01} N	Ti _{0.85} Al _{0.15} N	Ti _{0.84} Al _{0.15} Si _{0.01} N	Zr _{0.85} Al _{0.15} N
Cr _{0.75} Al _{0.25} N	Cr _{0.69} Al _{0.28} Si _{0.03} N	Ti _{0.72} Al _{0.28} N	Ti _{0.71} Al _{0.26} Si _{0.03} N	Zr _{0.77} Al _{0.23} N
Cr _{0.54} Al _{0.46} N	Cr _{0.52} Al _{0.43} Si _{0.05} N	Ti _{0.52} Al _{0.48} N	Ti _{0.52} Al _{0.43} Si _{0.05} N	Zr _{0.59} Al _{0.41} N
Cr _{0.46} Al _{0.54} N	Cr _{0.40} Al _{0.52} Si _{0.08} N	Ti _{0.39} Al _{0.61} N	Ti _{0.38} Al _{0.54} Si _{0.08} N	Zr _{0.50} Al _{0.50} N
Cr _{0.30} Al _{0.70} N	Cr _{0.24} Al _{0.65} Si _{0.11} N	Ti _{0.18} Al _{0.82} N	Ti _{0.19} Al _{0.72} Si _{0.09} N	Zr _{0.35} Al _{0.65} N
Cr _{0.09} Al _{0.91} N	Cr _{0.07} Al _{0.81} Si _{0.12} N	Ti _{0.09} Al _{0.91} N	Ti _{0.06} Al _{0.82} Si _{0.12} N	Zr _{0.13} Al _{0.87} N

In each sample, the concentrations of elements were obtained from EPMA/WDX measurements performed in 41 points.

apparatus π -80 produced by PLATIT AG (Grenchen, Switzerland) that works with two vertical laterally rotating arc cathodes placed in the front of the vacuum chamber [23]. One cathode was made from the transition metal (Cr, Ti or Zr), the other from Al or from Al with 11% Si for deposition of coatings without and with Si, respectively. In order to be able to compare coatings with different chemical composition, the parameters of the deposition process were kept the same for all deposited materials. The base pressure was 5×10^{-3} Pa, the working pressure of the nitrogen atmosphere 1.3 Pa. The deposition temperature was approximately 450 °C. The current on the transition metal cathode was 80 A, the current on the Al or Al–Si cathode 120 A. The bias voltage was –75 V. Polished plates of cemented carbide were used as substrates. They were distributed horizontally with equal distances from each other on a cylindrical substrate holder that was placed in the centre of the vacuum chamber [16]. In each deposition run, seven samples of the respective series were produced without any rotation of the substrates. The samples had different distances to the respective cathode, which allowed the series of the samples to be deposited with different ratios between the transition metal contents, aluminium and silicon contents, $[M]/([M] + [Al] + [Si])$.

The overall chemical composition of the Cr–Al–(Si–)N, Ti–Al–(Si–)N and Zr–Al–N coatings was measured using electron probe microanalysis with wavelength-dispersive X-ray spectroscopy (EPMA/WDX) on the electron probe microanalyzer JXA 8900 RL from Jeol. The concentrations of the expected elements (the respective transition metal, Al, Si, N) were obtained from the intensity of their spectral K lines using the ZAF correction procedure (the correction of the effects due to the atomic number Z, absorption A and fluorescence F) and external standards. Due to the overlap of the spectral lines $L_i(\text{Ti})$ and $K(\text{N})$, the amount of nitrogen in the Ti–Al–(Si–)N coatings could not be measured directly. Thus, it was calculated from the analytical total and verified by glow-discharge optical emission spectroscopy (GDOES). Within the accuracy of the experimental methods for chemical analysis, the nitrogen amount was 50 at.%. The chemical composition of all samples under study is summarised in Table 1. Hardness of the Cr–Al–(Si–)N, Ti–Al–(Si–)N and Zr–Al–N coatings was calculated from the indentation load–displacement curve according to the Oliver–Pharr method [24]. The Berkovich indenter was used for all measurements.

The analysis of the phase composition was done using the glancing-angle X-ray diffraction (GAXRD); the conventional phase analysis was complemented by a precise measurement of the stress-free lattice parameters as suggested in [6]. Because of a strong anisotropy of elastic constants in most samples, the stress-free parameters were determined using three complementary approaches that are based on the $\sin^2\psi$ method [25]. Two of them [26,27] eliminate the elastic anisotropy by using a known functional dependence of the elastic constant on the crystallographic direction and yield consequently the elastic lattice deformation in the direction of the maximum stiffness, i.e. in $\langle 100 \rangle$ for the fcc transition metal nitrides. The third procedure employs the crystallites group method [28] and reveals the lattice parameters as measured on the lattice planes (200). In all three approaches, the

stress-free lattice parameters were calculated from the dependence of the lattice parameters a_{ψ}^{hkl} on $\sin^2\psi$:

$$a_{\psi}^{hkl} = (a_{\parallel}^{hkl} - a_{\perp}^{hkl}) \sin^2\psi + a_{\perp}^{hkl} \quad (1)$$

for

$$\sin^2\psi_0 = \frac{2\nu^{hkl}}{\nu^{hkl} + 1} \quad (2)$$

The parameters a_{\parallel}^{hkl} and a_{\perp}^{hkl} in Eq. (1) have the meaning of the in-plane and out-of-plane lattice parameters, respectively. ψ is the angle between the diffracting lattice planes and the sample surface. ν^{hkl} in Eq. (2) is the Poisson ratio in the crystallographic direction $\langle hkl \rangle$. For the fcc-(Ti, Al) N and fcc-(Ti, Al, Si) N phases having a relatively low anisotropy of the elastic constants, the Poisson ratio of 0.3 [29] was used. For the fcc-(Cr, Al) N, fcc-(Cr, Al, Si) N and fcc-(Zr, Al) N showing a much larger anisotropy of the elastic constants, the Poisson ratios $\nu^{100}(\text{CrN})=0.214$ and $\nu^{100}(\text{ZrN})=0.186$ from [30] were employed. In the first approximation, it was assumed that the Poisson ratio does not change with the Al and Si contents.

Crystallite size was calculated from the dependence of the integral broadening of the XRD lines measured in the GAXRD geometry on the sine of the diffraction angle by taking the partial coherence of crystallites for X-rays into account [31]. For partially coherent nanocrystallites, i.e. for nano-sized crystallites with a very small mutual disorientation, XRD recognises besides their size also their mutual disorientation and the size of clusters that are composed of these partially coherent nanocrystallites [32]. In selected samples, the crystallite and cluster size obtained from the GAXRD experiments were confirmed using transmission electron microscopy with high resolution (HRTEM).

GAXRD measurements were performed on a D8 Advance diffractometer (from Bruker AXS) equipped with a sealed X-ray tube with copper anode ($\lambda=0.15418$ nm) and with a Goebel mirror in the primary beam. A Soller collimator with the divergence of 0.12° and a flat LiF monochromator were inserted into the diffracted beam. XRD measurements that employed the crystallites group method were performed on an X'Pert PRO MRD diffractometer (from PANalytical) with a sealed X-ray tube with copper anode. The diffractometer was equipped with an Eulerian cradle, a polycapillary optics in the primary beam, a Soller

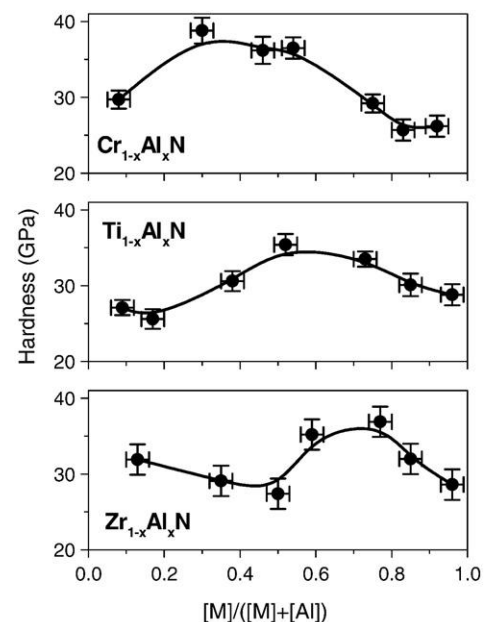


Fig. 1. Hardness of the Cr–Al–N, Ti–Al–N and Zr–Al–N coatings plotted as a function of the transition metal contents.

collimator having the acceptance angle of 0.27° and a flat graphite monochromator in the diffracted beam. HRTEM was done on a 200 kV analytical high-resolution transmission electron microscope JEM 2010 FEF (from Jeol). The high resolution was achieved by using ultra-high-resolution objective lens ($C_s = 0.5$ mm) and an in-column energy filter to remove the inelastic electrons from the HRTEM micrograph. The specimens for HRTEM were prepared in the plane-view orientation. They were mechanically pre-thinned, etched by an ion beam and plasma cleaned.

3. Results

3.1. Hardness and phase composition

The hardness of the (Ti, Al) N, (Cr, Al) N and (Zr, Al) N coatings increased with the addition of Al until a maximum was reached that was followed by a decrease of the hardness with further increasing Al contents (Fig. 1). The Al contents, for which the maximum hardness was observed, i.e. 35 at.% Al in $\text{Cr}_{0.30}\text{Al}_{0.70}\text{N}$, 24 at.% Al in $\text{Ti}_{0.52}\text{Al}_{0.48}\text{N}$ and 12 at.% Al in $\text{Zr}_{0.77}\text{Al}_{0.23}\text{N}$, decreased with increasing intrinsic lattice parameter of the respective binary nitride, which is a_0 (CrN) = 0.41485 nm, a_0 (TiN) = 0.42418 nm and a_0 (ZrN) = 0.45823 nm according to [33]. The samples with the maximum hardness consisted of two crystalline phases, fcc-(M, Al) N and w-AlN, having approximately the same volume ratio. Unfortunately, a precise quantitative phase analysis was difficult because of the strong three-dimensional preferred orientation of crystallites [16,17].

At the lowest Al contents, all samples contained only fcc-(M, Al) N. In the single-phase regions, the stress-free lattice parameters decreased linearly with increasing Al contents (Fig. 2). These Vegard-like dependences were approximated by the following functions: a ($\text{Cr}_{1-x}\text{Al}_x\text{N}$) = $[0.41486(2) - 0.00827(1) \cdot x]$ nm, a ($\text{Ti}_{1-x}\text{Al}_x\text{N}$) = $[0.42418(2) - 0.01432(2) \cdot x]$ nm and a ($\text{Zr}_{1-x}\text{Al}_x\text{N}$) = $[0.458(1) - 0.026(1) \cdot x]$ nm (the lattice parameters for the stoichiometric binary nitrides shown in Fig. 2 were taken from the ICSD database [33]). The decrease of the

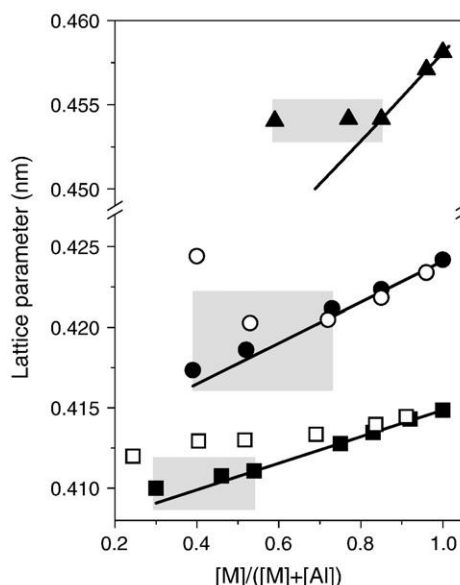


Fig. 2. Dependence of the stress-free lattice parameters on the transition metal contents in fcc-(Cr, Al, Si) N (boxes), fcc-(Ti, Al, Si) N (circles) and fcc-(Zr, Al) N coatings (triangles) as measured in the samples, in which fcc-(M, Al, Si) N was the dominating phase. Solid symbols are used for Si-free coatings, open symbols for coatings containing Si. The stress-free lattice parameters of fcc-(Cr, Al, Si) N and fcc-(Ti, Al, Si) N were taken from Refs. [18] and [6], respectively. Error bars of the stress-free lattice parameters are smaller than the symbols. Solid lines indicate hypothetical Vegard-like dependences for $\text{Cr}_{1-x}\text{Al}_x\text{N}$, $\text{Ti}_{1-x}\text{Al}_x\text{N}$ and $\text{Zr}_{1-x}\text{Al}_x\text{N}$ (see text). Large grey boxes mark the composition ranges of the maximum hardness from Fig. 1.

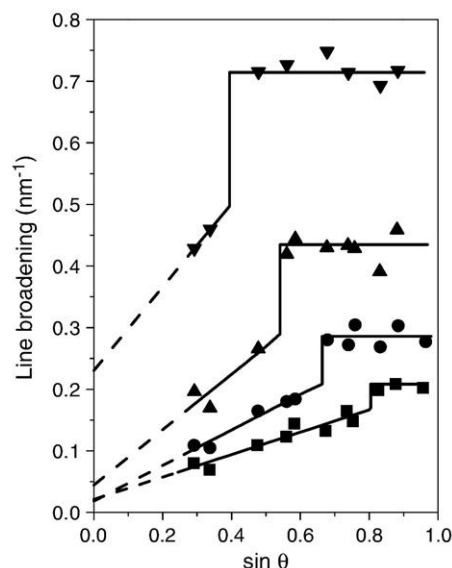


Fig. 3. Dependence of the integral line broadening on sine of the diffraction angle as observed for the fcc phase of the samples $\text{Zr}_{0.96}\text{Al}_{0.04}\text{N}$ (boxes), $\text{Zr}_{0.85}\text{Al}_{0.15}\text{N}$ (circles), $\text{Zr}_{0.77}\text{Al}_{0.23}\text{N}$ (triangles) and $\text{Zr}_{0.59}\text{Al}_{0.41}\text{N}$ (bottom up triangles). Horizontal solid lines show the saturated XRD line broadening that was used for calculation of the crystallite size. Dashed lines show the extrapolation of the XRD line broadening from partially coherent crystallites to $\sin \theta = 0$ that was used for the estimation of the cluster size.

stress-free lattice parameters with increasing Al contents becomes faster with increasing intrinsic lattice parameter of the respective binary transition metal nitride. In the dual-phase coatings, the stress-free lattice parameters of fcc-(M, Al) N were larger than the lattice parameters predicted from the respective Vegard-like dependence for the “overall” chemical composition of the coatings as revealed by EPMA/WDX. The reason is that a part of Al atoms segregates from the host structure of the fcc-(M, Al) N. Thus, the fcc phase contains less Al than the mixture of fcc-(M, Al) N and w-AlN, which chemical composition was analysed using EPMA/WDX. The segregation of Al from fcc-(M, Al) N is responsible for the apparent increase of the lattice parameter in the cubic phases.

Accordingly, the composition ranges, in which the stress-free lattice parameters of fcc-(M, Al) N deviate from the hypothetical Vegard-like dependence, match well with the composition ranges, in which the presence of two crystalline phases and the increase of the hardness were observed. The phase decomposition starts at $\text{Cr}_{0.54}\text{Al}_{0.46}\text{N}$, $\text{Ti}_{0.72}\text{Al}_{0.28}\text{N}$ and $\text{Zr}_{0.85}\text{Al}_{0.15}\text{N}$. The maximum Al contents in the fcc phases of the samples under study were $\text{Cr}_{0.44}\text{Al}_{0.56}\text{N}$, $\text{Ti}_{0.48}\text{Al}_{0.52}\text{N}$ and $\text{Zr}_{0.85}\text{Al}_{0.15}\text{N}$ as calculated back from the minimum lattice parameters and from the Vegard-like dependences shown above. As Si present in the Cr–Al–Si–N and Ti–Al–Si–N coatings segregates from the host structure of fcc-(M, Al, Si) N by forming amorphous silicon nitride [1,34], the segregation of Si could not be confirmed directly using the XRD phase analysis. Nevertheless, it was concluded from the comparison of the stress-free lattice parameters of fcc-(M, Al) N and fcc-(M, Al, Si) N in samples containing a single crystalline phase (Fig. 2) that fcc-(Cr, Al) N can accommodate more Si than fcc-(Ti, Al) N. In fcc-(Cr, Al, Si) N, silicon inflates the stress-free lattice parameter as described in [18]. In the Ti–Al–Si–N coatings, superfluous Si causes a complete segregation of Ti, Al and Si into fcc-TiN, w-AlN and amorphous silicon nitride [6], as it can also be seen on the increase of the stress-free lattice parameter of fcc-(Ti, Al) N towards stoichiometric TiN. Another effect of silicon on the microstructure of the M–Al–Si–N coatings will be discussed in the next section.

3.2. Microstructure of the coatings

Mayrhofer and co-workers [9,11,19] regarded the segregation of Al and B from the host structure of the fcc titanium nitride as a self-

organization process that considerably modifies the microstructure and mechanical properties of the Ti–Al–N and Ti–B–N coatings. Therefore, a detailed knowledge of the microstructure of the M–Al–Si–N thin film nanocomposites deposited using CAE can help in understanding the microstructure formation and in explaining the mechanical properties of these nanocomposites. The crucial technique used in this study was the analysis of the XRD line broadening; its results were confirmed and complemented by HRTEM and TEM. The dependence of the integral line broadening on the sine of the diffraction angle that was observed in all CAE M–Al–Si–N nanocomposites under study is shown in Fig. 3 on the example of the Zr–Al–N coatings with different Al contents. As described in [31] and [32], this dependence can be divided into two parts. At low diffraction angles, an increase of the XRD line broadening with increasing diffraction angle is observed similarly to the classical Williamson–Hall plot [35]. Within the classical kinematical diffraction theory, the extrapolation of the linear dependence of the XRD line broadening to $\sin \theta = 0$ yields the reciprocal size of crystallites, i.e. the reciprocal size of coherent domains that can contain structure defects, e.g. dislocations. These structure defects are responsible for the increase of the XRD line broadening with increasing diffraction angle [36]. In nanocrystalline materials and in nanocomposites with a strong preferred orientation of neighbouring nanocrystallites, the extrapolation of the linear dependence of the XRD line broadening to $\sin \theta = 0$ (dashed lines in Fig. 3) yields the reciprocal size of domains (clusters), which parts are partially coherent for X-rays [32]. The effect of the partial coherence disappears at a certain diffraction angle [31] that is observed as a steep increase of the XRD line broadening (Fig. 3). The position of the steep increase of the XRD line broadening was used for determination of the mutual disorientation of the parts of the domains [32]. In the second part of the modified Williamson–Hall plot, where the partial coherence of the nanocrystallites within the clusters is absent, a constant XRD line broadening is typically observed. This maximum line broadening corresponds to the reciprocal size of nearly defect-free nanocrystallites as it is often calculated using the classical Scherrer formula [37].

The size of clusters consisting of partially coherent nanocrystallites was (47 ± 8) nm in the Cr–Al–N and Cr–Al–Si–N coatings, (26 ± 6) nm in the Ti–Al–N and Ti–Al–Si–N coatings and (50 ± 9) nm in the Zr–Al–N coatings as calculated from the extrapolation of the XRD line broadening to $\sin \theta = 0$. A TEM micrograph of the clusters is shown in Fig. 4 for the sample $\text{Cr}_{0.30}\text{Al}_{0.70}\text{N}$. The cluster size obtained from the XRD line broadening did not change significantly with the Al and Si contents. However, the accuracy of the cluster size determination de-

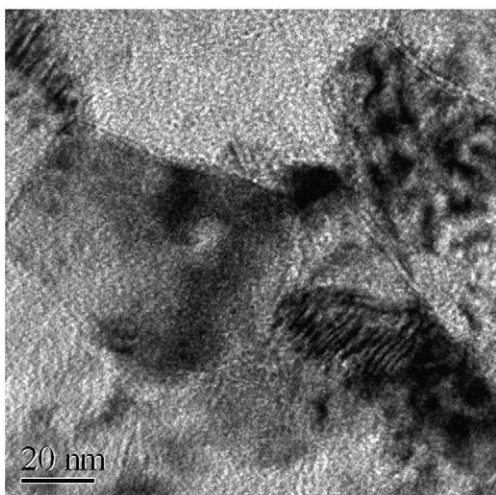


Fig. 4. Diffraction contrast TEM micrograph of the sample $\text{Cr}_{0.30}\text{Al}_{0.70}\text{N}$ showing the objects, which were identified using XRD as nanostructured clusters with the size of (47 ± 8) nm.

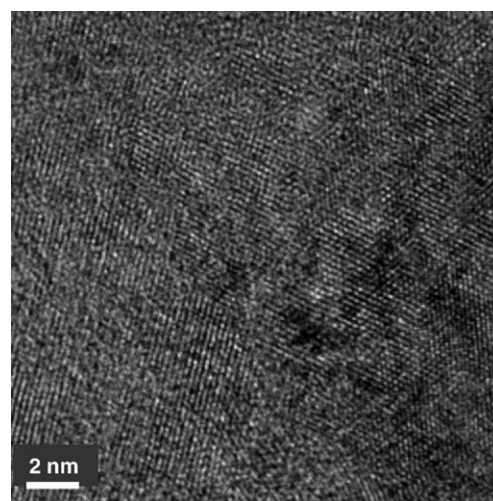


Fig. 5. HRTEM micrograph of the sample $\text{Cr}_{0.30}\text{Al}_{0.70}\text{N}$ showing the internal structure of the nanostructured clusters from Fig. 4. The size and the mutual disorientation of the nanocrystallites as obtained from XRD was (6.5 ± 0.3) nm and $(0.75 \pm 0.05)^\circ$, respectively.

creased rapidly with increasing Al and Si contents, because the range of the constant XRD line broadening shifted to smaller diffraction angles. Thus, only few experimental points could be used for the extrapolation of the line broadening within the region of the partial coherence (Fig. 3). The TEM micrograph from Fig. 4 indicates a possible internal structure of the clusters, which was proven by HRTEM and quantified by XRD. In this particular sample with the overall chemical composition $\text{Cr}_{0.30}\text{Al}_{0.70}\text{N}$, XRD revealed the cluster size of (47 ± 8) nm, which matches well with the size of the large domains in Fig. 4. Furthermore, XRD resolved the internal structure of the clusters in this sample and found out that they consist of partially coherent nanocrystallites having the size of (6.5 ± 0.3) nm and the mutual disorientation of $(0.75 \pm 0.05)^\circ$. The presence of individual nanocrystallites gives obviously rise to the occurrence of the diffraction contrast within the clusters in Fig. 4. However, it is not completely clear from the TEM micrograph if the diffraction contrast is caused by the mutual disorientation of the nanocrystallites or by the local strain fields within the clusters. Because of the low mutual disorientation of nanocrystallites, HRTEM cannot recognise the crystallites boundaries very well (Fig. 5). The existence of nanocrystallites within the clusters can much better be seen in the HRTEM micrograph of the sample

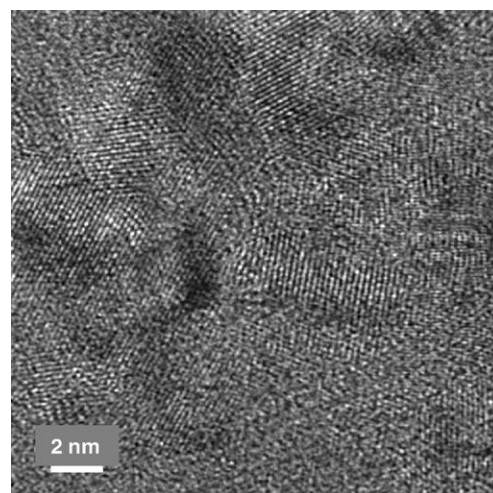


Fig. 6. HRTEM micrograph of the sample $\text{Cr}_{0.40}\text{Al}_{0.52}\text{Si}_{0.08}\text{N}$. The crystallite size calculated from the XRD line broadening was (4.5 ± 0.3) nm. The neighbouring crystallites were non-coherent for XRD.

$\text{Cr}_{0.40}\text{Al}_{0.52}\text{Si}_{0.08}\text{N}$ (Fig. 6). According to the results of XRD, this sample contains non-coherent nanocrystallites having the size of (4.5 ± 0.3) nm. This crystallite size agrees well with the size of the nanocrystallites seen by HRTEM. The mutual disorientation of the non-coherent nanocrystallites in this sample was sufficiently high in order to be able to recognise their boundaries using HRTEM – more than 1.45° as obtained from XRD.

The size of crystallites and their mutual disorientation within the clusters are plotted in Figs. 7 and 8 as functions of the chemical composition of the coatings. The crystallite size was calculated from the constant XRD line broadening, the mutual disorientation of neighbouring crystallites from the position of the steep increase of the XRD line broadening using the numerical routine that was described in Ref. [31]. In all coatings under study, the crystallite size was much smaller than the cluster size and decreased with increasing Al and Si contents. In the transition-metal-rich Cr–Al–(Si)–N and Ti–Al–(Si)–N coatings, the size of crystallites was approximately 4 times smaller than the cluster size. In the Zr-rich Zr–Al–N coatings, this ratio was larger than 10. In the Si-free M–Al–N coatings, the fastest decrease of the crystallite size was observed at the beginning of the phase decomposition, i.e. below $\text{Cr}_{0.54}\text{Al}_{0.46}\text{N}$, $\text{Ti}_{0.72}\text{Al}_{0.28}\text{N}$ and $\text{Zr}_{0.85}\text{Al}_{0.15}\text{N}$. The mutual disorientation of the neighbouring nanocrystallites increased in all M–Al–N coatings with increasing Al contents. In the Cr–Al–N coatings, the increase of the crystallite disorientation with increasing Al contents was faster in the single-phase region than in the two-phase region. The Ti–Al–N and Zr–Al–N coatings behaved conversely to the Cr–Al–N coatings: the increase of the disorientation of neighbouring nanocrystallites was faster in the two-phase region than in the single-phase region. The addition of Si speeded up the reduction of the crystallite size both in the Cr–Al–Si–N and Ti–Al–Si–N coatings. The mutual disorientation of crystallites was affected by the addition of Si mainly in the Ti–Al–Si–N coatings. In the Cr–Al–Si–N coatings, a larger disorientation of neighbouring nanocrystallites as compared to the Cr–Al–N coatings was only observed at the highest Si contents. In both sample series, Cr–Al–Si–N and Ti–Al–Si–N, the disorientation of crystallites exceeded the limit for their partial coherence at the Si concentration of 4 at.%,

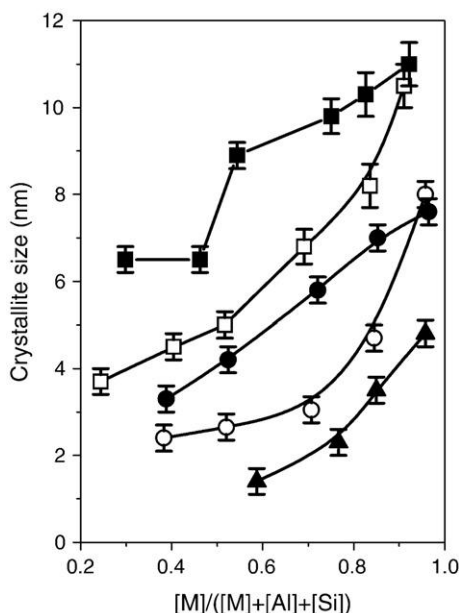


Fig. 7. Crystallite size in the fcc phases of the Cr–Al–N (solid boxes), Cr–Al–Si–N (open boxes), Ti–Al–N (solid circles), Ti–Al–Si–N (open circles) and Zr–Al–N (solid triangles) nanocomposites as a function of the transition metal contents. The crystallite sizes for fcc-(Cr, Al, Si) N were taken from Ref. [18].

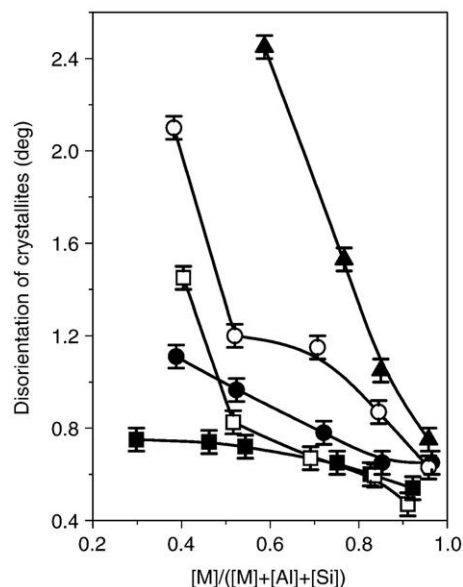


Fig. 8. Dependence of the mutual disorientation of partially coherent fcc nanocrystallites on the transition metal contents in the Cr–Al–N (solid boxes), Cr–Al–Si–N (open boxes), Ti–Al–N (solid circles), Ti–Al–Si–N (open circles) and Zr–Al–N (solid triangles) nanocomposites. The fcc crystallites in the coatings with the overall chemical compositions $\text{Cr}_{0.40}\text{Al}_{0.52}\text{Si}_{0.08}\text{N}$ and $\text{Ti}_{0.38}\text{Al}_{0.54}\text{Si}_{0.08}\text{N}$ were non-coherent for X-ray diffraction; thus their mutual disorientations could only be estimated to exceed 1.45° and 2.1° , respectively. The disorientations of fcc nanocrystallites in the Cr–Al–Si–N coatings were taken from Ref. [18].

3.3. Microstructure defects

Formation of clusters of partially coherent nanocrystallites is an important process that influences the microstructure development in the M–Al–(Si)–N nanocomposites. The ratio between the cluster size and the crystallite size complemented by the disorientation of the neighbouring crystallites can be used to describe the development of the fragmentation with increasing Al and Si contents. It follows from the small disorientation of the neighbouring nanocrystallites, which was below 2.5° in the most samples under study, that the neighbouring nanocrystallites are separated by small-angle boundaries. Such a fragmentation of the clusters was already observed in the single-phase samples with the smallest Al (and Si) contents, in which the disorientation of the neighbouring crystallites ranged between 0.50° for

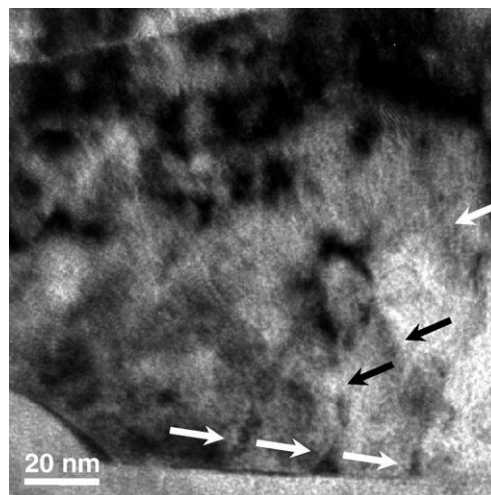


Fig. 9. An example of the dislocation structure as seen by the diffraction contrast in TEM. Some dislocations are labelled by arrows.

$\text{Cr}_{0.92}\text{Al}_{0.08}\text{N}$ and 0.75° for $\text{Zr}_{0.96}\text{Al}_{0.04}\text{N}$. The addition of Si into the transition-metal-richest samples had a negligible effect both on the crystallite size (Fig. 7) and on the crystallite disorientation (Fig. 8). Therefore, neither the phase decomposition nor the segregation of Si from the host structure of the fcc-(M, Al, Si) N is responsible for the primary fragmentation of the clusters into the nanocrystallites. TEM micrographs of the transition-metal-richest samples revealed dislocation networks that are illustrated on the example of the sample $\text{Cr}_{0.92}\text{Al}_{0.08}\text{N}$ in Fig. 9. The distances between the dislocations were about 20 nm. A detailed analysis of the dislocations has shown that they behave like screw dislocations with the Burgers vector $\vec{b} = \frac{1}{2}a\langle 110 \rangle$ [18]. According to Frank [38], the dislocations with the Burgers vector \vec{b} and with the distance L causes the local lattice rotation of:

$$\alpha = 2 \arcsin \left(\frac{|\vec{b}|}{2L} \right) \quad (3)$$

For the sample $\text{Cr}_{0.92}\text{Al}_{0.08}\text{N}$ with the (stress-free) lattice parameter of 0.41429 nm and with the distances between screw dislocations of approximately 20 nm, the local lattice rotation calculated according to Eq. (3) is roughly 0.8° . This value is slightly higher than the disorientation of nanocrystallites that was obtained from the XRD line broadening (Fig. 8). This disagreement can have two reasons. First, no “calibration” was used for the analysis of the nanocrystallite disorientations from the XRD line broadening. Certainly, the analysis of the XRD line broadening can reliably be used for a relative analysis of the disorientation of nanocrystallites, but its absolute accuracy was not sufficiently proven yet. The second reason could be related to the different capabilities of XRD and TEM. Using TEM, the local lattice rotation was calculated for two adjacent crystallites separated by screw dislocations, whereas the mean value of the crystallite disorientation obtained from XRD was averaged over all neighbouring nanocrystallites within the coherence length of X-rays, which is approximately 1 μm . For a “zig-zag” mutual rotation of the nanocrystallites, XRD would see smaller mean crystallite disorientations of more distant neighbours than it would correspond to the disorientation of the next neighbours.

Assuming that the clusters in the transition-metal-richest coatings are split into nanocrystallites by dislocations, the distances between the dislocation and the respective lattice rotations as calculated using Eq. (3) should have a relationship to the crystallite size and to the disorientation of crystallites as obtained from the XRD line broadening. This is true for the coatings with the overall chemical composition $\text{Cr}_{0.92}\text{Al}_{0.08}\text{N}$ and $\text{Ti}_{0.96}\text{Al}_{0.04}\text{N}$. The size of crystallites in $\text{Ti}_{0.96}\text{Al}_{0.04}\text{N}$ (7.6 nm) was about 1.4 times smaller than the size of crystallites in $\text{Cr}_{0.92}\text{Al}_{0.08}\text{N}$ (11 nm). The distances between dislocations calculated from the crystallite disorientations of 0.50° for $\text{Cr}_{0.92}\text{Al}_{0.08}\text{N}$ and 0.65° for $\text{Ti}_{0.96}\text{Al}_{0.04}\text{N}$, i.e. 34 nm and 26 nm, were nearly in the same ratio (1.3). The coatings containing a very small amount of Si, $\text{Cr}_{0.91}\text{Al}_{0.08}\text{Si}_{0.01}\text{N}$ and $\text{Ti}_{0.96}\text{Al}_{0.04}\text{Si}_{0.00}\text{N}$ behave similarly. The distance between dislocations in the sample $\text{Zr}_{0.96}\text{Al}_{0.04}\text{N}$ should be 15 nm as expected for the crystallite size of 4.8 nm and the same relative decrease of the crystallite size and the distance between dislocations. However, the distance between dislocations calculated from the disorientation of nanocrystallites of 0.75° was 24 nm. This means that the disorientation of the neighbouring nanocrystallites must be much larger than the disorientation obtained from the XRD line broadening, in order to arrive at the smaller expected distance between dislocations. This phenomenon could be explained by pronounced “zig-zag” disorientation of nanocrystallites or it could be related to the bad “calibration” of the XRD analysis of the nanocrystallite disorientations as discussed above.

4. Discussion

As based on the above results, the following model of the microstructure formation in Cr–Al–(Si–)N, Ti–Al–(Si–)N and Zr–Al–N nanocomposite coatings deposited using cathodic arc evaporation can

be suggested. During the cathodic arc evaporation, the coatings were built up from clusters of the respective fcc phase, which had the size of several tens of nanometers. The size of the clusters was different in the coatings containing Cr, Ti and Zr, but for the particular transition metal it did not change with the addition of Al and Si within the experimental accuracy of the XRD line profile analysis. The clusters consisted of fcc nanocrystallites that had very small mutual disorientations and that were partially coherent for XRD in the most cases. In the transition-metal-richest coatings, the fcc nanocrystallites were separated by features that seemed like dislocations for TEM.

Increasing Al contents in the coatings caused a (further) reduction of the size of the fcc nanocrystallites and an increase of their mutual disorientation. A more pronounced increase of the crystallite disorientations was observed after w-AlN appeared in the coatings that can be explained by a larger lattice misfit between fcc-(M, Al) N and w-AlN with increasing volume of the w-AlN crystallites. The appearance and increase of the size of the w-AlN nanocrystallites accelerated the reduction of the size of fcc crystallites. Although the mutual disorientation of fcc crystallites increased with increasing Al contents, it was below 2.5° in all M–Al–N coatings that contained fcc-(M, Al) N as the dominant phase. This small disorientation of crystallites implies that w-AlN forms during the segregation of Al from fcc-(M, Al) N and that the strong local preferred orientation of fcc crystallites is still transferred through the hexagonal phase. The latter was observed in the Ti–Al–N coatings [6], where the following correlation of the crystallographic directions in fcc-(Ti, Al) N and w-AlN was found: $\langle 110 \rangle_{\text{fcc}} \parallel \langle 110 \rangle_{\text{w}}$ and $[001]_{\text{fcc}} \parallel [110]_{\text{w}}$. Furthermore, the transfer of the preferred orientation of crystallites during the deposition process was confirmed by the presence of a pronounced three-dimensional macroscopic texture in the Cr–Al–(Si–)N [17] and Ti–Al–(Si–)N [16] coatings. The maximum hardness was observed in the dual-phase (M, Al) N coatings, in which the internal lattice strain developed at the interfaces between fcc-(Ti, Al) N and w-AlN. The increase of the hardness of the Ti–Al–N coatings due to the segregation of AlN was also reported in [20]. Formerly, a clear correlation between the hardness and the residual stresses was shown for the dual-phase CrN–Cr₂N, TiN–TiB₂ and TiC–TiB₂ nanocomposites in [5].

The addition of Si in the Cr–Al–Si–N and Ti–Al–Si–N coatings speeded up the reduction of the size of the fcc crystallites. In the Ti–Al–Si–N coatings, the addition of Si led additionally to a larger disorientation of fcc crystallites in comparison with the Ti–Al–N coatings. In the Cr–Al–Si–N coatings, a rapid increase of the disorientation of fcc crystallites was first observed at the Si contents exceeding 2.5 at.%. At the Si contents higher than approximately 4 at.%, the mutual disorientation of fcc crystallites exceeded the limit of their partial coherence for X-rays both in the Cr–Al–Si–N and in the Ti–Al–Si–N coatings. Because of the observed gradual decrease of the size of the fcc crystallites (Fig. 7) that was accompanied by the gradual increase of their mutual disorientation (Fig. 8), we can assume that the superfluous elements (Al and Si) segregate at the existing microstructure defects, i.e. at the boundaries of the partially coherent fcc nanocrystallites, which are defined by dislocation networks. The segregation of the superfluous elements at the crystallite or grain boundaries in the ternary nitride thin films was described in [39] and [40]. The effect of Si on the increase of the defect density in arc evaporated $\text{Ti}_{1-x}\text{Si}_x\text{N}$ coatings was reported in [41].

The segregation of Al and Si at the dislocation networks is followed by the growth of “bulky” w-AlN and amorphous Si_xN_y at higher Al and Si concentrations. The segregation of Al from the host structure of fcc-(M, Al) N and the growth of w-AlN were directly confirmed by the analysis of the stress-free lattice parameters and by the XRD phase analysis, respectively. Additional information about the growth of w-AlN and a- Si_xN_y at the present microstructure defects was obtained from the XRD analysis of the mutual disorientation of fcc crystallites. The very small mutual disorientation of neighbouring fcc nanocrystallites in the transition-metal-rich samples confirmed that the nanocrystallites are partially coherent and that they originate from

the same cluster. The strong local preferred orientation of fcc nanocrystallites in M–Al–N coatings containing w-AlN as a second phase supports the theory that w-AlN forms during the deposition process as a consequence of the segregation of elements or as a consequence of the spinodal decomposition of M–Al–N as suggested in [11,15,42–45]. On the other hand, the transfer of the local preferred orientation between fcc crystallites through w-AlN is supported by the orientation relationship between the fcc phases and w-AlN and by similar interplanar spacings of certain lattice planes in both compounds. Consequently, the mutual disorientation of fcc crystallites is larger for a larger lattice parameter of the respective fcc-(M, Al) N phase that causes a larger lattice misfit between fcc-(M, Al) N and w-AlN. The different mutual disorientations of fcc crystallites in the Cr–Al–N, Ti–Al–N and Zr–Al–N coatings were illustrated in Fig. 8. Small amount of Si influences the microstructure of the Cr–Al–Si–N and the Ti–Al–Si–N coatings differently. The decrease of the crystallite size and the increase of the mutual disorientation of the partially coherent nanocrystallites are faster with increasing Si contents in the Ti–Al–Si–N coatings than in the Cr–Al–Si–N coatings. At higher Si contents, both systems behave similarly.

5. Conclusions

In this study, the following phenomena were investigated and related to the formation of structure defects and other microstructure features in cathodic arc evaporated Cr–Al–(Si–)N, Ti–Al–(Si–)N and Zr–Al–N coatings: the fragmentation of clusters during the deposition process into partially coherent nanocrystallites, the formation of dislocation networks, the segregation of Al and Si at the crystallite boundaries and at dislocation networks, and the growth of w-AlN and α -Si₃N₄. It was found that the cluster size depends on the transition metal species, but it does not change substantially with increasing Al and Si contents for the same transition metal. On the contrary, the size of the nanocrystallites decreases and the defect density increases with increasing Al and Si contents. The microstructure features under study were correlated with the hardness of the coatings. The fragmentation of clusters into nanocrystallites and the formation of dislocation networks were considered as reasons for increasing hardness of the coatings at the lowest concentrations of Al and Si. The hardness of the coatings increased with increasing density of microstructure defects and with decreasing size of nanocrystallites, which were caused by the segregation of Al and Si from the host structure of the transition metals at higher Al and Si contents. The maximum hardness was observed for the coatings, which contained two crystalline phases, fcc-(M, Al, Si) N and w-AlN, in similar volume ratios.

Acknowledgements

The authors thank the German Scientific Council (DFG) for supporting the project # RA-1050/9-1. The HRTEM JEM 2010 FEF was financed through DFG in frame of the Priority program # 1062. Hardness measurements were performed by Dr. Thomas Modes (FEP Dresden) and by Steffen Wolf (TU Bergakademie Freiberg).

References

- [1] S. Veprek, S. Reiprich, *Thin Solid Films* 268 (1995) 64.
- [2] E.O. Hall, *Proc. Phys. Soc. Lond.*, B 64 (1951) 747.
- [3] N.J. Petch, *J. Iron Steel Inst.* 174 (1953) 25.
- [4] P.H. Mayrhofer, G. Tischler, C. Mitterer, *Surf. Coat. Technol.* 142–144 (2001) 78.
- [5] P.H. Mayrhofer, C. Mitterer, J. Musil, *Surf. Coat. Technol.* 174–175 (2003) 725.
- [6] D. Rafaja, A. Poklad, V. Klemm, G. Schreiber, D. Heger, M. Šíma, M. Dopita, *Thin Solid Films* 514 (2006) 240.
- [7] D. Rafaja, A. Poklad, V. Klemm, G. Schreiber, D. Heger, M. Šíma, *Mater. Sci. Eng., A* 462 (2007) 279.
- [8] S. Veprek, A.S. Argon, *Surf. Coat. Technol.* 146–147 (2001) 175.
- [9] P.H. Mayrhofer, C. Mitterer, H. Clemens, *Adv. Eng. Mater.* 7 (2006) 1071.
- [10] A. Niederhofer, T. Bolom, P. Nesladek, K. Moto, C. Eggs, D.S. Patil, S. Veprek, *Surf. Coat. Technol.* 146–147 (2001) 183.
- [11] P.H. Mayrhofer, A. Hörling, L. Karlsson, J. Sjöln, T. Larsson, C. Mitterer, L. Hultman, *Appl. Phys. Lett.* 83 (2003) 2049.
- [12] F. Adibi, I. Petrov, L. Hultman, U. Wahlström, T. Shimizu, D. McIntyre, J.E. Greene, J.-E. Sundgren, *J. Appl. Phys.* 69 (1991) 6437.
- [13] H.-D. Männling, D.S. Patil, K. Moto, M. Jílek, S. Veprek, *Surf. Coat. Technol.* 146 (2001) 263.
- [14] A. Hörling, L. Hultman, M. Odén, J. Sjöln, L. Karlsson, *J. Vac. Sci. Technol., A, Vac. Surf. Films* 20 (2002) 1815.
- [15] R.F. Zhang, S. Veprek, *Acta Mater.* 55 (2007) 4615.
- [16] D. Rafaja, A. Poklad, G. Schreiber, V. Klemm, D. Heger, M. Šíma, *Z. Metallkd.* 96 (2005) 736.
- [17] M. Dopita, D. Rafaja, C. Wüstefeld, M. Růžicka, V. Klemm, D. Heger, G. Schreiber, M. Šíma, *Surf. Coat. Technol.* 202 (2008) 3199.
- [18] D. Rafaja, C. Wüstefeld, M. Dopita, M. Růžicka, V. Klemm, G. Schreiber, D. Heger, M. Šíma, *Surf. Coat. Technol.* 201 (2007) 9476.
- [19] P.H. Mayrhofer, C. Mitterer, L. Hultman, H. Clemens, *Prog. Mater. Sci.* 51 (2006) 1032.
- [20] A. Escudero Santana, A. Karimi, V.H. Derflinger, A. Schütze, *Thin Solid Films* 469–470 (2004) 339.
- [21] R.F. Zhang, S.H. Sheng, S. Veprek, *Appl. Phys. Lett.* 91 (2007) 031906.
- [22] S. Veprek, M.G.J. Veprek-Heijman, *Surf. Coat. Technol.* 201 (2007) 6064.
- [23] P. Holubář, M. Jílek, M. Šíma, *Surf. Coat. Technol.* 133/134 (2000) 145.
- [24] W.C. Oliver, G.M. Pharr, *J. Mater. Res.* 7 (1992) 1564.
- [25] I.C. Noyan, J.B. Cohen, *Residual stresses – measurement by diffraction and interpretation*, Springer, New York, 1987.
- [26] D. Rafaja, V. Valvoda, R. Kužel, A.J. Perry, J.R. Treglio, *Surf. Coat. Technol.* 86–87 (1996) 302.
- [27] D. Rafaja, M. Dopita, M. Růžicka, V. Klemm, D. Heger, G. Schreiber, M. Šíma, *Surf. Coat. Technol.* 201 (2006) 2835.
- [28] R. Kužel, R. Černý, V. Valvoda, M. Blomberg, M. Merisalo, *Thin Solid Films* 247 (1994) 64.
- [29] C. Kral, W. Lengauer, D. Rafaja, P. Ettmayer, *J. Alloys Compd.* 265 (1998) 215.
- [30] F. Attar, T. Johansson, *Thin Solid Films* 258 (1995) 205.
- [31] D. Rafaja, V. Klemm, G. Schreiber, M. Knapp, R. Kužel, *J. Appl. Crystallogr.* 37 (2004) 613.
- [32] D. Rafaja, V. Klemm, M. Dopita, *Int. Union Crystallogr.* 34 (2007) 7 <http://www.iucr-cpd.org/Newsletters.htm>.
- [33] ICSD Database, Version 2007-2, FIZ Karlsruhe & NIST (2007).
- [34] P.J. Martin, A. Bendavid, J.M. Cairney, M. Hoffman, *Surf. Coat. Technol.* 200 (2005) 2228.
- [35] G.K. Williamson, A.H. Hall, *Acta Metall. Mater.* 1 (1953) 22.
- [36] M.A. Krivoglaz, *X-ray and Neutron Diffraction in Non-ideal Crystals*, Springer, Berlin, 1996, p. 357.
- [37] P. Scherrer, *Gött. Nachr.* 56 (1918); A.L. Patterson, *Phys. Rev.* (1939) 978.
- [38] F.C. Frank, Report on the Symposium on Plastic Deformation of Crystalline Solids (Carnegie Institute of Technology and Office of Naval Research, U.S. Government Printing Office, Washington, 1950, p. 150).
- [39] C.S. Sandu, R. Sanjinés, M. Benkahoul, M. Parlinska-Wojtan, A. Karimi, F. Lévy, *Thin Solid Films* 496 (2006) 336.
- [40] C.S. Sandu, R. Sanjinés, M. Benkahoul, F. Medjani, F. Lévy, *Surf. Coat. Technol.* 201 (2006) 4083.
- [41] A. Flink, T. Larsson, J. Sjöln, L. Karlsson, L. Hultman, *Surf. Coat. Technol.* 200 (2005) 1535.
- [42] P.H. Mayrhofer, D. Music, J.M. Schneider, *Appl. Phys. Lett.* 88 (2006) 071922.
- [43] R.F. Zhang, S. Veprek, *Phys. Rev., B* 76 (2007) 174105.
- [44] R.F. Zhang, S. Veprek, *Mater. Sci. Eng., A* 448 (2007) 111–119.
- [45] P.H. Mayrhofer, F.D. Fischer, H.J. Böhm, C. Mitterer, J.M. Schneider, *Acta Mater.* 55 (2007) 1441.

Chapter 8

Dopita M., Rafaja D.,
X-ray residual stress measurement in titanium nitride thin films,
Zeitschrift für Kristallographie, **23**, (2006), 67-72.

X-ray residual stress measurement in titanium nitride thin films

M. Dopita^{1*}, D. Rafaja²

¹Charles University, Faculty of Mathematics and Physics, Ke Karlovu 3, 121 16 Praha 2, Czech Republic

²Institute of Physical Metallurgy, TU Bergakademie Freiberg, Gustav-Zeuner-Str. 5, D-09599 Freiberg, Germany

*Contact author, e-mail: dopita@mag.mff.cuni.cz

Keywords: X-ray diffraction, thin films, residual stress

Abstract. This contribution compares and discusses three different approaches commonly used for determination of the residual stresses from X-ray diffraction data – the $\sin^2\psi$, $f(\psi)$ and the Direct Solution method. For the calculation of the X-ray elastic constants (XECs), three grain interaction models were compared – Reuss, Voigt and Neerfeld-Hill. The best reliability of the results was achieved using the $f(\psi)$ method because of its highest statistical relevance. The elastic grain interaction of the thin films was most accurately described by the Reuss model.

Introduction

Thin polycrystalline films play a very important role in many technical applications. In particular, TiN thin films are extensively used as coatings for drills and cutting tools because of their ultra-high hardness and high corrosion and wear resistance. Crucial parameters influencing strongly the mechanical properties of the thin films are the residual stress and the degree of the mechanical anisotropy, which is caused by the anisotropy of the elastic constants and related to the interaction between neighbouring crystallites. In this study, we investigated the microstructure of CVD thin TiN films on sintered tungsten carbides in terms of the stress-free lattice parameters, residual stresses and mechanical interaction between neighbouring crystallites (i.e. elastic grain interaction). A precise knowledge of the stress-free lattice parameter, together with the information on the overall chemical composition, specifies whether foreign atoms are accommodated in the host crystal structure or not. Three approaches were used for data analysis: the $\sin^2\psi$ method [1], the $f(\psi)$ method [2] (a modification of this method is known as the crystallite group method [3]) and the Direct Solution method [4].

Experimental details

Thin films of titanium nitride were deposited using CVD on cemented carbide substrates at approximately 900°C. Two samples are discussed in this study, which were deposited on

substrates with slightly different Co and (Ta, Nb) C contents in the tungsten carbide. Thickness of the thin films was roughly 4 μm . The substrate material was mechanically pre-cleaned and chemically cleaned before deposition.

The X-ray diffraction measurements were performed with $\text{CuK}\alpha$ radiation on a Seifert PTS 3000 diffractometer equipped with an Eulerian cradle (ψ -diffractometer). Such diffractometer allows the sample to be tilted about the angle ψ from the coplanar geometry. This setup requires an X-ray tube with a point focus. Because of a rapid decrease of the diffracted intensity with increasing diffraction angle 2θ (due to the small thickness and high surface roughness of the thin films), only first few reflections were recorded. The step size was 0.05° in 2θ , the counting time 40 s per step. Specimens were tilt between -25° and 25° from the symmetrical position; the increments of the tilting angle were chosen to obtain equidistant steps in $\sin^2 \psi$. For higher ψ , diffracted intensity was too low (due to the collimation of the primary beam, small thickness and high surface roughness of the thin films) to get useful diffraction data. For each sample, pole figures were measured to get information on the preferred orientation of crystallites.

For an accurate calculation of the residual stress, the lattice strain has to be measured with the relative accuracy of 10^{-4} or better. Therefore, the effect of the instrumental aberrations on the peak positions must be corrected. For the ψ -diffractometer, the main sources of the instrumental aberrations are the shift of the zero position of the diffractometer and the sample displacement like for conventional diffractometers, and the shift of the incident beam from the ψ axis (irradiated area is displaced from the ψ axis). For all aberrations mentioned above, particular analytical expressions exist. However, the combination of these errors results in too many instrumental parameters, which cannot be refined together with the parameters of the microstructure model (see below). For this reason, the instrumental aberrations were determined using silicon standard. To keep the position of the sample possibly unchanged, the samples were measured once without standard and once with the silicon powder brought on the sample surface. Each calibration measurement was done in the same 2θ and ψ range as investigated samples were measured. The shift of the diffraction lines of silicon was described by a general quadratic function:

$$\Delta 2\theta = b_1 \theta^2 \psi^2 + b_2 \theta^2 \psi + b_3 \theta \psi^2 + b_4 \theta^2 + b_5 \psi^2 + b_6 \theta \psi + b_7 \theta + b_8 \psi + b_9, \quad (1)$$

The coefficients of the correction function, b_i , were refined using the least-squares method.

Residual stress analysis using X-ray diffraction

The analysis of the residual stresses using the X-ray diffraction methods is based on the measurement of the interplanar spacing in different macroscopic directions. This yields information on the elastic lattice deformation that must be recalculated into the residual stress using suitable diffraction elastic constants. Assuming a rotationally symmetrical biaxial state of the residual stress (quasi-isotropic specimen, no shear stress), which is usually satisfied in the case of thin films, the dependence of the elastic lattice deformation ε_{ψ}^{hkl} on the inclination from the perpendicular direction ψ can be expressed in the form of the so-called $\sin^2 \psi$ formula [1]:

$$\varepsilon_{\psi}^{hkl} = \frac{d_{\psi}^{hkl} - d_0}{d_0} = \frac{a_{\psi}^{hkl} - a_0}{a_0} = \left(2s_1^{hkl} + \frac{1}{2}s_2^{hkl} \sin^2 \psi \right) \sigma_{\parallel}, \quad (2)$$

In (2), the symbols hkl are the Miller indices of the crystallographic planes. s_l^{hkl} are the X-ray elastic constants (XECs) that are, in general, dependent on the crystallographic direction.

In our study, the XECs were calculated from the single-crystalline elastic constants [5] using alternatively Voigt [6], Reuss [7] and Neerfeld-Hill [8, 9] models. The Voigt model supposes the same strain tensor in all crystallites independent of their orientation. The Reuss model assumes the same stress tensor in all crystallites. In a material composed from elastically anisotropic crystallites, the lattice strain within the Reuss model depends consequently on the crystallographic direction. The Neerfeld-Hill model [8, 9] yields the XECs as an average of the elastic constants obtained from the Voigt and Reuss models.

Experimental results

1) The $\sin^2\psi$ method

An example of the dependence of the lattice parameters a_ψ^{hkl} on $\sin^2\psi$ is shown in figure 1. a_ψ^{hkl} were calculated from the corrected line positions using the Bragg equation and the relationship between the d-spacing and the lattice parameter. The mechanical anisotropy of the thin film is apparent from different offsets and different slopes of the a_ψ^{hkl} vs. $\sin^2\psi$ plots for different crystallographic planes. The residual stress $\sigma_{||}$ can be calculated from (2), if the XECs are known for the respective crystallographic direction $\{hkl\}$. The stress-free lattice parameter, a_0 , is obtained from the a_ψ^{hkl} vs. $\sin^2\psi$ plot at $\sin^2\psi_0 = -4 s_l^{hkl} / s_2^{hkl}$.

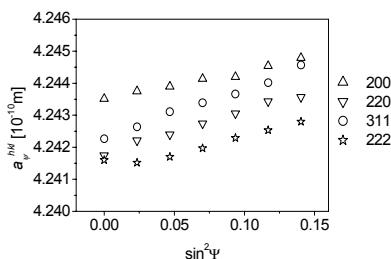


Figure 1. The $\sin^2\psi$ plot for reflections hkl measured in the sample B.

2) The $f(\psi)$ method

The $f(\psi)$ method involves the XECs directly into the construction of the dependence of the measured lattice parameters on the macroscopic direction. The lattice parameters are plotted as a function of $f(\psi) = 2s_l^{hkl} + 1/2 s_2^{hkl} \sin^2\psi$. All crystallographic directions are taken into account during the calculation of the residual stress and the stress-free lattice parameter, which improves the reliability of results. Still, an appropriate grain interaction model must be used for calculation of the XECs. The residual stress is calculated from the slope of the a_ψ^{hkl} vs. $f(\psi)$ plot; the stress-free lattice parameter is to be found at $f(\psi) = 0$. An example illustrating the effect of the mechanical anisotropy is shown in figure 2. The Voigt model is apparently not suitable for fitting the experimental data as it cannot explain the observed anisotropy of the lattice deformation (the dependence of the lattice deformation on the crystallographic direction).

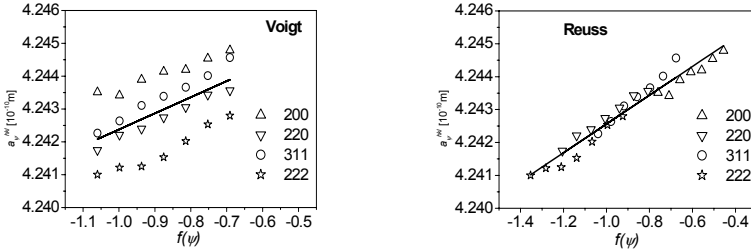


Figure 2. The a_{ψ}^{hkl} vs. $f(\psi)$ plot for Voigt and Reuss crystallite interaction models. Data were taken on the sample A.

3) Direct Solution method

The last method in this comparison uses mechanical (averaged) elastic constants s_i^{mech} for the calculation of the dependence of the elastic lattice deformation on the macroscopic direction ψ (for detailed description of the method, see [4]):

$$\varepsilon_{\psi}^{hkl} = \frac{a_{\psi}^{hkl} - a_0}{a_0} = \left\{ 2s_1^{mech} + 2K_2 \left(\Gamma - \frac{1}{5} \right) + \left[\frac{1}{2} s_2^{mech} - 3K_2 \left(\Gamma - \frac{1}{5} \right) \right] \sin^2 \psi \right\} \sigma_{\parallel} \quad (3)$$

The mechanical elastic constants can easily be calculated from the Young's modulus E and from the Poisson ratio ν : $s_1^{mech} = -\nu / E$, $\frac{1}{2} s_2^{mech} = (1 + \nu) / E$. To be able to compare the different grain interaction models, s_1^{mech} and s_2^{mech} were calculated from the XECs, see [4]. $\Gamma(hkl) = (h^2 k^2 + h^2 l^2 + k^2 l^2) / (h^2 + k^2 + l^2)^2$ is the well-known cubic orientation factor. K_2 is a parameter that quantifies the effect of the anisotropy of the single-crystalline elastic constants on the crystallographic anisotropy of the observed lattice strain in a polycrystalline sample. It can either be calculated from the respective grain interaction model or refined by using the least-squares method [4]. A combination of both approaches was applied in our work. K_2 was taken from [4] and fixed in the first step of the refinement; only a_0 and σ_{\parallel} were refined. In the second step of the fitting procedure, the parameter K_2 was refined additionally. The effect of the starting grain interaction model on the refined data is illustrated in figure 3.

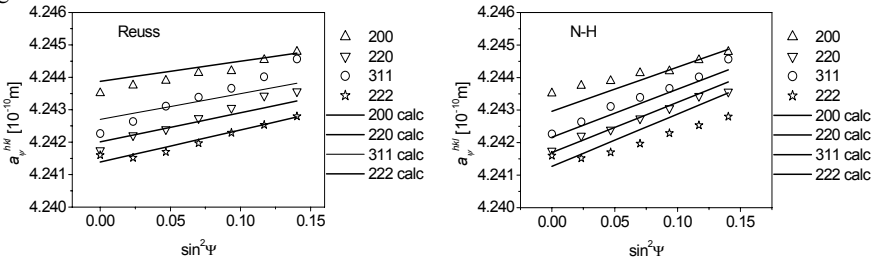


Figure 3. Measured (symbols) and fitted (lines) data for measured reflections and Reuss and Neerfeld-Hill (N-H) interaction models using Direct Solution method. The data were taken for the sample B.

Table 1 summarises the residual stresses and the stress-free lattice parameters for the samples A and B as obtained using the $\sin^2 \psi$ and $f(\psi)$ methods. Table 2 summarises the residual

stresses, stress-free lattice parameters and the degree of anisotropy of the lattice deformation for both samples as calculated using the Direct Solution method.

Table 1. Residual stress and stress-free lattice parameter for both samples obtained using the $\sin^2\psi$ and $f(\psi)$ methods. Standard deviations in estimation of individual stress free lattice parameter are of order of 10^{-4} - 10^{-3} Å, those for residual stresses of 0.1 GPa.

sample	A						B					
	Reuss		Voigt		N-H		Reuss		Voigt		N-H	
model	σ [GPa]	a_0 [Å]	σ [GPa]	a_0 [Å]	σ [GPa]	a_0 [Å]	σ [GPa]	a_0 [Å]	σ [GPa]	a_0 [Å]	σ [GPa]	a_0 [Å]
$\sin^2\psi$												
200	0.96	4.2487	0.71	4.2491	0.98	4.2489	1.06	4.2478	0.87	4.2477	0.96	4.2480
220	0.79	4.2480	0.86	4.2478	0.84	4.2479	1.09	4.2470	1.12	4.2468	1.13	4.2479
311	0.77	4.2475	0.75	4.2475	0.76	4.2475	1.16	4.2473	1.21	4.2470	1.35	4.2477
222	0.95	4.2463	1.00	4.2458	1.02	4.2461	0.99	4.2460	0.96	4.2453	0.88	4.2460
<hkl>	0.87	4.2476	0.83	4.2475	0.90	4.2476	1.08	4.2470	1.04	4.2467	1.08	4.2474
e.s.d.	0.10	0.0009	0.13	0.0014	0.12	0.0012	0.07	0.0008	0.15	0.0010	0.21	0.0009
$f(\psi)$												
	1.01	4.2486	0.94	4.2484	0.95	4.2498	1.00	4.2470	0.92	4.2458	0.97	4.2470

Table 2. Residual stress, stress-free lattice parameter and the degree of the mechanical anisotropy for both samples obtained using the Direct Solution method.

sample	A			B		
	K_2 [TPa ⁻¹]	a_0 [Å]	σ [GPa]	K_2 [TPa ⁻¹]	a_0 [Å]	σ [GPa]
Reuss	-0.76(8)	4.2487(6)	0.97(6)	-0.79(9)	4.2472(4)	0.96(7)
Voigt	0	4.2483(11)	0.91(13)	0	4.2463(12)	0.85(15)
N-H	-0.48(11)	4.2497(9)	0.95(9)	-0.51(10)	4.2470(8)	0.92(11)

The microstructure parameters obtained from the $\sin^2\psi$ -method (a_0 and σ) vary for individual reflections. The amount of this variation (e.s.d. in table 1) indicates the suitability or unsuitability of the respective grain interaction model. Although the same XECs were used for the $\sin^2\psi$ and the $f(\psi)$ methods, the arithmetic means of the residual stresses and the stress-free lattice parameters obtained from the $\sin^2\psi$ method (<hkl> in table 1) were not identical with the parameters obtained from the $f(\psi)$ method. The reason is different averaging of the refined parameters in both approaches. The microstructure parameters calculated using the direct solution method match with those obtained from the $f(\psi)$ method within the experimental accuracy. This is consistent with the result that the starting K_2 -value was only insignificantly changed during the refinement.

It is evident that the linear fits in figures 2 and 3 do not approximate the experimental data exactly. The departure of the experimental data from the solid lines correlates with the variation of the microstructure parameters calculated for different crystallographic directions from the $\sin^2\psi$ method. The differences between the experimental data and the linear fit shows furthermore that none of the grain interaction models can doubtless be applied to the thin films under study. The reasons could be a different interaction between crystallites in samples with tensile (our samples) and compressive residual stresses [4] and/or different origin of the residual stress. In our samples, the residual stress results from a combination of the

different thermal expansion of the substrate and the thin film with the diffusion of carbon into the thin films during the CVD deposition process. The penetration of carbon into the thin films was indicated by the observed increase of the stress-free lattice parameters comparing with the intrinsic value of 4.2418 \AA [10], and confirmed by wavelength-dispersive X-ray analysis (WDX). The presence of tensile residual stress of $(1.0 \pm 0.1) \text{ GPa}$ in our samples can cause a development of local cracks or voids in the thin films, which can modify the interaction between adjacent crystallites and change the observed anisotropy of the lattice parameters with respect to the applied grain interaction model.

Summary

In the CVD TiN thin films deposited on cemented carbides, a strong anisotropy of the measured lattice parameters – dependence of the lattice parameter on the crystallographic direction – was observed. The difference between the lattice parameters measured on the lattice planes $\{h00\}$ and the stress-free lattice parameter is significantly smaller than the departure of the lattice parameters obtained from the interplanar spacing of the lattice planes $\{hhh\}$ from the stress-free lattice parameter. Such anisotropy is related to the $\{111\}$ easy deformation direction as known for TiN and similar compounds [11,12]. Tensile residual stress of $(1.0 \pm 0.1) \text{ GPa}$ was found in both samples. To compare the three approaches discussed above, we can summarise that we achieved the best reliability of the microstructure parameters using the grain interaction model, which yields anisotropic lattice strain in a polycrystalline sample, in conjunction with a method of the residual stress calculation, which uses whole set of measured data. For our samples, the most reliable results were obtained using the Reuss model and $f(\psi)$ or the Direct Solution methods.

References

1. Noyan I.C., Cohen J.B., 1987, *Residual Stress*, (Berlin: Springer Verlag).
2. Perry A.J., Valvoda V. and Rafaja D., 1992, *Thin Solid Films*, **214**, 169.
3. Kuzel R., Cerny R., Valvoda V., Blomberg M., Merisalo M., 1994, *Thin Solid Films* **247**, 64.
4. Kamminga J.-D., De Keijser T.H., Mittemeijer E.J. and Delhez R., 2000, *J. Appl. Cryst.*, **33**, 1059.
5. Kim J.O., Achenbach J.D., Mirkarimi P.B., Shinn M., Barnett S.A., 1992, *J. Appl. Phys.*, **72**, 1805.
6. Voigt W., 1910, *Lehrbuch der Kristallphysik*, (Berlin, Leipzig: Teubner).
7. Reuss A., 1929, *Z. Angew. Math. Mech.*, **9**, 49.
8. H. Neerfeld, 1942, *Mitt. K.-Wilh.-Inst. Eisenforschg.*, **24**, 61.
9. Hill R., 1952, *Proc. Phys. Soc. London*, **65**, 349.
10. Pluger J., Fink J., Weber W. and Bohnen K.-P., 1984, *Phys. Rev. B*, **30**, 1155.
11. Rafaja D., 2004, *Adv. Eng. Mater.*, **6**, 577.
12. Rafaja D., Havela L., Kužel R., Wastin F., Colineau E. and Gouder T., 2005, *J. Alloys Comp.*, **386**, 87.

Acknowledgements. This work is a part of the research plan MSM 0021620834 financed by the Ministry of Education of the Czech Republic.

Chapter 9

Rafaja D., Klemm V., Dopita M.,
Practical aspects of partial coherence of nanocrystalline domains,
Newsletter of the Commission on Powder Diffraction, **34**, (2007), 7-12.

PRACTICAL ASPECTS OF PARTIAL COHERENCE OF NANOCRYSTALLINE DOMAINS

David Rafaja, Volker Klemm and Milan Dopita*

Institute of Materials Science, TU Bergakademie Freiberg, Gustav-Zeuner-Str. 5, D-09599 Freiberg, Germany, E-mail: rafaja@www.tu-freiberg.de

ABSTRACT

Partial coherence of crystallites is often observed in supra-hard nanocomposites having a strong texture as an effect causing the diffraction line “narrowing”. The degree of the partial coherence depends on the crystallite size, on the local preferred orientation of crystallites and on the size of the diffraction vector. Consequently, the microstructure parameters influencing the partial coherence of crystallites can be determined from the dependence of the diffraction line broadening on the size of the diffraction vector. In some thermodynamically unstable systems, like in Ti-Al-Si-N and Cr-Al-Si-N thin films, the strongly correlated orientation of adjacent crystallites that is a necessary condition for their partial coherence can be understood as an indicator of the spinodal decomposition.

INTRODUCTION

Nanocrystalline materials are employed in many industrial applications, e.g. in materials for catalytic converters, in production of self cleaning surfaces, in magnetic nanostructures or in supra-hard nanocomposites. Nano-sized structures combine advantages of excellent chemical and physical properties that are tailored by modification of the material’s microstructure. For these reasons, the microstructure analysis on nanocrystalline materials and nanocomposites is a very important issue for materials science. Obligatory methods for the microstructure analysis on nano-sized structures are the transmission electron microscopy (TEM) and the high-resolution transmission electron microscopy (HRTEM). The X-ray diffraction (XRD) offers still some benefits, the non-destructivity, a fast and easy sample preparation, and excellent statistics being few of them. Thus, XRD is still regarded as a very important experimental method for the microstructure analysis on nanocrystalline materials and nanocomposites [1 – 9].

X-RAY SCATTERING ON NANOCRYSTALS

Within the kinematical diffraction theory, the diffracting volume of a material under study is assumed to consist of individual coherently diffracting domains called crystallites. The X-ray scattering on atomic structures is usually described by the amplitude of the scattered wave, E , which is equal to the Fourier transformation (FT) of the electron density $\rho(\vec{r})$:

$$E(\vec{q}) = \int_V \rho(\vec{r}) \exp(i\vec{q} \cdot \vec{r}) d\vec{r} = \text{FT}[\rho(\vec{r})], \quad (1)$$

where \vec{q} is the diffraction vector and \vec{r} the positions of the scattering centres. Electron density of an infinite crystal can be described as a convolution of the elec-

tron density of the unit cell $\rho_{\text{cell}}(\vec{r})$ with the lattice function $L(\vec{r})$, see, e.g. [10]:

$$\rho_{\infty}(\vec{r}) = \rho_{\text{cell}}(\vec{r}) * L(\vec{r}), \quad (2)$$

where

$$L(\vec{r}) = \sum_{n_1, n_2, n_3 = -\infty}^{\infty} \delta(\vec{r} - \vec{r}_{n_1, n_2, n_3}). \quad (3)$$

In Eq. (3), δ means the Dirac delta function, n_1 , n_2 and n_3 are integers. Analogously, the electron density of an individual crystallite $\rho_{\text{Xtal}}(\vec{r})$ can be described by convolution the electron density of the unit cell $\rho_{\text{cell}}(\vec{r})$ with the lattice function $L(\vec{r})$ multiplied by a shape function $\Omega(\vec{r})$:

$$\rho_{\text{Xtal}}(\vec{r}) = \rho_{\text{cell}}(\vec{r}) * [\Omega(\vec{r}) \cdot L(\vec{r})] \quad (4)$$

$\Omega(\vec{r})$ is equal to unity within the crystallite and zero outside. The amplitude of the wave scattered by the crystallite is then given by the Fourier transformation of the electron density $\rho_{\text{Xtal}}(\vec{r})$:

$$\begin{aligned} E(\vec{q}) &= \text{FT}[\rho_{\text{Xtal}}(\vec{r})] = \text{FT}\{\rho_{\text{cell}}(\vec{r}) * [\Omega(\vec{r}) \cdot L(\vec{r})]\} = \\ &= \text{FT}[\rho_{\text{cell}}(\vec{r})] \cdot \text{FT}[\Omega(\vec{r}) \cdot L(\vec{r})] \end{aligned} \quad (5)$$

The last term in Eq. (5), $\text{FT}[\Omega \cdot L]$, describes the shape of three-dimensionally periodic reciprocal lattice points that are broadened due to the finite crystallite size. The Fourier transformation of the electron density of a unit cell is equal to the structure factor, which in the first approximation can be treated as a constant within the size of individual reciprocal lattice points:

$$\text{FT}[\rho_{\text{cell}}(\vec{r})] = F(\vec{q}) \approx F(hk\ell) \quad (6)$$

Within one reciprocal lattice point, the amplitude of the wave scattered by a finite crystallite is consequently given by a product of the structure factor of the unit cell and the Fourier transformation of the shape factor:

$$E(\vec{q}) = F(hk\ell) \cdot \text{FT}[\Omega(\vec{r})] \quad (7)$$

The intensity scattered by the diffracting volume of material is proportional to the modulus of the sum of the amplitudes of waves scattered by individual crystallites (domains):

$$I(\vec{q}) \propto \sum_{n=1}^N [F_{hk\ell} \cdot \text{FT}(\Omega)]_n^* \cdot \sum_{n=1}^N [F_{hk\ell} \cdot \text{FT}(\Omega)]_n \quad (8)$$

Asterisk in Eq. (8) denotes the complex conjugate. The summation is performed over all crystallites within the irradiated volume of the sample. The product of the sums in Eq. (8) can easily be rewritten into the following form, which is more suitable for explaining the coherence phenomena in nanocrystalline materials:

$$\begin{aligned} I(\vec{q}) &\propto \sum_{n=1}^N [F_{hk\ell} \cdot \text{FT}(\Omega)]_n^* \cdot [F_{hk\ell} \cdot \text{FT}(\Omega)]_n + \\ &+ 2 \sum_{m=1}^{N-1} \sum_{n=1}^{N-m} [F_{hk\ell} \cdot \text{FT}(\Omega)]_n^* \cdot [F_{hk\ell} \cdot \text{FT}(\Omega)]_{n+m} \end{aligned} \quad (9)$$

The first term in Eq. (9) describes the scattering of X-rays on identical domains, i.e. the interference of waves scattered by the same crystallites. The second term describes the interference of waves scattered by different

crystallites; the distance of the crystallites is hidden in the index m . Within the kinematical diffraction theory, different crystallites are assumed to be mutually non-coherent, thus the second term is neglected. This is valid only if

$$[F_{hkl} \cdot \text{FT}(\Omega)]_n^* \cdot [F_{hkl} \cdot \text{FT}(\Omega)]_m = 0 \quad (10)$$

for $n, m = 1, \dots, N$ and $n \neq m$, i.e. if the broadened reciprocal lattice points (from different crystallites) do not overlap each other.

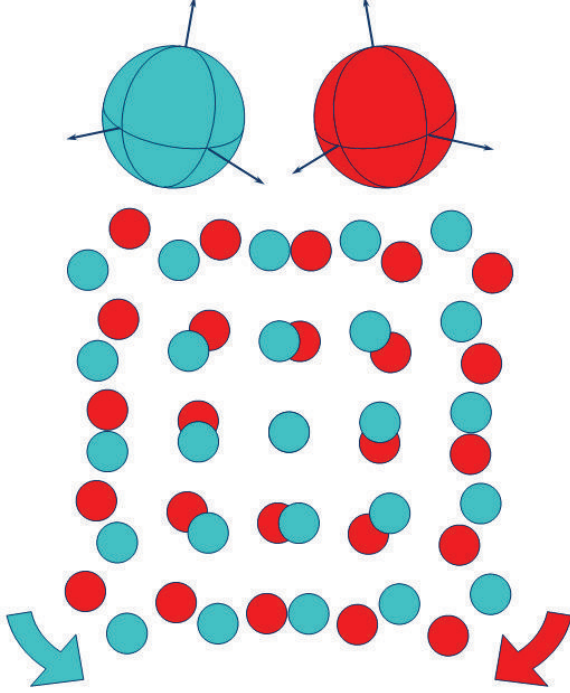


Fig. 1. Effect of the mutual disorientation of crystallites on the rotation of their reciprocal lattices. The overlap of the reciprocal lattice points from different crystallites decreases with their increasing distance from the origin of the reciprocal lattice.

A possible overlap of the reciprocal lattice points can be elucidated on the scheme shown in Fig. 1. Mutual rotation of crystallites causes opposing rotation of their reciprocal lattices around the origin of the reciprocal space. For small disorientations of nanocrystallites, i.e. crystallites having extremely broad reciprocal lattice points, some reciprocal lattice points do overlap partially (Fig. 1). This overlap can be understood as partial coherence of the crystallites. For two partially coherent crystallites, the intensity is given by the modulus of the sum of amplitudes of the waves scattered by individual crystallites, see Eq. (9):

$$I \propto |E_1 + E_2|^2 = |E_1|^2 + 2 \text{Re}(E_1^* E_2) \Gamma_{12} + |E_2|^2 \quad (11)$$

Mutual shift of crystallites modifies the phase φ of the amplitudes scattered by the respective crystallites,

$$E_1 = |E_1| \exp(i\varphi_1) \text{ and } E_2 = |E_2| \exp(i\varphi_2), \quad (12)$$

which takes effect on the “mixed” middle term in Eq. (11). Using Eq. (12), equation (11) can be rewritten into the following form:

$$I \propto |E_1|^2 + |E_2|^2 + 2|E_1||E_2| \cos(\varphi_1 - \varphi_2) \Gamma_{12} \quad (13)$$

The phase difference $(\varphi_1 - \varphi_2)$ is given by the scalar product of \vec{q} and \vec{R} , where \vec{R} is the distance between the two crystallites involved in the scattering process. The parameter Γ_{12} occurring in equations (11) and (13) characterises the degree of coherence of the radiation [11], which is related to the coherence length of the radiation in the longitudinal direction [12] that can be calculated from the Heisenberg uncertainty relation:

$$\Lambda = \frac{\lambda^2}{2\Delta\lambda} \quad (14)$$

The coherence length of the $\text{CuK}\alpha_1$ radiation emitted by a sealed X-ray tube ($\lambda = 1.54056 \text{ \AA}$, $\Delta\lambda = 3.615 \times 10^{-4} \text{ \AA}$) is approximately $0.33 \text{ }\mu\text{m}$, which is sufficient to accommodate up to a hundred of neighbouring nanocrystallites within the coherence length.

Another parameter influencing the degree of the coherence of adjacent crystallites is the product of $|E_1|$ and $|E_2|$ in Eq. (13). As discussed above, this product is non-zero only if the reciprocal lattice points from these crystallites are overlapping each other. Figures 2, 3 and 4 illustrate the effect of the overlap of the reciprocal lattice points on the shape of the two-dimensional intensity maxima in form of the $\Delta q_x/\Delta q_z$ -scans. Δq_x is proportional to the crystallite’s disorientation; Δq_z denotes the distance from the diffraction maximum. In the microstructure model used for simulation of the partial coherence phenomena that are shown in Figures 2 – 4, spherical crystallites were displaced along the z direction. Their displacement was equal to their size, which means that the crystallites were assumed to be in direct contact. For spherical crystallites, the Fourier transform of the shape factor is given by the equation:

$$\begin{aligned} \text{FT}[\Omega(\vec{q})] &= \int_{\text{Sphere}} \exp(i\vec{q} \cdot \vec{r}) d\vec{r} = \\ &= \frac{4\pi}{|\vec{q}|^2} \left(\frac{\sin|\vec{q}|R}{|\vec{q}|} - R \cos|\vec{q}|R \right), \end{aligned} \quad (15)$$

where R is the radius of the sphere and

$$|\vec{q}| = \frac{4\pi}{\lambda} \sin \theta \quad (16)$$

the size of the diffraction vector. In a polycrystalline material consisting of pairs of partially coherent crystallites, the reciprocal lattice points shown in Figures 2 – 4 are distributed along a sphere, for which $|\vec{q}| = \text{const}$. This distribution corresponds to different orientations of the pairs of partially coherent crystallites. Regarding the resolution of a diffractometer in the q_x direction, the registered intensity is, in fact, integrated over a broad q_x range:

$$I \approx \int [|E_1|^2 + |E_2|^2 + 2|E_1||E_2| \cos(\vec{q} \cdot \vec{R})] dq_x \quad (17)$$

and depends consequently only on q_z .

According to Eq. (7), the amplitudes E_1 and E_2 are given by the Fourier transformations of the shape factors of the disoriented crystallites that follow, for spherical crystallites with the radius R , from Eq. (15).

$$E_1 = FT[\Omega(\vec{q} + \Delta\vec{q})] = \frac{4\pi}{|\vec{q} + \Delta\vec{q}|^2} \left(\frac{\sin|\vec{q} + \Delta\vec{q}|R}{|\vec{q} + \Delta\vec{q}|} - R \cos|\vec{q} + \Delta\vec{q}|R \right) \quad (18)$$

$$E_2 = FT[\Omega(\vec{q} - \Delta\vec{q})] = \frac{4\pi}{|\vec{q} - \Delta\vec{q}|^2} \left(\frac{\sin|\vec{q} - \Delta\vec{q}|R}{|\vec{q} - \Delta\vec{q}|} - R \cos|\vec{q} - \Delta\vec{q}|R \right) \quad (19)$$

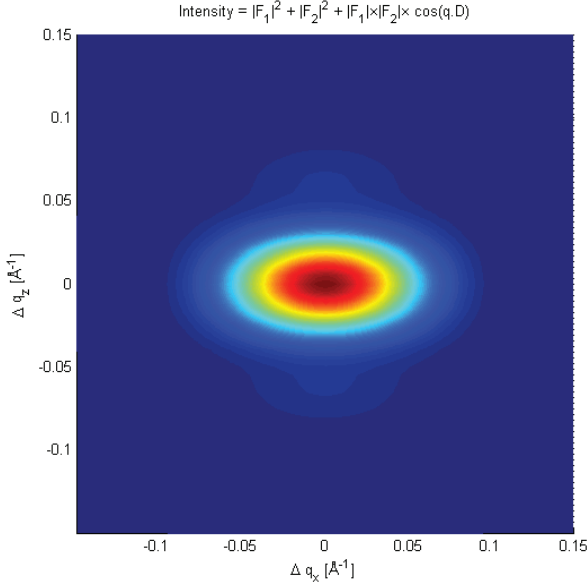


Fig. 2. Two-dimensional intensity distribution as calculated using Eqs. (7), (13) and (15) for fully coherent crystallites having the size of 30 Å. The reciprocal lattice points were completely overlapping each other.

Consequently, the radial intensity distribution, i.e. the dependence of the intensity on q_z , depends strongly on the degree of the partial coherence of crystallites, which is hidden in the coherence term of Eq. (17). The change of the line broadening and the change of the line shape are illustrated in Fig. 5. For non-coherent crystallites (Fig. 4), the scattered intensity corresponds to the sum of the intensities scattered by individual crystallites. Thus, the line width and the line shape remain the same as for individual crystallites, like in the classical kinematical diffraction theory. For fully coherent crystallites replaced in the z direction, the scattered intensity (Fig. 2) is modulated additionally by the cosine term from Eq. (17) in the q_z direction, which causes an obvious decrease of the line broadening in this direction (Fig. 5). For partially coherent crystallites (Fig. 3), the line broadening along q_z lies between the line broadening from fully coherent and non-coherent crystallites. Moreover, the diffraction lines from partially coherent crystallites become Cauchy-like in shape due to their long tails in the q_z direction, see Fig. 3.

DIFFRACTION LINE BROADENING

In [6], we have shown that the diffraction line broadening from partially coherent crystallites can be divided

into three regions that are shown in Fig. 6. For $\sin \theta \rightarrow 0$, the diffraction line broadening is given by the maximum size of domains, which consist of several partially coherent crystallites. At medium diffraction angles, the diffraction line broadening steeply increases with increasing diffraction angle as the degree of the partial coherence (as well as the overlap of the reciprocal lattice points, see Fig. 1) decreases in this range.

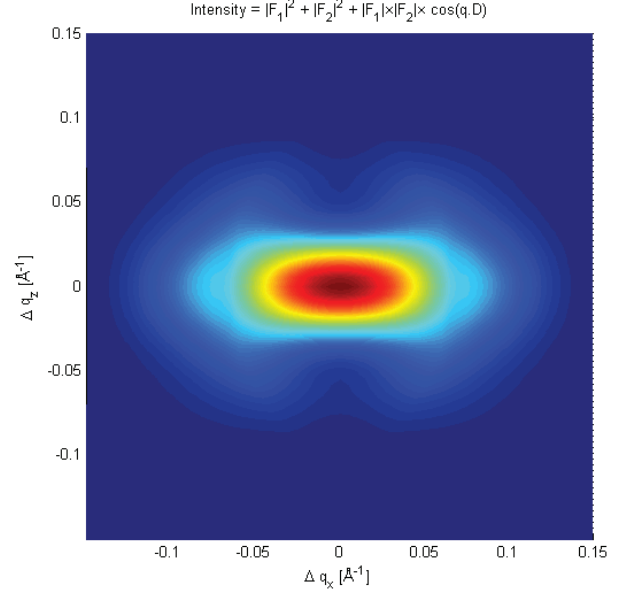


Fig. 3. Two-dimensional intensity distribution as calculated using Eqs. (7), (13), (15) for partially coherent crystallites having the size of 30 Å. The distance of the reciprocal lattice points was 0.09 Å⁻¹ along q_x .

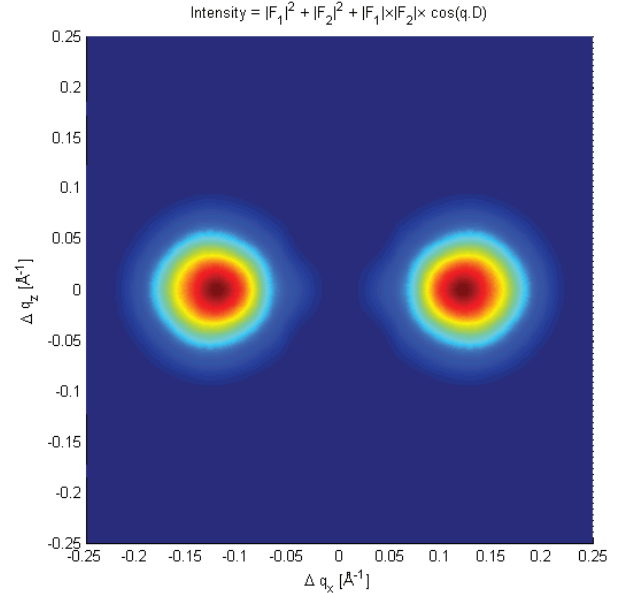


Fig. 4. Two-dimensional intensity distribution as calculated using Eqs. (7), (13), (15) for non-coherent crystallites having the size of 30 Å. The distance of the reciprocal lattice points was 0.15 Å⁻¹ along q_x .

At the largest diffraction angles, the reciprocal lattice points do not overlap, which means that the coherence

of neighbouring crystallites disappears completely. In this angular range, the diffraction line broadening remains constant, being approximately equal to the reciprocal size of individual (non-coherent) crystallites.

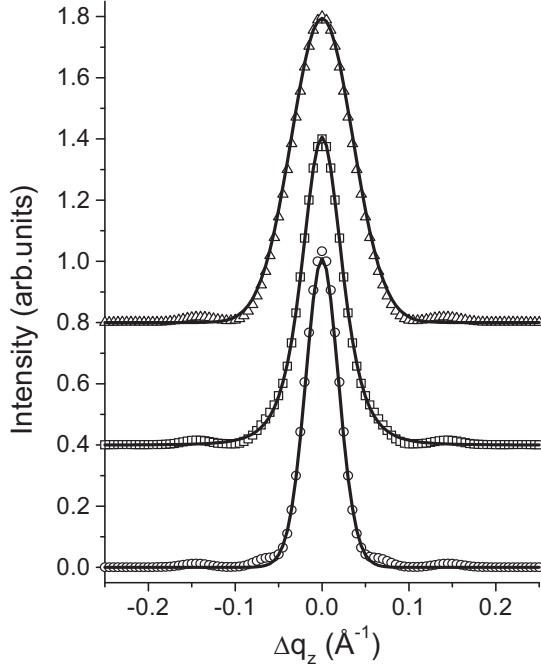


Fig. 5. Diffraction profiles calculated using equations (17), (18) and (19) for incoherent, partially coherent and fully coherent crystallites (from the top to the bottom). The displacement of the reciprocal lattice points is the same like in Figures 4, 3 and 2, respectively.

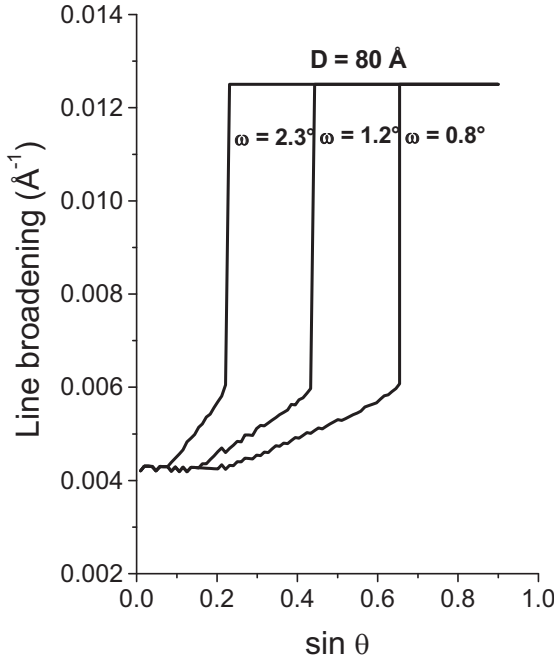


Fig. 6. Diffraction line broadening as calculated according to Ref. [6] for partially coherent crystallites with the size of 80 Å and with the disorientation of 0.8°, 1.2° and 2.3°. Small oscillations in the range of the in-

creasing line broadening are due to the numerical errors.

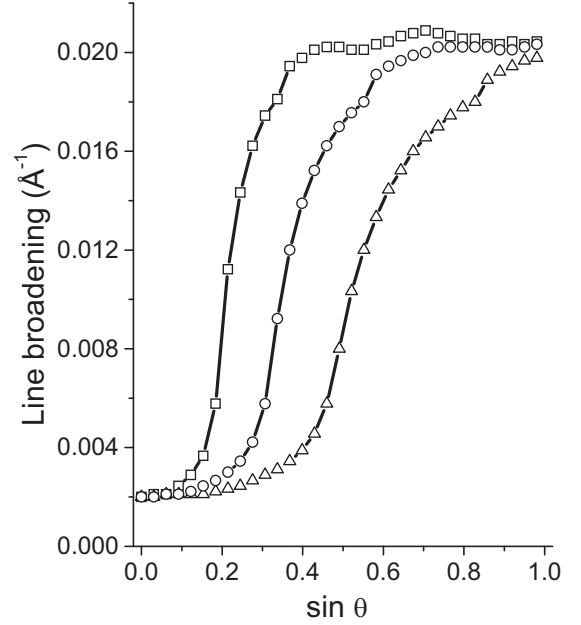


Fig. 7. Diffraction line broadening as calculated according to equations (17), (18) and (19) for partially coherent crystallites with the size of 50 Å and with the disorientation of 1.0° (triangles), 1.5° (circles) and 2.5° (boxes).

An analogous dependence of the diffraction line broadening on the diffraction angle can also be derived using the approach described in the previous Section. The line broadening shown in Fig. 7 was obtained from fitting the diffraction profiles calculated using equations (17), (18) and (19) by the Pearson VII function. Some examples of the line profile fitting are shown in Fig. 5. In both approaches discussed above, the minimum and the maximum diffraction line broadening correspond to the size of clusters of partially coherent crystallites and to the size of non-coherent crystallites, respectively. The main difference between these approaches is the steepness of the increase of the diffraction line broadening with increasing diffraction angle. The microstructural model described in [6] assumes a continuous distribution of the disorientations of neighbouring crystallites between zero and a maximum disorientation, which increases the degree of the coherence in the middle range of the diffraction angles and shifts the steep increase of the diffraction line broadening to larger diffraction angles. Consequently, the higher degree of the partial coherence of crystallites in the middle range of the diffraction angles causes a steeper increase of the diffraction line broadening at larger diffraction angles. The other microstructural model, which was used for the approach described in the previous Section, assumes a constant disorientation of neighbouring crystallites in the clusters of partially coherent crystallites, which leads to a gradual decay of the partial coherence of crystallites that is demonstrated by a slower increase of the diffraction line broadening with increas-

ing diffraction angle. These two approaches characterise approximately the limit cases of the scattering on partially coherent crystallites.

EXPERIMENTAL EXAMPLES

For the first time, the coherence of nanocrystalline domains was observed in the Ti-Al-N [6, 9] and Ti-Al-Si-N [9] nanocomposites, for which the spinodal decomposition was reported [13 – 16]. Recently, we observed the partial coherence of nanocrystallites in the Cr-Al-Si-N nanocomposites [17]. The relationship between the spinodal decomposition and the partial coherence of crystallites was discussed in [9] on the example of the Ti-Al-N and Ti-Al-Si-N systems. A requirement for the partial coherence of nanocrystallites is their small disorientation (see Figures 1, 2, 3, 6 and 7). The maximum amount of the disorientation of coherent nanocrystallites depends both on their size and on the minimum distance of the reciprocal lattice points from the origin of the reciprocal space, i.e. on the lattice parameter and the lattice type, but it typically does not exceed 3° . Ti-Al-N and Ti-Al-Si-N nanocomposites contain fcc-(Ti, Al) N phase with the NaCl structure and hexagonal AlN phase with the wurtzitic structure. As we have shown in [9], a very strong local preferred orientation of crystallites can be transferred between cubic crystallites through the hexagonal phase as some interplanar distances are similar in these particular crystal structures.

Two examples illustrating the partial coherence of nanocrystallites in the Cr-Al-Si-N nanocomposites having the chemical compositions $\text{Cr}_{0.40}\text{Al}_{0.52}\text{Si}_{0.08}\text{N}$ and $\text{Cr}_{0.91}\text{Al}_{0.08}\text{Si}_{0.01}\text{N}$ are shown in Fig. 8. The simulation of the line broadening for partially coherent crystallites was performed using the routine described in [6] and is shown by solid lines in Fig. 8. For the sample $\text{Cr}_{0.40}\text{Al}_{0.52}\text{Si}_{0.08}\text{N}$, the simulation yielded the crystallite size of $(47 \pm 3) \text{ \AA}$. The disorientations of crystallites are larger than 3° as estimated from the position of the steep increase of the line broadening with increasing diffraction angle; the crystallites are non-coherent in the accessible range of the diffraction angles. The crystallite size was verified by transmission electron microscopy with high resolution (HRTEM), see Fig. 9. The dependence of the diffraction line broadening on the size of the diffraction vector measured for the $\text{Cr}_{0.91}\text{Al}_{0.08}\text{Si}_{0.01}\text{N}$ nanocomposite indicated clearly the partial coherence of neighbouring crystallites. From the size of the diffraction vector, for which the steep increase of the line broadening was observed, and from the maximum (saturated) line broadening, the mean disorientation of crystallites of $(0.6 \pm 0.1)^\circ$ and the crystallite size of $(117 \pm 7) \text{ \AA}$ was determined, respectively. From extrapolation of the diffraction line broadening to $\sin \theta = 0$ (dashed line in Fig. 8), the size of the partially coherent domains was estimated to be between 500 and 600 \AA .

Thus, it can be concluded that the sample with the chemical composition $\text{Cr}_{0.91}\text{Al}_{0.08}\text{Si}_{0.01}\text{N}$ consists of small slightly disoriented crystallites that create large blocks containing 4 – 5 small partially coherent crystal-

lites. Large blocks are mutually strongly disoriented and therefore non-coherent. The microstructure of this sample is illustrated by the HRTEM micrograph in Fig. 10. One large block can be seen in the middle of the picture. It consists from several small partially coherent crystallites (dark regions in Fig. 10). Small disorientation of the partially coherent crystallites was confirmed by the presence of the moiré pattern [18].

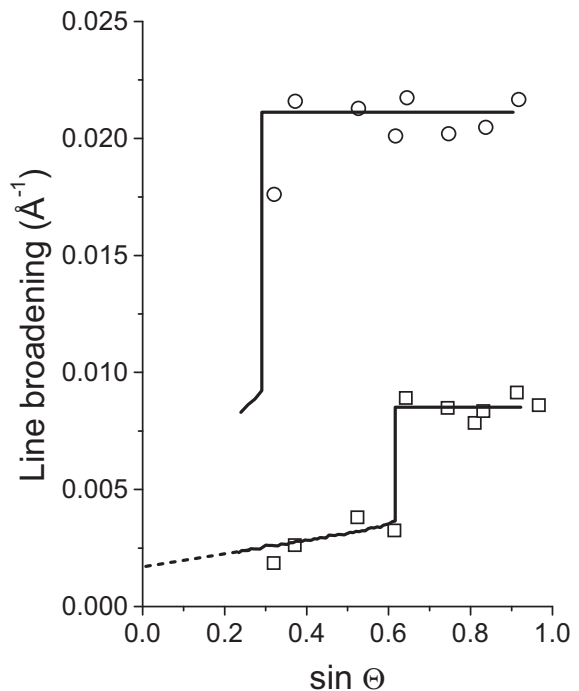


Fig. 8. Diffraction line broadening observed in samples $\text{Cr}_{0.40}\text{Al}_{0.52}\text{Si}_{0.08}\text{N}$ (circles) and $\text{Cr}_{0.91}\text{Al}_{0.08}\text{Si}_{0.01}\text{N}$ (boxes) [17]. The instrumental line broadening measured using the LaB_6 standard from NIST was subtracted from the experimental data.

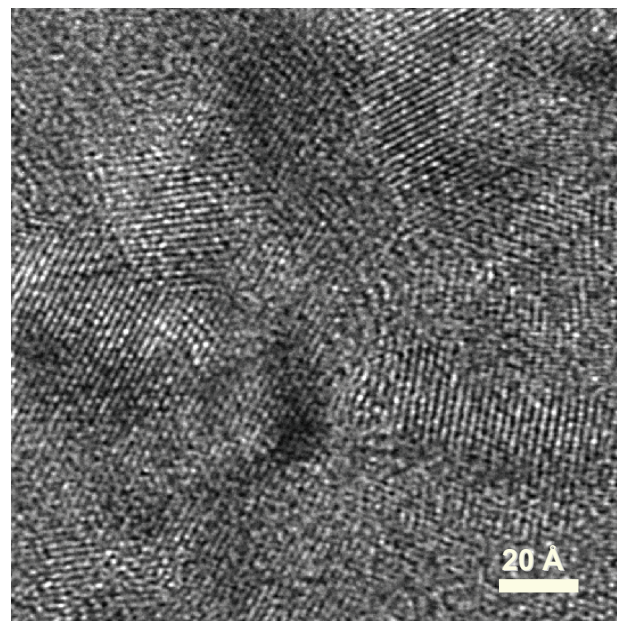


Fig. 9. HRTEM micrograph of the sample with the overall chemical composition $\text{Cr}_{0.40}\text{Al}_{0.52}\text{Si}_{0.08}\text{N}$.

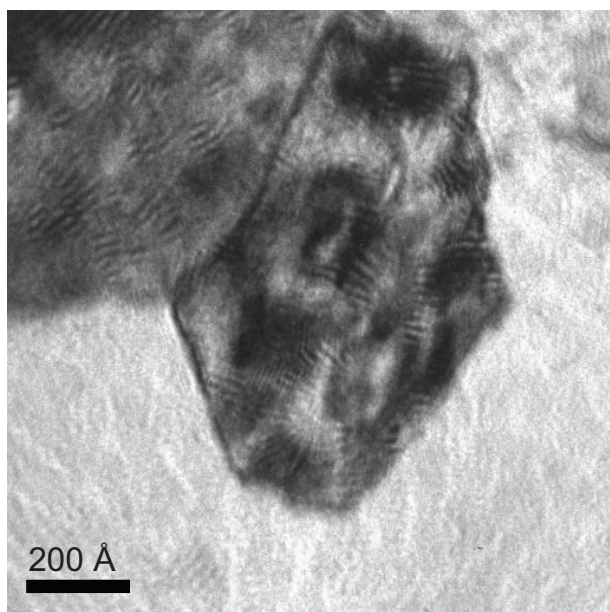


Fig. 10. HRTEM micrograph of the sample with the overall chemical composition $Cr_{0.91}Al_{0.08}Si_{0.01}N$.

CONCLUSIONS

It was shown that broad reciprocal lattice points from nanosized crystallites can overlap each other. This overlap of the reciprocal lattice points reduces the broadening of the diffraction lines as seen by X-ray diffraction. In the direct space, the overlap of the reciprocal lattice points is equivalent to the partial coherence of adjacent crystallites that “enlarges” their size as seen by X-rays. As the overlap of the reciprocal lattice points decreases with increasing size of the diffraction vector, the effect of the partial coherence of crystallites on the line broadening varies with the diffraction angle, which can be used to obtain the following microstructural information from the XRD line broadening.

- Size of individual partially coherent crystallites can be calculated from the maximum (saturated) diffraction line broadening observed for large diffraction angles.
- Mean local disorientation of the individual partially coherent neighbouring crystallites is related to the size of the diffraction vector, for which the partial coherence of crystallites disappears.
- Size of the blocks composed of individual partially coherent crystallites can be estimated from the extrapolation of the diffraction line broadening to $q = 0$.

The partial coherence of neighbouring crystallites was observed in materials consisting of nanocrystalline domains with a strong local preferred orientation of crystallites. Nanocrystalline domains are necessary for getting broadened reciprocal lattice points; strong local texture is needed for a sufficient overlap of the reciprocal lattice points from neighbouring crystallites. The last requirement for the partial coherence of nanocrystallites is that the distance of such nanocrystallites must be smaller than the coherence length of the X-rays used for the experiment, which is a general optical requirement for interference of scattered waves.

ACKNOWLEDGEMENTS

The authors appreciate the financial support of the project number RA-1050/9-1 through the German Research Council (DFG). The HRTEM JEM 2010 FEF was financed through DFG in the frame of the Priority program number 1062. Furthermore, we thank Dr. M. Šíma and M. Růžicka (SHM Ltd., Šumperk, Czech Republic) for providing us with samples of the Ti-Al-Si-N and Cr-Al-Si-N thin films nanocomposites.

REFERENCES

- * On leave from the Department of Condensed Matter Physics, Faculty of Mathematics and Physics, Charles University Prague, Czech Republic
- [1] R.L. Snyder, J. Fiala, H.J. Bunge: *Defect and Microstructure Analysis by Diffraction*, Oxford University Press, 1999.
- [2] N. Guillou, J.P. Auffrédic, D. Louër, *Powder Diffraction* **10** (1995) 236.
- [3] J.I. Langford, D. Louër, P. Scardi, *J. Appl. Cryst.* **33** (2000) 964.
- [4] A. Cervellino, C. Giannini, A. Guagliardi, *J. Appl. Cryst.* **36** (2003) 1148–1158.
- [5] D. Rafaja, M. Šíma, V. Klemm, G. Schreiber, D. Heger, L. Havela, R. Kužel, *J. Alloys Comp.* **378** (2004) 107.
- [6] D. Rafaja, V. Klemm, G. Schreiber, M. Knapp, R. Kužel, *J. Appl. Cryst.* **37** (2004) 613.
- [7] G. Ribárik, N. Auderbrand, H. Palancher, T. Ungár, D. Louër, *J. Appl. Cryst.* **38** (2005) 912.
- [8] A. Cervellino, C. Giannini, A. Guagliardi, M. Ladisa, *Phys. Rev.* **B72** (2005) 035412.
- [9] D. Rafaja, A. Poklad, V. Klemm, G. Schreiber, D. Heger, M. Šíma, M. Dopita, *Thin Solid Films* **514** (2006) 240–249.
- [10] C. Giacovazzo, H.L. Monaco, G. Artioli, D. Viterbo, G. Ferraris, G. Gilli, G. Zanotti, M. Catti: *Fundamentals of Crystallography*, 2nd Edition, IUCr Texts on Crystallography 7, Oxford University Press, 2002.
- [11] M. Born, E. Wolf: *Principles of Optics*, 7th Edition, University Press, Cambridge, 1999.
- [12] U. Pietsch, V. Holý, T. Baumbach: *High-Resolution X-Ray Scattering – From Thin Films to Lateral Nanostructures*, Springer, Berlin, 2004.
- [13] H.-D. Männling, D.S. Patil, K. Moto, M. Jílek, S. Veprek, *Surf. Coat. Technol.* **146** (2001) 263.
- [14] A.E. Santana, A. Karimi, V.H. Derflinger, A. Schütze, *Thin Solid Films* **469** (2004) 339.
- [15] A. Hörling, L. Hultman, M. Odén, J. Sjölen, L. Karlsson, *Surf. Coat. Technol.* **191** (2005) 384.
- [16] A. Flink, T. Larsson, J. Sjölen, L. Karlsson, L. Hultman, *Surf. Coat. Technol.* **200** (2005) 1535.
- [17] D. Rafaja, M. Dopita, M. Růžicka, V. Klemm, D. Heger, G. Schreiber, M. Šíma, *Surf. Coat. Technol.* **201** (2006) 2835–2843.
- [18] D.B. Williams, C.B. Carter: *Transmission Electron Microscopy III – Imaging*, Plenum Press, New York, 1996.